SCUOLA SUPERIORE MERIDIONALE

University of Naples Federico II

DOCTORAL THESIS

in Cosmology, Space Science & Space Technology

Aerodynamic Modeling and AI-Based Optimal Guidance and Control for Low Earth Orbit Missions

Author:
Emanuela Gaglio

Supervisors:
Ch.mo Prof. Raffaele Savino
Ch.mo Prof. Riccardo Bevilacqua

Submitted in fulfilment of the requirements for the degree of Doctor of Philosophy in Cosmology, Space Science & Space Technology.
Coordinator: Prof. Salvatore Capozziello.

"When it feels scary to jump, that is exactly when you jump, otherwise you end up staying in the same place your whole life."

— Abel Morales, A Most Violent Year (2014)

Acknowledgments

A special acknowledgment goes to Prof. Salvatore Capozziello, coordinator of the PhD program in Cosmology, Space Science and Space Technology at the Scuola Superiore Meridionale, for the many opportunities he offered me and for his constant support. His availability and trust in my abilities have been a constant presence over these years.

I wish to thank one of my supervisors, Prof. Raffaele Savino, with whom I have been collaborating for almost ten years. He has been a fundamental reference throughout my academic journey and in the development of all my theses: bachelor's, master's and doctoral. Thank you for the example of academic excellence and dedication you have passed on to me and for allowing me to spend part of my PhD in the United States, providing invaluable opportunities for growth.

A special acknowledgment also goes to my second supervisor, Prof. Riccardo Bevilacqua, with whom I have been collaborating since 2022 and thanks to whom I embarked on a new and stimulating research path. His scientific excellence and constant support allowed me to carry it forward successfully. I thank him for the opportunities he offered me and for being a fundamental point of reference, especially during my time in the United States. His "how are you?" messages during challenging moments always encouraged me to stay committed and not lose heart.

My sincere thanks go to Prof. Rodrigo Cassineli Palharini and his research group for the valuable collaboration and for providing the DSMC data, essential for comparison with the CFD results.

Further thanks go to the group led by Prof. Stefanos Fasoulas and, in particular, to Dr. Constantin Traub, for the collaboration and the precious scientific discussions on the collision avoidance study.

A warm thought goes to the colleagues from the "centro di calcolo", with whom I shared daily moments, mutual support and a great deal of science. To the "veterans": Stefano, a constant academic and personal reference since 2018; Sergio, with whom I began this journey and who went from colleague to friend and confidant; Antonio, always able to make me smile even despite our constant teasing; and Riccardo G., for his continuous support and for being a truly precious friend. My thanks also go to the "newcomers": Giusy, Daniele, the two Gennaros, Raffaele and Dylan, who, despite the short time spent together due to my stay in the United States, helped make the environment livelier, more serene and full of energy. A special thanks to Giusy, Daniele and Gennaro C., with whom I shared a bit more time after my return, finding sincere and affectionate people, offering support, companionship and many laughs.

My sincere thanks go to my colleagues at the SSM, in particular to my five travel companions now like brothers: Manuel, Tobia, Nicola, Davide and Alessio. Without you this journey would not have been the same. We shared unforgettable moments, through both joys and difficulties, and I hope that the end of this path does not mark the end of our friendship. I care deeply for you, as shown by the tear that falls as I write these acknowledgments.

Thanks also to all the other people I met at the SSM, in particular Marcello, Carmen, Teresa and Valentina. Without you this experience would not have been the same.

My heartfelt thanks go to the friends I met during my stay in the United States: Jhonathan, Omkar, Carlo, Luis, Pol, Alvaro, Katharine, John, Ryan, Nicolò and Khushboo for sharing with me such an important part of my PhD and for making my stay warmer, easier and more familiar. A special thanks goes to Katharine and John, with whom I shared a large and meaningful part of my life in the United States.

To my best friend Antimo, now like a brother. We have shared almost twenty years of experiences and I hope we will continue to do so for many more. Thank you for your constant support and for being close to me even when almost 10000 km separate us.

Thank you to Martina and Antonia, always ready to support me, despite the distance between me in the United States and them in Italy over the past years.

A special thank you to my dear friend Rita: every time we see each other, time seems to stand still. It is always a pleasure to share moments together.

My deepest thanks go to my family, who always supported me even in the middle of the emotional turmoil we were facing. To my father, for never giving up in life and for always pushing me not to be discouraged by difficulties. To my mother, for her constant support toward me and my choices, even when painful. To my sister, for her endless strength and her gentle and calm nature, capable of soothing my inner chaos like no one else.

I also wish to mention my Sicilian family, my grandmother Rosalia, aunt Roberta and uncle Nino. Thank you for always being there and for making me feel your love and support, despite the distance. I love you.

An affectionate acknowledgment goes to my boyfriend, for accompanying and supporting me through every step of this journey. Thank you for your patience, for embracing and supporting my choices even when they were difficult and for sharing part of the experience in the United States with me. Your presence has been a constant source of strength.

To conclude, a thank you to uncle Enzo and aunt Angela for their presence and constant affection.

Ringraziamenti

Un ringraziamento speciale va al Prof. Salvatore Capozziello, coordinatore del programma di dottorato in Cosmology, Space Science and Space Technology alla Scuola Superiore Meridionale, per le molteplici opportunità che mi ha offerto e per il suo costante supporto. La sua disponibilità e fiducia nelle mie capacità sono state per me una presenza costante in questi anni.

Desidero ringraziare uno dei miei supervisors, il Prof. Raffaele Savino, con cui collaboro ormai da quasi dieci anni. È stato un riferimento fondamentale in tutto il mio percorso accademico e nella realizzazione di tutte le mie tesi, triennale, magistrale e di dottorato. Grazie per l'esempio di eccellenza accademica e dedizione che mi ha trasmesso e per avermi permesso di trascorrere parte del mio dottorato negli Stati Uniti, offrendo così preziose esperienze di crescita.

Un ringraziamento speciale va anche al mio secondo supervisor, il Prof. Riccardo Bevilacqua, con cui collaboro dal 2022 e grazie al quale ho intrapreso un nuovo e stimolante filone di ricerca. La sua eccellenza scientifica e il supporto costante mi hanno permesso di portarlo avanti con successo. Lo ringrazio per le opportunità che mi ha aperto e per essere stato un punto di riferimento fondamentale, soprattutto durante la mia permanenza negli Stati Uniti. I suoi "come stai?" nei momenti difficili mi hanno sempre spronato a dare il meglio e a non perdermi d'animo.

Un sentito ringraziamento al Prof. Rodrigo Cassineli Palharini e al suo gruppo di ricerca per la preziosa collaborazione e per aver fornito i dati DSMC, fondamentali per il confronto con i risultati CFD.

Un ulteriore ringraziamento va al gruppo del Prof. Stefanos Fasoulas e, in particolare, al Dr. Constantin Traub, per la collaborazione e le preziose discussioni nella parte relativa al collision avoidance.

Un pensiero affettuoso va ai ragazzi del centro di calcolo, con cui ho condiviso momenti quotidiani, supporto reciproco e tanta scienza. A quelli "storici": Stefano, costante punto di riferimento accademico e personale fin dal 2018; Sergio, con cui ho iniziato questo percorso e che da collega è diventato amico e confidente; Antonio, capace di strapparmi sempre un sorriso anche nonostante i nostri continui "punzecchiamenti"; e Riccardo G., per il suo sostegno costante e per essere un amico prezioso. Un ringraziamento va anche ai "nuovi": Giusy, Daniele, Gennaro al quadrato, Raffaele e Dylan, che nonostante il poco tempo trascorso insieme, dato il mio soggiorno negli Stati Uniti, hanno contribuito a rendere l'ambiente più vivo, sereno e ricco di energia. Un grazie speciale a Giusy, Daniele e Gennaro C., con cui ho condiviso un pò di più dopo il mio rientro, ritrovando persone sincere e affettuose, tra supporto, compagnia e tante risate.

Un grazie sincero ai miei colleghi della SSM, in particolare ai miei cinque compagni di viaggio ormai fratelli: Manuel, Tobia, Nicola, Davide e Alessio. Senza di voi questo percorso non sarebbe stato lo stesso. Abbiamo condiviso momenti indimenticabili, tra gioie e difficoltà, e spero che la fine di questo cammino non segni la fine della nostra amicizia. Vi voglio bene, come dimostra la lacrimuccia che mi scende mentre scrivo questi ringraziamenti.

Un grazie anche a tutte le altre persone incontrate alla SSM, in particolare Marcello, Carmen, Teresa e Valentina. Senza di voi questa esperienza non sarebbe stata la stessa.

Un ringraziamento di cuore va ai ragazzi che ho incontrato durante la mia permanenza negli Stati Uniti: Jhonathan, Omkar, Carlo, Luis, Pol, Alvaro, Katharine, John, Ryan, Nicolò e Khushboo per aver condiviso con me una parte fondamentale del mio dottorato e per aver reso la mia permanenza più semplice, calda e familiare. Un grazie speciale a Katharine e John, con cui ho condiviso un grande pezzo della mia vita americana.

Al mio migliore amico Antimo, ormai come un fratello. Abbiamo condiviso quasi venti anni di esperienze e spero che continueremo a farlo ancora a lungo. Grazie per il tuo supporto costante e per la vicinanza, anche quando ci separano quasi 10000 km.

Grazie a Martina e Antonia, sempre pronte a sostenermi, nonostante la distanza tra me negli Stati Uniti e loro in Italia negli ultimi anni.

Un ringraziamento speciale alla mia cara amica Rita: ogni volta che ci rivediamo il tempo sembra fermarsi, ed è sempre un piacere condividere momenti insieme.

Un grazie profondo alla mia famiglia, che mi ha sempre sostenuta anche nel mezzo del tornado emotivo che stavamo vivendo. A mio padre, per non essersi mai arreso alla vita e per avermi sempre spinto a non lasciarmi abbattere dalle difficoltà. A mia madre, per il suo supporto costante verso di me e le mie scelte, anche quando dolorose. A mia sorella, per la sua forza infinita e il carattere dolce e pacato, capace di placare il mio caos interiore come nessun altro.

Non dimentico la mia famiglia siciliana, mia nonna Rosalia, zia Roberta e zio Nino. Grazie per esserci sempre e per farmi sentire il vostro affetto e supporto, nonostante la lontananza. Vi voglio bene.

Un ringraziamento affettuoso al mio fidanzato, per avermi accompagnata e sostenuta in ogni passo di questo viaggio. Grazie per la tua pazienza, per aver accolto e appoggiato le mie scelte anche quando sono state difficili e per aver condiviso con me parte dell'esperienza negli Stati Uniti. La tua presenza è stata una certezza.

Per concludere, un grazie a zio Enzo e zia Angela per il loro sostegno e la loro vicinanza.

Abstract

The Low Earth Orbit (LEO) environment is currently experiencing a significant evolution, largely driven by the surge of small satellites, such as CubeSats, and the deployment of large-scale constellations. While LEO provides strategic advantages such as proximity to Earth, reduced communication latency, and lower launch costs, these benefits come at the expense of increasingly complex operational challenges. Among the most significant issues are the non-negligible influence of aerodynamic actions, which necessitate continuous orbit maintenance and maneuvers, as well as the growing threat posed by space debris and potential collisions. These factors demand a new generation of guidance and control (G&C) strategies capable of ensuring the success of the mission and, at the same time, the long-term sustainability. The situation is particularly critical for small satellite platforms, including CubeSats, often operating with stringent constraints on mass, volume, and safety, making traditional propulsion systems impractical or unfeasible. As a result, there is an growing need to explore alternative, propellantless methods of control that are not only efficient but also compatible with the limited resources available on board these platforms. At the same time, the increasing number of satellites in the LEO environment requires these methods to be highly precise, adaptive, and capable of real-time execution to support autonomous maneuvering, de-orbiting, and collision avoidance. This dissertation fits in this framework by proposing an integrated G&C framework actively exploiting aerodynamic forces as the primary mechanism for orbital maneuvering and control. The research is developed through two complementary and interdependent steps. The first involves a high-fidelity aerodynamic characterization of re-entry systems, including both inflatable and deployable systems with flaps embedded at the end of the heatshield, which are designed to exploit atmospheric forces for orbit modification. This is achieved through an extensive campaign of numerical simulations combining Computational Fluid Dynamics (CFD) and Direct Simulation Monte Carlo (DSMC) techniques. By capturing the complex flow interactions across a wide range of altitudes and flow regimes, from the rarefied environment to transitional and continuum, these models provide a robust foundation for an accurate prediction of the forces. The deployable concept, featuring control flaps at the end of the heatshield, was further analyzed to assess its capability for attitude control through multiple flap deflection combinations. The second component of this work introduces a novel hybrid G&C architecture that merges optimal control theory with Artificial Intelligence (AI) techniques to enable autonomous, onboard decision-making. This approach is designed to preserve optimality while exploiting AI-driven methods to significantly reduce computational cost and response time, as well as to robustly manage unpredictable perturbations. This aspect is particularly critical in LEO, where aerodynamic forces are difficult to predict with accuracy and external disturbances can be substantial. As a result, the system is capable of solving complex control problems in real-time, a critical requirement for autonomous space operations. The proposed methodology has been rigorously validated through

three representative mission scenarios. The first focuses on the development of a time-optimal drag-based de-orbiting algorithm, capable of precisely targeting locations at the re-entry interface. The second investigates a controlled atmospheric re-entry and landing strategy based on AI for adaptive feedback in response to variable aerodynamic conditions. The third explores a collision avoidance framework based on aerodynamic maneuvering, designed to maximize the miss distance from incoming debris while minimizing orbital perturbations and preserving mission objectives. As a whole, the proposed work delivers a comprehensive and forward-looking contribution to the field of aerodynamics and G&C in LEO. The dissertation not only advances the state-of-art in propellantless orbital maneuvering but also lays the groundwork for more sustainable, autonomous, and resilient operations in a progressively more congested and contested orbital environment.

Contents

1 Introduction

1.1 Motivation

Space activities in Low Earth Orbit (LEO) are undergoing a revolution that began in the middle of the last decade, with the sudden and rapid increase in the launches of small satellites, including CubeSats, and has become clearly evident with the deployment of the first large constellations of satellites [1].

LEO provides an ideal environment for multiple scientific purposes ranging from research to hardware testing for exploration use and crew training [2]. It offers different advantages. First, it is relatively easy to reach with the current available launch technology, requiring less energy and rocket power than higher orbits. Additionally, its proximity to the Earth results in minimal latency for signals, making it suitable for applications that require real-time communication. It also allows for high-resolution imaging and detailed observation of the surface of the Earth. Furthermore, LEO satellites can transmit and receive data at a faster rate, enabling higher data throughput and efficient data transfer. LEO satellites can be organized in constellations to provide global coverage for various services, including internet access and communication. On the other hand, it also presents disadvantages. First, a satellite in LEO exhibits a limited coverage area compared to those located in higher orbits, reflecting the need for large constellations for continuous global coverage. Additionally, in LEO, the aerodynamic forces, particularly drag, are not negligible, requiring continuous re-boosting or replacements. Furthermore, the increasing number of objects in LEO raises concerns about collisions and the generation of space debris, potentially impacting future missions and astronomical observations. Overall, LEO is a critical region for current and future space activities, offering a balance of accessibility, performance, and cost-effectiveness for different applications [2–5].

This dissertation fits within this framework by addressing key topics related to space missions in LEO. In particular, it focuses on fluid dynamics aspects, as well as guidance and control (G&C) strategies that exploit aerodynamic forces as control mechanisms, crucial for successful missions of satellites operating in this orbital region. This is in response to the increasing number of satellites, such as CubeSats, that are not equipped with propulsion systems due to safety concerns or mass and weight constraints. In these cases, aerodynamic forces can be exploited for G&C purposes to reach a desired target. That is one of the main reasons why accurate aerodynamic modeling in LEO is crucial. Some technological solutions to affect the aerodynamic characteristics of a satellite include the employment of retractable tape-spring booms [6, 7] or mechanisms able to modulate the drag by varying the aerodynamic shape of the spacecraft [8–11]. In the current dissertation, both strategies will be aerodynamically investigated in different conditions.

1.2 Objectives

The main objective of this thesis is to provide a comprehensive assessment of a novel integrated fluid dynamics and hybrid G&C framework for satellites operating in LEO. This will be achieved by exploring innovative methodologies aligned with current technological and research trends. To support the primary goal, the following specific objectives are pursued:

1. Develop a detailed aerodynamic characterization of inflatable and deployable re-entry systems under various representative flight conditions. This includes the use of both Computational Fluid Dynamics (CFD) and Direct Simulation Monte Carlo (DSMC) methods, selected according to the flow regime, ranging from continuum to rarefied.

2. Design and implement a novel hybrid G&C framework that combines optimal control theory with Artificial Intelligence (AI). This hybrid approach aims to:

    - Enable a flexible customization of the cost functions to accommodate different mission objectives;
    - Integrate AI techniques to enhance accuracy and robustness to perturbations, as well as, reduce the computational cost, ensuring the framework is suitable for real-time, on-board implementation.

    Multiple relevant space scenarios will be examined, with tailored strategies proposed for each case.

3. Investigate the coupling between aerodynamic forces and G&C strategies to assess their mutual influence and potential synergies in satellite performance and maneuverability.

1.3 Outline

This dissertation is organized as follows. Chapter 2 provides an overview of the state-of-art related to aerodynamic-based control for satellites operating in LEO and during atmospheric re-entry. After presenting the main technological solutions available to achieve propellantless control, the chapter proceeds to discuss the principal G&C strategies applicable in these scenarios. Chapter 3 introduces the main methodologies employed in this work, including fluid dynamics, optimal control theory, and AI aspects. Chapters 4 and 5 focus on the aerodynamic assessment of inflatable and deployable re-entry systems, respectively. Each chapter describes the system configuration and geometric specifications, followed by the aerodynamic set-up and grid generation, and concludes with a detailed discussion of the simulation results and comparisons of the two approaches. Chapters 6, 7, and 8 address the G&C framework applied to relevant mission scenarios in LEO: de-orbiting, atmospheric re-entry, and collision avoidance. Each chapter begins with a description of the mission context, followed by an assessment of the optimal control algorithms used to train the AI-based architectures described at the end. Finally, a chapter of conclusions summarizes the main findings and relevant remarks of this thesis.

2 Relevant Literature

2.1 Aerodynamic-Based Control for Satellites in LEO and Atmospheric Re-entry

2.1.1 Propellantless Control in LEO

In recent years, the number of CubeSats and small satellites lacking an onboard propulsion system has significantly increased, primarily due to safety constraints, mass limitations, and the advantages of standardized platforms. As a result, there is growing interest in propellantless control strategies to accomplish the space mission objectives.

One adopted approach is the aerodynamic modulation by changing the attitude, affecting the effective section exposed to atmospheric flow without changing the geometric shape of the satellite. This method relies on the re-orientation of the device to control the aerodynamic forces, typically by varying the angle of attack. An example of this approach is represented by the SOURCE CubeSat (Stuttgart Operated University Research CubeSat for Evaluation and Education), shown in Figure 2.1. It is a 3U+ CubeSat developed by the Small Satellite Student Group (KSat e.V.) and the Institute of Space Systems at the University of Stuttgart, scheduled for launch by the European Space Agency (ESA) as part of Fly Your Satellite! program [12–14].The smallest projected area is achieved at zero angle of attack, while the maximum area corresponds to 90°, when the panels are fully exposed to the flow.

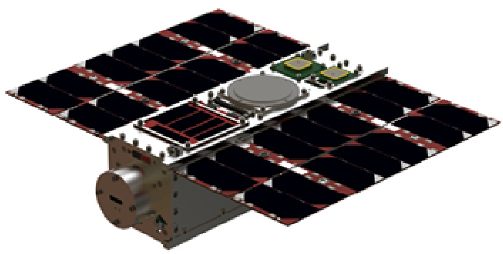

Figure 2.1: Example of satellite with panels (SOURCE CubeSat).

An alternative control strategy involves the modification of the external geometry of the satellite. A representative example is the Drag Deorbit Device (D3) [6, 15–17], shown in Figure 2.2, which is equipped with four retractable tape-spring booms that deploy to increase the drag and enable controlled orbital decay.

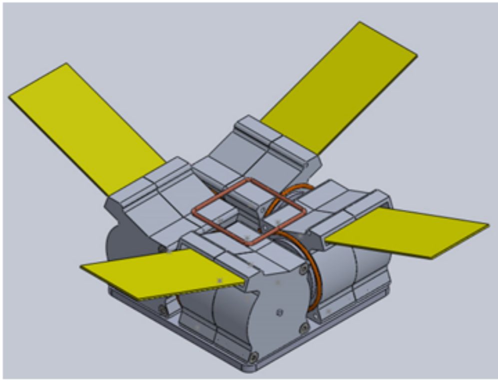

Figure 2.2: Schematic of the D3 deorbit system.

Another representative example of propellantless control in LEO is presented and discussed in the next section.

2.1.2 Deployable and Inflatable Systems

Deployable and inflatable aerodynamic decelerators have emerged as promising solutions for enabling the re-entry and recovery of small satellites after missions in Low Earth Orbit. Compared to rigid heat shields, these systems are more compact and lightweight, remaining stowed during launch and deploying only when needed.

The first conceptual design exploiting a deployable system solution was the ParaShield project, developed during the fall of 1988. It is considered a turning point for deployable re-entry systems not only because of its role as a pathfinder for this technology but also for changing how the design of Entry Descent and Landing (EDL) systems was approached, aiming at the reduction of the Ballistic Coefficient B in Equation 2.1:

$$B = \frac{m}{SC_D} \tag{2.1}$$

As shown in [18, 19], reducing the ballistic coefficient significantly decreases the peak heating rate and deceleration loads. Following this concept, the University of Maryland developed a prototype named Skidbladnir in 1989. The suborbital flight onboard the SET-1 launch vehicle was not successful due to insufficient thrust, which prevented the rocket from lifting off [18].

Following these early efforts, research diverged into two main directions: inflatable systems and mechanically deployable systems. The first one was explored in programs such as the Inflatable Re-entry and Descent Technology (IRDT), initiated under the Mars-96 program by the Babakin Space Center and ESA [20, 21]. In parallel with ESA's efforts to implement the IRDT program, NASA decided to invest resources in a research program directed at the development and the performance assessment of Hypersonic Inflatable Aerodynamic Decelerators (HIADs) [22]. The focus on these subjects required to address three main challenges: surviving the heat pulse during atmospheric entry, demonstrating system performance at relevant scales, and demonstrating controllability in the atmosphere. Results of the extensive analyses carried out throughout the years, including the NASA's Inflatable Re-entry Vehicle Experiment (IRVE), are presented in a wide collection of peer-reviewed papers available in the scientific literature [22–31].

Mechanically deployable systems were pioneered with the BREMSAT-2 capsule, developed by the University of Bremen in 1992. This design featured an umbrella-like deployable heat shield called Parashield, significantly increasing the frontal area and allowing the use of commercial thermal protection materials [20]. Subsequent concepts attempted to integrate similar systems into 3U and 6U CubeSat platforms, although the limited volume and mass availability imposed strict constraints on the payload.

To overcome this limitation, some concepts proposed wrapping the re-entry system around the CubeSat form factor. Two major programs exploited this approach. The Adaptive Deployable Entry and Placement Technology (ADEPT) project be NASA introduces a lightweight umbrella-shaped shield compatible with 3U and 12U configurations [32–34]. At the same time, the Italian program IRENE (Italian Re-Entry Nacelle) is designed to support the recovery of payloads from the ISS and reusable scientific experiments in LEO through a similar deployable mechanism [35].

2.1.3 Control Challenges in Deployable Systems

Deployable re-entry systems offer significant advantages in terms of mass and volume, but also present challenges in spacecraft control. One major design change is the elimination of the traditional backshell, which typically provides thermal and aerodynamic protection to the payload during its return through the atmosphere [24]. This is due to the reduction in thermal and mechanical loads achieved by reducing the ballistic coefficient. Moreover, the absence of a backshell facilitates access to the payload during integration and allows direct structural and electrical interfaces with the launch vehicle.

However, this new configuration limits the options for implementing traditional Reaction Control Systems (RCS). Thrusters located close to sensitive areas may generate undesired interactions due to hot exhaust plumes or chemical contamination [36, 37]. Additionally, placing the RCS near the center of mass may reduce its effectiveness for attitude control [38].

To address these limitations, NASA's Space Technology Mission Directorate (STMD) launched the Pterodactyl project in 2018 [37]. The main objective was to explore alternative guidance and control strategies that could be integrated with Deployable Entry Vehicles (DEVs) and function effectively without conventional thrusters. After some investigations, a system based on flaps resulted the option experiencing the best performance. On the same wavelength, Italy proposed a similar concept with a deployable heat shield equipped with flaps for controllability and maneuverability purposes [8].

2.2 Guidance and Control in LEO

Within the growing interest in aerodynamic-based satellite control, various strategies have been explored. This dissertation focuses on G&C techniques based on optimal control theory and artificial intelligence. These methods are applied to three key mission scenarios: de-orbiting, atmospheric re-entry, and collision avoidance.

2.2.1 Drag-Based De-Orbiting and Re-Entry

Since the beginning of human activity in space, protecting people and properties from spacecraft-related damage has become a crucial consideration for engineers [39, 40]. To ensure a satellite or capsule lands in a desired location, and to avoid debris damage to population and ground assets, a controlled de-orbiting is imperative, for both manned and unmanned space missions. In addition to protecting objects on the ground, controlled de-orbiting is also important for missions involving scientific experiments demanding the recovery of samples for further analysis (e.g., biological samples, medical monitoring equipment, pharmaceutical testing).

In most of the existing literature, the focus is on satellite de-orbiting performed using a de-orbit burn, which is based on the application of thrust in an opposite direction with respect to the satellite motion to reduce the orbital speed and subsequently lower the orbit. An alternative de-orbiting control mechanism, and object of the current work, is drag modulation, which exploits atmospheric drag variation to achieve the necessary orbital energy reduction from the initial condition to the re-entry interface. Even though the drag is employed as control mechanism in different space applications, a limited number of works focuses on its application to achieve a controlled de-orbit [15–17, 41, 42].

In [41], authors propose a drag-based de-orbiting algorithm to be used in the $\Delta DSat$ mission [43]. The algorithm relies on an analytical solution to determine the ballistic coefficient profile necessary to reach a desired de-orbiting point. The profile is based on a two phases decay trajectory and the ballistic coefficient C_b is defined in Eq. 2.2:

$$C_b = \frac{C_d S}{2m} \tag{2.2}$$

In the first phase, the satellite is supposed to maintain a constant parameter C_{b1} until reaching a specific value of semi-major axis a_{swap}. After that, during then second phase, the satellite switches to a different ballistic coefficient C_{b2}. The method is based on an analytical solution to establish a mapping between the initial conditions, control inputs (C_{b1}, C_{b2}, a_{swap}) and the resulting re-entry point. This mapping is then used to analytically calculate the control parameters needed to target a desired location. However, the use of an analytical solution presents some limitations:

- The use of an analytical exponential density model, without accounting for possible fluctuations.
- The assumptions of a circular orbit and a monotonically decreasing semi-major axis. In fact, due to the Earth's oblateness, the J_2 perturbation introduces significant variations in both altitude and semi-major axis throughout each orbit. As a result, the assumptions that atmospheric density depends solely on the semi-major axis and that the semi-major axis decreases monotonically are restrictive.
- The analytical solution involves the evaluation of a complex function that is often computationally expensive. To simplify this, authors reformulated the control parameters in terms of ΔC_b and a_{swap}, but the problem still presents many local minima in the targeting error. As a result, even when the target point is not directly under the orbital path, local minima can occur near the closest approach to the desired location.

In [42], the ballistic coefficient profile to guarantee land or break-up in a specific location is generated using the optimization tool developed by NASA: Program to Optimize Simulated Trajectories II. The optimizer is not tackled for this problem and thus does not have performance or convergence characteristics of an optimization scheme that is based on orbital mechanics principals. In additions, the methods are computationally expensive and may be unsuitable for onboard use

In [15–17], authors exploits another numerical technique for the modulation of the ballistic coefficient and reach a desired de-orbiting point. A trajectory is generated in which the spacecraft maintains a certain ballistic coefficient C_{b1} until a time t_{swap}, C_{b2} until t_{term}, and $C_{b\text{tem}}$ until the de-orbiting point, fixed at an altitude of 70 km. The adopted procedure is based on the estimation of the control parameters C_{b1}, C_{b2}, and t_{swap} to reduce the final error between the desired and the evaluated de-orbiting point. However, this procedure only attempts to minimize the final error on the de-orbiting point without considering the maneuver duration. In addition, it relies on the assumption that the x-axis of both the Earth-Centered Inertial (ECI) and Earth-Centered Earth-Fixed (ECEF) frames are aligned at the beginning of the maneuver. This is a strong assumption, as the x-axis of the ECI frame is defined relative to the Greenwich meridian, which depends on the specific date and time.

A de-orbiting maneuver, reaching a target point at the re-entry interface, is crucial also to ensure re-entry and landing in a designated area on Earth. Most of the relevant literature addresses the aerodynamic-based re-entry for larger devices, such as spaceplane. Only few of them addresses the problem for smaller concepts of devices. The authors in [8] investigated the feasibility of a control system based on flaps for a deployable device. In [44] an algorithm for precise re-entry and landing for this device has been proposed, based on the de-orbit point identification to ensure reaching a desired landing point. Even though the work presents noteworthy results, it is characterized by limitations relying on the accuracy of the initial de-orbit point determination, which is sensitive to uncertainties in atmospheric models and in-flight conditions.

2.2.2 Collision Avoidance

The increasing number of satellites in LEO led to a rapid increase in space debris, posing an imminent and substantial threat by elevating the number of conjunctions which increase the risk of collisions [45]. If unaddressed, this growing hazard could significantly interfere with future space operations, highlighting the critical need for effective mitigation measures [46]. In recent years, significant advances in autonomous trajectory generation algorithms for spacecraft slew maneuvers [47] and for de-orbiting with multiple collision avoidance [48] has been made. In addition, deterministic artificial intelligence has been proven to permit uncertainty control of microsatellites [49] and applied as a novel learning approach for the control of nonlinear spacecraft dynamics [50].

If the satellite under investigation is equipped with a propulsion system, the latter can be used for active collision avoidance. If, however, a satellite encounters challenges related to mass or weight constraints and consequently is lacking a dedicated propulsion system, the natural environment of the satellite represents an alternative means to enable propellant-free orbit control, e.g. using electrodynamic tethers [51], solar-radiation pressure [52] or the geomagnetic Lorentz force [53]. The most logical approach in LEO is to exploit the most dominant perturbation effect for the orbit regime of interest.

A limited number of studies have explored the use of aerodynamic drag for controlled collision avoidance. In particular, the authors in [54] proposed a time-optimal analytical solution to achieve a specific miss distance between a satellite and nearby debris by modulating the ballistic coefficient of the spacecraft. However, their approach is subject to typical limitations of analytical formulations, such as the assumption of constant atmospheric density, a non-rotating atmosphere, and circular orbits. These simplifications, while enabling closed-form solutions, affects the accuracy of the model when applied to real-world scenarios involving atmospheric density fluctuations due to solar activity, orbital eccentricity, or Earth's rotation.

Koenig and D'Amico [55] investigated the arrangement of satellite constellations aimed at minimizing long-term collision risks. Nevertheless, the work did not tackle the challenge posed by the abrupt emergence of an impending impact scenario with an uncooperative and previously unidentified space object.

Mishne and Edlerman [56] employed aerodynamic drag and solar pressure to avoid an impending collision, focusing on the maximization of the miss distance to the debris object.

Turco et al. [57] built upon the work of Omar and Bevilacqua [54] and proposed a planning tool for aerodynamically controlled collision avoidance maneuvers and applied it in a case study to the Flying Laptop satellite [58].

Since all of these methods are based on simplified assumptions, such as constant density values, a non-rotating atmosphere or a perfectly circular orbit, they are unable to accurately depict the complicated dynamics of real-world scenarios.

2.3 Relevant Work by the Author

The research activities carried out by Emanuela Gaglio within this doctoral work provide original and high-impact contributions to the fields of atmospheric re-entry, aerodynamic control, and space traffic management. Her research work was carried under the supervision of Prof. Raffaele Savino (University of Naples Federico II) and Prof. Riccardo Bevilacqua (Embry Riddle Aeronautical University - Daytona Beach Campus). She dedicated 30 months of her PhD program in Italy, at the Scuola Superiore Meridionale, and 18 months abroad at the Embry-Riddle Aeronautical University (ERAU), joining the ADvanced Autonomous MUltiple Spacecraft (ADAMUS) lab under the guidance of Prof. Riccardo Bevilacqua.

In addition to her primary supervisors, she collaborated with several academic and research institutions in both European and overseas institutions. Her research has been primarily directed toward two main areas:

- Under the guidance of Prof. Raffaele Savino, a comprehensive aerodynamic assessment was conducted under relevant flight conditions, considering both deployable and inflatable systems. The analysis considers different phases of the mission, including both LEO environment and atmospheric re-entry, and employs both Computational Fluid Dynamics (CFD) and Direct Simulation Monte Carlo (DSMC) methods depending on the flow regime. This dual approach enabled robust modeling of transitional regimes and led to the development of a bridging function to connect the continuum and rarefied flow domains. Additionally, a flap-based control mechanism integrated into a deployable system was evaluated to assess its aerodynamic performance and control effectiveness. The DSMC simulations have been performed by Prof. Rodrigo Cassineli Palharini and his research team as part of an international collaboration. Their simulations were used for comparison with the CFD analysis, providing a comprehensive characterization of the aerodynamic behavior of the system. The work resulted in the publication of 3 journal papers on Aerospace Science and Technology [59–61], one under review on AIAA Journal of Spacecraft and Rockets and 3 proceedings for the 73rd International Astronautical Congress (IAC), the 25th AIAA International Space Planes and Hypersonic Systems and Technologies Conference and the 34th ICAS Congress 2024 [11, 62, 63]. Additionally, under the guidance of Prof. Savino, during her PhD, Emanuela

Gaglio authored a paper in the AIAA Journal of Spacecraft and Rockets [64], presented a proceeding at the ASCEND 2021 powered by AIAA [65], and contributed as co-author to another work from the same research group [66], which will not be included in this dissertation. Other works co-authored by Emanuela Gaglio and not part of the dissertation are under review.

- Under the guidance of Prof. Riccardo Bevilacqua, a novel G&C framework for propellantless maneuvering of satellites in LEO was proposed and applied to three relevant mission scenarios: de-orbiting, collision avoidance, and atmospheric re-entry. The proposed methodology combines optimal control theory with AI. Optimal control enables the formulation of customized cost functions tailored to each scenario, while AI techniques support real-time implementation suitable for onboard systems. This hybrid strategy maintains the optimality of the solution while significantly reducing the computational cost, making it a suitable solution for real-time use onboard satellites.

  In the context of drag-based de-orbiting, she developed a time-optimal targeting algorithm based on a novel class of optimal solutions that she identified [67]. She further enhanced the approach by integrating an AI-driven framework trained on a dataset of optimal control solutions, achieving a substantial reduction in computational cost while maintaining solution optimality [68, 69]. Her work also addressed the atmospheric re-entry phase. In addition to formulating an optimal control algorithm [70], she implemented an AI-based closed-loop feedback control system to ensure precise targeting in the presence of disturbances and [71]. Applying a similar strategy to collision avoidance, she first designed an optimal control algorithm based on a joint cost function that maximizes miss distance while minimizing orbital decay [72, 73]. Subsequently, she developed an AI-based framework to reduce computational effort and enhance performance in off-nominal conditions [74, 75].

  This research path brought to the publication of 6 papers on Acta Astronautica [67, 69, 71, 73, 75, 76] and 5 international proceedings for the 74th International Astronautical Congress (IAC), the 4th IAA Conference on Space Situational Awareness, and the 2nd International Symposium on Very Low Earth Orbit Missions and Technologies and the 35th AAS/AIAA Space Flight Mechanics Meeting [68, 70, 72, 74, 77]. Additionally, under the guidance of Prof. Bevilacqua, during her PhD, Emanuela Gaglio contributed as co-author to another proceeding for the AIAA 2024 SciTech and paper on Acta Astronautica from the same research group [78, 79], which will not be discussed in this dissertation. Other works co-authored by Emanuela Gaglio and not part of this dissertation are under review.

Together, these contributions represent a unified, innovative, and application-ready approach to propellantless orbital control using advanced aerodynamics and AI.

2.3.1 Journal Papers (chronological order)

1. Gaglio, E., Visone, M., Lanzetta, M., Mungiguerra, S., Cecere, A., & Savino, R. (2023). Mixed-Compression Supersonic Intake and Engine–Airframe Integration. *Journal of Spacecraft and Rockets*, 60(4), 1100-1111. DOI
2. Gaglio, E., & Bevilacqua, R. (2023). Time Optimal Drag-Based Targeted De-Orbiting for Low Earth Orbit. *Acta Astronautica*, 207, 316-330. DOI
3. Olave, D. R., Jara, N. C., Palharini, R. C., Palharini, R. S. A., Gaglio, E., & Savino, R. (2023). Inflatable aerodynamic decelerator for CubeSat reentry and recovery: Altitude effects on the flowfield structure. *Aerospace Science and Technology*, 138, 108358. DOI
4. Jara, N. C., Olave, D. R., Palharini, R. C., Gaglio, E., Palharini, R. S. A., & Savino, R. (2023). Inflatable aerodynamic decelerator for CubeSat reentry and recovery: IAD geometrical effects on the flowfield structure. *Aerospace Science and Technology*, 141, 108571. DOI
5. Gaglio, E., & Bevilacqua, R. (2024). Drag-based analytical optimal de-orbiting guidance from low earth orbit via Deep Neural Networks. *Acta Astronautica*, 218, 383-397. DOI
6. Caqueo, N., Palharini, R. C., Palharini, R. S. A., Gaglio, E., & Savino, R. (2024). Inflatable aerodynamic decelerators for CubeSat reentry and recovery: Surface properties. *Aerospace Science and Technology*, 149, 109151. DOI
7. Gaglio, E., & Bevilacqua, R. (2025). Machine Learning-Based Quasi-Optimal Feedback Control for a Propellantless Re-Entry. *Acta Astronautica*, 228, 274-284. DOI
8. Gaglio, E., Traub, C., Turco, F., Murcia-Pineros, J. O., Bevilacqua, R., & Fasoulas, S. (2025). Optimal drag-based collision avoidance: balancing miss distance and orbital decay. *Acta Astronautica*, 228, 295-305. DOI
9. Gaglio, E., Traub, C., Sannino, A., Mungiguerra, S., Turco, F., Fasoulas, S., Savino, R., & Bevilacqua, R. (2025) Quasi-Optimal Control for Drag-Based Collision Avoidance in Very Low Earth Orbit Using Machine Learning. *Acta Astronautica*, 235, 362-374. DOI
10. Sannino, A., Gaglio, E., Mungiguerra, S., Cecere, A., & Savino, R. (2025). Aerodynamic Study of a 3U CubeSat for Drag-Based In-Plane Orbital Maneuvers in Very Low Earth Orbit. *Acta Astronautica*, 236, 1-13. DOI
11. Gaglio, E., & Bevilacqua, R. (2025). Cislunar satellite motion prediction via hybrid parametric and deep learning models. *Acta Astronautica*, 237, 381-394. DOI
12. Murcia-Piñeros, J. O., Bevilacqua, R., Gaglio, E., Prado, A. F., & de Moraes, R. V. (2026). Spaceplane Model Predictive Control and guidance for aerogravity assisted maneuvers above Earth. *Acta Astronautica*, 238, Part A, 1266-1279. DOI

2.3.2 International Conference Proceedings (chronological order)

1. Gaglio, E., Cecere, A., Mungiguerra, S., Savino, R., Visone, M., & Lanzetta, M. (2021). Aerodynamic study of airframe-engine integration of a supersonic business jet. In *ASCEND 2021* (p. 4200). DOI

2. Gaglio, E., Guida, R., Cecere, A., Mungiguerra, S., & Savino, R. (2022). Assessment of a deployable aerodynamic control system for microsatellites recovery. In *Proceedings of IAC 2022*.

3. Gaglio, E., Cecere, A., Guida, R., Mungiguerra, S., Savino, R., Caqueo Jara, N., & Cassineli Palharini, R. (2023). Aerodynamic analysis of a flap-based deployable re-entry system in different flight conditions. In *25th AIAA International Space Planes and Hypersonic Systems and Technologies Conference* (p. 3000). DOI

4. Gaglio, E., & Bevilacqua, R. (2023). Machine Learning Based Guidance for Optimal Spacecraft De-Orbiting. In *Proceedings of IAC 2023*.

5. Murcia-Piñeros, J., Bevilacqua, R., Gaglio, E., Prado, A. B., & De Moraes, R. V. (2024). Optimization of Aero-gravity assisted maneuvers for spaceplanes at high atmospheric flight on Earth. In *AIAA SCITECH 2024 Forum* (p. 1459). DOI

6. Gaglio, E., & Bevilacqua, R. A novel time-optimal algorithm for an aerodynamic-based targeted re-entry. *4th IAA Conference on Space Situational Awareness*

7. Gaglio, E., Traub, C., Turco, F., Murcia-Pineros, J. O., Bevilacqua, R., & Fasoulas, S. Optimal spacecraft collision avoidance using aerodynamic drag. *4th IAA Conference on Space Situational Awareness*

8. Sepúlveda, D. V., Palharini, R. C., Gaglio, E., & Savino, R. Aerodynamic analysis of a flap-based deployable re-entry system under rarefied conditions. In *Proceedings of the 34th Congress of the International Council of the Aeronautical Sciences (2024)*.

9. Gaglio, E., Traub, C., Sannino, A., Mungiguerra, S., Turco, F., Fasoulas, S., Savino, R., & Bevilacqua, R. Machine Learning-Based Quasi-Optimal Feedback Control for a Propellantless Collision Avoidance in (Very) Low Earth Orbit. In *2nd International Symposium on Very Low Earth Orbit Missions and Technologies (VLEO2025)*, Stuttgart, Germany, 13–14 January 2025 (paper n. VLEO2025-9-03)

10. Gaglio, E., & Bevilacqua, R. Hybrid strategies for cislunar stability and motion. In *35th AAS/AIAA Space Flight Mechanics Meeting*, Kaua'i, Hawaii, USA, 19–23 January 2025 (paper n. AAS 25-401)

2.3.3 Submitted / Under Review

1. Gaglio, E., Guida, R., Sannino, A., Mungiguerra, S., Cecere, A., Savino, R., Sepúlveda, D. V., & Palharini, R.C. Aerodynamic performances of a deployable re-entry satellite with flap control. Under review on *AIAA Journal of Spacecraft and Rockets*.

2. Sannino, A., Gaglio, E., Mungiguerra, S., & Savino, R. Pitch Stability Considerations of 3U CubeSats for Differential Drag exploitation in VLEO. Under review on *Aerospace Science and Technology*.

3. Trincone, D., Gaglio, E., Cassese, S., Corbi, G., Mungiguerra, S., & Savino, R. A Hybrid AI Framework Bridging Experiments and Simulations in Hypersonic Flow Modeling. Under review on *Aerospace Science and Technology*.

4. Trincone, D., Costanzo, R., Cassese, S., Corbi, G., Mungiguerra, S., Savino, R, & Gaglio, E. AI-Driven Analysis and Characterization of Hypersonic Plasma Flows for Wind Tunnel Testing. Submitted for the *27th AIAA International Space Planes and Hypersonic Systems and Technologies Conference*.

5. Gaglio, E., & Bevilacqua, R. AI-driven Framework for the Analysis and Prediction of Hypersonic Shock Wave Boundary Layer Interaction. Submitted for the *ASCEND 2026*.

6. Gaglio, E., & Bevilacqua, R. A novel multi-layer autonomous missile swarm guidance and control. Submitted for the *ASCEND 2026*.

7. Rea, S., Bevilacqua, R., & Gaglio, E. On the analytical study and convergence properties of state-dependent linearization of the CR3BP in the cislunar region. Under review on *Acta Astronautica*.

3 Models and Tools

This chapter provides a comprehensive overview of the primary models and computational tools employed throughout this thesis to address its multidisciplinary aspects. It begins with an in-depth discussion of the fluid dynamics models, carefully examining the underlying governing equations and the variety of modeling approaches adopted according to the specific flow regimes encountered, ranging from continuum to rarefied conditions.

Following the fluid dynamics section, the chapter introduces the theoretical framework and methodologies underpinning the G&C components. In particular, it details the optimal control theory techniques employed for trajectory optimization, as well as the integration of AI principles aimed at enhancing system adaptability and robustness. Together, these sections establish the foundation for the multidisciplinary analysis conducted in the subsequent chapters.

3.1 Fluid dynamics

Depending on the flight regime, either CFD or DSMC is used to ensure an appropriate modeling accuracy. The choice of the proper approach depends on the Knudsen Number Kn, defined as the ratio between the mean free path λ and the characteristic length L, as in the Equation 3.1:

$$Kn = \frac{\lambda}{L} \tag{3.1}$$

Its value is representative of the specific flight regime and is summarized in Table 3.1, from [80].

Knudsen Number	Flight Regime
$Kn > 10$	Free Molecular Flow
$0.01 < Kn < 10$	Transition Regime
$Kn < 0.01$	Continuum Regime

Table 3.1: Classification of flow regimes based on Knudsen number [80].

Conventional computational techniques for solving fluid dynamics problems are not adequate for flows with a significant level of rarefaction ($Kn > 0.1$) [81], requiring a molecular-based approach.

3.1.1 Computational Fluid Dynamics (CFD)

CFD is the technique employed when dealing with conditions representative of continuum regime. In these scenarios, the flow behavior is governed by the Navier-Stokes equations, describing the conservation of mass, momentum, and energy. These equations are numerically solved by discretizing the computational domain and applying appropriate boundary conditions and models. In this thesis, the Reynolds-Averaged Navier-Stokes (RANS) equations are employed to simulate the aerodynamic behavior under high-speed conditions. This approach offers a compromise between computational cost and physical accuracy, enabling the prediction of flow fields and key aerodynamic features.

The present work focuses on steady-state CFD simulations, solving the compressible Navier-Stokes equations and modeling the flow as an ideal gas, governed by the following equation of state:

$$P = \rho R T \tag{3.2}$$

A density-based solver is adopted for the simulations due to its stability and precision in the case of compressible super/hypersonic flows with high-density fluctuation as the current one. About the numerical scheme, the choice fell on a second-order upwind one, taking advantage of an explicit formulation.

The governing equations for continuity, momentum, and enthalpy in the compressible form can be written as follows [64]:

Continuity:

$$\frac{\partial \rho}{\partial t} + \nabla \cdot (\rho \mathbf{V}) = 0 \tag{3.3}$$

Momentum:

$$\frac{\partial}{\partial t}(\rho \mathbf{V}) + \nabla \cdot (\rho \mathbf{V}\mathbf{V}) + \nabla P = \nabla \cdot \left[2\mu (\nabla \mathbf{V})_0^s\right] + \rho \mathbf{a} \tag{3.4}$$

Enthalpy:

$$\rho \frac{Dh}{Dt} - \frac{Dp}{Dt} = \nabla \cdot (\lambda \nabla T) + 2\mu (\nabla \mathbf{V})_0^s : (\nabla \mathbf{V})^s + \rho \mathbf{a} \cdot \mathbf{V} \tag{3.5}$$

Where:

$$(\nabla \mathbf{V})_0^s = (\nabla \mathbf{V})^s - \frac{1}{3}(\nabla \cdot \mathbf{V})\mathbf{I}, \quad (\nabla \mathbf{V})^s = \frac{\nabla \mathbf{V} + (\nabla \mathbf{V})^T}{2} \tag{3.6}$$

The turbulence is modeled with SST $k - \omega$ model [82].

Validation of CFD solver

This section describes the validation process for CFD solvers employed in this work and described in [64].The assessment of the fluid dynamic models is based on experimental data available in [83, 84]. In [83], experimental studies were conducted in the cold flow Mach 4 blowdown facility at NASA Langley Research Center to parametrically investigate inlet-isolator performance in an airframe-integrated ramjet/scramjet engine. Figure 3.1 summarizes the geometry specifications of the intake employed for the validation.

A two-dimensional grid consisting of 60000 polyhedral cells was employed for the numerical simulations. Regarding the boundary conditions, the external domain was assigned the same flowfield conditions as those used in the experimental tests, while the intake outlet was modeled as a pressure outlet. The fluid dynamic models adopted were identical to those used in the present study. Numerical analyses were performed under the same conditions as the experimental tests.

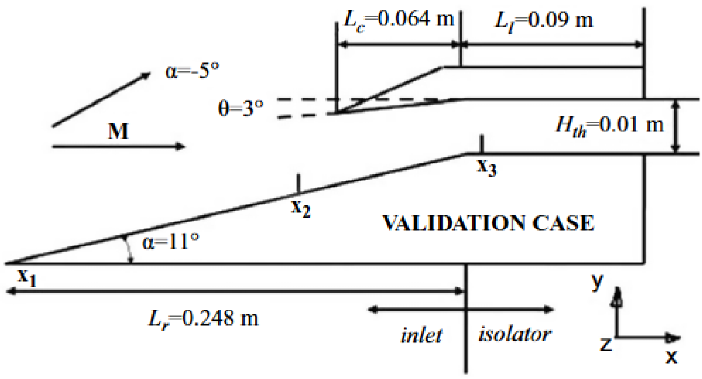

Figure 3.1: Geometry specifications of the intake used for the validation of the CFD solvers [83, 84].

Figure 3.2 presents a comparison between the efficiency trends obtained experimentally and those predicted by the simulations. An excellent agreement is observed, providing a satisfactory validation of the fluid dynamic models adopted in this work.

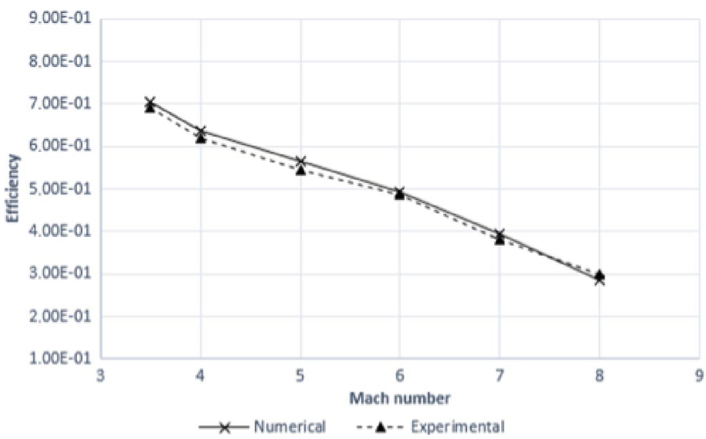

Figure 3.2: Comparison between experimental and numerical efficiency trends for the CFD solvers validation [64].

After validating the models, a cross validation has been performed by comparing the CFD results with two different software: Siemens Star CCM+ and Ansys Fluent. The results deeply described in [64] demonstrate a satisfying validation also for different software further demonstrating the robustness of the hypersonic CFD set-up employed.

3.1.2 Direct Simulation Monte Carlo (DSMC)

High-speed non-equilibrium flow in the transition regime can be directly associated with the first stages of atmospheric re-entry. Under these flow conditions, the effects of intermolecular collisions are insufficient to maintain a molecular velocity distribution near the Maxwellian equilibrium distribution, making this assumption invalid in continuum-based models [85]. Furthermore, high gradients and small length scales, such as those within the strong shock layers associated with hypersonic flight, can further deviate the molecular velocity distribution function from equilibrium [86]. To model the complex physical phenomena associated with thermal non-equilibrium, the molecular nature of the gas must be explicitly accounted for [87]. In this context, the DSMC method [88, 89] has been widely adopted and applied for the aerodynamic investigation of space vehicles at high altitudes. The DSMC method describes a dilute gas at the level of the single-particle distribution function without the need to solve the time-dependent nonlinear Boltzmann equation [88, 90]. Collisions are treated stochastically with scattering rates and post-collision velocity distributions determined from kinetic theory and thus subject to the same assumptions: molecular chaos and the dilute gas assumption [91]. The DSMC method introduces inherent assumptions as well. First, the impact parameters during a collision are considered random and do not need to be deterministically simulated. Second, only the simulation of a small fraction of the real number of molecules is required to obtain a full molecular description of the flow [89]. Another essential assumption of the DSMC method is that molecular motion and intermolecular collisions are uncoupled over time intervals much smaller than the mean collision time (MCT) [92]. Therefore, it is required that the time step size must be a fraction smaller than the MCT of the gas. The computational domain is divided into cells in order to sample the macroscopic properties. In DSMC simulations, the typical cell size should be a fraction of the freestream mean free path [88]. To promote near-neighbor collisions, the cells are further divided into subcells such that the collision partner of any chosen particle is selected from the same subcell [93].

Validation of the DSMC solver

This section presents the validation of the dsmcFoam+ solver. The code, developed within the OpenFOAM framework and written in C++ [94, 95], supports simulations involving multiple gas species in both reacting and non-reacting conditions. It includes models for internal energy exchange, as well as specular and diffusive gas-surface interactions with variable thermal accommodation.

In the present work, the Variable Hard-Sphere (VHS) model [88] was used to compute molecular collisions, while the Larsen–Borgnakke model [96] handled energy redistribution among translational and internal degrees of freedom. The No-Time-Counter (NTC) algorithm [97] was employed to select collision pairs, using eight subcells per computational cell.

Validation was conducted by comparing dsmcFoam+ results with experimental and numerical reference data. Experiments were performed in the SR3 low-density wind tunnel at CNRS-Meudon [98–100], using a 70° blunt cone geometry representative of the Mars Pathfinder probe, as defined by the AGARD Working Group [101, 102]. The geometry employed in both the experimental and numerical campaigns is shown in Figure 3.3.

The validation included three experimental cases involving non-reactive nitrogen flow over the probe. The freestream conditions were the same across all tests and are summarized in Table 3.2. These conditions were also applied in the present numerical simulations.

In the SR3 experiments, three distinct measurements were conducted:

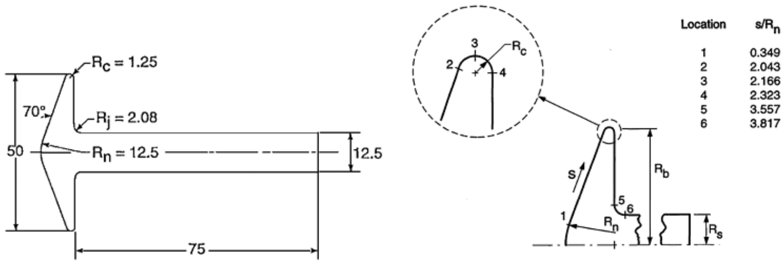

Figure 3.3: Dimensions of the Mars Pathfinder probe used in the SR3 wind tunnel [mm] [59].

Parameter	Value	Unit
V_∞	1502.56	m/s
T_∞	13.316	K
n_∞	3.719×10^{20}	m^{-3}
ρ_∞	1.73×10^{-5}	kg/m^3
p_∞	6.833×10^{-2}	Pa
λ_∞	1.691×10^{-3}	m

Table 3.2: Freestream conditions used in the SR3 experiments [103].

- The spatial distribution of density, temperature, and Mach number with a measurements' precision of 10%;
- Aerodynamic forces with a global uncertainty of approximately 3%;
- Surface heat flux with an uncertainty of around 10%.

Each experiment was performed with a specific wall temperature (290 K, 350 K, and 300 K respectively).

In the present work, dsmcFoam+ simulations were conducted by Prof. Rodrigo Cassineli Palharini and his research group, using the same geometry and freestream conditions. The boundary conditions applied in the simulations are illustrated in Figure 3.4. The symmetry boundary condition is applied to side I, at the front and back. At side II, freestream conditions are specified and DSMC particles are able to enter the computation domain. The vacuum condition is defined in side III. A diffuse reflection model with full thermal accommodation was applied at the surface, and the wall temperature was set to match the corresponding experimental case.

The accuracy of the dsmcFoam+ solver was assessed by comparing its results with both experimental data and those obtained with DSMC Analysis Code (DAC) by NASA. Figure 3.5 shows the normalized density (ρ/ρ_∞) distribution around the probe, highlighting the good agreement among all three datasets. Figure 3.6 compares the overall temperature and Mach number fields computed with dsmcFoam+ and DAC, again showing close correspondence, with further details and plots thoroughly discussed in [59].

In conclusion, the validation and verification process confirmed that dsmcFoam+ is capable of accurately reproducing the macroscopic flow features of rarefied hypersonic gas dynamics. The solver provided results consistent with both experimental data and established DSMC numerical tools, thereby demonstrating its suitability for high-fidelity rarefied flow simulations.

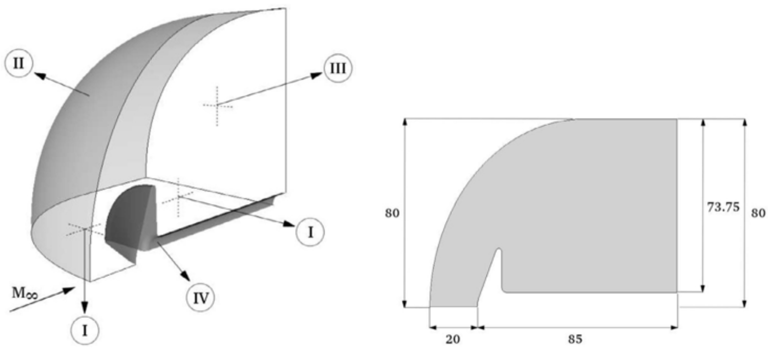

Figure 3.4: Boundary conditions and computational domain for the Mars Pathfinder simulations [59].

3.2 Optimal Control Theory

This section provides an overview of the principles of optimal control theory, which lays the foundation of the GPOPS-II software used in this dissertation.

A P-phase optimal control problem can be stated in the following general form. Determine the state,

$$\mathbf{y}^{(p)}(t) \in \mathbb{R}^{n_y^{(p)}}, \tag{3.7}$$

control,

$$\mathbf{u}^{(p)}(t) \in \mathbb{R}^{n_u^{(p)}}, \tag{3.8}$$

initial time,

$$t_0^{(p)} \in \mathbb{R}, \tag{3.9}$$

final time,

$$t_f^{(p)} \in \mathbb{R}, \tag{3.10}$$

integrals,

$$\mathbf{q}^{(p)} \in \mathbb{R}^{n_q^{(p)}}, \tag{3.11}$$

in each phase $p \in [1, \ldots, P]$, and the static parameters,

$$\mathbf{s} \in \mathbb{R}^{n_s}, \tag{3.12}$$

that minimize the cost functional

$$\begin{aligned} J = \phi\Big[&\mathbf{y}^{(1)}\left(t_0^{(1)}\right), \ldots, \mathbf{y}^{(P)}\left(t_0^{(P)}\right), t_0^{(1)}, \ldots, t_0^{(P)}, \\ &\mathbf{y}^{(1)}\left(t_f^{(1)}\right), \ldots, \mathbf{y}^{(P)}\left(t_f^{(P)}\right), t_f^{(1)}, \ldots, t_f^{(P)}, \\ &\mathbf{q}^{(1)}, \ldots, \mathbf{q}^{(P)}, \mathbf{s}\Big]. \end{aligned} \tag{3.13}$$

subject to the dynamic constraints

$$\dot{\mathbf{y}}^{(p)} = \mathbf{a}^{(p)}\left[\mathbf{y}^{(p)}, \mathbf{u}^{(p)}, t^{(p)}, \mathbf{s}\right], \quad (p = 1, \ldots, P), \tag{3.14}$$

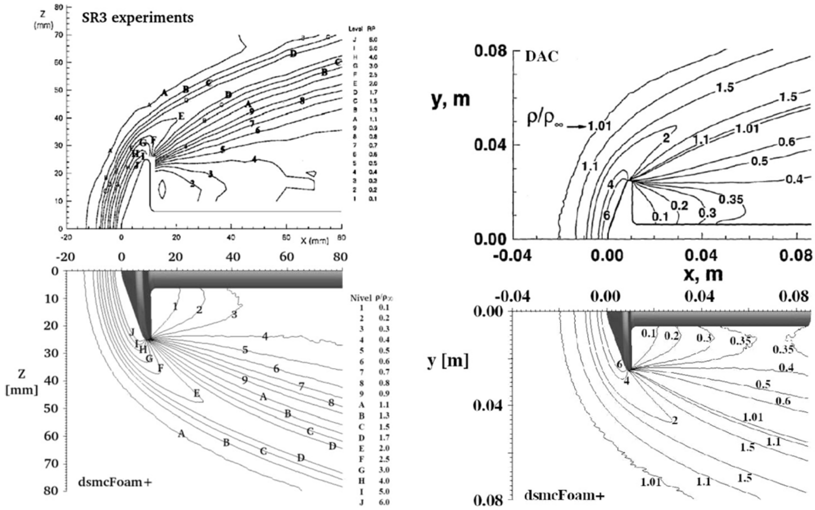

Figure 3.5: Normalized density distribution (ρ/ρ_∞) around the Mars Pathfinder probe [59].

the event constraints

$$\begin{aligned}
\mathbf{b}_{\min}^{(g)} \leq \mathbf{b}\Big[& \mathbf{y}^{(1)}\left(t_0^{(1)}\right), \ldots, \mathbf{y}^{(P)}\left(t_0^{(P)}\right), t_0^{(1)}, \ldots, t_0^{(P)}, \\
& \mathbf{y}^{(1)}\left(t_f^{(1)}\right), \ldots, \mathbf{y}^{(P)}\left(t_f^{(P)}\right), t_f^{(1)}, \ldots, t_f^{(P)}, \\
& \mathbf{q}^{(1)}, \ldots, \mathbf{q}^{(P)}, \mathbf{s}\Big] \leq \mathbf{b}_{\max}^{(g)}, \quad (g = 1, \ldots, G),
\end{aligned} \tag{3.15}$$

the inequality path constraints

$$\mathbf{c}_{\min}^{(p)} \leq \mathbf{c}^{(p)}\left[\mathbf{y}^{(p)}, \mathbf{u}^{(p)}, t^{(p)}, \mathbf{s}\right] \leq \mathbf{c}_{\max}^{(p)}, \quad (p = 1, \ldots, P), \tag{3.16}$$

and the integral constraints

$$\mathbf{q}_{\min}^{(p)} \leq \mathbf{q}^{(p)} \leq \mathbf{q}_{\max}^{(p)}, \quad (p = 1, \ldots, P), \tag{3.17}$$

where

$$q_i^{(p)} = \int_{t_0^{(p)}}^{t_f^{(p)}} Q_i\left[\mathbf{y}^{(p)}, \mathbf{u}^{(p)}, t^{(p)}, \mathbf{s}\right] dt, \quad (i = 1, \ldots, n_q^{(p)};\ p = 1, \ldots, P). \tag{3.18}$$

Although the problems are often composed of multiple phases, it must be emphasized that these phases do not necessarily need to be executed sequentially. Indeed, any two phases may be linked, provided that the independent variable remains monotonic, meaning that it progresses in the same direction throughout all linked phases.

The method employed in the current dissertation and at the basis of the software GPOPS-II is an hp-adaptive version of the Legendre-Gauss-Radau (LGR) orthogonal collocation method, firstly introduced and described in detail in [104].

It is based on the combination of two refinement strategies:

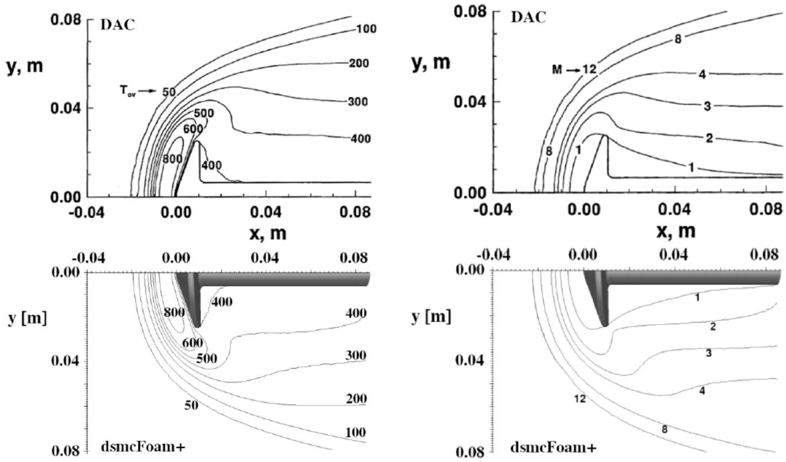

Figure 3.6: Comparison of overall temperature and Mach number between DAC and dsmcFoam+ [59].

- The p-refinement is based on increasing the number of collocation points within a time segment to improve the accuracy of the polynomial approximation.
- The h-refinement is based on subdividing a time segment into smaller subsegments to better capture local non-uniform variations.

The method starts by discretizing the time interval $[t_0, t_f]$ into S segments $[t_{s-1}, t_s]$, each with N_s collocation points, which are typically chosen as Gauss-Lobatto nodes. After formulating the optimal control problem in discrete form via the pseudospectral method, the problem is transformed into a nonlinear programming problem (NLP), which is solved using a suitable solver.

The algorithm is characterized by an iterative structure as follows:

1. Initialization: The user specifies an initial number M of collocation points per segment. The time domain is divided into an initial set of segments.
2. NLP Solution: Solve the discretized NLP with the current grid distribution.
3. Evaluation of the error: For each segment, check the dynamic constraints, path constraints, and bounds on state and control at the midpoints between collocation points. If the tolerance criterion is not met, the segment is marked for refinement.
4. Refinement Criteria: Segments with relatively uniform error are refined using the p-refinement, i.e., by increasing the number of collocation points by a user-specified amount L. Segments with non-uniform error, where the error is concentrated in specific regions, are refined using h-refinement, i.e., by splitting the segment at prescribed points; each new segment receives a minimum number of collocation points (e.g., $M = 5$).
5. Iteration: After updating the grid, resolve the NLP with the new discretization and repeat until all segments satisfy the tolerance.

This approach offers several key advantages. First, it achieves high accuracy without a substantial increase in the total number of collocation points. Moreover, it efficiently concentrates computational effort on segments with more complex dynamics. Finally, the combination of p-refinement and h-refinement allows for the method to adapt effectively to both global and localized errors.

3.3 Artificial Intelligence Techniques

This section focuses on the main elements of the AI approach adopted in this dissertation. After an introduction on Neural Networks (NNs) and Deep Neural Networks (DNNs), the most common activation functions are described. The section concludes by detailing the training process of the networks and the supervised learning approach, employed in this work.

3.3.1 General Information about (Deep) Neural Networks

Neural Networks (NNs) are machine learning models composed of interconnected units, commonly referred to as neurons, nodes, or units. They are organized into layers, with input and output neurons defining the structure of the model, and intermediate connections enabling the flow of information. A set of neurons located at the same depth within the network constitutes a so-called layer. When a model includes more than one intermediate layer, it is referred to as a Deep Neural Network (DNN).

An analogy is often drawn between artificial and biological neurons. The human brain is composed of billions of biological neurons that continuously exchange information through small electrical impulses.

The dendrites receive the input signals, which are then processed in the body of the cell and finally transferred out to the next neuron through the tail-like axon.

The same principles are followed by the artificial neurons (or perceptron), schematized in Figure 3.7.

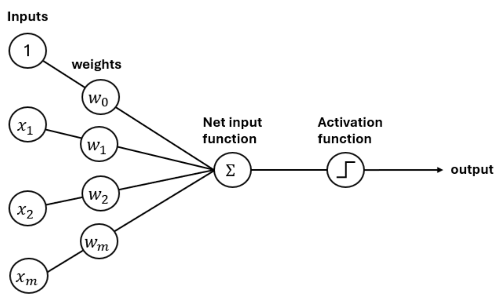

Figure 3.7: Schematization of an artificial neuron.

Every neuron receives inputs, identified by X_1 to X_m, which can be represented by structured or unstructured data, like images. The inputs represent the features of the model. Accordingly to Figure 3.7, there are many weights, identified by w_1 to w_m, as the number of the inputs. They are real numbers that can assume both positive and negative values which are not pre-determined but are assigned during the training process. Every neuron has one bias, identified by w_0. There is always only one bias per neuron, independently from the number of inputs, and is a real number.

The net input function is described as the sum of the products of the inputs and their corresponding weights and the bias. Since all of the variables are numbers, the result of the Net Input Function is just a number, a real number. The output of the net input function is fed as input to the activation function. And the output of the activation function is the final output of the neuron.

3.3.2 Activation Function

The activation functions play a crucial role in the training process by adjusting the outputs of the neurons. A function is attached to each neuron in the network and decides if it should be activated or not, based on whether its input is relevant for the prediction of the model. Some activation functions also help to normalize the outputs of the neurons. Early NNs used to employ not differentiable binary activation functions, such as the step and sign functions. It was then established that the use of differentiable activation functions enables the users to use simple, yet effective, training algorithms. DNNs typically use non-linear activation functions that allow to create complex non-linear mappings between the given inputs and the produced outputs, which are essential for learning and modeling complex data, such as images, video, audio and in general datasets in which the relations between the inputs and the desired outputs are non-linear.

Different activation functions are available, and well summarized here [105]. The most used ones are:

- **Sigmoid**: it is also known as "logistic function" and has the advantage of leading to clear divisions, as it tends to produce results near the limits of its range $(0, 1)$. It is also worth mentioning that its output can be directly interpreted as a probability. It is given by the Equation 3.19:

$$\alpha(u) = \frac{1}{1 + e^{-u}} \tag{3.19}$$

  One of its disadvantages lies in the fact that it could lead NNs in being trapped in low gradient regions, leading the process of learning on a plateau, because only small changes are made in each training update.

- **tanH**: it is the hyperbolic tangent represented by Equation 3.20:

$$\alpha(u) = \frac{e^{u} - e^{-u}}{e^{u} + e^{-u}} \tag{3.20}$$

  Like sigmoid, it can suffer from vanishing gradients, but unlike sigmoid, its output is centered around 0, which can improve learning.

- **Softmax**: it takes a vector of m neurons states of a layer l as an input and normalizes it into a probability distribution consisting of m probabilities proportional to the exponentials of the input numbers. The softmax of a single neuron i in a layer l is given by the Equation 3.21:

$$\alpha\left(u_i^{\ell}\right) = \frac{e^{u_i^{\ell}}}{\sum_{j=1}^{m} e^{u_j^{\ell}}} \tag{3.21}$$

  It has the property of generating probabilities for its output because the sum of all the generated results of a layer is always 1. It is able to handle multiple classes, giving the probability of the input value being in a specific class. Thus, it is typically used only in the last layer of a Neural Network.

- **ReLu**: it is called "Rectified Linear Unit" and is one of the most used activation functions. It is characterized by the Equation 3.22

$$\alpha(u) = \begin{cases} 0 & u \leq 0 \\ u & u > 0 \end{cases} \tag{3.22}$$

An issue of ReLU is that all the negative values become zero immediately, which decreases the ability of the model to train from the data properly, since all the neurons that have negative states, immediately “turn off”. To overcome this limitation, many variations were created, like Leaky ReLU [106], Parametric ReLU [107] and Exponential Linear Unit (eLU) [108].

- **eLu**: In contrast to ReLU, eLU has negative values which push the mean of the activations closer to zero. As proved in [108], mean activations that are closer to zero enable faster learning as they bring the gradient closer to the natural gradient. Different to other activation functions, it has an extra constant, denoted with a, which should be positive. It is very similar to ReLU except for negative inputs. eLU becomes smooth slowly until its output equals to $-a$. It is defined by Equation 3.23:

$$\alpha(u) = \begin{cases} \mathrm{a}\,(e^{u} - 1) & u \leq 0 \\ u & u > 0 \end{cases} \tag{3.23}$$

3.3.3 Training process

The training is the process during which the NN learns and iteratively adjusts its internal parameters (weights and bias) to minimize a cost function (also knows as loss) and representing the difference between its predicted output and the actual target output for a given training set. Each cost function has a slope, its derivative, revealing the direction that should be followed during the training process, in order to minimize the cost/error. Given this inclination, a local or even a global minimum can be found in the optimization space. One of the most used cost function is the Mean Squared Error (MSE), defined as the the sum of the square of individual errors in the output layer, employing the l_2 norm. One of its variant is the Mean Absolute Error (MAE), which employs the l_1 norm instead and has the feature of not being sensitive to outliers. Another quite common cost function is the cross-entropy which can be binary or categorical depending if the problem is binary or multi-class. Further details about these cost functions and other models can be found in [109].

The minimization of the cost function is at the basis of the the appropriate optimization parameters of a NN. It is used a backpropagation algorithm to achieve this, calculating the gradient of the cost function with respect to the bias and the weights of the network. It is based on an iteration through the layers backwards, right after the data have been forward passed, calculating the gradients for each neuron of each layer. By applying the chain rule, it is possible to make these calculations for every layer and not only the last one. Thanks to the backpropagation algorithm DNNs can be used, exploiting their ability to represent complicated functions.

After that, using the cost function and the backpropagation algorithm, it is possible to perform the training process of the NN. This process involves the assessment of the appropriate values for the bias and weight of the network, as well as, its optimization parameters. In order to do this, they need to be updated by exploiting the gradients that the backpropagation algorithm calculates. Updates can be applied in many different ways, which has led to the creation of multiple optimizers, described in detail in [109].

3.3.4 Supervised learning approach

A supervised learning approach has been used in the space applications presented in this dissertation and involving the use of AI. This is one of the most widely used approaches, involving a model trained on a labeled dataset to learn the mapping between input features and their corresponding outputs. The goal is to minimize the difference between predicted and actual labels through an iterative optimization process. This technique is mainly employed in classification tasks and regression problems. The performance of supervised learning is strictly dependent on the quality and representativeness of the labeled data. Common algorithms include decision trees, k-nearest neighbors (KNN), and NNs/DNNs. Figure 3.8 provides a schematic overview of the supervised learning process, highlighting the main phases of training, testing and validation.

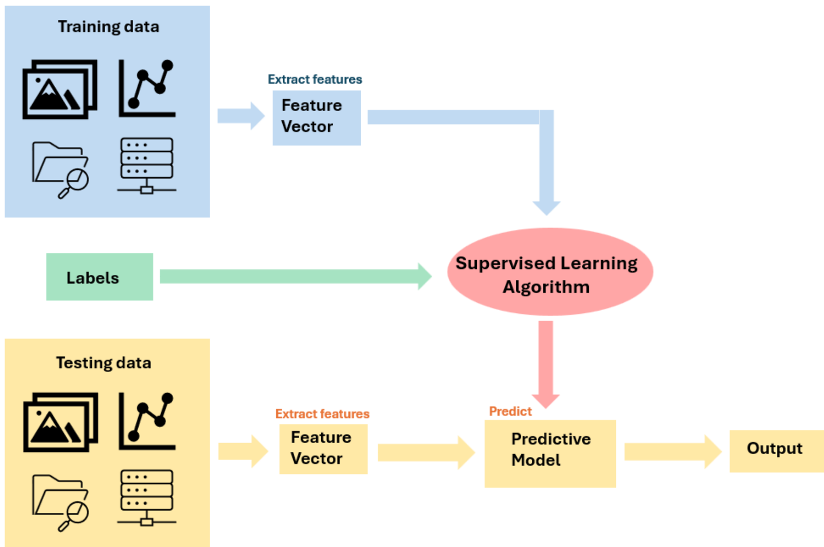

Figure 3.8: Schematization of supervised learning approach.

During the training phase, raw data, such as images or tabular datasets, are coupled with their corresponding labels and processed through feature extraction to produce the feature vectors, compact numerical representations of the key characteristics of the data. These labeled feature vectors are then used by the supervised learning algorithm to train a predictive model, enabling it to learn the underlying relationship between inputs and outputs. In the testing phase, new and unseen data undergo the same feature extraction process, after which the trained model generates Predictions that approximate the expected labels, demonstrating its ability to generalize to new, real-world examples.

4 Fluid Dynamic Assessment of Inflatable Systems

This chapter focuses on the aerodynamic assessment of an Inflatable Aerodynamic Decelerator (IAD) [59]. Representative conditions along the re-entry trajectory are selected and analyzed using both CFD and DSMC, depending on the flow regime associated with each case. The DSMC simulations were carried out by Prof. Rodrigo Cassineli Palharini and his research team as part of a joint collaborative effort. The influence of key parameters on aerodynamic performance is also investigated. After describing the geometry of interest, the effect of altitude on the evolution of the flow field is examined, including a comparison between the two methodologies.

4.1 Computational and geometrical parameters

For the current analysis, the simulated IAD geometry took inspiration by the work [110] and is considered fully inflated during the re-entry phase. The IAD is characterized by a 0.3 m radius, 600 mm cone diameter, 120 mm nose radius, and 68.82° cone angle. A 2U CubeSat is considered, where 1U is used to store the IAD system and the second unit to accommodate the required payload, as shown in Figure 4.1.

The freestream conditions considered in the numerical simulations correspond to those experienced by the IAD at altitudes ranging from 115 km to 95 km with 0° angle of attack. The freestream velocity and the surface temperature are assumed to be constant at 7000 m/s and 1000 K, respectively. Considering the IAD nose radius as the characteristic length, the Knudsen number ranges from 13.23 to 0.43 for the altitudes of 115 km and 95 km, respectively. In this way, the simulations have been performed in the transitional and free molecular flow regimes. At these regimes, the flow field structure results to be very dependent on the degree of rarefaction [88]. Tables 4.1 and 4.2 show the freestream conditions and number density for each molecular and atomic specie, as well as altitude considered in this investigation.

A schematic view of the boundary conditions and numerical grid is shown in Figure 4.2. In order to reduce the computational cost and take advantage of axisymmetric geometry, the simulations have been performed using a quarter geometry where in surface I, specular boundary condition is applied. At this boundary condition, all flow gradients normal to the surface are zero. In surfaces, II and III, specified freestream condition and vacuum boundary condition are employed. The option for vacuum is suitable for an out-flowing gas since there are no particles moving upstream with Mach number greater than 3 [88].

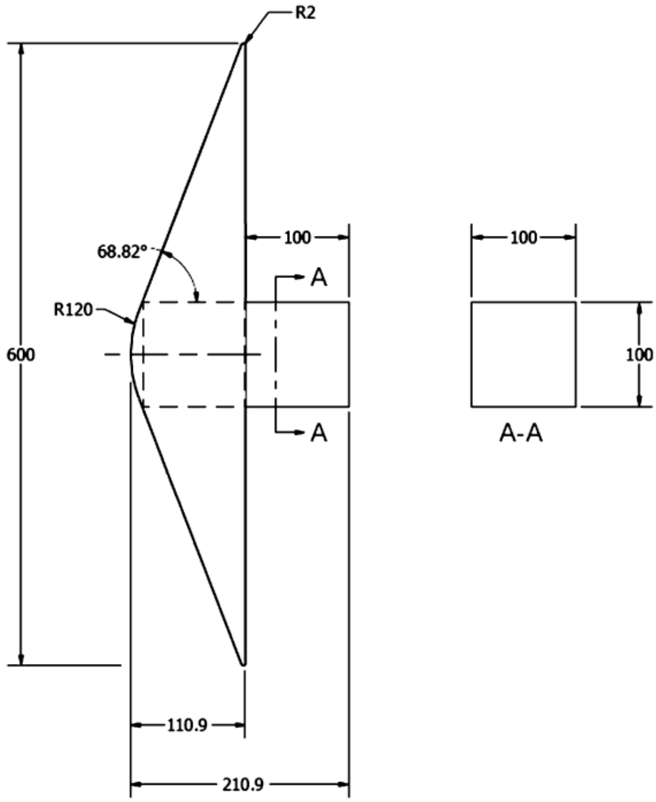

Figure 4.1: Geometry and physical dimensions of the IAD configuration.

Altitude (km)	ρ_∞ (kg/m^3)	P_∞ (Pa)	n_∞ (m^{-3})	T_∞ (K)	λ_∞ (m)
115	4.289×10^{-8}	4.008×10^{-3}	2.920×10^{19}	300.0	1.587
110	9.709×10^{-8}	7.104×10^{-3}	1.189×10^{19}	240.0	0.725
105	2.325×10^{-7}	1.428×10^{-2}	5.021×10^{18}	208.8	0.312
100	5.604×10^{-7}	3.011×10^{-2}	2.144×10^{18}	195.1	0.125
95	1.393×10^{-6}	7.596×10^{-2}	9.681×10^{17}	188.4	0.051

Table 4.1: Freestream conditions considered in the aerodynamic investigation for the IAD system [111].

4.2 Numerical results and discussion

This section discusses in detail the influence of the altitude on the flow field structure around the IAD. The macroscopic properties profiles, including the velocity, density, pressure, and temperature, are shown for five positions perpendicular to the IAD and at the wake region. The Profiles P1,

Altitude (km)	n_{N_2} (m^{-3})	n_O (m^{-3})	n_{O_2} (m^{-3})
115	7.254×10^{17}	1.428×10^{17}	9.646×10^{16}
110	1.641×10^{18}	2.303×10^{17}	2.621×10^{17}
105	3.883×10^{18}	3.406×10^{17}	7.645×10^{17}
100	9.210×10^{18}	4.298×10^{17}	2.151×10^{18}
95	2.268×10^{19}	4.365×10^{17}	5.830×10^{18}

Table 4.2: Number density employed in the aerodynamic assessment of IAD for each molecule/atomic species and altitude [111].

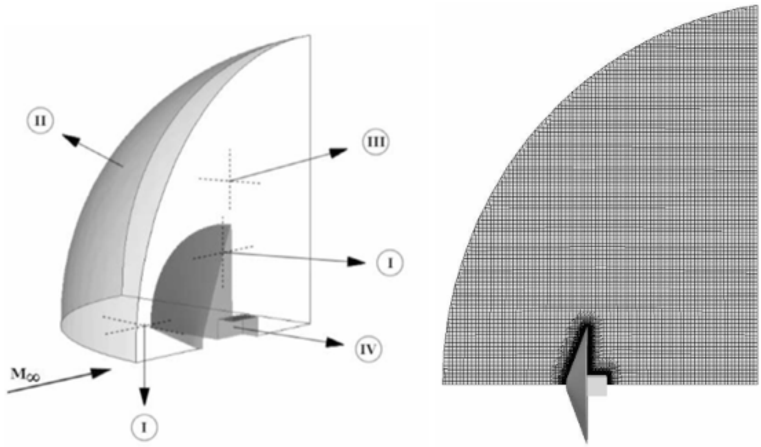

Figure 4.2: Schematic view of boundary conditions and computational grid for the IAD geometry.

P2, P3, P4 and P5 are normal to the surface in the points $x_1 = (0.0, 0.0)$, $x_2 = (0.0511, 0.15)$, $x_3 = (0.1099, 0.30)$, $x_4 = (0.1609, 0.05)$ and $x_5 = (0.2109, 0.05)$, respectively. Profile 1 (P_1) corresponds to the stagnation streamline, Profile 2 (P_2) is normal to the halfway point between the stagnation point and IAD shoulder, Profile 3 (P_3) is located at IAD shoulder, Profile 4 (P_4) is located perpendicularly to the lateral face of the CubeSat, and Profile 5 (P_5) is located at the end of the lateral face of the CubeSat. In addition, to get a general and comprehensive description of the flowfield structure as a function of the altitude, macroscopic properties contours are presented for each condition considered in the present investigation. The DSMC results are first presented and subsequently compared with those obtained from CFD simulations.

4.2.1 The velocity flow field

The macroscopic properties are computed from local averages of the microscopic properties. Thus, the local macroscopic velocity vector is given by Equation 4.1:

$$\mathbf{c}_0 = \frac{\overline{m\mathbf{c}}}{\bar{m}} = \frac{\sum_{j=1}^{N} m_j \mathbf{c}_j}{\sum_{j=1}^{N} m_j} \tag{4.1}$$

where m and c represent the mass and the velocity vector of each individual particle, and N is the total number of simulated particles within a cell. Figures 4.3 and 4.4 show the velocity contours along with streamlines around the IAD and CubeSat.

On the left side, the entire computational domain is shown while the right side represents a closer view from the velocity contours and streamlines at the IAD and CubeSat geometries. According to these plots, the velocity magnitude at the inlet of the computational domain is 7000 m/s and, as the flow moves towards the IAD surface, the magnitude of the velocity decreases progressively and reaches lower values in correspondence of the IAD surface. Due to the rarefaction effects, it can be noticed that the low velocity region extends further upstream of the IAD at 115 km altitude, while it is contained close to the IAD surface at 95 km. At the highest altitude, the molecular mean free path is 1.6 m and the molecules reflected from the flexible heat shield have more space to travel upstream until colliding with another molecule. However, at 95 km altitude and with a mean free path of 0.051 m, the collision frequency is high and there is not enough space for the molecules to travel upstream. The freestream disturbance caused by the IAD is X = 2.4 m, X = 1.5 m, X = 1.0 m, X = 0.7 m, and X = 0.5 m for 115 km, 110 km, 105 km, 100 km, and 95 km altitude. With reference to Figures 4.3 and 4.4 , it can be observed that the streamlines show a straight path until reaching the proximity of the IAD.

At the surface, the flow reached velocities of less than 1000 m/s, which increases as the flow moves over the surface and expands at the IAD shoulder. At this expansion region, just behind the IAD, the velocity is low, and it is increased as the flow is developed along the wake region. Very low particle velocity is found at the wake region, and no recirculation zones were observed for the geometry and altitudes considered in the present investigation. For an analysis in greater detail of the behavior of the flow velocity during atmospheric re-entry, Figure 4.5 shows the velocity distribution along the five profiles at the altitudes considered in this investigation.

In Profile 1, the velocity distribution is evaluated along the stagnation streamline. A decrease in molecular velocity is observed as the flow approaches the heat shield, becoming more pronounced at lower altitudes due to increased molecular collisions. At 115 km, the flow deceleration begins around 2.4 m from the IAD nose, while at 95 km it starts at about 0.5 m. Profile 2 shows a similar trend. The velocity remains low near the heat shield and decreases further toward the IAD shoulder. Measurements are taken from the shoulder up to the inlet boundary. In Profile 3, the velocity is low near the shoulder but increases rapidly due to local flow expansion. At high values of Z, it approaches the freestream velocity V_∞. This expansion becomes more evident at lower altitudes. Profiles 4 and 5 describe the velocity distribution in the wake region downstream of the IAD, measured from the CubeSat surface to the inlet boundary. As shown in Figures 4.3 and 4.4, this region is characterized by low velocity due to flow expansion around the shoulder. In Profile 4, the velocity near the CubeSat remains below 250 m/s across all altitudes. In Profile 5, it reaches 500 m/s at 95 km and 750 m/s at 115 km. From the CubeSat surface to $Z = 0.3$ m (the IAD radius), velocity increases up to 3000 m/s, and continues rising beyond this point toward the boundary.

4.2.2 Temperature flow field

The overall temperature (T_{ov}) for a non-equilibrium gas is defined as the weighted average of the translational temperature (T_{tra}), rotational temperature (T_{rot}), and vibrational temperature (T_{vib}), with respect to their respective degrees of freedom (ζ) [88], as specified in the Equation 4.2:

$$T_{ov} = \frac{3T_{tra} + \bar{\zeta}_{rot}T_{rot} + \bar{\zeta}_{vib}T_{vib}}{3 + \bar{\zeta}_{rot} + \bar{\zeta}_{vib}} \tag{4.2}$$

Translational, rotational and vibrational temperatures are obtained for each cell in the computational domain through the following equations:

$$T_{\text{tra}} = \frac{1}{3k_B} mc^2 = \frac{1}{3k_B} \frac{\sum_{j=1}^{N} m_j c^2}{N} \tag{4.3}$$

$$T_{\text{rot}} = \frac{2m\bar{\varepsilon}_{\text{rot}}}{k_B \zeta_{\text{rot}}} = \frac{2}{k_B \zeta_{\text{rot}}} \frac{\sum_{j=1}^{N} (\varepsilon_{\text{rot}})_j}{N} \tag{4.4}$$

$$T_{\text{vib}} = \frac{\Theta_{\text{vib}}}{\ln\left(1 + \frac{k_B \Theta_{\text{vib}}}{\bar{\varepsilon}_{\text{vib}}}\right)} = \frac{\Theta_{\text{vib}}}{\ln\left(1 + \frac{1}{N} \frac{k_B \Theta_{\text{vib}}}{\sum_{j=1}^{N} (\varepsilon_{\text{vib}})_j}\right)} \tag{4.5}$$

where k_B represents the Boltzmann constant, c' is the thermal velocity, ϵ_{rot} and ϵ_{vib} are the average rotational and vibrational energies per particle computed within the respective cell, and Θ_{vib} is the characteristic vibrational temperature.

Figure 4.6 shows the overall temperature contours around the IAD and CubeSat from 115 km to 95 km of altitude.

According to these plots, it can be noticed a shock wave formation upstream of the IAD surface, which is characterized by a high-temperature zone. Due to the high-temperature shock wave formation upstream the vehicle, chemical reactions such as dissociation, exchange, or even ionization may occur. However, they are not taken into account in the current investigation. At 115 km of altitude, the diffuse nature of the shock wave is observed and, as the device re-enters and moves towards a denser portion of the atmosphere, the high temperature region gets thinner and closer to the IAD surface. This region extends to 1.2 m, 0.8 m. 0.5 m, 0.3 m, 0.2 m, for 115 km, 110 km, 105 km, 100 km, 95 km altitude, respectively. It can be also observed that the shock wave peak temperature increased from 11197 K to 16660 K and the temperature at the wake region remained approximately constant at 7000 K for all altitudes considered in the present investigation. Figure 4.7 shows the overall temperature distribution along five profiles located at different positions perpendicularly to IAD and CubeSat surface. According to this set of plots, Profiles 1 and 2 exhibit similar behavior: the overall temperature remains low far from the IAD, rises to a maximum at the center of the shock wave, and then decreases toward the heat shield. The peak of overall temperature occurred at 11197 K, 11533 K, 12530 K, 14353 K, and 16660 K at 0.45 m, 0.3 m, 0.15 m, 0.12 m, and 0.061 m from the IAD surface for altitudes ranging from 115 km to 95 km altitude. Profile 3 shows the overall temperature distribution normal to the IAD shoulder. The temperature at the domain boundary corresponds to the freestream temperature. As the high-temperature zone formed upstream of the IAD moves over the flexible thermal protection system, it is observed overall temperature at the shoulder varied from 3000 K to 4500 K. Just above the shoulder, where the high-temperature region expansion takes place, the altitude resulted to have a significant influence on the peak temperature. At 115 km the maximum overall temperature is 8500 K and, at 95 km altitude, the peak overall temperature is 11700 K. The influence of altitude in the overall temperature distribution at the wake region is shown in Figure 4.7, Profiles 4 and 5.

The overall temperature profiles are measured from the CubeSat surface to the inlet boundary condition. At altitudes of 105 km, 100 km, and 95 km, a similar trend is observed: the temperature starts at approximately 1000 K near the CubeSat surface, increases to a peak around $Z = 0.45$ m, and then gradually decreases toward the boundary. This temperature peak occurs just downstream of the IAD shoulder, following the flow expansion.

In contrast, this behavior is not observed at altitudes of 115 km and 110 km. At these higher altitudes, the increased degree of rarefaction leads to a longer molecular mean free path due to the flow expansion in the wake region. As a result, molecular collisions are significantly reduced, making accurate measurement of the overall temperature more difficult.

4.2.3 The density flow field

The density within the computational cells on the dsmcFoam+ code is obtained using the Equation 4.6:

$$\rho_s = n\bar{m} = \frac{\bar{N} F_N}{V_c} \cdot \frac{\sum_{j=1}^{N} m_j}{N} \tag{4.6}$$

where n is the local number density, m is the molecular mass, and $\bar{N}$ and N are, respectively, the average and total number of simulated particles within a given cell. Furthermore, F_N represents any number of real particles and V_c is the computational cell volume. Figure 4.8 shows the density contours over the IAD and CubeSat from 115 km to 95 km altitude.

From the contours, it is evident that most particles are concentrated near the IAD surface due to flow deceleration induced by the surface geometry. At an altitude of 11 km, the high-density region extends up to $X = -0.04$ m upstream of the IAD, a result of the high degree of rarefaction. When the gas particles collide with and are diffusely reflected from the IAD surface, collisions between the reflected particles and incoming freestream particles are unlikely at this altitude.

As the CubeSat descends into denser layers of the atmosphere, a reduction in the extent of the high density layer near the IAD surface is observed. This is attributed to a decrease in the mean free path and a corresponding increase in the frequency of collisions between reflected and incoming particles.

Additionally, as the flow expands around the IAD shoulder, a low-density region forms in the wake. In this region, only a few molecular collisions occur, and considerable computational time is required to accurately calculate macroscopic flow properties.

To assess the influence of altitude on the density distribution over the IAD and CubeSat, density profiles were extracted along five lines normal to the IAD and nanosatellite surface, covering altitudes from 115 km to 95 km. As shown in Figure 4.9, particularly in Profiles 1 and 2, a progressive increase in density is observed as the flow approaches the IAD surface. This behavior is consistent with the high-density regions identified in the contour plots of Figure 4.8.

It is worth noting that at 95 km altitude, the density near the IAD surface is approximately two orders of magnitude higher than that observed at 115 km. In Profile 3, high-density particles generated over the heat shield are seen moving toward the IAD shoulder. Although this region is influenced by flow expansion, the density remains relatively high near the IAD surface and gradually decreases toward the upper boundary.

Profiles 4 and 5, located in the wake region, show the density distribution measured normal to the lateral face of the CubeSat. These profiles reveal the formation of a low-density wake caused by flow expansion around the upstream section of the IAD. As particles move downstream into the near wake, the maximum density values progressively decrease. The density is lowest near the CubeSat surface, increases up to $Z = 0.3$ m (the IAD radius), and then remains approximately constant toward the inlet boundary.

4.2.4 Pressure flow field

The pressure determined by the dsmcFoam+ code is obtained using Equation 4.7:

$$p = \frac{1}{3} n m \overline{c^2} = \frac{1}{3} \frac{\overline{N F_N}}{V_c} \cdot \frac{\sum_{j=1}^{N} m_j c^2}{N} \tag{4.7}$$

where n is the local number density, m is the molecular mass, c' is the thermal velocity, $\bar{N}$ and N are, respectively, the average and total number of simulated particles within a given cell, and V_c is the computational cell volume. Figure 4.10 shows the pressure contours around the IAD and CubeSat. According to this set of plots, it is observed increase in the surface pressure as the small satellite moves from 115 km to 95 km altitude. For altitudes of 115 km, 110 km, 105 km, 100 km and 95 km, the maximum surface pressures are 2.15 Pa, 4.92 Pa, 11.69 Pa, 27.23 Pa and 67.0 Pa, respectively.

In addition, at 115 km altitude, the maximum surface pressure is 536 times the freestream pressure, while at 95 km altitude the maximum surface pressure increase is 882 times the freestream pressure. At the wake region, very low pressure is observed in Figure 4.10 with no significant variations. Figure 4.11 shows the pressure distributions along the five profiles normal to the IAD and CubeSat surfaces. According to this set of plots, Profiles 1 and 2, it is noticed that the pressure remains constant from $X = -0.6$ m to $X \approx -0.3m$.

At $X = -0.3$ m, the pressure increases due to shock wave formation, reaching a maximum at the IAD surface. This rise is significantly less pronounced at 115 km and 110 km because of the high rarefaction. As particles from the high-pressure region move toward the IAD shoulder, the pressure decreases, as shown in Profiles 1–3. At 115 km, the maximum pressure on the IAD shoulder is 0.45 Pa, representing 20.9% of the peak shock wave pressure at that altitude. At 95 km, the maximum shoulder pressure is 19.68 Pa, or 29.4% of the local peak. Profiles 4 and 5 (Figure 4.11) show the pressure distribution in the wake, measured normal to the lateral face of the CubeSat. The pressure is low near the CubeSat, increases up to $Z = 0.35$–0.44 m, then decreases toward the upper boundary. This pressure rise is more pronounced at 105 km, 100 km, and 95 km, while at 115 km and 110 km it remains mild due to the rarefied wake. In Profile 4, the minimum pressure near the CubeSat is 6.0×10^{-5} Pa at 115 km (1.5% of the freestream value), increasing to 0.0262 Pa at 95 km (34.5%). For Profile 5, minimum pressures are 2.65×10^{-4} Pa and 0.10 Pa at 115 km and 95 km, corresponding to 6.6% and 131.6% of the freestream pressure, respectively. The maximum pressures are observed further downstream: at 115 km, 0.171 Pa at $Z = 0.44$ m in Profile 4, and 0.119 Pa at $Z = 0.55$ m in Profile 5. At 95 km, these values increase to 10.33 Pa (Profile 4, $Z = 0.40$ m) and 7.60 Pa (Profile 5, $Z = 0.44$ m).

4.2.5 Comparison between DSMC and CFD results

In this section, continuum-based computational results are compared with those obtained using the dsmcFoam+ code. The primary objective is to assess the capability of a CFD solver to predict flow behavior within the transitional regime. The CFD software solves the conservation equations for mass and momentum across all flow regimes. The conservation of energy is also accounted for when heat transfer or compressibility effects are significant. For reacting flows or gas mixtures, species conservation equations are additionally solved.

The freestream conditions applied in the CFD simulations are consistent with those used in the DSMC analyses, as previously described. The geometry described in Figure 4.1 was used in the CFD simulations to ensure consistency with the dsmcFoam+ setup. A refined aerodynamic grid, with resolution comparable to that used in the DSMC simulations, was employed. The boundary conditions implemented in the CFD cases replicated those employed in the DSMC simulations, ensuring consistency between the two approaches.

All simulations were conducted assuming zero angle of attack and a constant wall temperature of 1000 K. A no-slip condition was applied to the surfaces of both the IAD and the CubeSat. The external flow domain was modeled as a pressure far-field, with assigned pressure, temperature, and species concentrations. A constant freestream velocity of 7000 m/s was imposed in all cases, corresponding to Mach numbers ranging from 20.2 at 115 km altitude to 25.5 at 95 km altitude.

The air was modeled as a mixture of chemical species, with the composition defined earlier. The Reynolds number, based on a capsule radius of 0.3 m, varied from 5.5 at 115 km to 164.8 at 95 km altitude. Figure 4.12 presents velocity contours and streamlines obtained from the CFD simulations across the evaluated altitudes.

As shown in these plots, the shock wave stand-off distance decreases as the vehicle descends into denser layers of the atmosphere. Specifically, at 95 km altitude, the shock wave is located closer to the body, while at 115 km, it appears further upstream. Furthermore, no recirculation regions were detected, which aligns with the results obtained from the dsmcFoam+ simulations. Figure 4.13 shows the pressure contours computed in the CFD simulations at the various altitudes considered.

Similar to the dsmcFoam+ results, a significant increase in pressure is observed near the surface of the IAD, confirming consistency between the two modeling approaches. Table 4.3 summarizes the static pressure values at the stagnation point on the IAD, computed using both DSMC and CFD methods, along with their percentage differences.

Altitude [km]	Pressure (DSMC) [Pa]	Pressure (CFD) [Pa]	Difference
115	2.15	3.0	28.0%
110	4.92	5.5	10.5%
105	11.7	12	2.5%
100	27.2	26	4.4%
95	67.0	64.6	3.6%

Table 4.3: Static pressure values at the IAD stagnation point from 115 km to 95 km altitude, computed via DSMC and CFD simulations.

These results are in line with expectations. At higher altitudes, the flow is highly rarefied, and continuum-based solvers are unable to accurately capture the physical behavior. However, as the Knudsen number decreases with altitude due to increased atmospheric density, good agreement is observed between the DSMC and CFD results at 105 km, 100 km, and 95 km. At these altitudes, the difference in stagnation pressure remains below 5%.

Figure 4.14 shows the temperature distribution along the stagnation streamline at 95 km altitude, comparing results from dsmcFoam+ and CFD.

On the left side of Figure 4.14, the overall and translational temperatures obtained using DSMC are compared to the temperatures predicted with CFD assuming both constant and variable specific heat (C_p). The peak overall temperature from DSMC closely matches the CFD result assuming constant C_p, although the DSMC curve is broader and shifted upstream. In the CFD solution, the temperature peak is located closer to the vehicle surface, while the DSMC simulation shows a thicker shock layer. Notably, when a variable C_p is used in the CFD model, the resulting temperature is significantly lower than both the overall and translational DSMC temperatures.

The right side of Figure 4.14 presents the temperature distribution along the stagnation streamline at 115 km and 95 km altitude, comparing DSMC overall temperatures and CFD results with constant C_p. At 115 km, the influence of rarefaction on shock thickness and peak temperature is evident. The DSMC results show a diffuse shock extending far upstream, with the temperature peak located at $X = -0.4$ m. In contrast, the CFD simulation predicts a much thinner shock located closer to the body, with a peak at $X = -0.17$ m.

As the CubeSat with the IAD descends into denser layers of the atmosphere , better agreement is observed between the two computational approaches in terms of shock peak temperature. However, the shock thickness remains slightly greater in the DSMC simulations compared to CFD.

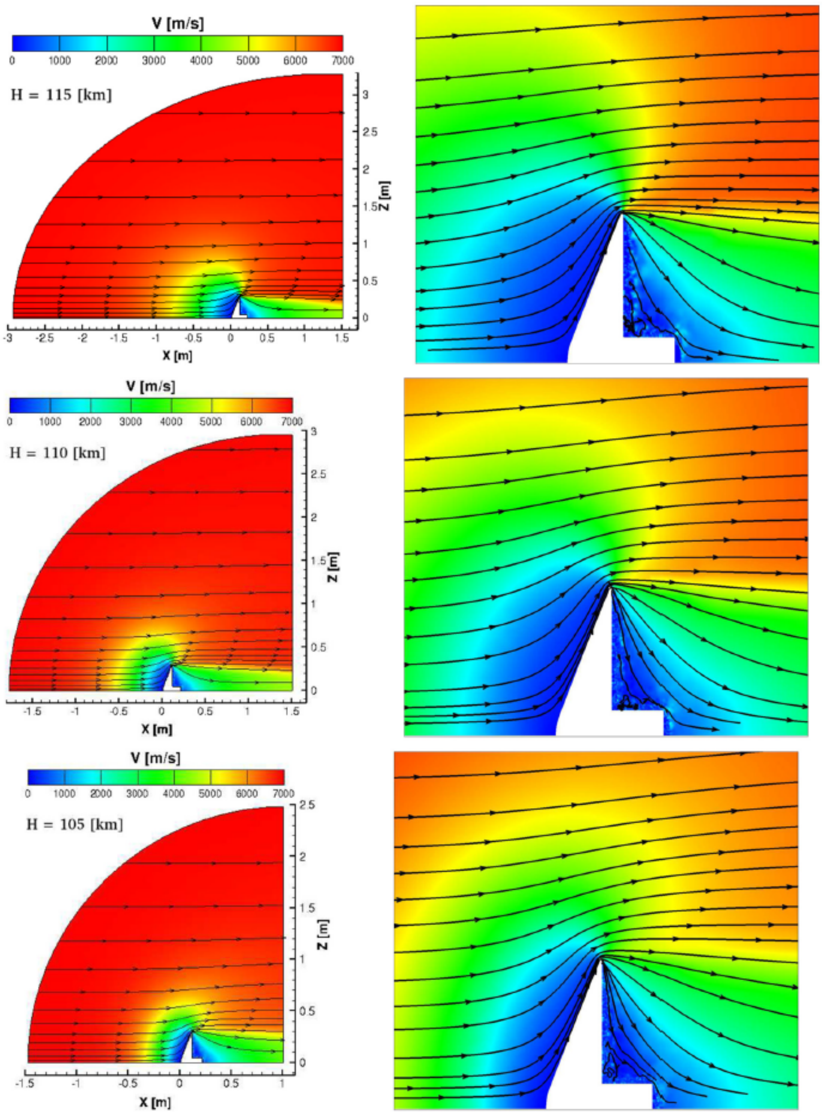

Figure 4.3: Velocity distribution and streamlines around the IAD and CubeSat during the re-entry phase at 115 km, 110 km, and 105 km altitude.

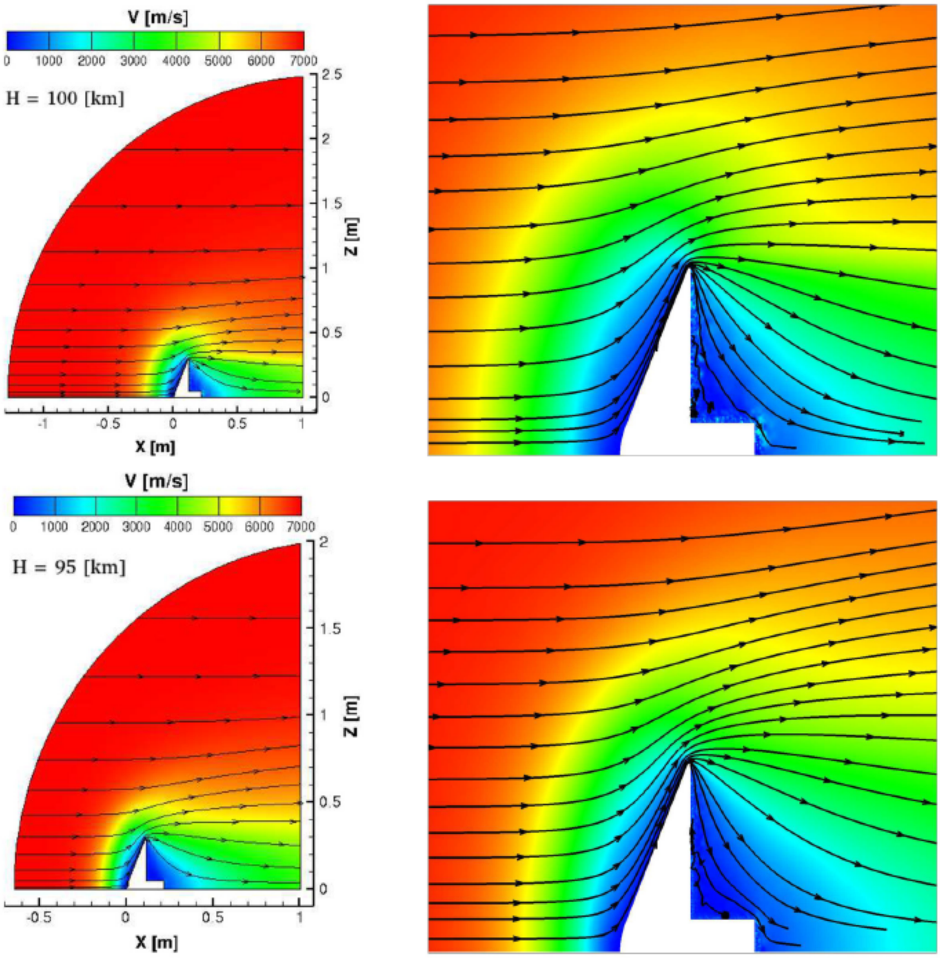

Figure 4.4: Velocity distribution and streamlines around the IAD and CubeSat during the re-entry phase at 100 km and 95 km altitude.

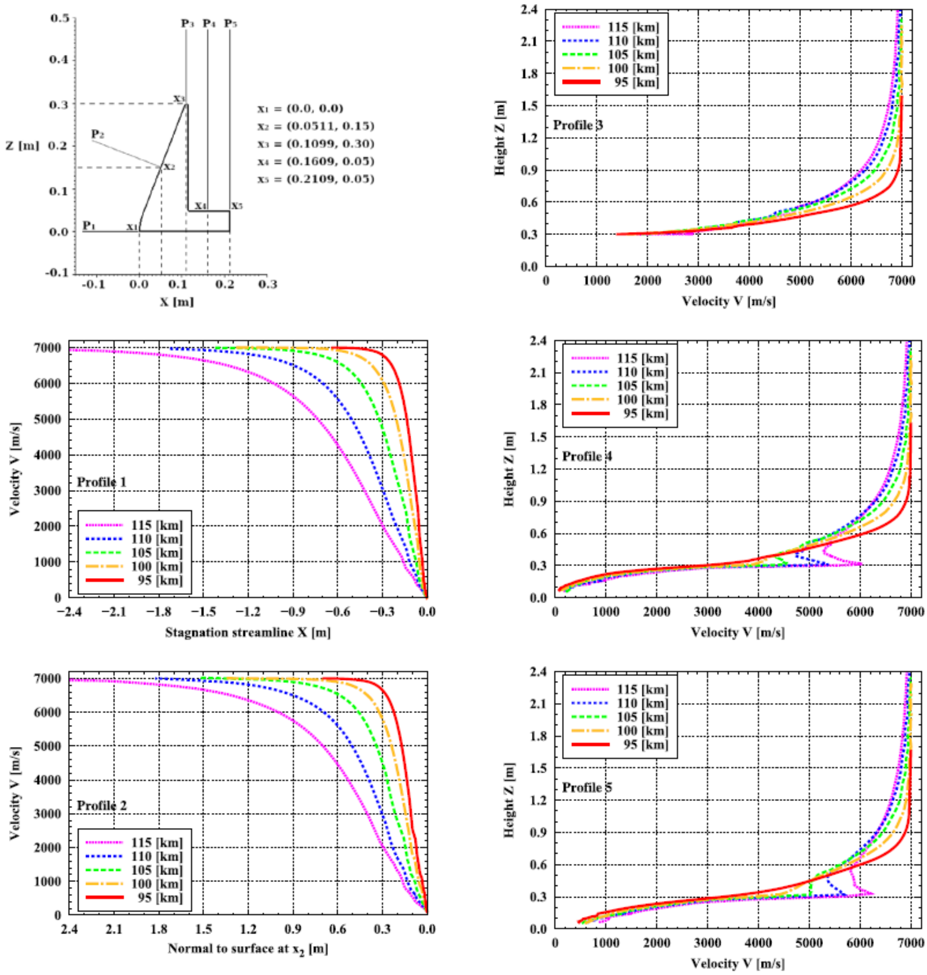

Figure 4.5: Velocity distribution along the profiles located at different positions normal to the geometry surface for each altitude considered in the present investigation.

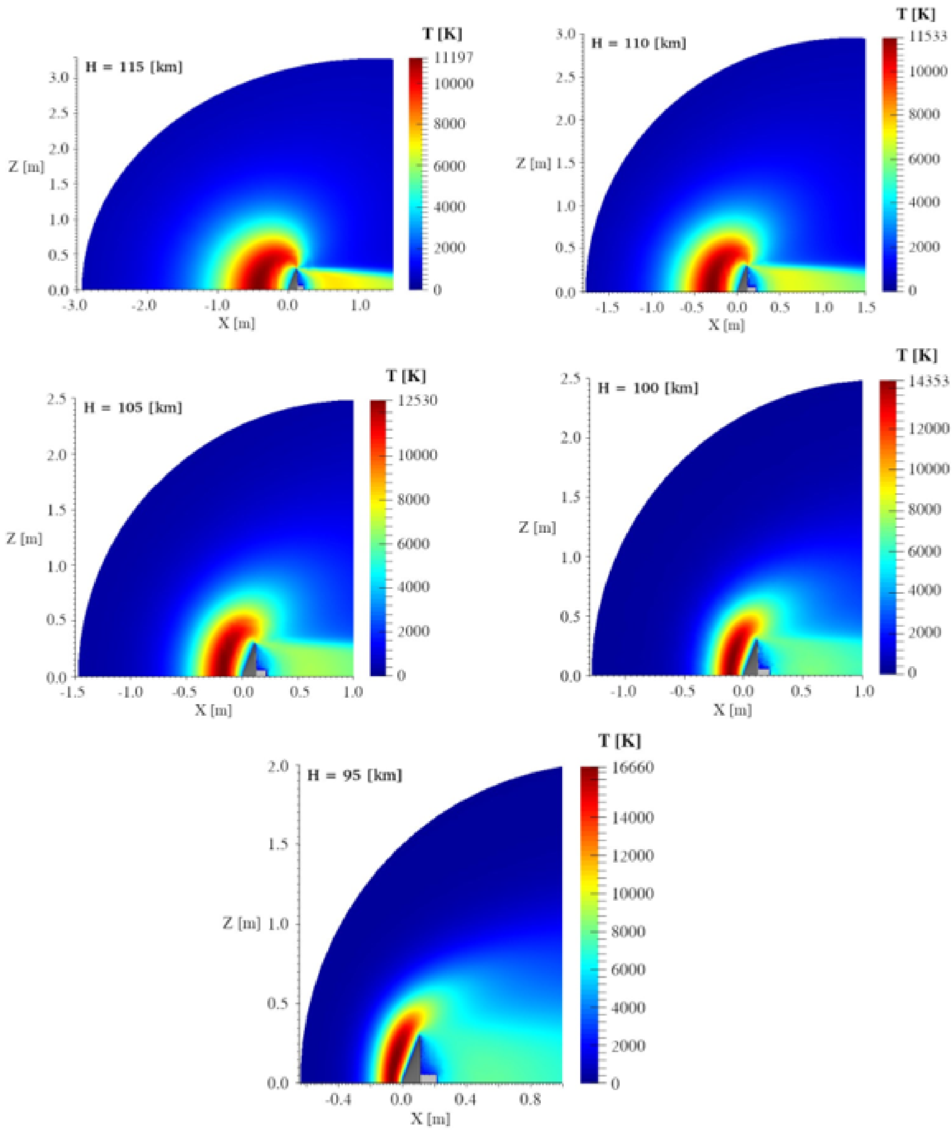

Figure 4.6: Temperature distribution around the IAD and CubeSat during the reentry phase from 115 to 95 km altitude.

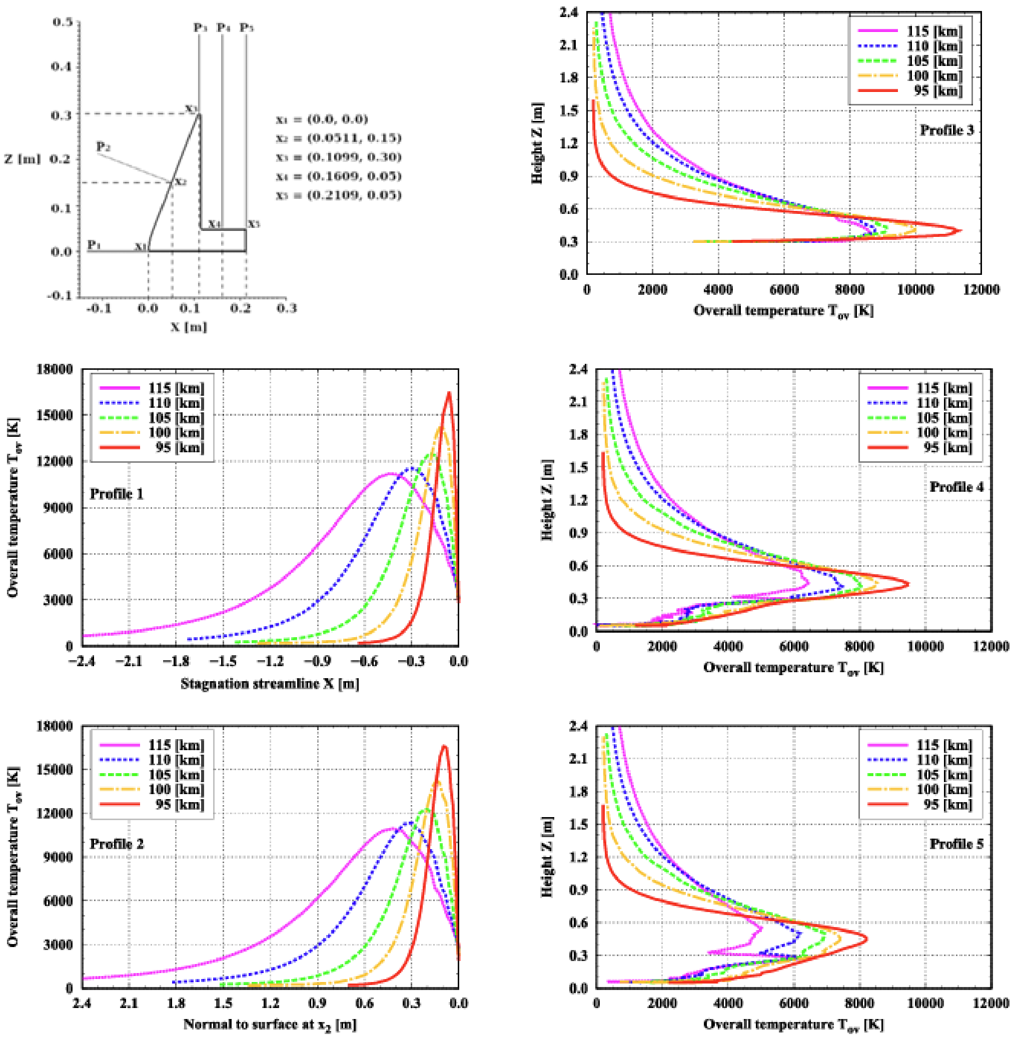

Figure 4.7: Temperature distribution along the profiles located at different positions normal to the geometry surface for each altitude considered in the present investigation.

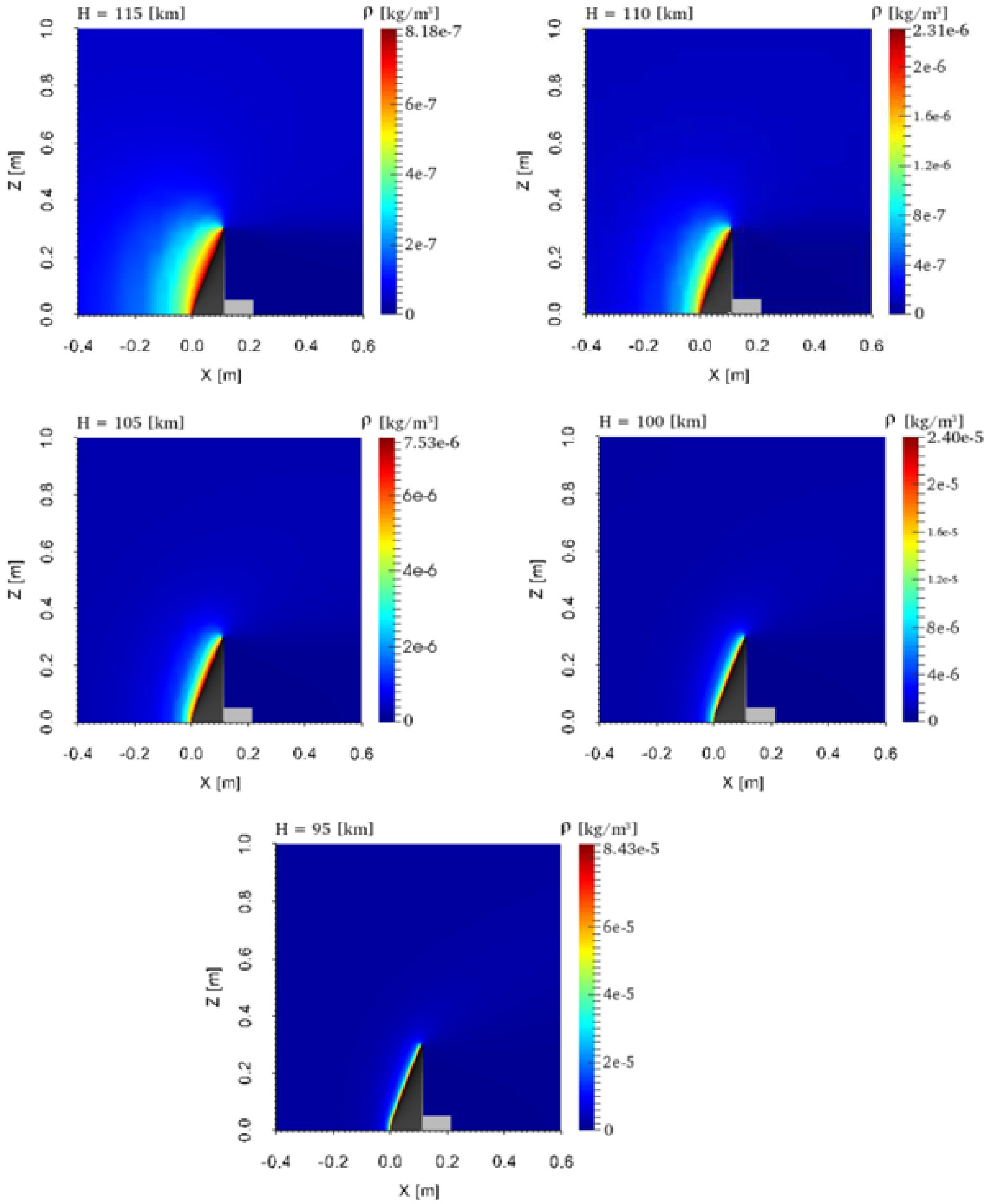

Figure 4.8: Density distribution around the IAD and CubeSat during the re-entry phase from 115 km to 95 km altitude.

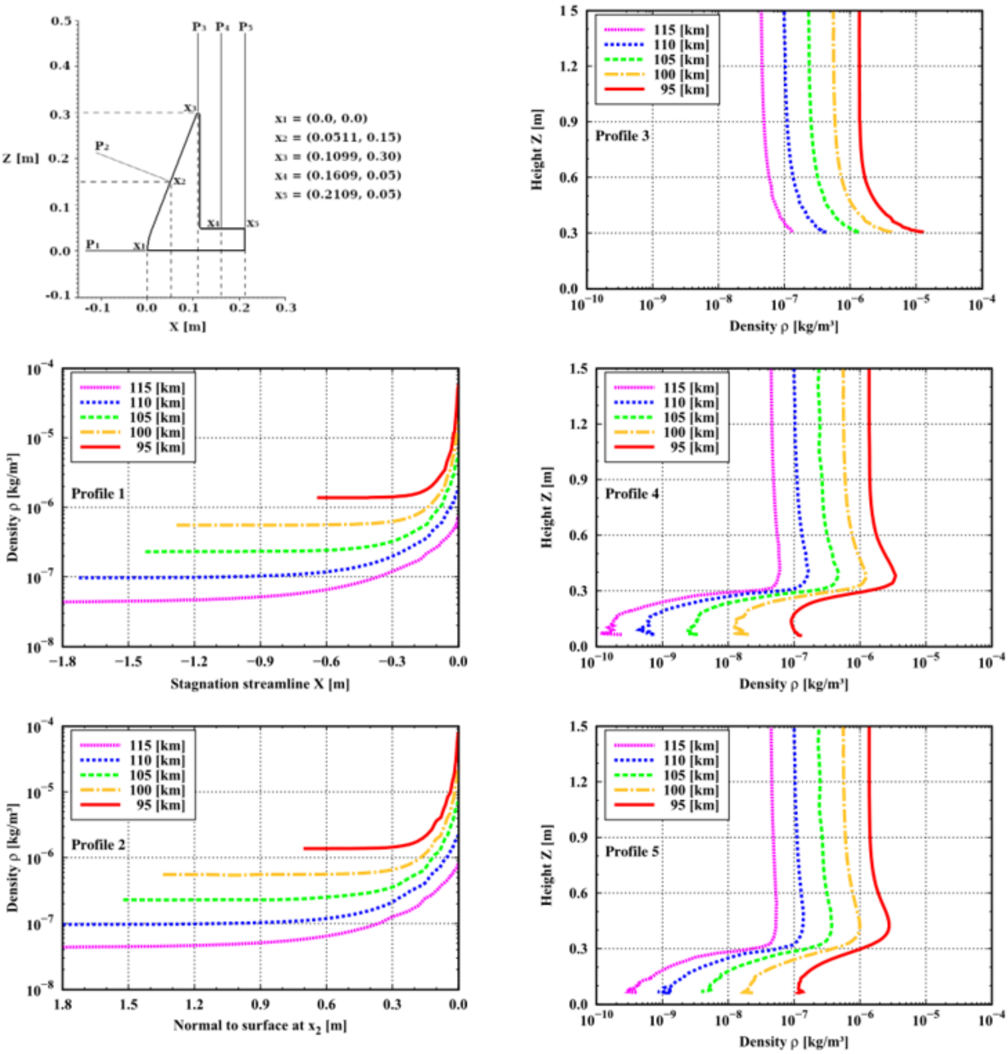

Figure 4.9: Density distribution along the profiles located at different positions normal to the geometry surface for each altitude considered in the present investigation.

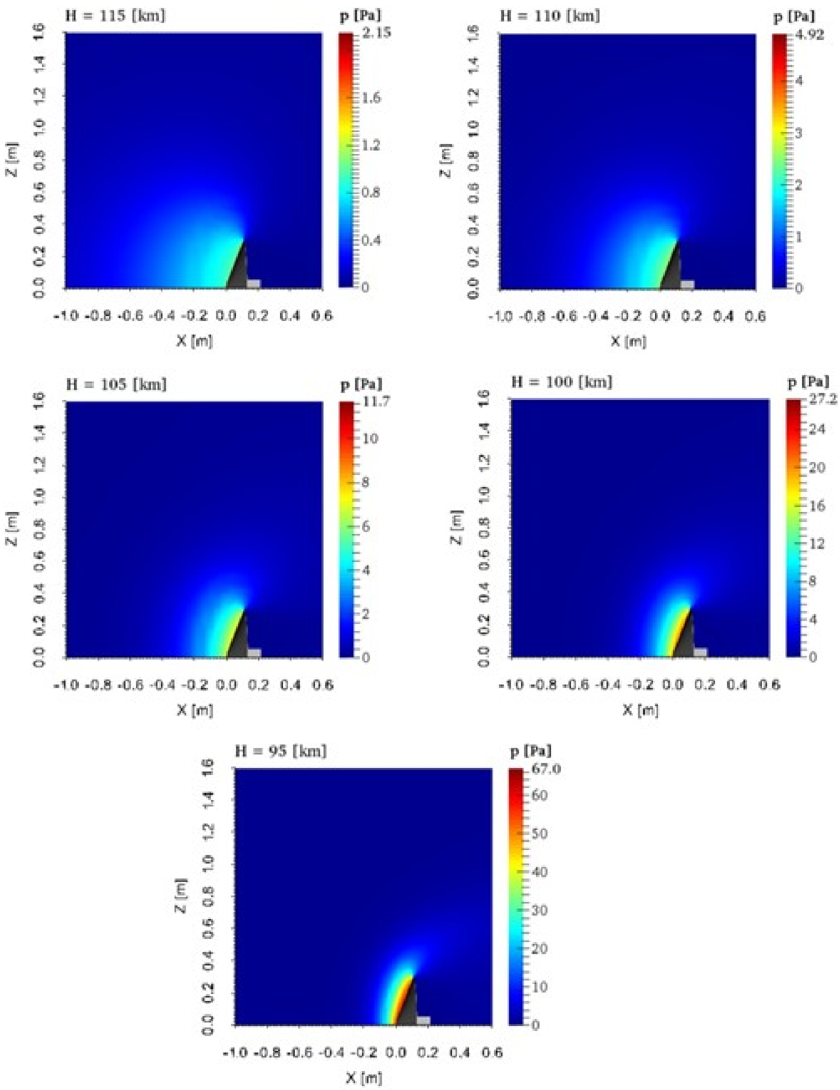

Figure 4.10: Pressure distribution around the IAD and CubeSat during the re-entry phase from 115 km to 95 km altitude.

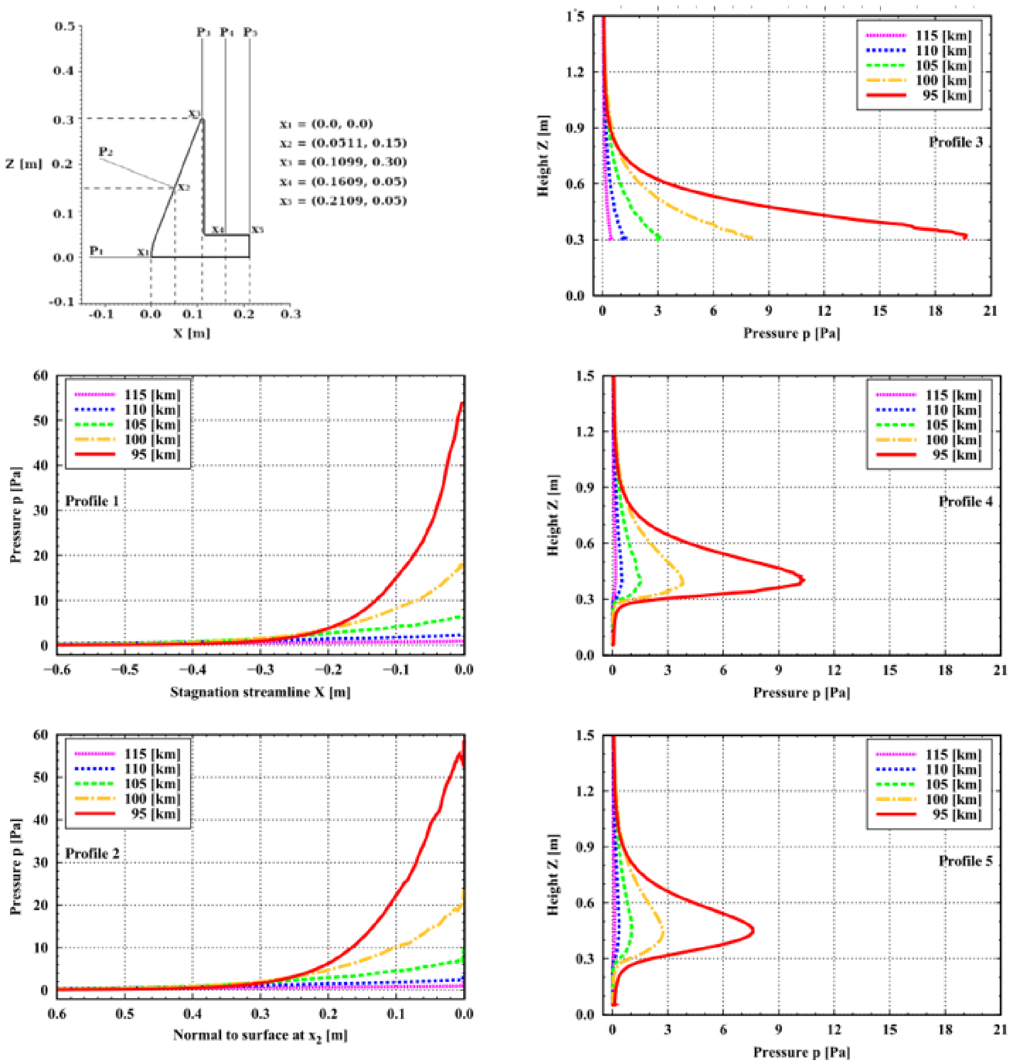

Figure 4.11: Pressure distribution along the profiles located at different positions normal to the geometry surface for each altitude considered in the present investigation.

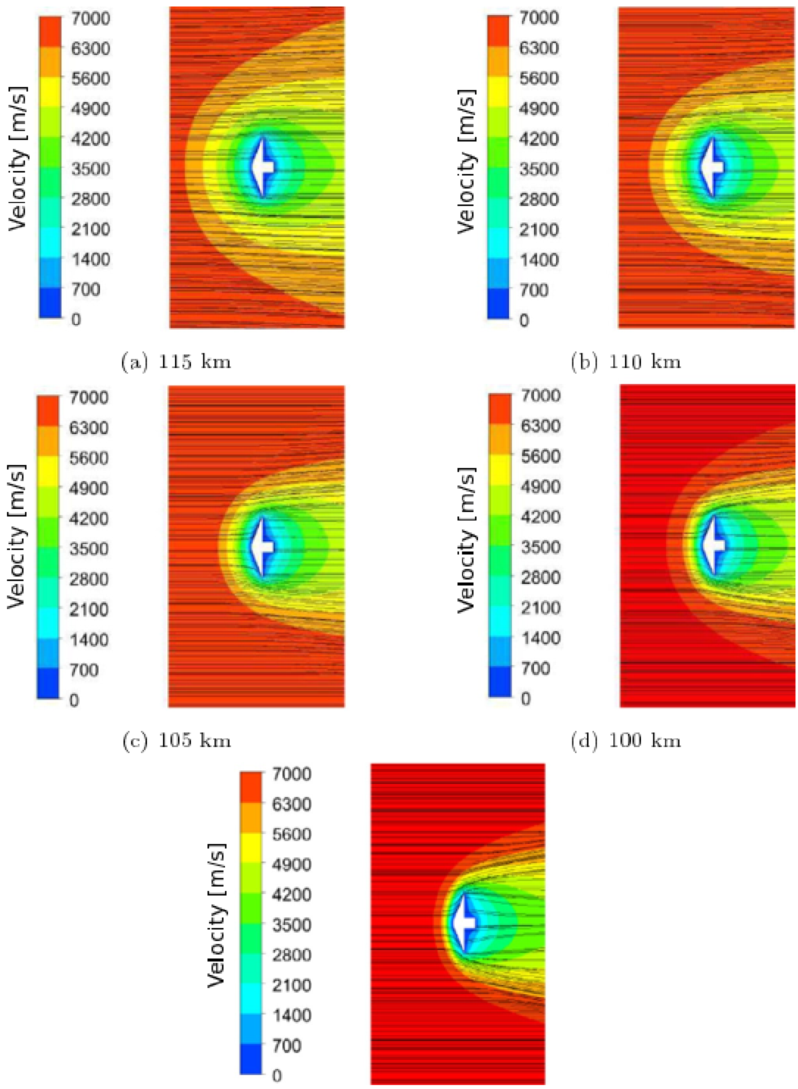

(a) 115 km

(b) 110 km

(c) 105 km

(d) 100 km

(e) 95 km

Figure 4.12: Velocity contours and streamlines around the IAD and CubeSat during the re-entry phase from 115 km to 95 km altitude: CFD results.

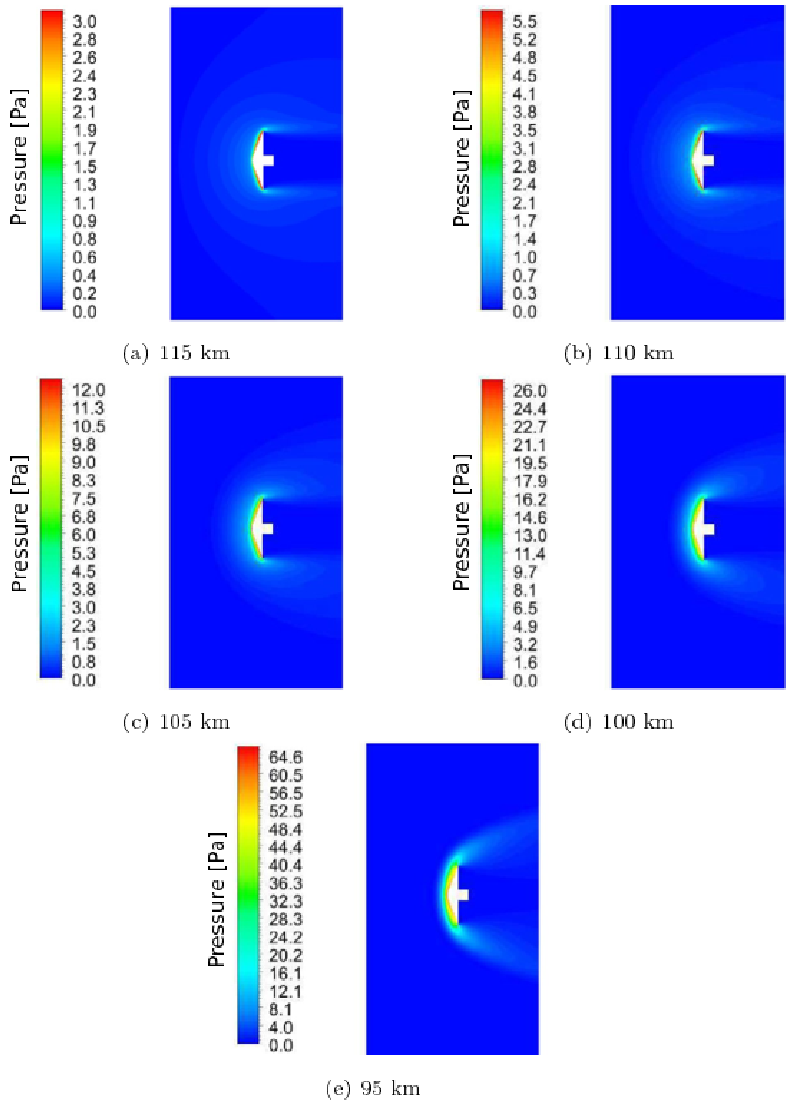

Figure 4.13: Pressure contours and streamlines around the IAD and CubeSat during the re-entry phase from 115 km to 95 km altitude: CFD results.

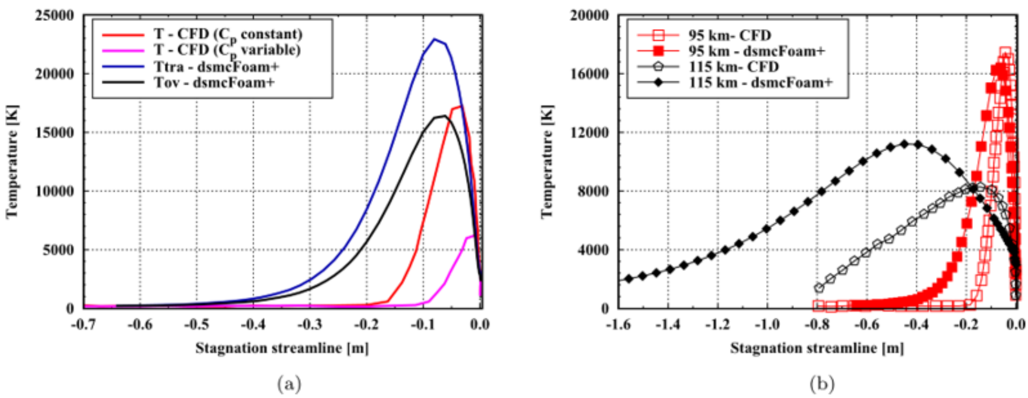

Figure 4.14: Temperature distribution along the stagnation streamline.

5 Fluid Dynamic Assessment of a Deployable System

Building on the approach described in the previous chapter, this chapter investigates the aerodynamics of a deployable re-entry system. As in the previous analysis, the DSMC simulations were carried out by Prof. Rodrigo Cassineli Palharini and his research team as part of a joint collaborative effort. It concludes with an analysis of a flap-based control system positioned at the trailing edge of the heat shield, evaluating its effectiveness as a propellantless control mechanism [11, 62].

5.1 Geometry definitions and computational parameters

In this chapter, a satellite coupled with a deployable heat shield with 8 flaps is investigated for re-entry and recovery purposes. An overview of the device and geometric specifications is shown in Figure 5.1 and Table 5.1, respectively.

The adaptability and maneuverability of the device result from the contributions of different flap configurations to the yaw, roll, and pitch moment coefficients. This strategy is based on the rotation of flaps to influence the trim of the capsule, generating sufficient lift and lateral force to enable controlled maneuvers throughout the re-entry trajectory. Unlike conventional re-entry capsules, which typically allow only directional changes, the control system here enables modulation of both the magnitude and orientation of the resulting aerodynamic forces. This capability extends control ability over a wide range of flight conditions, enhancing the overall adaptability and maneuverability of the re-entry system, as discussed in [112]. The versatility of the design is highlighted by its ability to dynamically adjust aerodynamic forces, representing a promising advancement in optimizing spacecraft control during re-entry.

However, detailed descriptions of the mechanical design are not included here, as these aspects are outside the scope of this work.

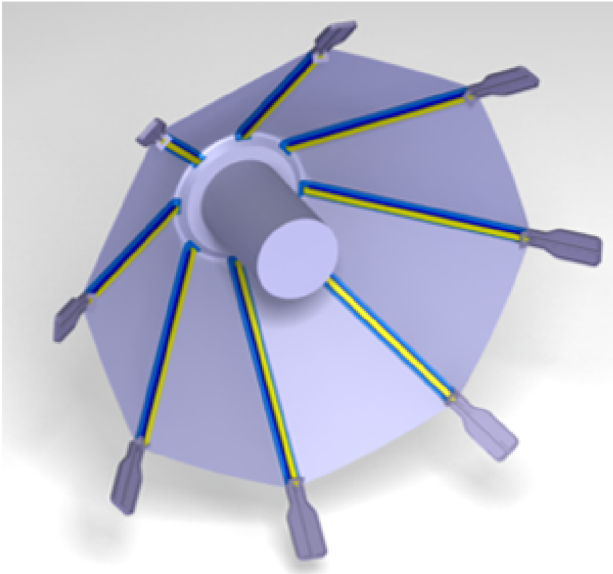

Figure 5.1: Representation of the capsule in the deployed configuration [11].

Geometric specification	Value
Diameter in deployed configuration	1.5 m
Diameter in folded configuration	0.5 m
Length of the module in folded configuration	0.8 m
Reference surface	1.77 m^2
Single flap surface	0.021 m^2

Table 5.1: Main geometric specifications of the deployable device.

5.1.1 Simulation conditions

Relevant conditions for the numeric analysis are identified after generating a re-entry trajectory, considering a rotating Earth and the J_2 gravity model [113].

A detailed discussion of the terms in the equations, the convention, and reference frames is reported in [113].

Table 5.2 summarizes the initial conditions, while Figure 5.2 shows the trajectory considered in terms of altitude as a function of the Mach number.

The simulation conditions for the aerodynamic analysis are defined based on the trajectory outlined in Figure 5.2, serving as the primary reference. This investigation includes the assessment at two additional higher altitudes, 150 km and 200 km, to provide a more comprehensive understanding of the aerodynamic behavior across different atmospheric regimes. For aerodynamic assessment along the re-entry trajectory, the angle of attack is assumed as $\alpha = 0°$. The freestream conditions considered for the numerical simulations are summarized in Table 5.3, where the Knudsen number is calculated using the maximum diameter in the deployed configuration as the characteristic length

Altitude	120 km
Velocity	7800 m/s
γ	$-0.5°$

Table 5.2: Initial conditions considered for the re-entry trajectory.

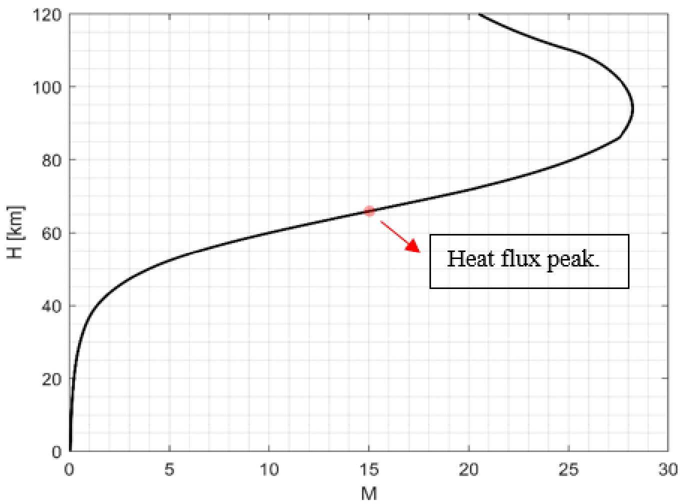

Figure 5.2: Re-entry trajectory with a focus on the heat-flux peak condition, represented by the red point.

Altitude [km]	V_∞ [m/s]	p_∞ [Pa]	T_∞ [K]	ρ_∞ [kg/m^3]	λ_∞ [m]	Kn [-]
95	7800	7.6×10^{-2}	188	1.4×10^{-6}	5.79×10^{-2}	0.0386
100	7800	3.2×10^{-2}	195	5.6×10^{-7}	1.42×10^{-1}	0.0947
105	7800	1.4×10^{-2}	209	2.3×10^{-7}	3.36×10^{-1}	0.224
110	7800	7.1×10^{-3}	240	9.7×10^{-8}	7.88×10^{-1}	0.525
150	7800	4.5×10^{-4}	634	2.08×10^{-9}	3.30×10^{1}	22
200	7800	8.5×10^{-5}	855	2.5×10^{-10}	2.40×10^{2}	160

Table 5.3: Flight conditions considered for the aerodynamic analysis of the deployable system [111].

Altitude [km]	n_{N_2} (m^{-3})	n_{O_2} (m^{-3})	n_O (m^{-3})
95	2.27×10^{19}	5.83×10^{18}	4.37×10^{17}
100	9.21×10^{18}	2.15×10^{18}	4.29×10^{17}
105	3.88×10^{18}	7.65×10^{17}	3.41×10^{17}
110	1.64×10^{18}	2.62×10^{17}	2.30×10^{17}
150	3.12×10^{16}	2.75×10^{15}	1.78×10^{16}
200	2.93×10^{15}	1.92×10^{14}	4.05×10^{15}

Table 5.4: Atmospheric composition at different altitudes [111].

of the spacecraft. Similarly, the atmospheric composition for the altitudes is shown in Table 5.4.

5.2 Computational approaches

The wide range of altitudes considered in this investigation encompasses varying degrees of flow rarefaction, spanning from continuum to highly rarefied regimes. Consequently, the aerodynamic analysis of the re-entry system has been conducted using a comprehensive, multi-fidelity approach, combining CFD and DSMC methods, selected based on the flight conditions. CFD simulations were employed for altitudes between 95 km and 110 km, while DSMC analyses were carried out at 100 km, 150 km, and 200 km. Notably, the 100 km altitude case was investigated using both CFD and DSMC techniques to enable a comparative assessment.

5.2.1 CFD method

This section outlines the CFD methodology, including the geometry, aerodynamic grid, models, and boundary conditions adopted. For the CFD analysis, a simplified representation of the satellite is used, retaining only the components that significantly influence its aerodynamic behavior. A half-model is employed by leveraging the symmetry of the configuration, excluding flap deflections and angle of attack to reduce computational complexity. A three-dimensional trimmed mesh is generated, based on five volumetric controls designed to guide mesh refinement and optimize cell distribution around the vehicle based on the expected flow phenomena. A conical volumetric control encompasses the entire capsule to capture the bow shock generated by the interaction between the blunt body and the hypersonic flow. In the wake region behind the heat shield, characterized by reduced aerodynamic activity, a volumetric box with a lower cell density is applied. An additional

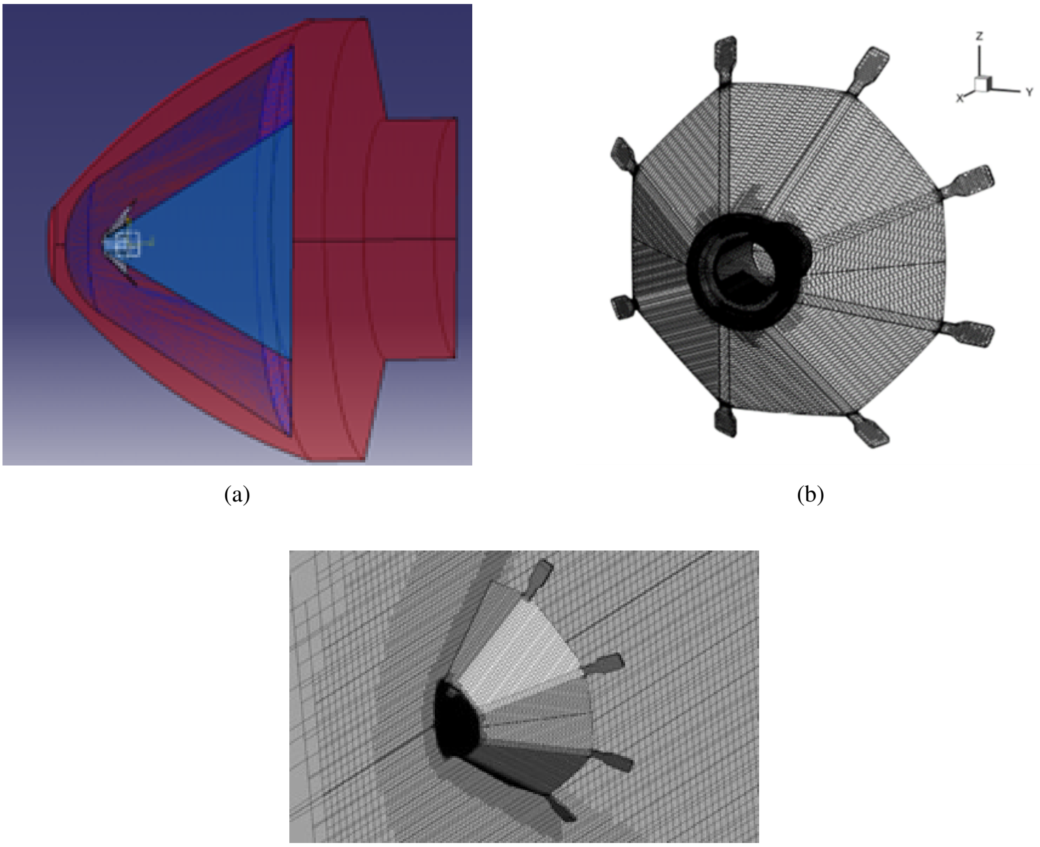

(a) (b) (c)

Figure 5.3: Volumetric controls for three-dimensional grid, surface grid on the capsule, three-dimensional grid close to the capsule.

volumetric control surrounds the previous ones to track the shock wave propagation downstream of the vehicle. Two more external volumes are defined to enclose all inner regions, allowing a gradual coarsening of the mesh and minimizing the total number of cells without compromising accuracy.

Figure 5.3a illustrates the volumetric controls used in the three-dimensional grid, with a detailed view of the capsule shown in Figure 5.3c.

The outer domain is represented as a cylinder with a hemispherical cap to reduce the total number of cells, as shown in Figure 5.4. Furthermore, its dimensions are chosen to avoid interference with the evolution of the flow field around the capsule. In addition, the capsule is characterized by an isothermal wall that imposes a surface temperature of 1000 K. Both the inlet and the external part of the domain are modeled as pressure farfield, specifying the Mach number, pressure, and temperature conditions related to the altitude. The domain outlet is defined as a pressure outlet with atmospheric conditions at the given altitude.

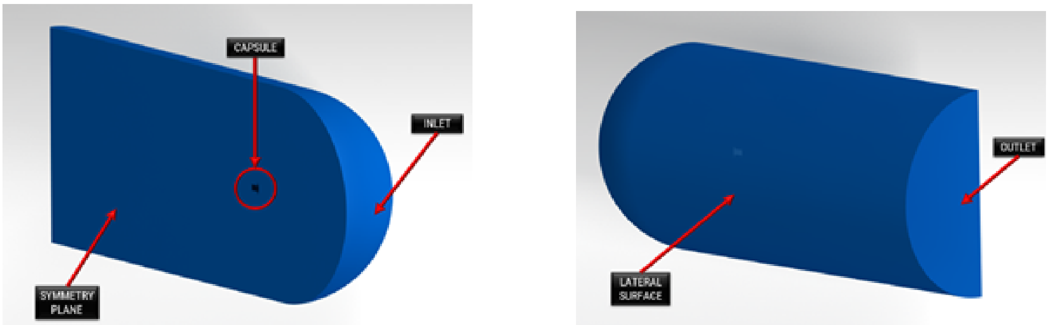

(a) (b)

Figure 5.4: Representation of the CFD domain with the different boundary conditions.

5.2.2 DSMC method

To assess the behavior of the deployable system in the rarefied region of the atmosphere, the DSMC method has been applied for altitudes ranging from 200 km to 100 km. In order to reduce the computational cost while taking advantage of the axisymmetric geometry of the capsule, a quarter-section of the computational domain has been used. Specular boundary conditions, equivalent to symmetry conditions in CFD, have been applied along the planes resulting from the quarter-domain reduction. A localized mesh refinement has been applied near the capsule surface to improve the accuracy of the aerodynamic coefficient predictions. At the downstream boundary, located behind the capsule, a vacuum boundary condition has been imposed, based on the assumption that the probability of particles moving upstream with a Mach number greater than three is negligible, as in [88]. The capsule surface has been modeled using a diffuse reflection boundary condition with full thermal accommodation. On the remaining boundaries, where the particles enter the computational domain, an inlet condition has been set based on freestream properties. The freestream velocity has been assumed to be 7800 m/s, while the surface temperature has been set to 1000 K, which is representative of the thermal conditions near the stagnation point.

5.3 Numerical results and discussions

This section describes the main results of the aerodynamic analysis. The first subsection, focused on the CFD results, is followed by another one that discusses the DSMC simulation results. A conclusive subsection discusses a comparison between the two methodologies in the flight condition corresponding to an altitude of 100 km.

5.3.1 CFD analysis

The results of the CFD analysis for the deployable system in terms of velocity, pressure and temperature are shown in Figure 5.5, considering altitudes from 95 km to 110 km. The hypersonic interaction between the capsule and the flow field induced a bow shock wave, which is responsible for the generation of accentuated fluctuations in fluid dynamic properties. The velocity distributions showed a remarkable trend in the shock wave separation along the re-entry trajectory. In particular, the shock wave stand-off distance increases under ascending conditions. At the lowest altitude of 95 km, the shock wave is close to the body and is characterized by a more defined structure. However, at the highest altitude of 110 km, the shock wave is farther away from the body and has a more evanescent nature. A distinct recirculation zone, characterized by velocities of the order of a few meters per second and very low-pressure values, is observed below the heat shield. The flowfield begins to accelerate gradually from the rear section within the heat shield, extending further downstream. The pressure distributions show an increase in surface pressure values from 110 km to 95 km. The bow shock wave is responsible for a static pressure jump from atmospheric to values ranging from 77 Pa for the lowest altitude to 9 Pa at 110 km. In this regard, Table 5.5 summarizes the pressure values at the stagnation point in each case, showing a behavior which is in accordance with the theory. As the altitude increases, the pressure gradients are weaker, thus reducing the influence of the backward flow. In relation to the temperature, the nose of the capsule is the area most exposed to thermal loads reflecting in temperature peaks. It shows a decreasing trend for increasing values of altitude, ranging from 23185 K at 95 km altitude to 12615 K at 110 km altitude. Similar to the velocity profile, a low-temperature zone is observed in the wake region within the heat shield, with temperature values gradually increasing from the rear section inside the heat shield to the downstream region. The significant thermal stresses that characterize the re-entry underscore how a robust thermal control system is imperative to ensure the structural integrity of the device. Finally, the drag estimation under the different conditions is presented. The drag coefficient exhibits an increasing trend with altitude (as summarized in Table 5.7), ranging from 1.57 at 95 km to 3.39 at 110 km. On the contrary, the absolute value of the drag (as shown in Table 5.8) decreases with altitude due to the progressive rarefaction of the atmosphere, resulting in a decreasing value of the density. However, as the altitude increases, the reliability of the CFD decreases as a result of the rarefaction of the flow field. So, an increase in estimation error is expected during the ascending phase of the trajectory, in line with the results achieved also for the IAD system in the previous chapter.

5.3.2 DSMC analysis

This section presents the results of DSMC simulations at altitudes of 100 km, 150 km, and 200 km. The velocity, pressure, temperature, and density contours are shown in Figure 5.6. The analysis highlights how rarefaction effects and mean free path differences significantly influence the flowfield structure across the altitudes. At 200 km, the flow decelerates more gradually in front of the capsule, with the low-speed region extending further upstream. As altitude decreases, the flow deceleration becomes stronger, and the low-speed region is increasingly confined to the surface. This behavior is driven by the shorter mean free path at lower altitudes, which increases the frequency of intermolecular collisions, limiting the upstream influence of reflected particles. The flow expansion past the capsule shoulder is abrupt at high altitudes, rapidly reaching freestream conditions. At lower altitudes, the expansion is more gradual, with streamlines deviating more noticeably and tending to align with the shield angle after the shoulder. These differences are due

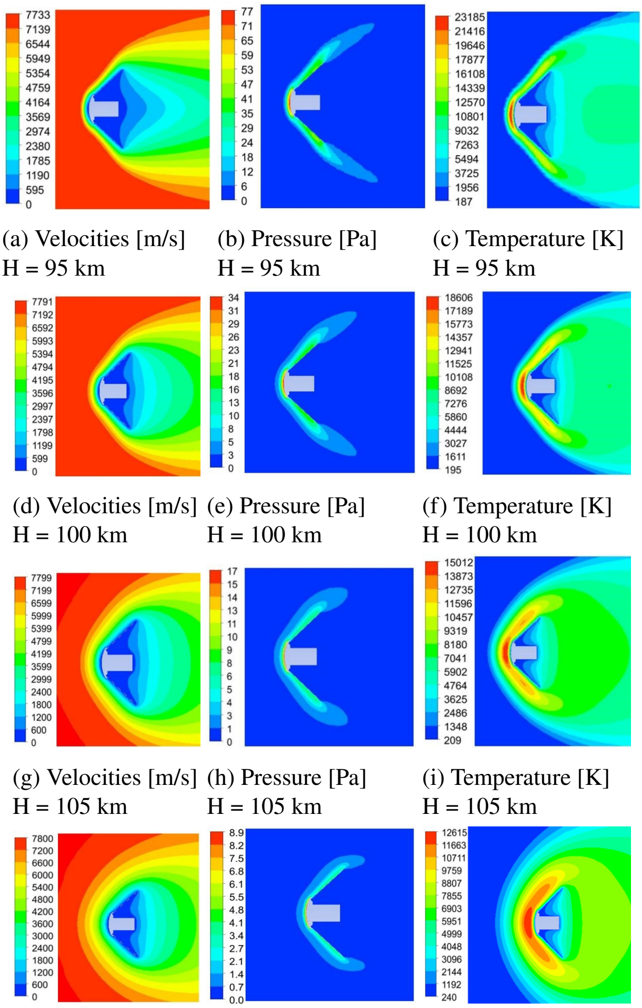

(a) Velocities [m/s] H = 95 km

(b) Pressure [Pa] H = 95 km

(c) Temperature [K] H = 95 km

(d) Velocities [m/s] H = 100 km

(e) Pressure [Pa] H = 100 km

(f) Temperature [K] H = 100 km

(g) Velocities [m/s] H = 105 km

(h) Pressure [Pa] H = 105 km

(i) Temperature [K] H = 105 km

(j) Velocities [m/s] H = 110 km

(k) Pressure [Pa] H = 110 km

(l) Temperature [K] H = 110 km

Figure 5.5: Comparison of Velocities, Pressure, and Temperature at different altitudes for the deployable re-entry system.

to the increasing influence of molecular collisions as the atmospheric density rises with decreasing altitude. Pressure contours reveal that the maximum pressure shifts upstream and increases with decreasing altitude. At 200 km, peak pressure reaches about 0.017 Pa, nearly 200 times the ambient level. At 100 km, it exceeds 36.9 Pa, over 1000 times the local atmospheric pressure. This increase is associated with denser air and higher collision rates, particularly near the capsule's nose, where kinetic energy converts into pressure. Temperature distributions show that the shock wave is diffuse and detached at higher altitudes, with a peak of 17171 K at 200 km. As altitude decreases, the shock becomes thinner and closer to the body, reaching 26412 K at 100 km. At 200 km and 150 km, high-temperature regions reach the surface near the shoulder. At 100 km, a mid to low-temperature layer separates the shock from the surface. Additionally, at higher altitudes, streams of mid-temperature gas extend from the shoulder into the wake, due to reduced collision frequency. In all cases, a low-temperature layer persists near the capsule surface and in the wake region. The mass density contours mirror the pressure field but appears more compact. At 200 km, the reflected particles travel farther upstream due to fewer collisions, expanding the affected region. At 100 km, the higher collision rate confines high-density areas close to the surface. Peak density at 200 km reaches 5.2×10^{-9} kg/m³ (20 times ambient), while at 100 km it exceeds 3.9×10^{-5} kg/m^3 (around 68 times ambient). A local drop in density is observed near the capsule's shoulder at 200 and 150 km, indicating flow expansion. At 100 km, this region extends downstream, aligned with the shield angle, similar to the translational temperature pattern. Furthermore, a low-density region appears between the nose and shield mantle, caused by flow alignment with the surface of the shield, limiting particle accumulation in that gap. Finally, the drag force increases along the descent, while the drag coefficient decreases due to changing atmospheric conditions (Tables 5.8 and 5.7). As a result, the mass-to-drag ratio improves with altitude, indicating better aerodynamic performance at higher altitudes.

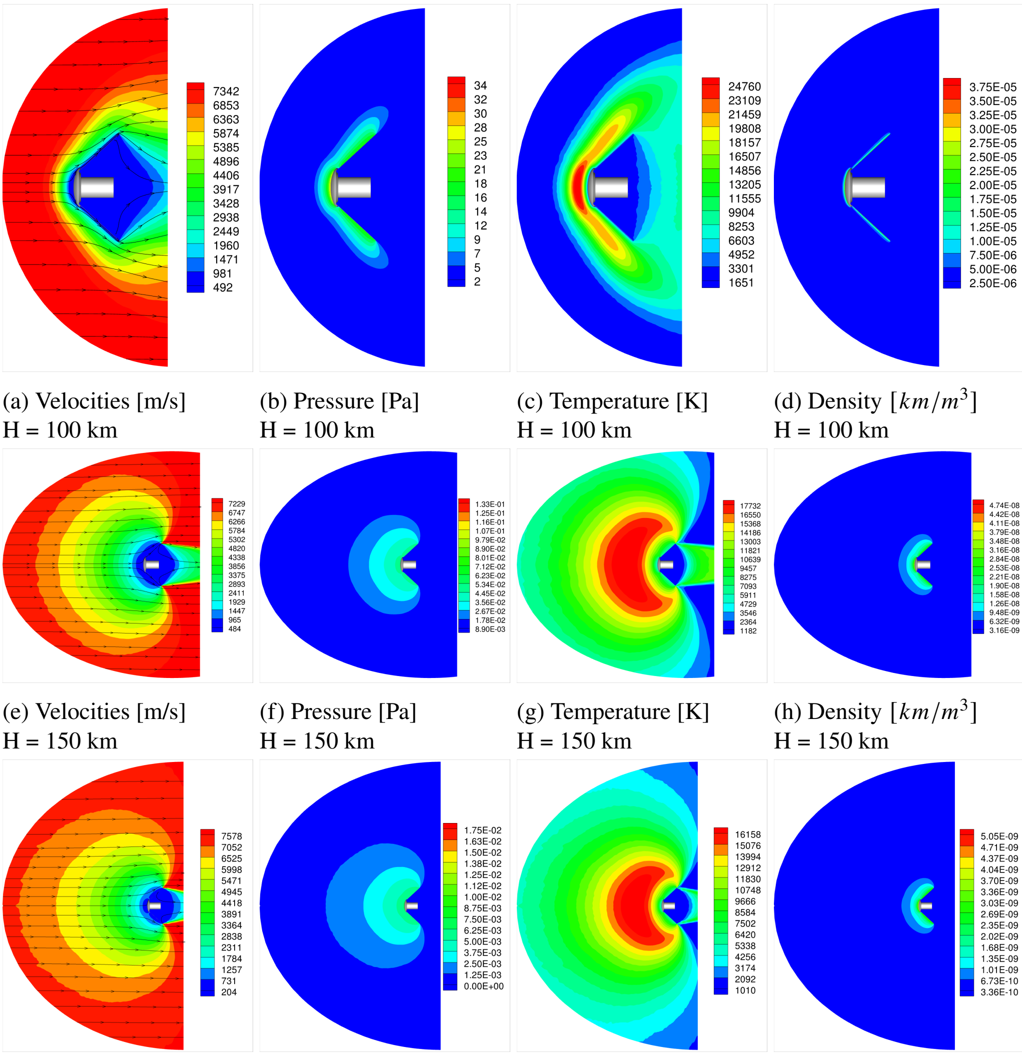

(a) Velocities [m/s] H = 100 km
(b) Pressure [Pa] H = 100 km
(c) Temperature [K] H = 100 km
(d) Density $[km/m^3]$ H = 100 km

(e) Velocities [m/s] H = 150 km
(f) Pressure [Pa] H = 150 km
(g) Temperature [K] H = 150 km
(h) Density $[km/m^3]$ H = 150 km

(i) Velocities [m/s] H = 200 km
(j) Pressure [Pa] H = 200 km
(k) Temperature [K] H = 200 km
(l) Density $[km/m^3]$ H = 200 km

Figure 5.6: DSMC contours for different altitudes for the deployable system.

5.3.3 Comparison between CFD and DSMC

The concluding section of this aerodynamic assessment discusses a comparative analysis of the two methodologies used at a common altitude. Figure 5.8 illustrates a comparison of velocity fields resulting from CFD and DSMC at an altitude of 100 km. In addition, Tables 5.5, 5.6, 5.8 and 5.7 summarize the main parameters, such as stagnation pressure point, maximum temperature, drag force and drag coefficients in the two cases. The velocity distributions illustrated in Figure 5.8 highlight the presence of a bow shock wave in both methodologies, with the DSMC simulation showing a slightly larger stand-off distance. This suggests its suitability for a more precise representation of rarefied flow phenomena at high altitudes. In the DSMC case, a pronounced wake region forms behind the heat shield, with lower velocities (shown in dark blue) extending farther downstream, indicating slower flow recovery and delayed acceleration. Conversely, in the CFD case, the velocity begins to increase closer to the rear of the heat shield, transitioning from blue to warmer colors, reflecting an earlier acceleration in the wake. As previously discussed, the static pressure contours experience a similar situation, with a stagnation pressure of 34 Pa in CFD and 36.9 Pa in DSMC, as in Table 5.5. According to Figure 5.7, there are noticeable differences between the two methodologies. The DSMC simulation indicates higher temperatures, reaching 26412 K in the nose of the capsule, compared to the 18606 K observed in the CFD case.

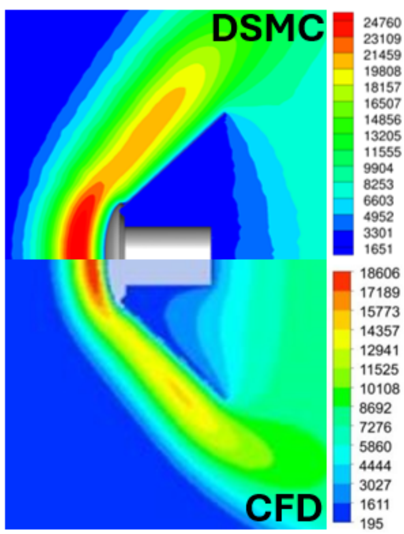

Figure 5.7: Comparison DSMC and CFD temperature field results for 100 km altitude case.

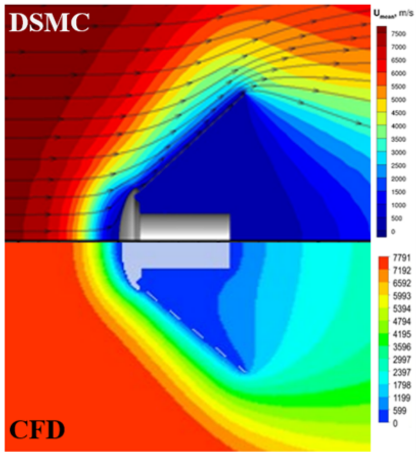

Figure 5.8: Comparison DSMC and CFD velocity fields result for 100 km altitude case.

This discrepancy is probably due to the explicit modeling of molecular interactions by DSMC, which improves its capability to precisely capture high-temperature regions. In conclusion, a difference in drag coefficients is experienced, with CFD slightly overestimating it (approximately 11% higher than DSMC) at 100 km altitude. In summary, although both approaches offer valuable insight into flow behavior, their differences highlight the importance of choosing an appropriate methodology based on the particular flow conditions and the desired accuracy level.

5.4 Control capabilities of the flaps

After a comprehensive fluid dynamic assessment, this chapter concludes with an example of the control capabilities of the flaps. For this purpose, a matrix of CFD simulations has been performed under the most prohibitive condition, corresponding to the heat flux peak shown in Figure 5.2. In order to study the effectiveness of flaps as control surfaces and to generate an extensive aerodynamic database, each flap should be deflected individually to estimate its contribution. This approach, however, would result in an unfeasible number of CFD simulations, leading to high computational cost and time. In this regard, the same methodology followed in [114] is considered, neglecting the aerodynamic interference between the flaps and the heat shield. In [114], a study was conducted to verify this assumption by deflecting each flap independently to determine the aerodynamic influence between the flaps and the heat shield. Despite the satisfactory results, additional analysis has been performed in the current work to further support this hypothesis. Two different configurations have been compared by means of CFD simulations: the capsule alone and another provided with flaps at the end. A perfect overlap of pressure profiles on the heatshield in both cases is observed, highlighting a negligible influence of the flaps (Figure 5.9).

CFD simulations were conducted over a matrix of angles of attack, taking into account the reference frame and the flap numbering convention shown in Figure 5.10.

As a conclusion, a preliminary aerodynamic database has been developed. It represents a key element to assess the performance and effectiveness of the capsule as an aerodynamic control system, enabling the quantification of flap deflection effects on the pitching, yawing, and rolling moment

Altitude [Km]	Pressure in stagnation point [Pa]	
	CFD	DSMC
95	77.0	-
100	34.0	36.9
105	17.0	-
110	8.9	-
150	-	0.142
200	-	0.017

Table 5.5: Pressure in the stagnation point as a function of the altitude.

Altitude [Km]	Maximum Temperature [K]	
	CFD	DSMC
95	23185	-
100	18606	26412
105	15012	-
110	12615	-
150	-	18922
200	-	17171

Table 5.6: Maximum temperature as a function of the altitude.

Altitude [Km]	Drag coefficient C_D [-]	
	CFD	DSMC
95	1.57	-
100	1.82	1.73
105	2.34	-
110	3.39	-
150	-	2.28
200	-	2.36

Table 5.7: Drag coefficient as a function of the altitude.

Altitude [Km]	Drag force [N]	
	CFD	DSMC
95	118	-
100	55.9	52.12
105	30.4	-
110	18.8	-
150	-	0.255
200	-	0.0317

Table 5.8: Drag force as a function of the altitude.

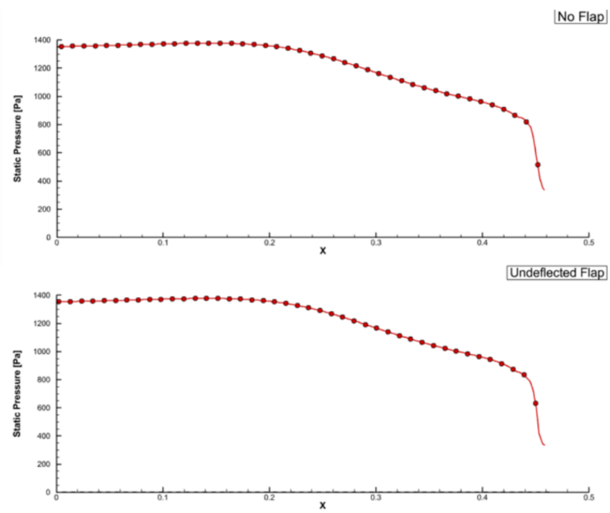

Figure 5.9: Pressure profile on heatshield in case of capsule alone and on capsule with flaps embedded.

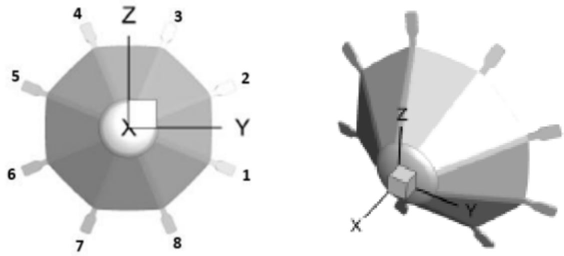

Figure 5.10: Capsule reference frame.

coefficients. In particular, results related to the undeflected configuration and flap deflections of 10°, 20°, and 30° will be discussed. In Figure 5.11, the drag coefficient trend as a function of angle of attack is shown. In the undeflected configuration, the drag coefficient exhibits a trend, which is quasi-constant and tends to become parabolic in the deflected flap configurations. In particular, the greater the deflection angle, the more pronounced the parabolic trend, with the maximum C_D value occurring at zero angle of attack. The lift coefficient is only slightly influenced by flap deflection.

Figures 5.12-5.14 show the contribution of each flap to C_{mX}, C_{mY}, and C_{mZ}, varying both deflection and angle of attack.

Flaps 1, 2, 5, and 6 contribute more to C_{mZ} due to their positions relative to the z-axis. C_{mY}, on the other hand, is primarily influenced by flaps 3, 4, 7, and 8, as confirmed in Figure 5.13. The same flaps also provide a greater contribution to C_{mX} (Figure 5.12). These results indicate that the control system will have access to multiple combinations of flap deflections to achieve a wide variety of attitude changes.

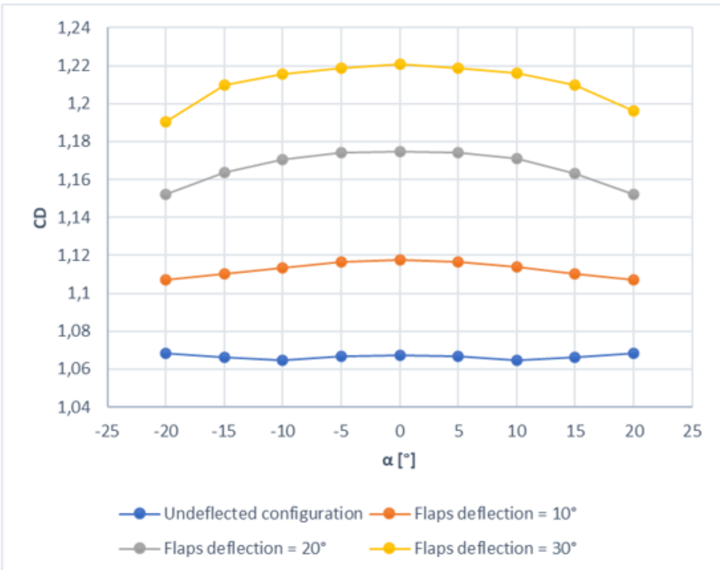

Figure 5.11: Drag coefficient profile for each capsule configuration, from null deflection to 30° flaps' deflection.

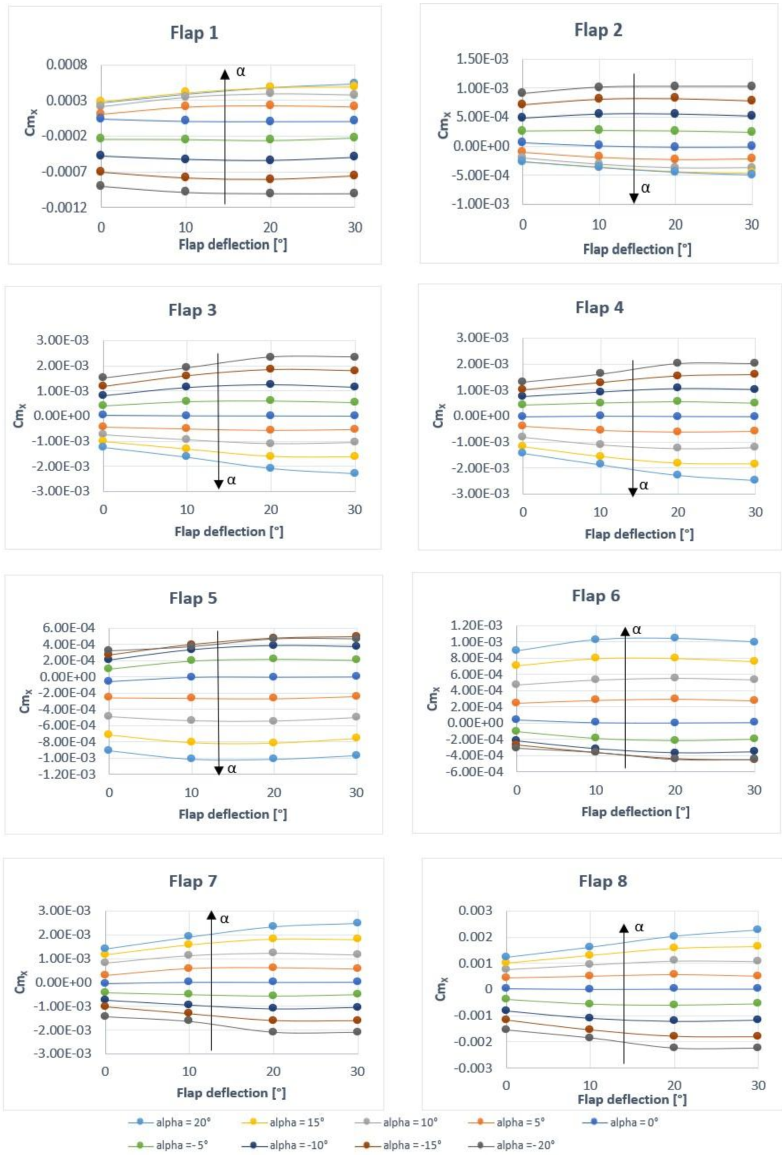

Figure 5.12: Flaps contribution to C_{mX} for variable deflections and angle of attack.

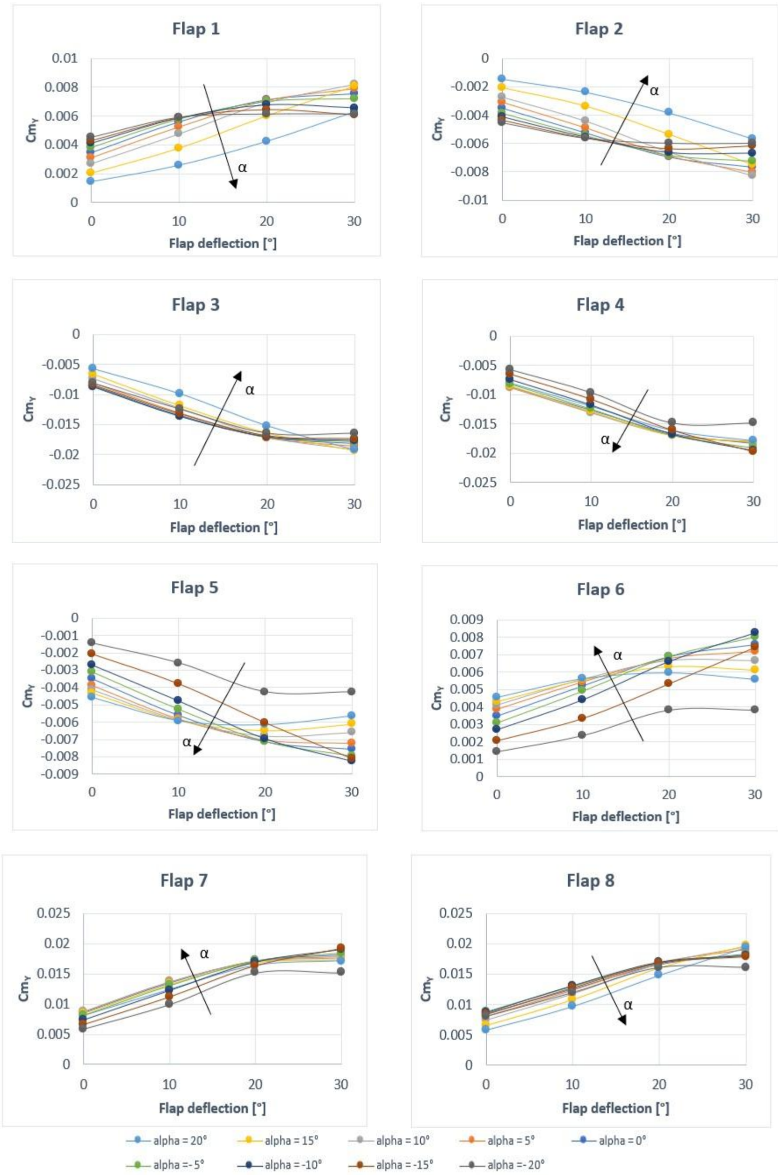

Figure 5.13: Flaps contribution to C_{mY} for variable deflections and angle of attack.

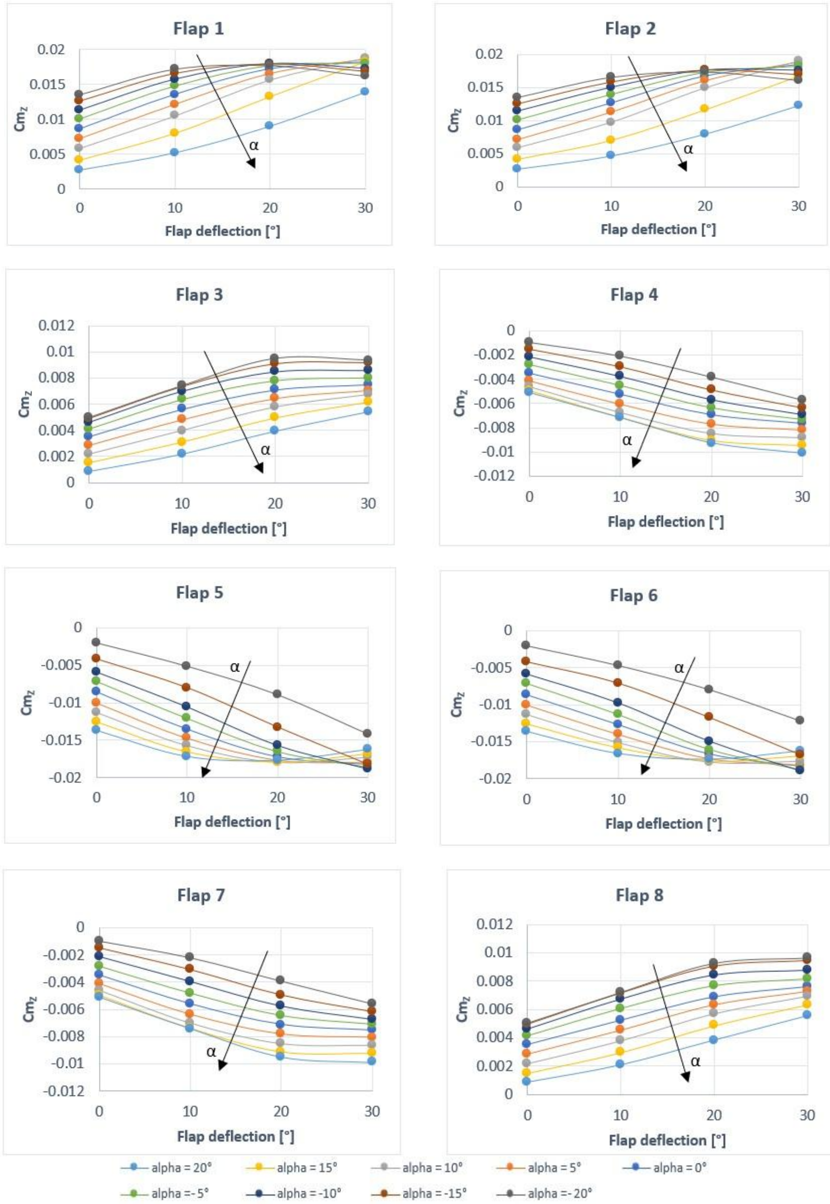

Figure 5.14: Flaps contribution to C_{mZ} for variable deflections and angle of attack.

6 De-Orbiting

This chapter focuses on the assessment of a G&C algorithm for a time-optimal drag-based targeted de-orbiting to ensure the reaching of a desired point at the re-entry interface. The adopted approach combines optimal control theory with AI techniques [67–69]. First, the optimal control problem is presented, including the formulation of the dynamics, the structure, and the results. This algorithm is then employed to generate a comprehensive dataset of optimal control trajectories, which serves as a training set for a DNN, designed to estimate the control parameters in real time, while maintaining solution optimality. The chapter concludes with a discussion of the outcomes and effectiveness of the proposed methodologies.

6.1 Optimal control algorithm

The goal of the optimal control algorithm is to reach a desired point at the re-entry interface in the minimum time and with high accuracy. It is formulated as a single-stage optimization, based on a hp adaptive Gaussian quadrature orthogonal collocation method [115–118] and is solved with the MATLAB software GPOPS-II [115, 116], considering the exposed surface of the de-orbiting device as the control variable.

6.1.1 Formulation of dynamics

The dynamics of the problem is described in terms of modified equinoctial orbital parameters (p, f, g, h, k, L), resulting particularly suitable for trajectories analysis and optimization [119–121]. They are related to the classical ones by the following equations:

$$p = a\left(1 - e^2\right) \tag{6.1}$$

$$f = e\cos(\omega + \Omega) \tag{6.2}$$

$$g = e\sin(\omega + \Omega) \tag{6.3}$$

$$h = \tan\left(\frac{i}{2}\right)\cos\Omega \tag{6.4}$$

$$k = \tan\left(\frac{i}{2}\right)\sin\Omega \tag{6.5}$$

$$L = \Omega + \omega + \theta \tag{6.6}$$

Where L is the True Longitude, defined referring to a fixed direction, the First Point of Aries, implies its value repeats every $2\pi n$, where $n \in Z$. It is a parameter of interest for the optimal control algorithm.

The differential equations of motion of the orbiting satellite are:

$$\dot{p} = \frac{dp}{dt} = \frac{2p}{w}\sqrt{\frac{p}{\mu}}\Delta_t \tag{6.7}$$

$$\dot{f} = \frac{df}{dt} = \sqrt{\frac{p}{\mu}}\left[\Delta_r \sin L + [(w+1)\cos L + f]\,\frac{\Delta_t}{w} - (h\sin L - k\cos L)\,\frac{g\Delta_n}{w}\right] \tag{6.8}$$

$$\dot{g} = \frac{dg}{dt} = \sqrt{\frac{p}{\mu}}\left[-\Delta_r \cos L + [(w+1)\sin L + g]\,\frac{\Delta_t}{w} + (h\sin L - k\cos L)\frac{g\Delta_n}{w}\right] \tag{6.9}$$

$$\dot{h} = \frac{dh}{dt} = \sqrt{\frac{p}{\mu}}\frac{s^2\Delta_n}{2w}\cos L \tag{6.10}$$

$$\dot{k} = \frac{dk}{dt} = \sqrt{\frac{p}{\mu}}\frac{s^2\Delta_n}{2w}\sin L \tag{6.11}$$

$$\dot{L} = \frac{dL}{dt} = \sqrt{\frac{\mu}{p}}\left(\frac{w}{p}\right)^2 + \frac{1}{w}\sqrt{\frac{p}{\mu}}(h\sin L - k\cos L)\Delta_n \tag{6.12}$$

Where:

$$w = 1 + f\cos L + g\sin L \tag{6.13}$$

$$r = \frac{p}{w} \tag{6.14}$$

$$\alpha^2 = h^2 - k^2 \tag{6.15}$$

$$s = \sqrt{1 + h^2 + k^2} \tag{6.16}$$

A change of independent variable from time to true longitude is applied to reduce the computational cost. This approach has also proven effective in other similar optimization problems involving long time spans.

The terms Δ_r, Δ_t, and Δ_n represent the non-two-body perturbing accelerations in the radial, tangential, and normal directions, respectively. Specifically:

- The radial perturbation Δ_r acts along the geocentric radius vector.
- The tangential perturbation Δ_t is perpendicular to the radius and acts in the orbital motion direction.

- The normal perturbation Δ_n is positive along the angular momentum vector of the satellite orbit.

The total perturbation acceleration term Δ is modeled as:

$$\Delta = \Delta_g + \Delta_d \tag{6.17}$$

where Δ_g and Δ_D are the gravitational acceleration due to Earth oblateness and the contribution due to aerodynamic drag respectively. The non-spherical gravitational acceleration can be expressed as:

$$g = g_N \hat{I}_N - g_r \hat{I}_r \tag{6.18}$$

where:

$$\hat{I}_N = \frac{\hat{e}_N - (\hat{e}_N^T \hat{I}_r)\hat{I}_r}{\|\hat{e}_N - (\hat{e}_N^T \hat{I}_r)\hat{I}_r\|} \tag{6.19}$$

And

$$\hat{e}_N = \begin{bmatrix} 0 & 0 & 1 \end{bmatrix}^T \tag{6.20}$$

with the subscript N identifying the local north direction while r the radial one. The contributions due to the zonal gravity effects of J_2, J_3 and J_4 are given by the following formulation:

$$g_N = -\frac{\mu \cos\varphi}{r^2} \sum_{k=2}^{4} \left(\frac{R_e}{r}\right)^k P'_k J_k \tag{6.21}$$

$$g_r = -\frac{\mu}{r^2} \sum_{k=2}^{4} (k+1) \left(\frac{R_e}{r}\right)^k P_k J_k \tag{6.22}$$

where μ represents the gravitational parameter, r the geocentric distance of the satellite, R_e the equatorial radius of the Earth, φ the geocentric latitude, J_k the zonal gravity coefficient, and P_k is the k_{th} order Legendre polynomial. Therefore, the acceleration due to the oblateness in rotating coordinates is:

$$\Delta_g = Q^T g \tag{6.23}$$

where Q is the transformation matrix between rotating and Earth Centered Inertial (ECI) coordinates. Its columns are respectively defined as:

$$\left[\hat{i}_r = \frac{r}{\|r\|}, \hat{i}_t = \hat{i}_n \times \hat{i}_r, \hat{i}_n = \frac{r \times v}{\|r \times v\|}\right] \tag{6.24}$$

A similar approach is followed for the aerodynamic drag acceleration term Δ_D, which has been modeled as:

$$\Delta_D = Q^T a_d \tag{6.25}$$

where a_d is the acceleration due to drag in the ECI reference frame and is given by:

$$a_d = -\frac{1}{2m} \rho S C_D V^2 \tag{6.26}$$

in which m is the mass of the satellite, ρ is the atmospheric density, C_D is the drag coefficient and V is the spacecraft to atmosphere relative velocity, defined considering the atmosphere rigid and rotating with the Earth:

$$V = v - \omega_e \times r \tag{6.27}$$

where ω_e is the angular velocity of the Earth. In the optimal control problem formulation, the control variable is the exposed surface, S, which can be modulated to minimize the cost function. The atmospheric density has been modeled as exponential, considering variations due to the altitude, to reduce the computational cost of simulations. However, the algorithm has also the possibility to be applied with the more precise NRLMSISE-00 model with a greater computational cost.

6.1.2 Optimal control problem

The initial conditions of the problem are defined in terms of the classical orbital elements $(a, e, i, \Omega, \omega, \theta)$, which are more intuitive, and then transformed into the equinoctial ones with the equations previously described. The final values of the state variables are left free, except for the true longitude for which a specific value is imposed, resulting from the algorithm explained in the following subsections. In the optimal control problem, the final time is defined as the terminal cost function to be minimized. This:

$$J = t_f \tag{6.28}$$

To ensure the satellite reaches a desired de-orbiting point, different conditions are imposed in terms of altitude, latitude, and longitude. The definition of an event constraint on the altitude guarantees its fial value is within an acceptable range. It is defined as:

$$H = r - R_e \tag{6.29}$$

The application of the proposed algorithm guarantees the desired final values of latitude and longitude. It attempts to define the optimal control problem parameters, in terms of the final true longitude and the number of its complete cycles, to obtain the desired latitude and longitude values. The optimal control problem is based on an intelligent initial guess of the solution, relying on the analytical solution of the problem with an intermediate value of the control variable.

After the assessment of the general set-up of the optimal control problem, an algorithm was defined to determine the final true longitude and the corresponding number of complete cycles, ensuring the target point at the re-entry interface is reached. The steps leading to the definition of the final algorithm follows.

Class of optimal control solutions

The oscillatory and discontinuous behavior of latitude and longitude during de-orbiting has made their direct inclusion in the cost function of the optimal control problem unfeasible. As a consequence, an alternative approach was developed to ensure these variables remain within the desired range. To this end, a parametric analysis was conducted to solve the optimal control problem, using the initial conditions listed in Table 6.1, across different values of the final true longitude and its full cycles. This analysis yielded the class of solutions illustrated in Figure 6.1.

Initial orbital parameter	Value
a_0	6680 km
e_0	0.0007
i_0	51.64°
ω_0	130°
θ_0	80.8°
Ω_0	300°

Table 6.1: Initial conditions used to generate the class of optimal solutions.

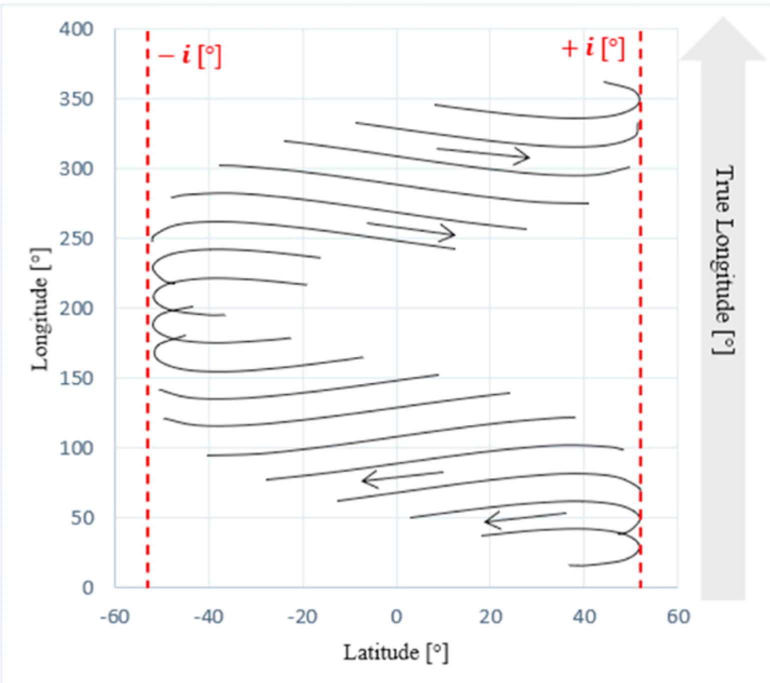

Figure 6.1: Example of class of optimal solutions, for different values of final true longitude and its complete cycles.

The complete cycles of the true longitude represent the number of times its value repeats, starting from the first solution, where the control variable is nearly at its maximum, up to the final one. The total range of these cycles can be estimated by performing simulations using the extreme values of the control variable, which in this case corresponds to the exposed surface S. The evolution of the latitude-longitude pairs is evaluated by varying both the final true longitude and the number of complete cycles. Each curve in the graph corresponds to the solution of the optimal control problem for a fixed final true longitude and a varying number of cycles, which increase in the direction indicated by the black arrows. The solutions are characterized by latitude values between negative inclination and positive inclination accordingly. The longitude can achieve values between 0° and 360° and exhibits an increasing trend with true longitude, as identified by the vertical gray arrow to the right of the graph. In fact, each curve refers to a specific final value of true longitude, increasing with the direction of the gray thick arrow in Figure 6.1. Once a desired de-orbit latitude-longitude pair is identified, only a finite number of curves can give a solution. Consequently, the search area for the final true longitude of the solution is obtained. In the following subsection, the influence of the main orbital parameters on the solution trends is analyzed.

Influence of the Right Ascension of the Ascending Node

This subsection discusses the effect of different initial values of the Right Ascension of Ascending Node, Ω, on the optimal solution. For this purpose, optimal control simulations are computed considering the initial conditions in Table 6.1, with the exception of Ω, which is varied in the range [50°, 350°]. The final fixed value of true longitude has been randomly chosen to be 121°. Figure 6.2 represents the evolution of latitude-longitude optimal pairs for the different initial values of Ω. A combination of all curves in the same graph is also represented in Figure 6.2h.

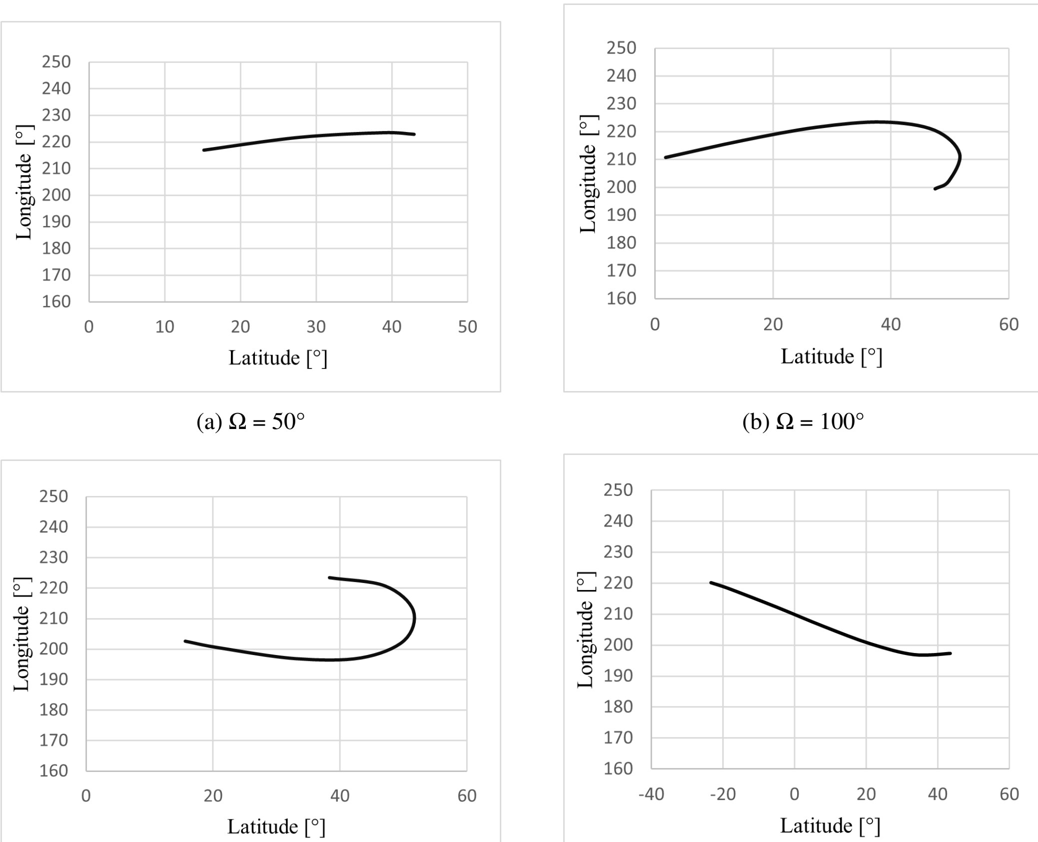

(a) Ω = 50°

(b) Ω = 100°

(c) Ω = 150°

(d) Ω = 200°

Figure 6.2: Evolution of the optimal control problem solution as function of Ω (part 1).

The combination of all the solutions (Figure 6.2h) results in an infinite-like shape, from now

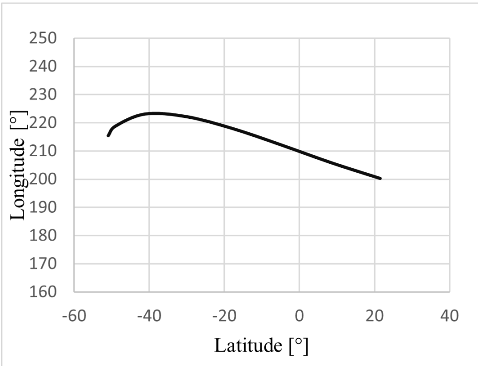

(e) Ω = 250°

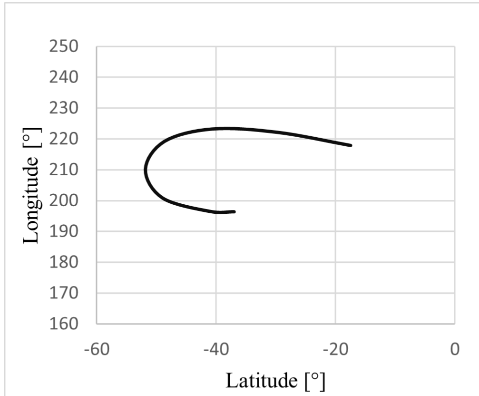

(f) Ω = 300°

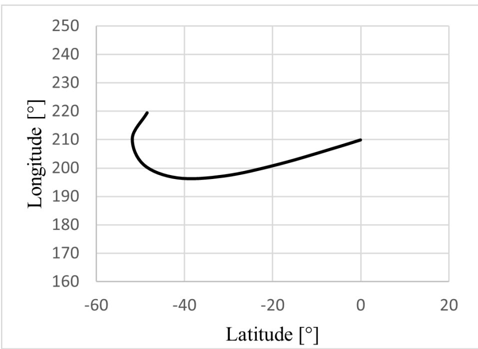

(g) Ω = 350°

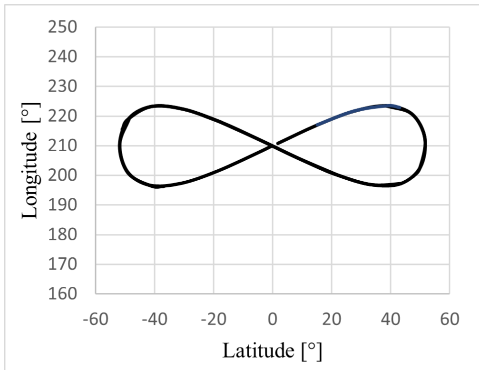

(h) Combination of all curves.

Figure 6.2: Evolution of the optimal control problem solution as function of Ω (cont.).

on defined as ∞_s, centered at a 0° of latitude and a longitude dependent on the final value of true longitude. The same analysis has been repeated for different final values of true longitude to investigate its influence on the the optimal latitude-longitude pairs. Figure 6.3 reports the ∞_s corresponding to the solutions for the following final values of true longitude: 64°, 121°, 288° and 351°.

These specific values have been chosen to clearly represent the different ∞_s in the plane without overlapping. Figure 6.3 shows that different final values of true longitude result in a rigid translation of ∞_s in the longitude-latitude plane without affecting its shape. The only differences between each case are the longitude value corresponding to the ∞_s center and the starting point, identified by the red point, which represents the first solution for the lowest value of Ω.

In conclusion, a different initial Ω will result in a motion of the solution along an ∞_s with latitude values between negative inclination and positive inclination. Different final values of true longitude correspond to a rigid vertical translation of ∞_s in the longitude-latitude plane without changing its shape.

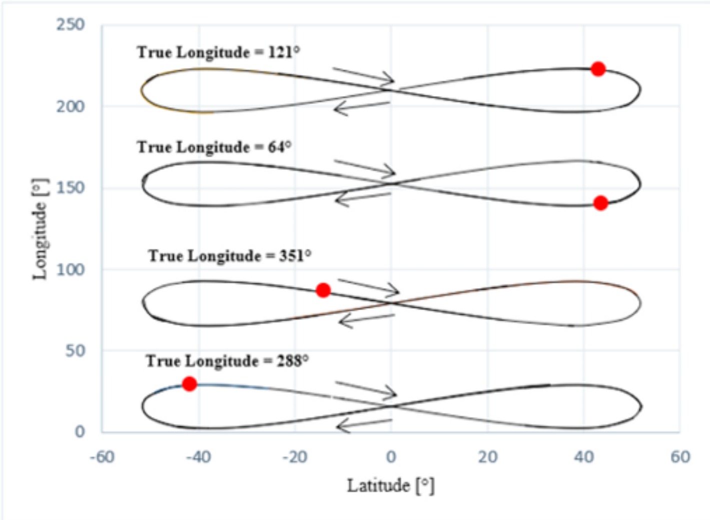

Figure 6.3: Evolution of the optimal control problem solution as function of Ω, for variable values of final true longitude.

Influence of semi-major axis

This subsection focuses on the influence of the semi-major axis, a, on the solution. In line with the previous approach, the optimal control solutions are evaluated considering the initial conditions in Table 6.1 for a fixed final true longitude, which has been randomly chosen as 60°, and a variable semi-major axis. Figure 6.4 compares the different solutions.

The graphs in Figure 6.4 exhibit a trend similar to that observed for variations in Ω. Specifically, changes in the semi-major axis cause the solution to move along an ∞_S curve centered at a latitude of 0°, with latitude values spanning from negative to positive inclination. Furthermore, as the semi-major axis a increases, the number of feasible longitude-latitude pairs grows, as illustrated in Figures 6.4a, 6.4b, and 6.4c. Since the upper and lower bounds on latitude and longitude remain unchanged, the shape and size of the ∞_S curve are not affected by variations in the semi-major axis.

Influence of orbital inclination

This paragraph investigates the effect of orbital inclination, i, on the optimal control solution. To this aim, they are computed considering the initial conditions in Table 6.1, fixing a final value of true longitude of 60°, and varying both Ω and i to investigate the influence of i on the ∞_S. Figure 6.5 represents the corresponding evolution of the solutions.

The ∞_S result is uniformly scaled along the latitude axis, ranging from negative to positive inclination, while its center position remains unchanged. The parameter Δ represents the interval of longitude values corresponding to a specific orbital inclination. It follows a parabolic trend with respect to the inclination, starting from 0° for an equatorial orbit with zero inclination, as illustrated in Figure 6.6. Consequently, Δ can be estimated solely based on the orbital inclination, without the need for additional simulations.

As a result, a change in orbital inclination affects only the dimensions of the ∞_S, while its center

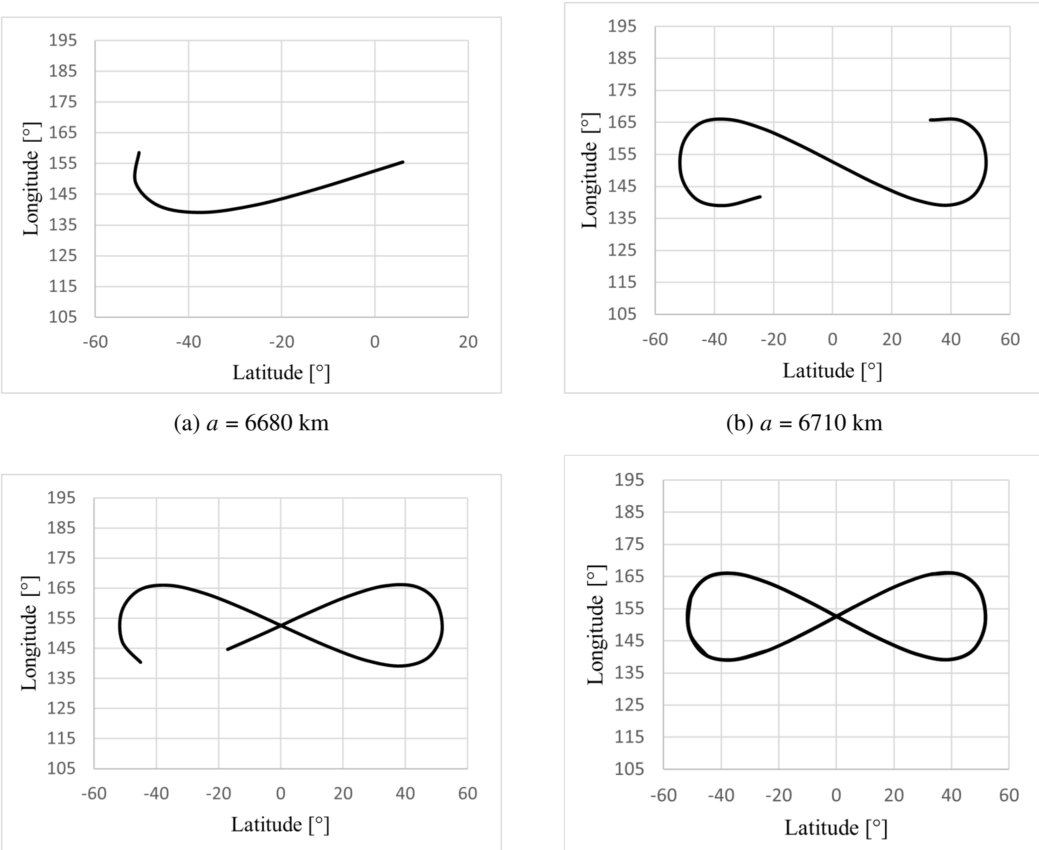

(a) a = 6680 km

(b) a = 6710 km

(c) a = 6730 km

(d) Combination of all curves.

Figure 6.4: Evolution of the optimal control problem solution as function of a.

position remains unchanged. The center position can be determined by performing an optimal control simulation for an equatorial orbit, varying the final true longitude between 0° and 360°. Figure 6.7 illustrates the trend of the centers in the true longitude-longitude plane, where the jump at x_0 corresponds to the condition in which the ∞_S longitude transitions from 360° back to 0°.

The graph shows a linear trend, with a unitary angular coefficient and a known term q equal to the longitude at the de-orbit point, evaluated for an equatorial orbit at a 0° value of true longitude. The second part of the curve is also linear with a unitary angular coefficient and starting from x_0. In this graph, the inclination effect will result in two parallel lines shifted by a quantity equal to $\Delta/2$ referring to the main line, corresponding to the center position. Therefore, once the desired longitude value at the re-entry interface is chosen, it is possible to get an estimation of the true longitude of the solution in interval range. The bounds of the interval can be evaluated by looking at the intersection of the two dashed lines with the desired longitude value.

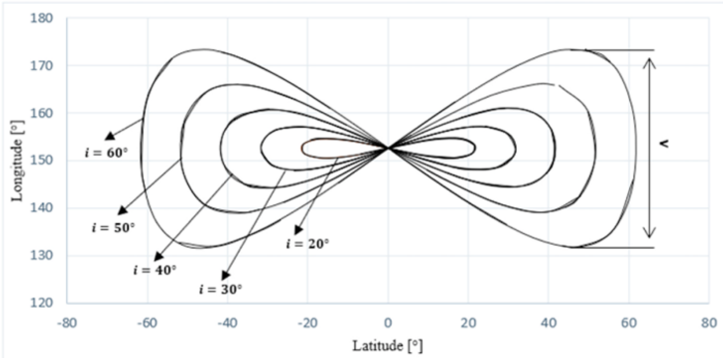

Figure 6.5: Evolution of optimal control problem solution as function of the orbital inclination i.

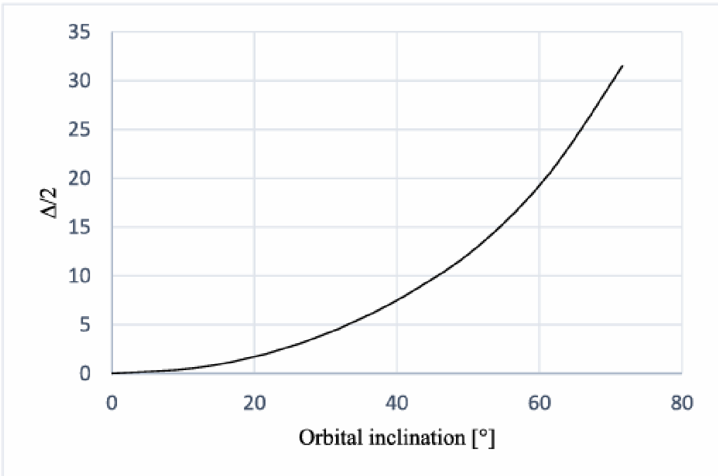

Figure 6.6: Parabolic trend of $\Delta/2$ as a function of the orbital inclination i.

Influence of the final date

This section describes the effect of the final date on the results. To this aim, the graph in Figure 6.7 is recreated, varying each term of the final date in Coordinated Universal Time (UTC), as year, month, day, hour, minute, and second, to investigate both their individual and combined effect on the solution. As shown in Figure 6.8, a variation of each parameter results in a horizontal rigid translation of the graph.

The final year (Figure 6.8a) and second (Figure 6.8f) have a negligible effect on the curve, a moderate effect is given by final minute (Figure 6.8e) and day (Figure 6.8c), while the greatest contribution results from a different final month (Figure 6.8b) and hour (Figure 6.8d). Table 6.2 summarizes the horizontal translation amount in each case.

Their combination results in a rigid horizontal translation of the curve in the true longitude–longitude plane. Consequently, the considerations made at the end of the previous subsection are generalizable, and the graph in Figure 6.7 can be applied to any final date by performing a single

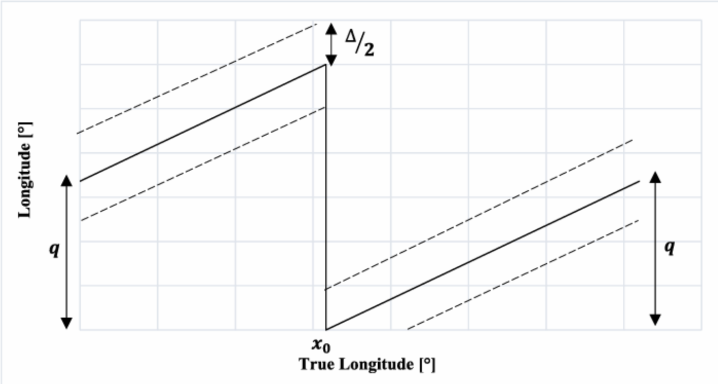

Figure 6.7: Schematization of centers trend in longitude-true longitude plane, considering the effect of inclination.

Date	Rigid translation amount
One year	0.25°
One month	30°
One day	5°
One hour	15°
One minute	0.25°
One second	0.0040°

Table 6.2: Horizontal rigid translation entities varying year, month, day, hour, minute and second of final date.

simulation for an equatorial orbit at a true longitude of 0° to determine the line intercept.

6.1.3 Algorithm implementation

The previous analysis enabled a comprehensive evaluation of the influence of various initial conditions and the final date on the solution of the optimal control problem. As a result, a general algorithm has been defined to compute an optimal control solution for any given set of initial conditions and a specific final date. The procedure can be summarized in the following steps:

1. Determination of true longitude cycles interval by evaluating optimal control solutions with the lowest and highest value of the control variable. They will correspond to the minimum and maximum time cases, respectively.

2. With reference to Figure 6.9, determination of the true longitude interval where to search for the solution with the following procedure:

    - Run an optimal control simulation for an equatorial orbit with a final true longitude of 0° to determine the intercept q of the line.
    - Define the first part of the line with a slope equal to 1 and intercept q, using the equation: $y = x + q$.

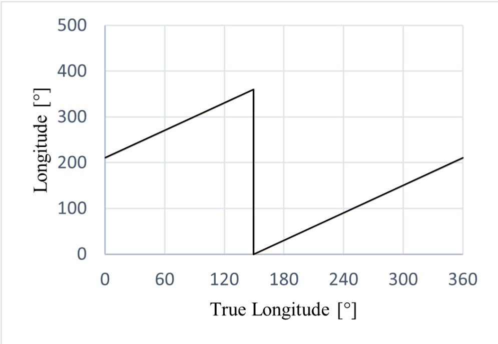

(a) Years

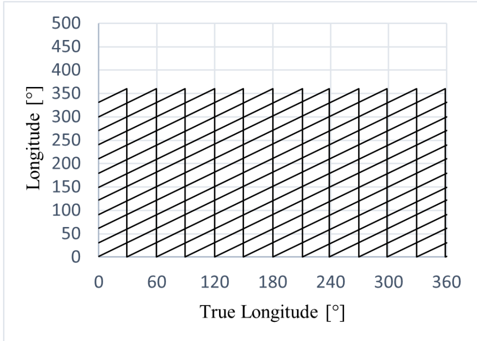

(b) Months

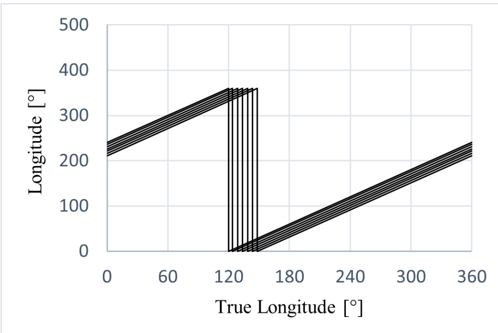

(c) Days

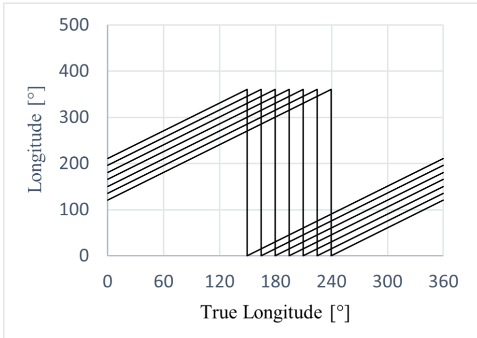

(d) Hours

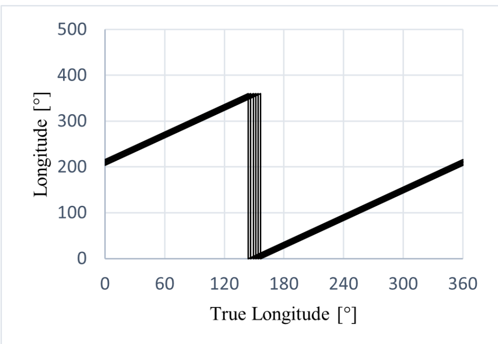

(e) Minutes

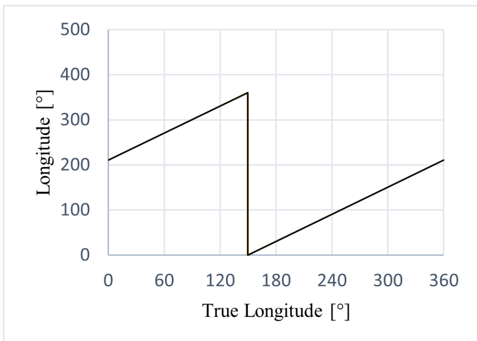

(f) Seconds

Figure 6.8: Evolution of the optimal control problem solution as function of the date.

- Identify the abscissa x_0 corresponding to $y = 360°$, which marks the discontinuity due to the wrap-around from 360° back to 0°.
- Define the second segment of the line after the discontinuity, maintaining the same slope: $y = x - x_0$.
- Determine the lower and upper bounds, $\Delta/2$, based on the orbital inclination. The

intersection of these bounds with the line y = desired longitude defines the interval of true longitude where the optimal solution must be searched. This interval is indicated by the two yellow stars in Figure 6.9.

3. Using the range estimated in the previous point, start an optimization cycle with a lower accuracy of 10^{-4}, varying the number of complete revolutions. Start from the highest value of the interval and compare the estimated longitude and latitude with the desired ones. Search for a possible couple of latitude and longitude respecting the threshold imposed by the user. At this point two different scenarios can occur:

   - If the condition at point 3 is satisfied, repeat the simulation with a higher accuracy, 10^{-6}. The optimal solution has been found.
   - If the condition at point 3 is not satisfied, repeat simulations for decreasing values of true longitude until condition 3.a is satisfied.

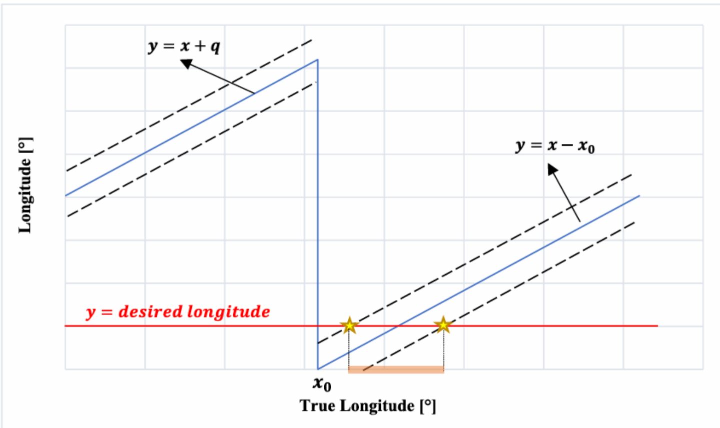

Figure 6.9: Schematization of the procedure to evaluate the true longitude search interval.

This algorithm is valid even in cases of different masses and drag coefficients of the satellites, showing its generalization and robustness.

6.1.4 Results

This subsection presents the results of the time-optimal targeted de-orbiting algorithm, previously discussed. First, it is applied to a case study, and its performance is compared with that of a non-optimized targeted algorithm found in the literature. Subsequently, the robustness of the algorithm is assessed through a Monte Carlo analysis.

Application to a case study

This case study represents a mission in which a satellite de-orbits from a LEO with the simulation conditions summarized in Table 6.3. The desired de-orbit point occurs at an altitude value of 102 km, a latitude of 30.4°, and a longitude of 29.84°. The final epoch has been fixed on 30/06/2022 at 08:15:00 UTC.

a_0	6680 km
e_0	0.0007
i_0	51.84°
ω_0	20°
θ_0	40°
Ω_0	150°
m	40 kg
C_D	2
$[S_{min}; S_{max}]$	$[0.2\ m^2; 1.9\ m^2]$

Table 6.3: Initial conditions and satellite parameters for the first case study on time-optimal targeted de-orbiting.

The estimated intercept q is 30.39°, resulting from the solution for an equatorial orbit at a zero final value of true longitude. The Δ value, and the correspondent dashed lined, are evaluated using the graph in Figure 6.9 for an orbital inclination of 51.84°. The intersection between the narrow lines and the desired longitude value of 29.84° in Figure 6.10 produced the true longitude solution interval: [58.0°; 85.0°].

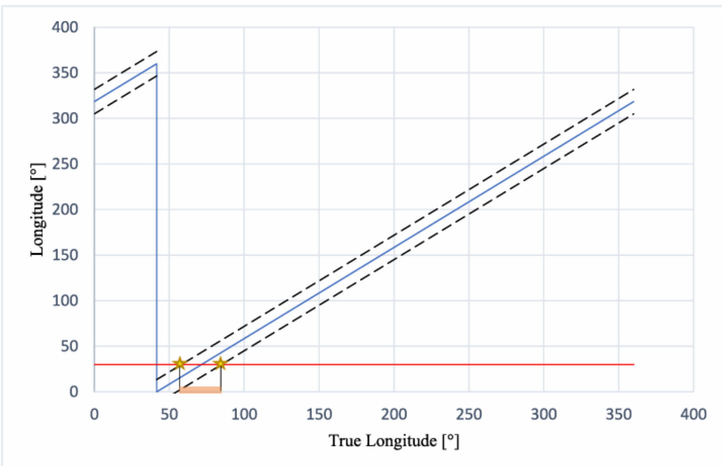

Figure 6.10: Schematization of the procedure to find the true longitude search interval, applied to the sample case study.

In particular, the desired value of longitude is represented by the horizontal red line, the dashed lines refer to the Δ corresponding to the orbital inclination, and the yellow stars identify the bounds of true longitude interval, in which to search for the solution. The application of the iterative procedure of point 3 from the algorithm previously described determined a final value of true longitude equal to 84.0°, which lies in the range estimated previously. Figures 6.11, 6.12, 6.13 provide the results of the optimal control problem, displaying the trends of the variables of interest as function of time, including a zoom to better appreciate oscillating regions.

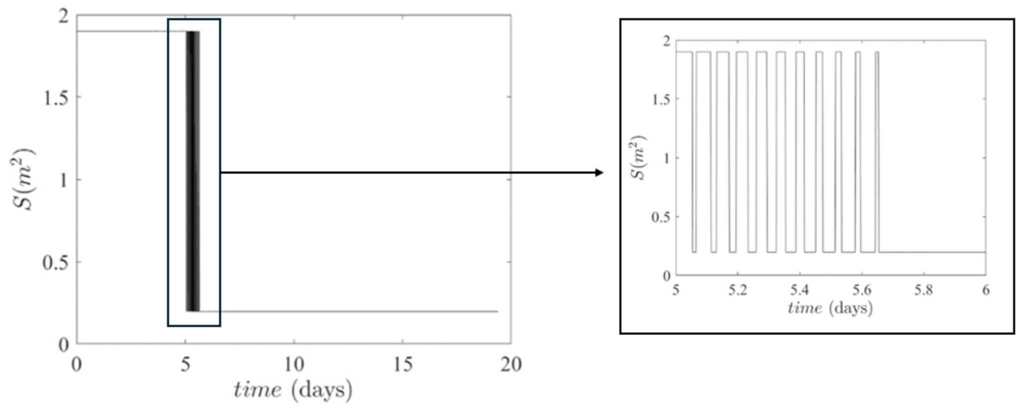

Figure 6.11: Time-optimal de-orbiting: control variable profile as a function of the time with a zoom to appreciate the oscillations.

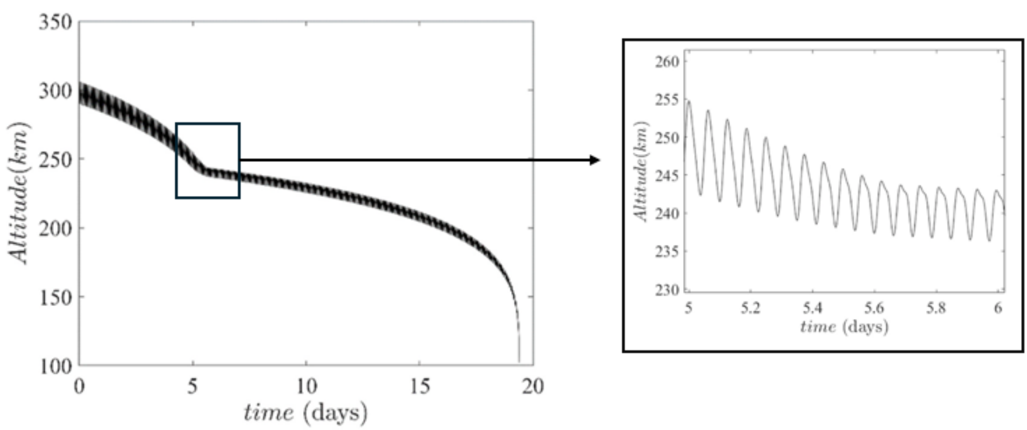

Figure 6.12: Time-optimal de-orbiting: profile of the altitude as a function of the time, with a zoom to appreciate the oscillations

The control variable exhibits a bang-bang optimal profile, seen in Figure 6.11, with values varying between the upper and lower bounds of the surface. Between the fifth and the sixth day, some oscillation occurs before the surface stabilizes to its lowest value. The altitude exhibits a decreasing trend Figure 6.12 characterized by the typical de-orbiting oscillations with a change in behavior corresponding to surface variation. Something similar is observed for the velocity (Figure 6.13), exhibiting an increasing trend. The de-orbiting time duration is 19 days, 9 h, 25 min, and 45

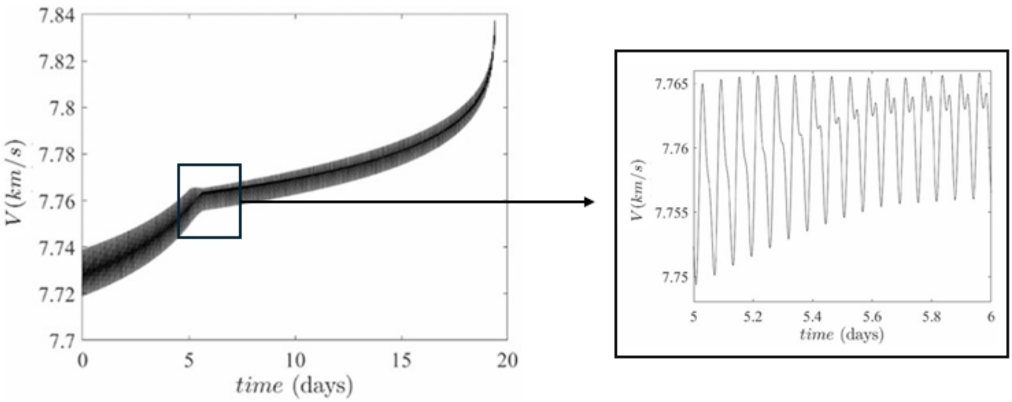

Figure 6.13: Time-optimal de-orbiting: profile of the velocity as a function of the time, with a zoom to appreciate the oscillations

s, with a corresponding initial date of 10/06/2022 at 22:49:15 UTC.

Comparison with another de-orbiting algorithm

The optimality of the algorithm is further demonstrated by solving another case study and comparing the de-orbiting time with the one resulting from the application of the non-optimal algorithm described in [15, 16].

For consistency between the two, the density model NRLMSISE-00 is also considered in the current algorithm.Table 6.4 summarizes the initial conditions of the case study in question.

a_0	6680 km
e_0	0.0007
i_0	51.84°
ω_0	10°
θ_0	20°
Ω_0	190°
m	40 kg
C_D	2
$[S_{\min}; S_{\max}]$	$[0.2\ m^2; 1.9\ m^2]$

Table 6.4: Simulation initial conditions and satellite characteristics for the comparison between the two de-orbiting algorithms.

Regarding the simulation epoch, after defining the final date as 30/01/2015 at 08:15:00 UTC, the corresponding initial date is computed by subtracting the de-orbiting time obtained through the algorithm proposed in this paper. For comparison, the algorithm presented in [15, 16], which instead requires a predefined initial date, has also been applied to the same case study. The application of the current algorithm results in a de-orbiting time of 10 days, 23 hours, 49 minutes, and 7 seconds, leading to an initial date of 19/01/2015 at 08:25:53 UTC. On the other hand, applying the algorithm from [15, 16] yields a de-orbiting time of 17 days, 23 hours, 2 minutes, and 47 seconds.

In conclusion, a significant reduction in de-orbiting time is achieved, further demonstrating the capability of the proposed method to generate minimum-time optimal trajectories.

Monte Carlo analysis

The robustness and generalization of the time-optimal de-orbiting algorithm are proven by its successful outcome in a wide range of scenarios, produced by a Monte Carlo analysis carried out over 500 cases. A uniform distribution of the initial mean orbital elements corresponding to a LEO is considered, with an epoch range of five years. Table 6.5 specifies the initial conditions and parameters range, as well as their probability distributions.

Parameter	Range	Probability distribution
a	[6670 km; 6720 km]	Uniform
Ω	[0°; 360°]	Uniform
i	[30°; 70°]	Uniform
ω	[0°; 360°]	Uniform
e	[0; 0.001]	Uniform
θ	[0°; 360°]	Uniform
Epoch	[31^{st} December 2017; 31^{st} December 2022]	Uniform

Table 6.5: Parameters employed in Monte Carlo analysis for the time-optimal de-orbiting algorithm.

The maximum acceptable error has been set at 1.5 %. Figure 6.14 shows the longitude-latitude pairs resulting from the Monte Carlo analysis. The light red box represents the zone where the maximum error on latitude and longitude is lower than 1.5 %, the threshold imposed by the user. The successful outcome of the algorithm is testified by all resulting pairs included in this region.

The analysis showed the validity and robustness of the algorithm, further demonstrating its ability to successfully model a wide range of conditions. In addition, even if the maximum threshold imposed by the user is 1.5 %, most of the longitude-latitude resulting pairs are characterized by an error of less than 0.5 %, proving the high precision of the results.

6.2 Approach based on Deep Neural Networks

Although the time-optimal targeted de-orbiting algorithm demonstrated robust performance and strong generalization across different conditions and scenarios, its computational cost remains a significant limitation. This restricts its practical application for real-time trajectory generation onboard the satellite. To overcome this, an optimal guidance algorithm based on DNNs is proposed, predicting the optimal control profile as a function of time. By leveraging the known general structure of the control profile, only a small set of parameters needs to be computed instantaneously to generate the reference trajectory. As illustrated in Figure 6.15, which represents the general structure of the optimal control law, the DNNs are employed to predict these key parameters.

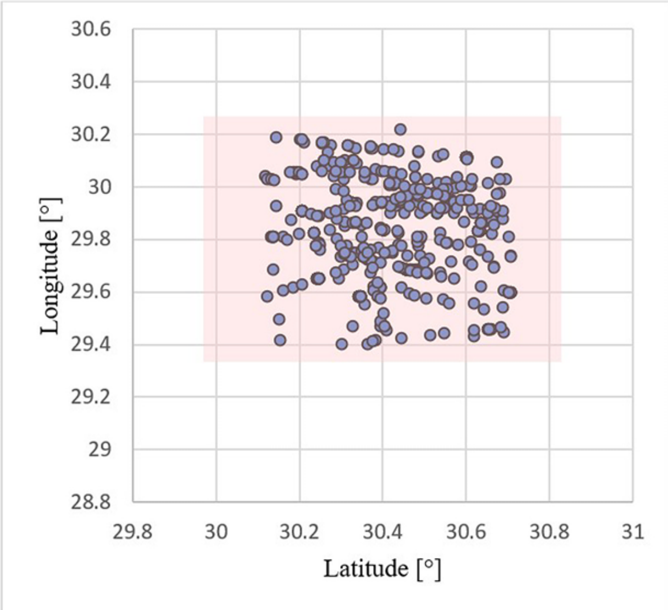

Figure 6.14: Longitude-Latitude pairs for the time-optimal de-orbiting algorithm resulting from the Monte Carlo analysis.

6.2.1 Parametric analysis

Following the same approach employed for the optimal control algorithm implementation, several parametric analyses were performed to define the key steps of the algorithm.

Prediction of the final true longitude and the number of its complete cycles

The parameters influencing the optimal control law, namely t_1, t_2, and the oscillations, depend on the initial conditions, the final true longitude, and the number of complete cycles. While the initial conditions are given by the specific mission scenario, the final true longitude and the number of cycles must be estimated using the optimization algorithm presented in the previous section [67].

This subsection proposes a faster method to predict these quantities through the resolution of a single optimal control problem. In particular, the application of the algorithm from [67] to a randomly generated test case (Table 6.6) is used as a reference to extend the results over a wide range of initial conditions, avoiding the need to solve additional optimal control problems.

The optimal control problem solution is characterized by a target true longitude of 179.8° and 179 complete cycles, ensuring the desired de-orbiting point. Based on this reference solution, it is possible to predict the corresponding values for a wide range of initial conditions. In particular, the final true longitude depends solely on the final date, whereas the number of complete cycles is influenced only by the initial right ascension of the ascending node, Ω_0. An analysis is therefore conducted by fixing the final date and varying Ω_0. Under these assumptions, the optimal control solutions share the same final true longitude, while the number of complete cycles increases linearly with Ω_0, as illustrated in Figure 6.16a.

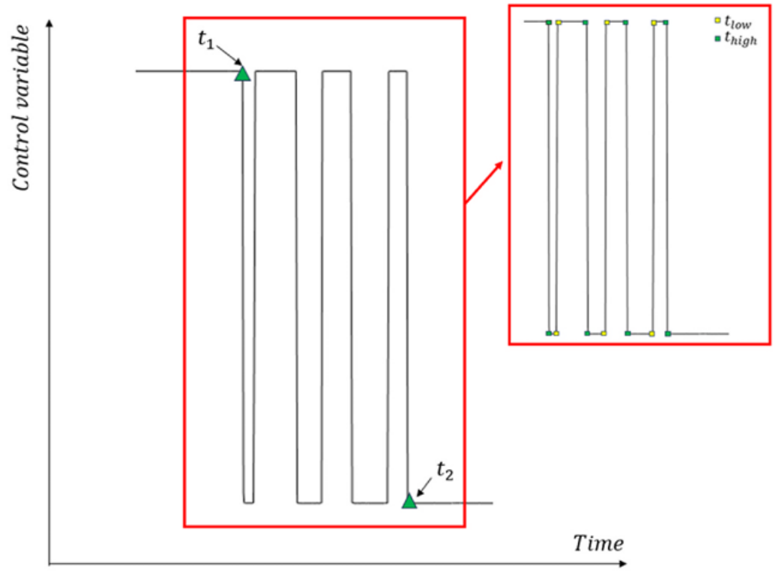

Figure 6.15: General structure of the optimal control law.

$$TL_{cycles} = k_c \bullet (\Omega_0 - \Omega_0^*) + TL^*_{cycles_0} \tag{6.30}$$

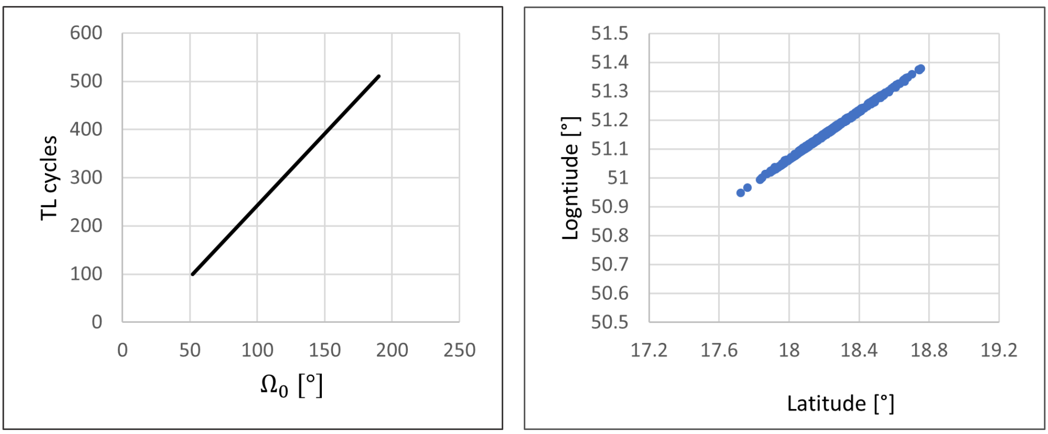

(a) (b)

Figure 6.16: True Longitude cycles (TL cycles) as a function of Ω_0 (a) and latitude and longitude values at the de-orbiting point (b).

Where $k_c = 3\ deg^{-1}$, Ω_0^* and $TL^*_{cycles_0}$ are the parameters resulting by the resolution of the optimal control problem in Table 6.6.

Initial orbital parameter	Value
a_0	6680 km
e_0	0.0007
i_0	51.84°
ω_0	95.12°
θ_0	50.48°
Ω_0	83.57°
Final date (UTC)	12/01/2022–01:44:00
Desired de-orbiting point (Latitude, Longitude and Altitude)	(18.3°, 51.0°, 103 km)

Table 6.6: Initial data for the optimal control simulation.

In addition, each point on the curve represents all mission scenarios characterized by a specific value of Ω_0, regardless of the values of e_0, ω_0, and θ_0. To further validate this observation, a Monte Carlo analysis involving 500 random samples is performed, demonstrating that the target de-orbiting point remains nearly unchanged. Figure 6.16b shows the latitude and longitude at the de-orbiting point for each case. The results lie within a narrow interval around the reference value, confirming the robustness of the solution with respect to variations in the remaining orbital elements. Finally, the final true longitude and the number of complete cycles are both functions of the final date, increasing respectively at a rate of +15° and 45 cycles per hour, as in [67].

Prediction of t_1 and t_2 with the DNNs

Once the final true longitude and the number of its complete cycles are estimated, the optimal control law can be predicted. Here, the estimation of t_1 and t_2, based on DNNs, is presented. The necessity to estimate them with high precision and their dependence on several parameters by non-elementary laws led the authors to follow this approach. At the same time, the computational cost associated with the generation of many optimal control solutions requires the use of high-performance computers to get the training set in a reasonable time. In the scientific literature, authors in [122] proposed a solution to tackle this issue for low-thrust transfer problems. It relies on an alternative resolution of optimal control problems, called "backward generation of optimal examples", to ensure the training set generation in a lower time and be able to obtain 4 million optimal trajectories. In the current work, the authors pursued a different path to face the problem, relying on the general training-set split into several smaller ones, drastically reducing the number of samples to get satisfactory results. A comprehensive parametric analysis has been carried on evaluating t_1 and t_2 for different combinations of different initial conditions and optimal control problem parameters to assess the most suitable combination for the training set generation. The first analysis investigates the effect of initial semi-major axis on t_1 and t_2. Simulations are carried out considering the parameters summarized in the second column of Table 6.7.

In Figures 6.17a - 6.17b, t_1 and t_2 are reported respectively, along with their trends as functions of semi-major axis, considering three different values of true longitude complete cycles.

The results of the analysis shown in Figures 6.17a - 6.17b highlight a parabolic trend for both t_1 and t_2 as functions of the semi-major axis. A variation in the number of complete true longitude cycles results in a rigid shift of the curves: as the number of cycles increases, the curves translate toward lower values of t_1 and t_2, and vice versa. This behavior is highlighted by the black arrows

Parameter	Range or value: semi-major axis	Range or value: true anomaly and argument of perigee
a_0	[6640 km; 6690 km]	6680 km
Ω_0	83.57°	0°
i_0	51.84°	51.84°
ω_0	95.12°	[0°; 360°]
e_0	0.0007	0.0007
θ_0	50.48°	[0°; 90°]
Final True Longitude	179.8°	179.8°
True Longitude complete cycles	[159; 179]	143 and 260

Table 6.7: Parameters employed for the parametric analysis on t_1 and t_2.

in the figures. The observed parabolic dependence of t_1 and t_2 on the semi-major axis can be exploited to predict their values for intermediate cases without performing additional simulations. Specifically, knowing the optimal solutions corresponding to three increasing values of the semi-major axis, a_1, a_2, and a_3, allows for interpolation within the range $[a_1, a_3]$. This capability implies that the semi-major axis does not need to be included as an input parameter in the training set, thereby simplifying the learning process. Instead, different training sets are constructed for fixed values of the semi-major axis, and the parabolic trend is used to generalize the predictions of t_1 and t_2 across a wider range of conditions. A further parametric analysis is carried out to evaluate the influence of the true anomaly and the argument of perigee on t_1 and t_2. The simulations are based on the configuration detailed in the third column of Table 6.7. As in the previous case, the final true longitude is fixed at 179.8°, while two different values of the number of complete true longitude cycles are considered to assess their impact. Figures 6.18a-6.18b show the trends of t_1 and t_2 as functions of the argument of perigee, considering 260 complete cycles and several fixed values of true anomaly in the range $[0°, 90°]$. Figures 6.18c -6.18d present the trends obtained for a fixed true anomaly of 60° and two different values of complete true longitude cycles, 143 and 260.

The results highlighted an oscillatory trend of t_1 and t_2 as functions of the argument of perigee, which is subjected to a rigid horizontal translation for different values of the true anomaly. Regarding the number of complete cycles, a variation will provide a rigid vertical translation of the curve without affecting its shape, as in the previous case. Further analyses on the right ascension of the ascending node, the final value of true longitude and the eccentricity showed a negligible influence on t_1 and t_2. In conclusion, the most influencing parameters on t_1 and t_2 are a_0, ω_0, θ_0, and the complete cycles of the true longitude. Consequently, the training set relies on a table of combination of Ω_0, ω_0, θ_0 and the number of complete cycles with the correspondent values of t_1 and t_2, fixing different values of semi-major axis. In addition, for each case, the general training set has been divided in nine sub-training sets considering Ω_0 variable between 0° and 360° due to its negligible influence on t_1 and t_2, the number of complete revolutions between the minimum and the maximum (dependent on the specific initial value of semi-major axis) and different combinations of ω_0 and θ_0 globally covering the range between 0° and 360°. This expedient led to a reduction of almost one order of magnitude of the ω_0 and θ_0 possible combinations that the DNN is required to learn. Figure 6.19 provides a schematization of the training set, highlighting the input and the corresponding output variables.

The semi-major axis is not directly included in the training parameters, exploiting the parabolic

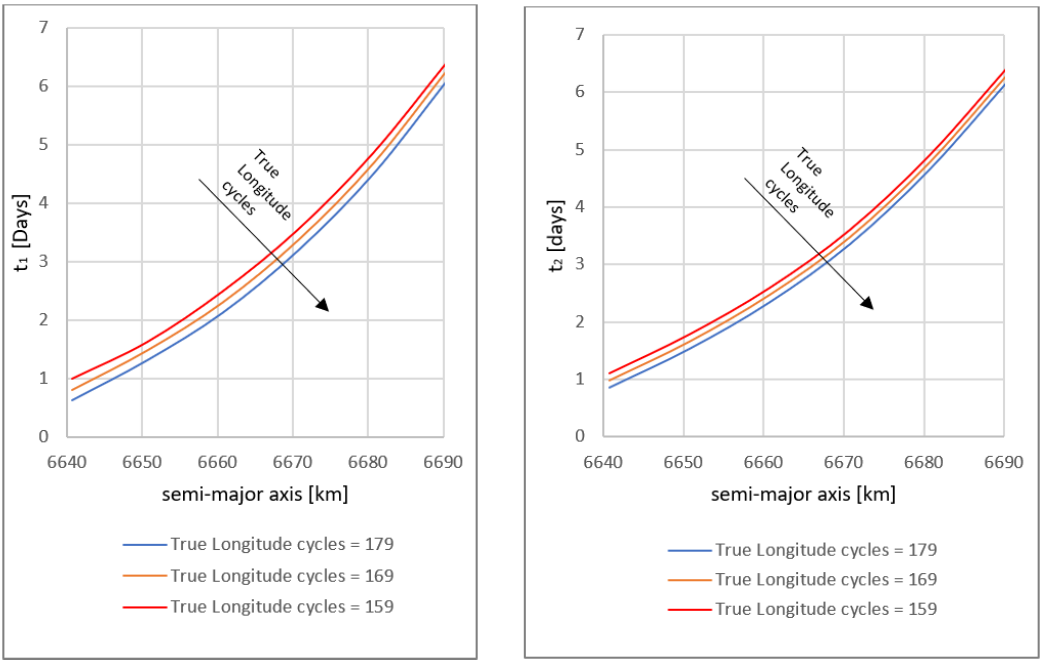

(a) (b)

Figure 6.17: t_1 and t_2 trend as function of semi-major axis, for different values of true longitude complete cycles.

trend of t_1 and t_2 for a further simplification of the training set. The nine sub-training sets in Figure 6.19 are generated for six fixed initial values of the semi-major axis between 6630 km and 6680 km with a step of 10 km, resulting in a total number of n = 9 n_{a_0}. If the initial value of the semi-major axis is included in the ones directly used to generate the sub-training sets, t_1 and t_2 will be directly predicted with the DNNs choosing the proper sub-training set associated with that specific value of a_0 and dependent on the combination of ω_0 and θ_0. If the initial value of the semi-major axis is not included in the ones used to generate the sub-training sets, t_1 and t_2 are predicted by exploiting the parabolic trends. Analogous to the previous case, the initial combination of the true anomaly and the argument of perigee leads to the choice of a proper sub-training set in Figure 6.19, for three values of a_0 including the value of interest. Thus, this case sees the use of three different sub-training sets, one for each value of a_0. The DNNs are then used to predict t_1 and t_2 in these three cases, and the correspondent results for the desired a_0 are achieved by exploiting the parabolic trend. The choice of not including the semi-major axis in the training parameters is due to two reasons:

- The initial value of the semi-major axis is one of the parameters most affecting the initial guess necessary to successfully get the optimal control solution. That would make the training set generation longer and difficult to automatize.
- In addition, the minimum and maximum values of the true longitude cycles are related to a_0, so a randomly generated combination of them could have led to infeasible problems.

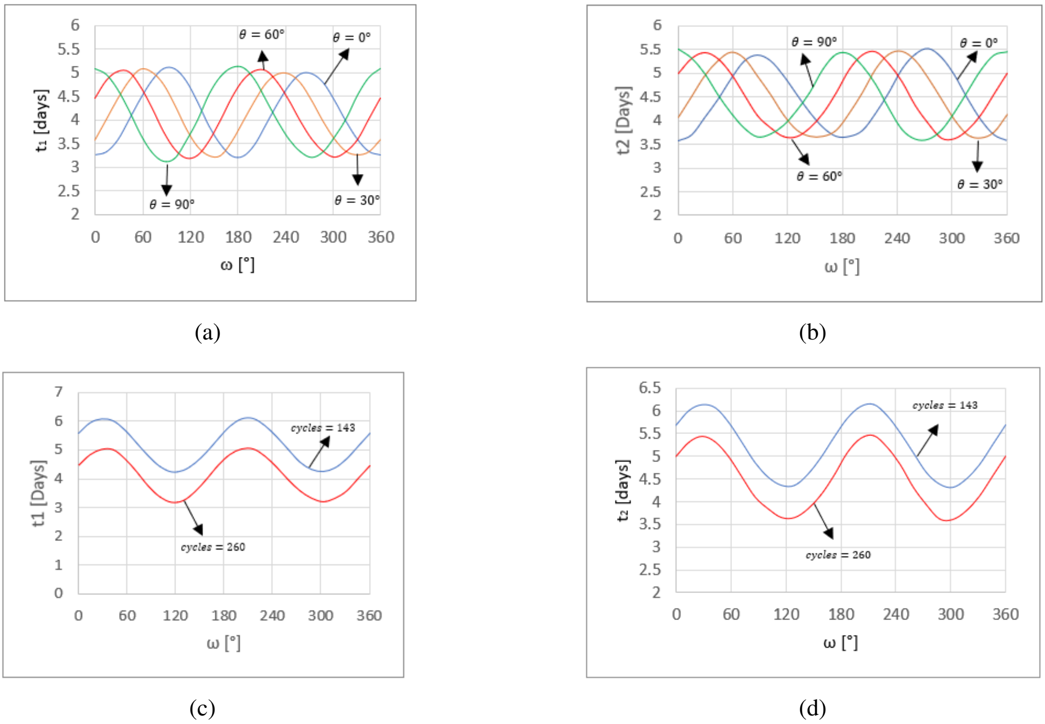

Figure 6.18: t_1 and t_2 trends as functions of the argument of perigee and true anomaly, considering two different values of true longitude complete cycles.

The generation of different "blocks" of training sets fixing different initial values of the semi-major axis resulted in the less computationally expensive option, guaranteeing at the same time a high precision of the results in all the conditions thanks to the parabolic trends.

The implementation of the Deep Learning model is carried out using the Python programming language within a Jupyter Notebook environment, integrated into the Anaconda Navigator platform. For the design of the DNN, an architecture with three layers is adopted, consisting of 15, 10, and 1 neuron(s), respectively. This configuration results in a total of 246 trainable parameters. The same DNN structure is used for the prediction of both t_1 and t_2. In each case, the network is trained separately: for t_1, the network is fed with data corresponding to the conditions shown in Figure 6.19, and analogously for t_2. The hidden layers take advantage of the Exponential Linear Unit (eLu) as the activation function, due to its favorable properties such as faster convergence and improved generalization. The output layer uses a linear activation function, appropriate for regression tasks. The training process is performed over 3500 epochs with a batch size of 4. A standard 80% - 20% split is used for training and testing, respectively. The loss function is the Mean Squared Error (MSE), and the optimization is handled by the Adam optimizer with a learning rate of 0.0001.

INPUT VARIABLES			
Ω_0	ω_0	θ_0	TL cycles
[0°; 360°]	[0°; 100°]	[0°; 100°]	Between minimum and maximum
[0°; 360°]	[0°; 100°]	[100°; 230°]	
[0°; 360°]	[0°; 100°]	[230°; 360°]	
[0°; 360°]	[100°; 230°]	[0°; 100°]	
[0°; 360°]	[100°; 230°]	[100°; 230°]	
[0°; 360°]	[100°; 230°]	[230°; 360°]	
[0°; 360°]	[230°; 360°]	[0°; 100°]	
[0°; 360°]	[230°; 360°]	[100°; 230°]	
[0°; 360°]	[230°; 360°]	[230°; 360°]	

OUTPUT VARIABLES	
t_1	t_2

Figure 6.19: Training set schematization, for a fixed value of semi-major axis.

Modeling of the number and time history of oscillations

This subsection focuses on modeling both the number and time distribution of the oscillations characterizing the optimal control profile. The estimation of the number of oscillations does not rely on DNNs, but instead is based on a semi-empirical relationship dependent on t_1 and t_2. During the generation of the training set, it was observed that the parameter

$$c = \frac{t_2 - t_1}{number\ of\ oscillations} \tag{6.31}$$

exhibited a distribution ranging around an almost constant value, as shown in Figure 6.20. The figure presents the distribution of c over 5000 randomly selected samples from the training set.

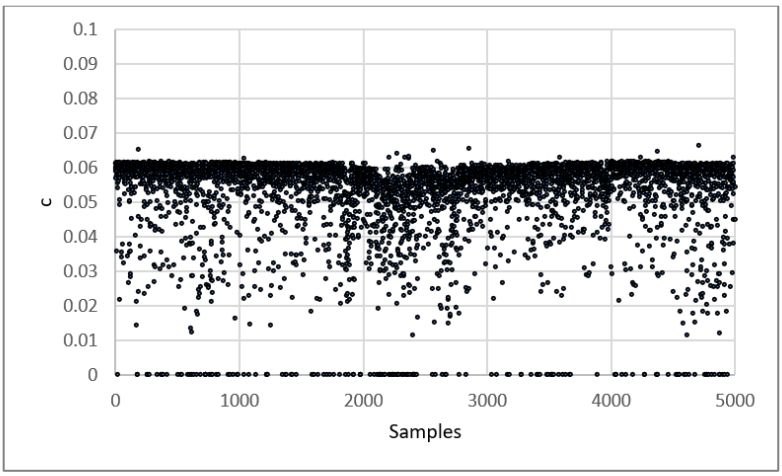

Figure 6.20: Distribution of the parameter c over 5000 randomly generated cases.

Samples with no oscillations are characterized by a null value of c. In cases with one oscillation, c falls within the interval $[0.01, 0.055]$, while for more than one oscillation, c lies in the more restricted interval $[0.055, 0.07]$. Based on this behavior, the number of oscillations can be estimated using the following piecewise definition:

$$\textit{number of oscillations} = \begin{cases} 0 & \text{if } t_2 - t_1 < 0.01 \\ 1 & \text{if } 0.01 \leq t_2 - t_1 < 0.055 \\ \dfrac{t_2 - t_1}{c} & \text{if } t_2 - t_1 \geq 0.055 \end{cases} \tag{6.32}$$

Several values of c were tested to identify the one that provides the most accurate estimation of the number of oscillations. Figure 6.21 summarizes the percentage of successful evaluations as a function of c. The value $c = 0.0607$, marked with a red triangle, ensures a success rate of 96.30%.

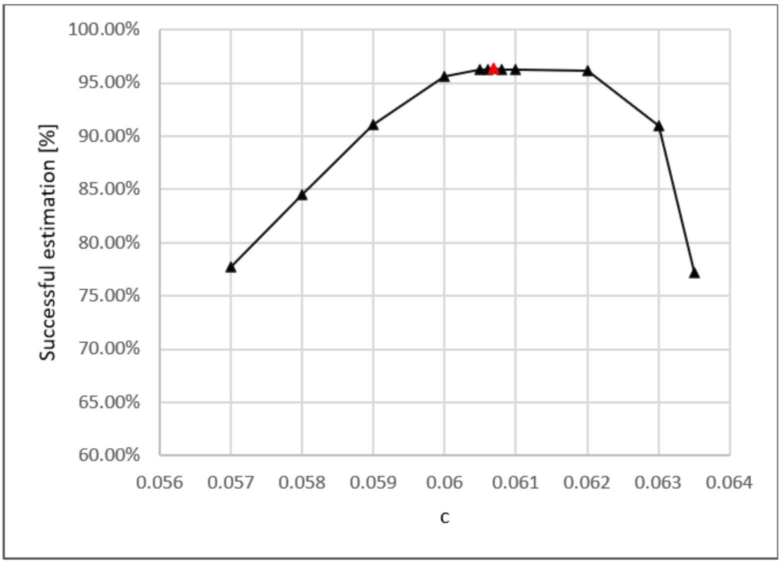

Figure 6.21: Success rate in estimating the number of oscillations as a function of c.

The final step involves determining the time distribution of the oscillations. Reference is made to the scheme shown in Figure 6.15, which illustrates an example of the optimal control profile and a zoomed view of the oscillatory region. Two vectors, t_{low} and t_{high}, are introduced to represent the time coordinates of the lower and upper switching points of the bang-bang control structure, respectively. These vectors have dimensions $n.o. + 1$ and $n.o.$, where $n.o.$ denotes the number of oscillations. Once t_1, t_2, and the number of oscillations are known, the control profile can be fully reconstructed by evaluating t_{low} and t_{high}. To this end, four representative cases are analyzed with fixed initial conditions: $a_0 = 6680$ km, $i_0 = 51.84°$, and $e_0 = 0.0007$, while varying Ω_0, ω_0, and θ_0. These cases exhibit different numbers of oscillations and serve as the basis to derive general trends. Table 6.8 summarizes the initial conditions along with the corresponding t_1, t_2, and number of oscillations obtained via GPOPS-II. The resulting values of t_{low} and t_{high} are plotted in Figure 6.22, showing that both can be accurately modeled using linear relations. This leads to the definition of a general formulation for predicting t_{low} and t_{high} under varying conditions.

For what concerns t_{high}:

Initial conditions	Case 1	Case 2	Case 3	Case 4
Ω_0 [°]	81.69	82.1	1.61	76.04
ω_0 [°]	37.96	71.81	9.86	98.16
θ_0 [°]	4.99	32.15	60.14	65.35
t_1 [days]	3.712	4.5193	3.7112	3.9303
t_2 [days]	4.3121	4.8788	4.6899	4.1622
Number of oscillations	10	6	16	4

Table 6.8: Initial conditions and corresponding data for the four GPOPS-II cases.

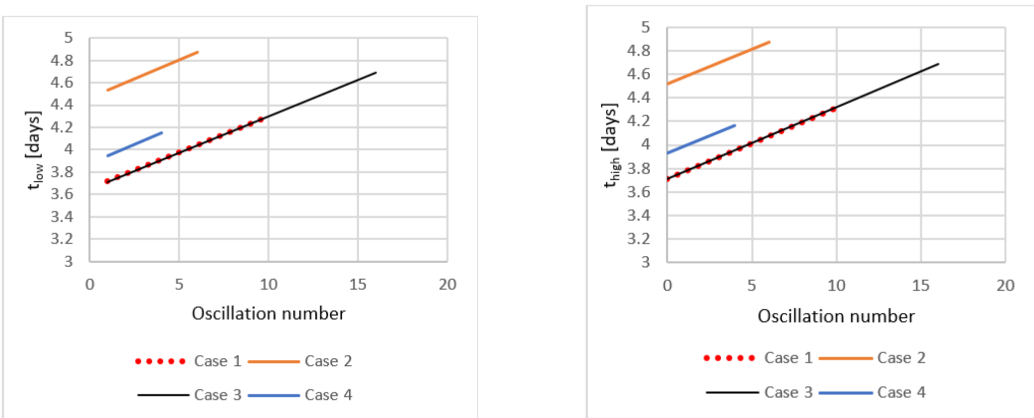

(a) (b)

Figure 6.22: t_{low} (a) and t_{high} (b) trend as function of the oscillation number for the four cases analyzed.

$$t_{\text{high}} = \frac{t_2 - t_1}{\text{number of oscillations}} \cdot x + t_1 \tag{6.33}$$

Where x represents the current oscillation number. A similar approach could be pursued to evaluate t_low with the difference that, in this case, two points belonging to the line are not known. To overcome the issue, t_1 and t_2 are slightly scaled in function of the number of oscillations following linear relations with angular coefficients 0.0006 and −0.001:

$$t_{\text{low}} = \frac{t_2^* - t_1^*}{(\text{number of oscillations} - 1)} \cdot x + t_1^* \tag{6.34}$$

6.2.2 Implementation of the guidance algorithm based on Deep Neural Networks

After the parametric analyses just discussed, the time-optimal de-orbiting guidance algorithm based on DNNs is summarized as in the following steps:

1. Definition of the problem scenario: initial and desired conditions in terms of latitude, longitude, altitude, and date.
2. Estimation of the final true longitude and the number of complete cycles with the procedure previously explained.
3. Evaluation of t_1 and t_2 for the desired initial semi-major axis with the following procedure:
    - With reference to Figure 6.19, choice of the specific training set depending on the initial values of θ_0 and ω_0.
    - Prediction of t_1 and t_2. Two different situations can occur:
        - If the initial semi-major axis value is included in the ones used to generate the different sub-training sets, t_1 and t_2 will be evaluated directly with the DNNs.
        - If the initial semi-major axis value is not included in the ones used to generate the sub-training sets, there is an additional step. Firstly, t_1 and t_2 are predicted considering the proper sub-training set depending on the combination of θ_0 and ω_0, for three different values of the semi-major axis including the one of interest (three sub-training sets in total). After that, t_1 and t_2 at the desired semi-major axis are evaluated exploiting their parabolic trend and the three values just predicted with the DNNs.
4. Evaluation of the number and time distribution of the oscillations, as previously discussed.

6.2.3 Results

This section presents the results of the time-optimal de-orbiting guidance algorithm based on DNNs. Three representative scenarios are analyzed, illustrating the steps leading to the final solution in each case. The first scenario involves an optimal control law characterized by a finite number of oscillations, with an initial value of the semi-major axis that belongs to the range used during training. In this case, the DNNs can be directly employed to predict t_1 and t_2. The second scenario corresponds to an optimal control law without oscillations and a value of the semi-major axis that falls outside the training set range. This requires an additional step to estimate t_1 and t_2, since the DNN cannot predict directly in this case. The third scenario is characterized by both a semi-major axis not included in the training set and the presence of oscillations in the optimal control law. This case combines the challenges of the previous two and highlights the full capability of the proposed methodology. Finally, a Monte Carlo analysis with over 1000 randomly generated samples is carried out to evaluate the robustness and generalization capability of the guidance algorithm.

Application to three relevant case studies

This paragraph provides the results of the guidance algorithm applied to three different cases study, characterized by the final date 12/01/2022 at 01:44:00 Universal Coordinated Time (UTC) and a target point relying on a latitude of 18.3 °, a longitude of 51.0 ° and an altitude of 103 km. Table 6.9 summarizes the initial conditions of the three examples.

Orbital parameter	First case	Second case	Third case
a_0 [km]	6680	6665.8	6674.8
e_0	0.0007	0.0007	0.0007
i_0 [°]	51.84	51.84	51.84
ω_0 [°]	305.1	35.3	132.4
θ_0 [°]	60.48	78.5	58.2
Ω_0 [°]	123.5	54.5	87.6

Table 6.9: Initial conditions for the DNNs-based de-orbiting guidance algorithm application to the three case studies.

After the problem scenario definition, the subsequent step of the guidance algorithm foresees the estimation of the final value of true longitude and the number of its complete cycles. They result respectively in 179.8° and 299 for the first case study, 179.8 ° and 92 for the second one and 179.8° and 179 for the third one. At this point, the DNN training leads to the prediction of t_1 and t_2, with the subsequent evaluation of the number of oscillations with the procedure previously explained. The first case is characterized by the semi-major axis included in the values used to generate the training set, implying the direct use of the DNNs to evaluate t_1 and t_2. The second and third cases require an additional step for the evaluation of t_1 and t_2 due to the semi-major axis outside the values used to generate the training set. The DNNs are used to predict t_2 and t_2 for $a = 6650$ km, $a = 6660$ km and $a = 6670$ km, which include $a = 6665.8$ km (second case) and $a = 6660$ km, $a = 6670$ km and $a = 6680$ km, which include $a = 6674.8$ km (third case). Figure 6.23 shows the correspondent parabolic trends while Table 6.10 summarizes the values of t_1, t_2 and the number of oscillations predicted in three cases.

Software	Variable	Case 1	Case 2	Case 3
GPOPS-II	t_1	2.9527	4.1767	3.118
	t_2	3.4919	4.1801	3.350
	Number of oscillations	9	0	4
DNNs	t_1	2.957	4.177	3.11
	t_2	3.494	4.182	3.358
	Number of oscillations	9	0	4

Table 6.10: Results of the DNNs-based guidance algorithm application to the three cases study and comparison with GPOPS-II.

In all the three cases, the DNNs-based algorithm predicted t_1 and t_2, with a relative error of less than 1%, leading to a correct estimation of the number of oscillations with the procedure previously

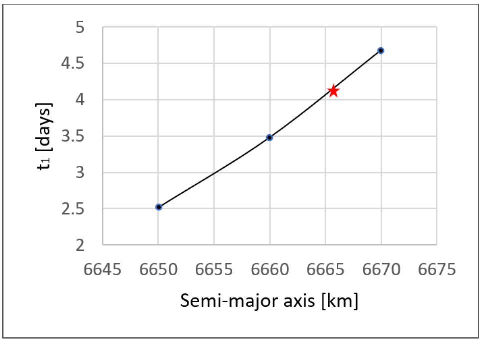

(a)

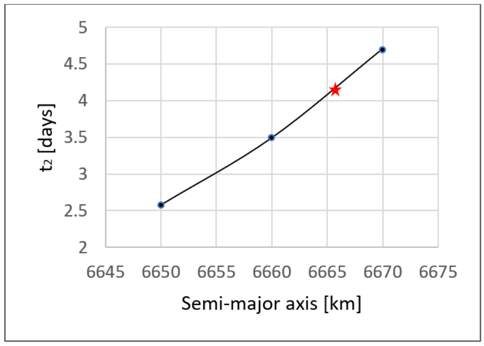

(b)

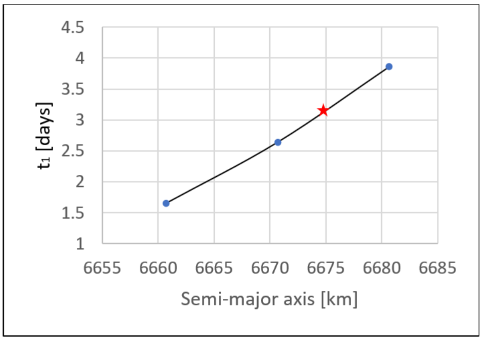

(c)

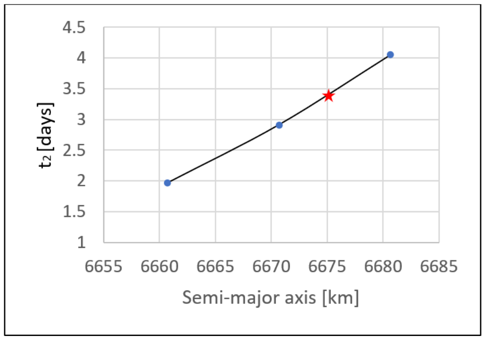

(d)

Figure 6.23: Parabolic trends used to evaluate t_1 and t_2 in the second case study ((a) and (b)) and third case study ((c) and (d)).

described.

Figure 6.24 provides the optimal control law predicted with GPOPs-II and Deep Neural Networks (DNNs) in the three cases, with a zoom in correspondence to the oscillations. Despite minor differences, the algorithm accurately predicted the optimal control law with great accuracy and a lower computational cost, from the order of minutes with the algorithm in [67] to seconds.

Figure 6.25 reports the correspondent altitude profile evaluated with both techniques, showing overlap between them with a final target error of less than 50 km.

Monte Carlo analysis

To analyze the performance and the effectiveness of the proposed guidance algorithm, a conclusive Monte Carlo analysis of over 1000 cases is performed, considering a uniform distribution of some initial mean orbital elements as in Table 6.11. In each case, the values of t_1 and t_2 are evaluated considering initial values of the semi-major axis included and not included in the ones used to generate the training set . The solutions are then propagated considering a high-fidelity and realistic atmospheric model.

The parameter used to define the performance of the DNNs is the difference between t_1 and t_2 evaluated with the DNNs (defined as t_{1DNN} and t_{2DNN}) and the ones resulting by GPOPS-II (named

Parameter	Range	Probability distribution
a	[6630 km; 6680 km]	Uniform
Ω	[0°; 360°]	Uniform
ω	[0°; 360°]	Uniform
θ	[0°; 360°]	Uniform

Table 6.11: Parameters employed in Monte Carlo analysis.

as $t_{1GPOPS-II}$ and $t_{2GPOPS-II}$: $\delta_1 = |t_{1DNN} - t_{1GPOPS-II}|$ and $\delta_2 = |t_{2DNN} - t_{2GPOPS-II}|$. Figure 6.26 provides the value of δ_1 and δ_2 for all the samples, highlighting in all cases their value less than 0.06. Figure 6.27 shows the correspondent cumulative frequency plots.

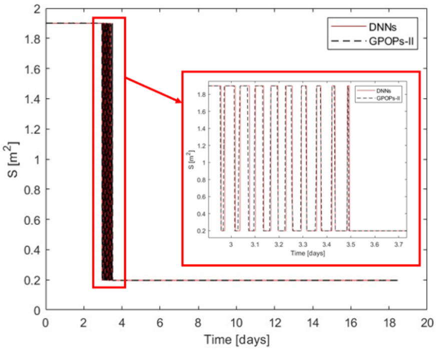

(a)

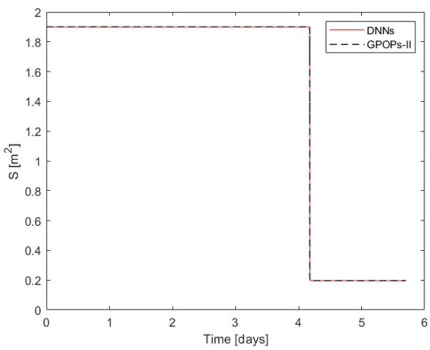

(b)

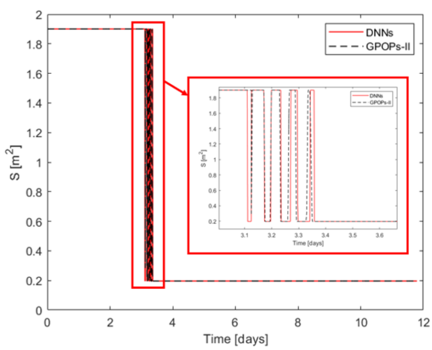

(c)

Figure 6.24: Optimal control law in the first (a), second (b) and third case study (c), estimated with GPOPS-II and DNNs.

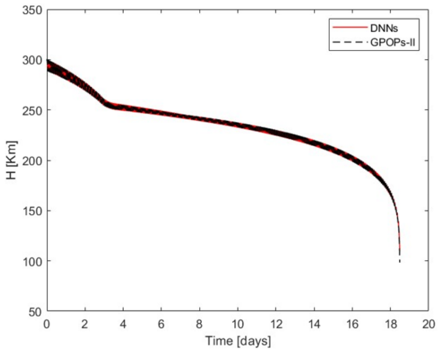

(a)

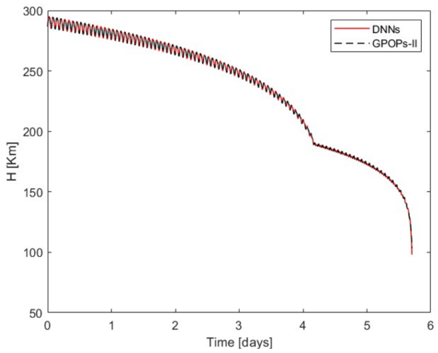

(b)

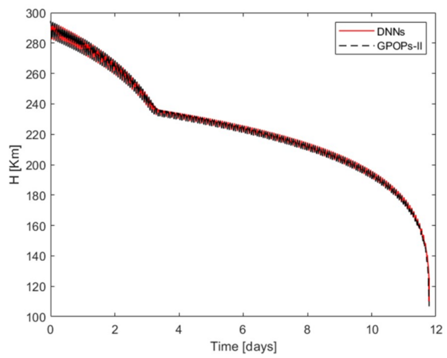

(c)

Figure 6.25: Altitude profile in the first (a), second (b) and third case study (c), estimated with GPOPs-II and DNNs.

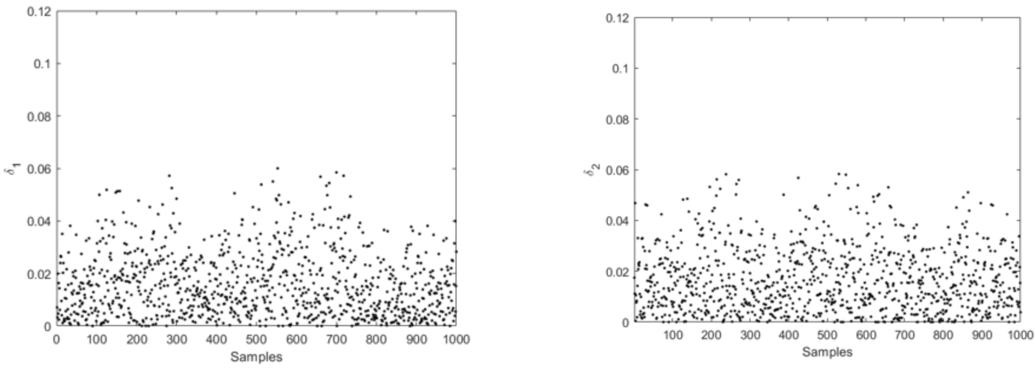

(a) (b)

Figure 6.26: δ_1 and δ_2 resulting by the Monte Carlo Analysis, as function of the samples.

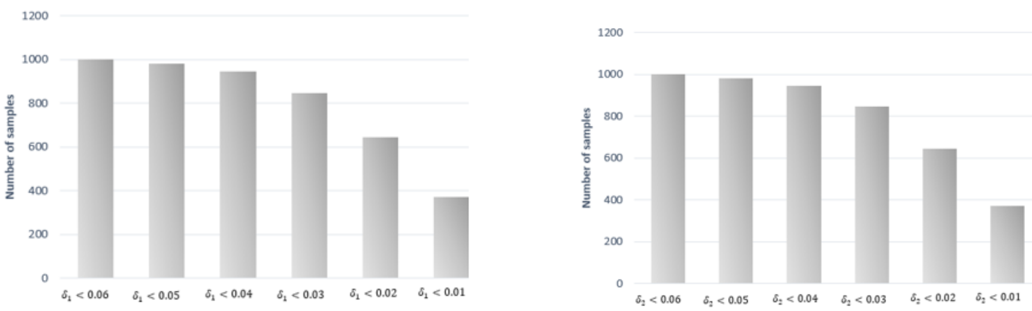

(a) (b)

Figure 6.27: Cumulative frequency plots relative to the values of δ_1 and δ_2 in the Monte Carlo Analysis.

7 Re-Entry

This chapter focuses on the assessment of a G&C algorithm for a time-optimal aerodynamic-based re-entry to ensure the reaching of a desired landing point. Similarly to the previous approach, it combines optimal control theory with AI techniques. First, the optimal control problem is presented, including the formulation of the dynamics, and the cost function. The algorithm is then employed to generate a training set for a DNN, designed to estimate the control parameters in real time, while maintaining solution optimality and facing unpredictable perturbations. The chapter concludes with a discussion of the outcomes and effectiveness of the proposed methodologies [70, 71].

7.1 Optimal control algorithm

The development of an optimal control algorithm for satellite re-entry and recovery is presented, exploiting the angle of attack and the bank angle as control variables. The problem is formulated as a single-stage optimization one, based on a hp-adaptive Gaussian quadrature orthogonal collocation method, and is solved using the MATLAB software GPOPS-II [115, 116]. The re-entry phase of a satellite is characterized by inherent complexities and requires precise control strategies to ensure both safety and accuracy in targeting. The re-entry trajectory can be conceptually divided into two different subsequent phases, each characterized by specific dynamics and control objectives. The first phase goes from the re-entry interface to an intermediate "switching" altitude. During this phase, the satellite follows a passive trajectory, adopting a configuration with maximum exposed surface area and no active control. This approach mitigates the prohibitive thermal loads encountered at higher altitudes and allows for a natural deceleration due to atmospheric drag. The main goal in this phase is to minimize heat flux and reduce the velocity of the vehicle. The final state reached at the end of this passive descent serves as the initial condition for the subsequent phase. The second phase, representing the focus of the present study, begins at the switching altitude and extends to the final landing or target point. Here, an active control is applied to guide the satellite with precision. A propellantless control strategy is considered, exploiting the modulation of the angle of attack and the bank angle, to reach the desired target point with high precision and minimum time. This formulation enables the separate treatment of the key challenges in re-entry: the first phase focuses on thermal protection and deceleration, while the second phase emphasizes trajectory accuracy and control. The focus of the present work is on this second phase, where active control can be introduced. The re-entry application considered relies on a deployable, propellantless control system based on aerodynamic appendages, such as deflectable flaps, which enable modifications of the vehicle attitude and aerodynamic coefficients. The feasibility assessment and the detailed sizing of such devices are not examined, as they fall outside the scope of the present study.

7.1.1 Equations of dynamics

The equations of dynamics governing the problem follow [113, 123]:

$$
\begin{aligned}
\frac{dV}{dt} &= -\frac{D}{m} - z_g \sin\gamma + x_g \cos\gamma + r\omega_\oplus^2 \cos\varphi(\cos\varphi \sin\gamma - \sin\varphi \sin\psi \cos\gamma) \\
V\frac{d\gamma}{dt} &= \frac{Lcos\sigma}{m} - z_g \cos\gamma + x_g \sin\gamma \sin\psi + \frac{V^2}{r}\cos\gamma + 2V\omega_\oplus \cos\varphi \cos\psi \\
&\quad + r\omega_\oplus^2 \cos\varphi(\cos\varphi \cos\gamma - \sin\varphi \sin\psi \sin\gamma) \\
V\frac{d\psi}{dt} &= \frac{Lsin\sigma}{m\cos\gamma} - \frac{V^2}{r}\cos\gamma \cos\psi \tan\varphi + x_g \frac{\cos\psi}{\cos\gamma} + 2V\omega_\oplus(\sin\psi \cos\varphi \tan\gamma - \sin\varphi) \\
&\quad - \frac{r\omega_\oplus^2}{\cos\gamma}\sin\varphi \cos\varphi \cos\psi \\
\frac{dr}{dt} &= V \sin\gamma \\
\frac{d\varphi}{dt} &= \frac{V\cos\gamma \sin\psi}{r} \\
\frac{d\theta}{dt} &= \frac{V\cos\gamma \cos\psi}{r\cos\varphi}
\end{aligned}
\tag{7.1}
$$

where x_g and z_g are the two components of the gravity vector, given by the following formulations:

$$
\begin{aligned}
z_g &= \frac{\mu}{r^2}\left[1 - \frac{3}{2}J_2\left(\frac{R_\oplus}{r}\right)^2\left(3\sin^2\phi - 1\right)\right] \\
x_g &= \frac{3\mu J_2}{r^2}\left(\frac{R_\oplus}{r}\right)^2 \cos\phi \sin\phi
\end{aligned}
\tag{7.2}
$$

The J_2 term is significantly larger than the higher order coefficients, so a first or second order approximation is considered enough for the re-entry modeling. The aerodynamic drag D and lift L are modeled as:

$$
\begin{aligned}
L &= \frac{1}{2}\rho V^2 S C_l \\
D &= \frac{1}{2}\rho V^2 S C_d
\end{aligned}
\tag{7.3}
$$

where S represents the exposed surface area, C_l and C_d are the lift and drag aerodynamic coefficients, respectively, and ρ is the atmospheric density. For the latter, this work adopts a simplified exponential atmospheric model. While more accurate models such as NRLMSISE-00 have also been tested with successful results, the exponential model is considered here to reduce computational cost. This simplification is justified, as the relatively short timescale of the re-entry phase limits the impact of variations caused by factors such as solar activity or time of day. A key aspect of aerodynamic modeling involves the behavior of the drag coefficient (C_d) and lift coefficient (C_l) as functions of the angle of attack, which significantly influence the dynamics of the device and its controllability during re-entry. The value of C_d throughout this phase is affected by multiple factors, including the flow regime, vehicle shape, orientation, and velocity. For example, in the hypersonic and supersonic regimes, re-entry vehicles such as capsules typically experience

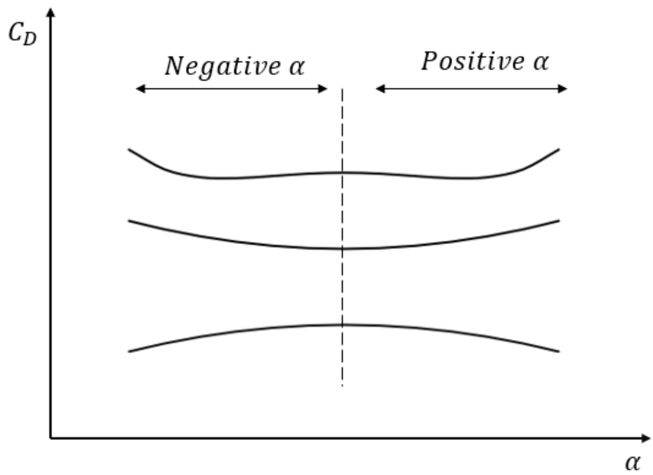

Figure 7.1: Schematic representation of typical drag coefficient trends with angle of attack.

elevated C_d values, primarily due to shock wave formation and intense aerodynamic heating. As the vehicle decelerates and transitions into the subsonic regime, C_d generally decreases. Modeling this aerodynamic behavior is non-trivial due to the complex physical phenomena involved, such as boundary layer evolution, shock wave interactions, and vortex dynamics. The C_d usually exhibits a parabolic trend with respect to the angle of attack. Conventional spacecraft, such as the Space Shuttle, typically show an upward-facing parabola, indicating increasing drag with increasing angle of attack. On the other hand, re-entry capsules may display more complex trends, including both increasing and decreasing behavior, or even an inversion of the curvature, initially decreasing and then increasing with higher angles of attack as also shown in Figure 5.11. A schematic illustration of possible C_d trends is shown in Figure 7.1.

The lift coefficient C_l also plays a critical role in determining both the trajectory and stability of the spacecraft during re-entry. In general, C_l follows a nearly linear relationship with the angle of attack. Vehicles like the Space Shuttle exhibit a positive slope, meaning lift increases with angle of attack. However, re-entry capsules may exhibit a negative slope, reflecting their unique aerodynamic properties.

In the current optimal control problem, the objective function is the minimization of final time. Constraints related to heat flux are not considered, as the trajectory segment under study occurs after the peak heating conditions have passed, and thus does not involve prohibitive thermal loads.

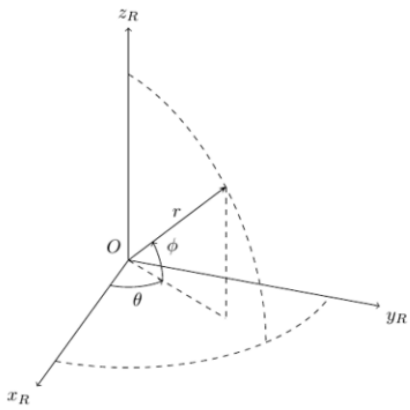

(a) ECEF reference frame

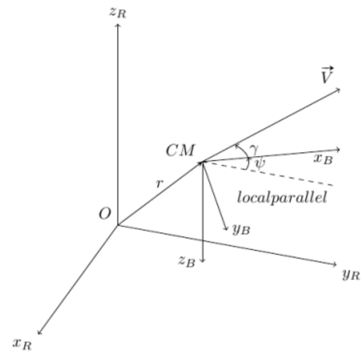

(b) Body reference frame

Figure 7.2: Reference frames employed: ECEF 7.2a and body reference frame 7.2b

7.1.2 Reference frames

In the current formulation, it is relevant to define the Earth Centered Earth Fixed (ECEF) (X_R, Y_R, Z_R) reference frame (Figure 7.2a) with the following characteristics:

- The origin is located in the center of the Earth
- The Z_R axis coincides with the direction of the Earth's rotation axis pointing the North Pole.
- The X_R axis is defined as the intersection of the plane orthogonal to Z_R and the Greenwich meridian.
- The Y_R axis is orthogonal to both of them, completing the reference frame.

In this reference frame, the longitude θ, the latitude ϕ, and the satellite position r are defined. The flight path angle γ is defined as the angle between the velocity vector and a local horizontal plane. The heading angle, identified by ψ, is the angle between the local parallel of latitude and the projection of the velocity vector on the horizontal plane. Following the convention, the flight-path angle, γ, is positive when the velocity vector lies above the local horizontal plane. On the other hand, the heading angle, ψ increases when turns are made toward the left and is zero when facing east. In conclusion, the body reference frame for the spacecraft under consideration is represented by (CM, X_B, Y_B, Z_B) (Figure 7.2b) [113].

Mass	40 kg
Surface	1.9 m^2
Minimum angle of attack	-40°
Maximum angle of attack	40°
Minimum bank angle	-20°
Maximum bank angle	20°

Table 7.1: Main characteristics of the satellite: geometric specifications and optimal control variables limits

Initial conditions	
Altitude	55 km
Flight path angle	-10.6°
Velocity	1021 m/s
Heading angle	43.8°
Latitude	22.14°
Longitude	21.8°
Target conditions	
Altitude	10 km
Latitude	23°
Longitude	23°

Table 7.2: Initial and target conditions for the case study

7.1.3 Results of the optimal control algorithm

This subsection describes the results of the optimal control algorithm. First, the application to a case study is presented, considering plausible trends and values for the aerodynamic coefficients. However, technological solutions to achieve these values will not be addressed, as they fall outside the scope of this work. Then, a Monte Carlo analysis is performed to test the robustness of the algorithm for different initial conditions. Object of study of the current work is a re-entry device with the geometric specifications and the bounds of the optimal control variables summarized in Table 7.1.

The case study analyzed is characterized by the initial and target conditions summarized in Table 7.2. The chosen switching altitude is set at 55 km. This altitude can be considered a good choice to start the targeting maneuvers as it is sufficiently distant from the heat flux peak, while ensuring lower velocity values, thus mitigating potential challenges.

The lift coefficient Cl has been modeled by the following linear trend:

$$Cl = Cl_0 + Cl_1\alpha \tag{7.4}$$

where $C_{l_0} = 0$, as re-entry capsules typically exhibit no lift at zero angle of attack, and $C_{l_1} = -2.5$. This linear profile has been modified for values of the angles of attack lower than $-40°$ and greater than $40°$, experiencing a reversal of trend. The drag coefficient Cd has been modeled by the following parabolic trend:

$$Cd = Cd_0 + Cd_1\alpha + Cd_2\alpha^2 \tag{7.5}$$

Variable	Range	Distribution
Altitude	55 km	Constant
Flight path angle	[-5°; -30°]	Uniform
Velocity	[950 m/s; 1350 m/s]	Uniform
Heading angle	[30°; 60°]	Uniform
Latitude	[19°; 22.3°]	Uniform
Longitude	[19°; 22.3°]	Uniform

Table 7.3: Conditions employed for the Monte Carlo analysis related to the optimal control algorithm

where $Cd_0 = 0.4$, $Cd_1 = 0.0$, and $Cd_2 = 0.1$. The assumption of a unique trend of the aerodynamic coefficients as a function of the angle of attack is a simplified hypothesis. Although it exhibits a similar profile in both supersonic and subsonic phases, the specific values vary. However, within this framework, the flow field regimes only encompass low supersonic and subsonic conditions, and an intermediate value is considered.

The behavior of main parameters during the re-entry is presented in Figure 7.3.

The Longitude-Latitude profile shown in Figure 7.3b increases from the initial conditions to the desired target point, highlighting the effectiveness of the optimal control algorithm.

Figure 7.3d illustrates the velocity profile during re-entry, revealing the characteristic decreasing trend over time. The final velocity reached is sufficiently low, ensuring a safe re-entry and subsequent landing.

Furthermore, the flight path angle, in Figure 7.3c, is characterized by different phases throughout the maneuver. Initially, it experiences an increase followed by a slight decrease before transitioning into a sharper decreasing trend. Then, it reaches a final value close to -80°.

The bank angle (Figure 7.3f) undergoes an initial phase, wherein it progressively decreases before increasing and stabilizing at nearly zero. This observed trend suggests a stabilizing response to the changing aerodynamic forces experienced during the initial time of the maneuver.

On the contrary, the angle of attack in Figure 7.3e initially experiences an increasing trend, followed by a subsequent decreasing profile, then maintaining near constancy at -32° for approximately 100 seconds. Subsequently, it experiences an increase before ultimately stabilizing at nearly 0°

To conclude, a Monte Carlo analysis has been conducted over 500 samples for different initial conditions at the switching altitude, with the distributions summarized in Table 7.3. The algorithm successfully evaluated the optimal control profiles in all cases, demonstrating its robustness in a wide range of conditions.

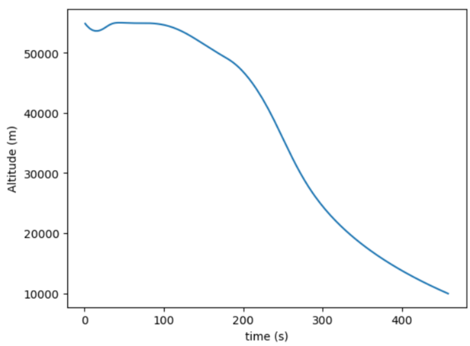

(a) Altitude

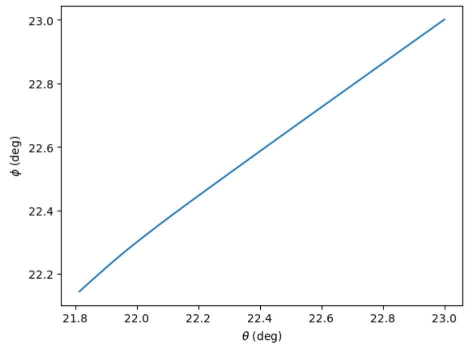

(b) Longitude - Latitude

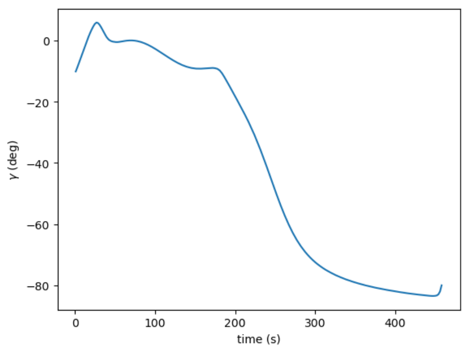

(c) Flight path angle

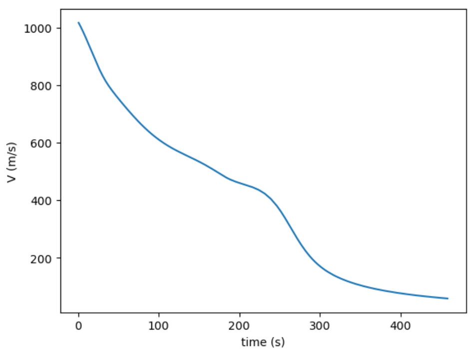

(d) Velocity

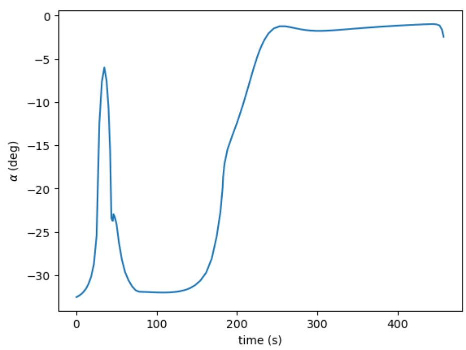

(e) Angle of attack

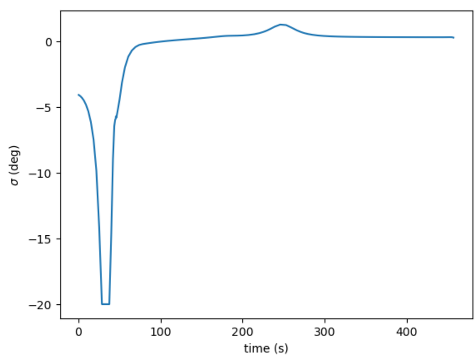

(f) Bank angle

Figure 7.3: Results of the optimal control re-entry algorithm applied to the case study

7.2 Feedback control based on Deep Neural Networks

This section describes an approach based on DNNs to perform a closed-loop feedback control to the optimal control trajectories defined with the algorithm previously described. The problem can experience significant uncertainties, primarily related to the aerodynamic model, leading to a re-entry point deviation from the nominal one. The choice of a DNNs-based approach is motivated by the high computational cost and numerical challenges intrinsically associated with solving an optimal control problem, often rendering such an approach unfeasible for onboard satellite systems requiring immediate responses. On the contrary, DNNs offer an alternative solution given their ability to predict desired outputs almost instantaneously once performing the training process on the ground. Furthermore, the lack of literature on this topic has motivated the authors to focus on this approach, further emphasizing its novelty and innovation.

Here, an imitation learning approach is chosen to perform a real-time closed-loop feedback control to handle unpredictable uncertainties and perturbations. The inputs of the DNN rely on the six states of the satellite, while the outputs consist of the two actions (angle of attack and bank angle). The choice fell on a fully connected DNN characterized by one input layer with 6 neurons, 8 hidden layers with 50 neurons each, and one output layer with 2 neurons corresponding to the outputs. The activation function is Exponential Linear Unit (eLU) for all the layers, except for the output layer characterized by a linear activation function. The training set relies on 750 optimal control trajectories, resulting in 98000 state-action couples. The optimizer is Adam, and the loss to minimize during the training process is the mean square error between the predicted and the reference trajectory. The switching altitude has been fixed to 55 km, while the other five state variables have varied to create a comprehensive training set representative of a proper number of different scenarios. A training set scheme is provided in Figure 7.4, highlighting the states and the correspondent optimal control actions.

The training process is performed considering 80 % samples, while 20 % is used for testing. In relation to the other parameters, the choice fell on a learning rate of 0.0001, batch size 75 and 600 epochs. Figure 7.5 shows the loss trend as a function of the number of epochs.

The training loss exhibits a decreasing trend over the epochs, indicative of the learning process. Following an initial phase of rapid decrease, the loss stabilizes, identifying the end of the training process. The final training and testing losses are 3.9 % and 4.3 %, respectively.

7.2.1 Validation

For validation, the DNN was trained, saved, and subsequently integrated into a propagator. It is employed to predict the angle of attack and bank angle profiles based on the satellite's actual state during the propagation. Here, one scenario is analyzed, considering the initial conditions in Table 7.2. The optimal control solutions and the correspondent state variables are compared to the DNN-driven solution in Figure 7.6.

The optimal control profiles exhibit minor discrepancies, explainable by the training error propagation. Nevertheless, an excellent degree of overlap between the state variables is achieved, especially for altitude, latitude and longitude, which are of interest for the targeting problem. The error in the final altitude is zero since the propagator is set to stop when the desired final altitude is reached. The error in the final latitude and longitude is negligible and is less than 0.1 km. The DNNs approach is then satisfactorily validated through a Monte Carlo analysis with the initial conditions distributions summarized in Table 7.4. Figure 7.7 shows the cumulative frequency plot relative

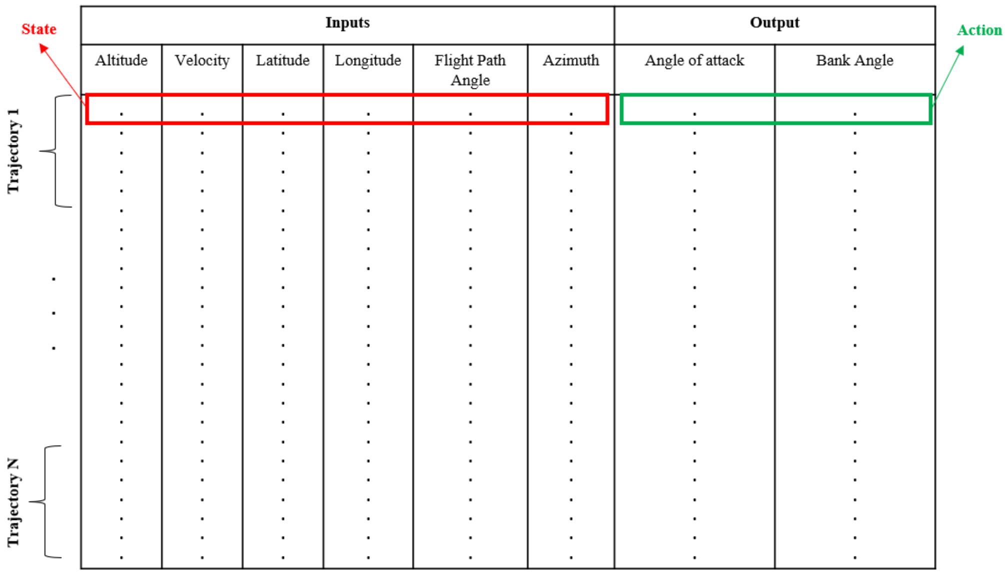

Figure 7.4: Schematization of the training set with inputs and output

to the latitude and longitude final error (km) for all the cases. The graph revealed a successful outcome in all the conditions analyzed, with most samples characterized by errors in the range 0 km - 1 km. These levels of error are acceptable and explainable by the DNN error propagating during the integration process. Even though, they are limited and the controller can be considered successfully validated.

Variable	Range	Distribution
Altitude	55 km	Constant
Flight path angle	[-5°; -20°]	Uniform
Velocity	[950 m/s; 1350 m/s]	Uniform
Azimuth angle	[40°; 50°]	Uniform
Latitude	[21.5°; 22.3°]	Uniform
Longitude	[21.5°; 22.3°]	Uniform

Table 7.4: Initial conditions distributions employed in the Monte Carlo analyses for the feedback controller

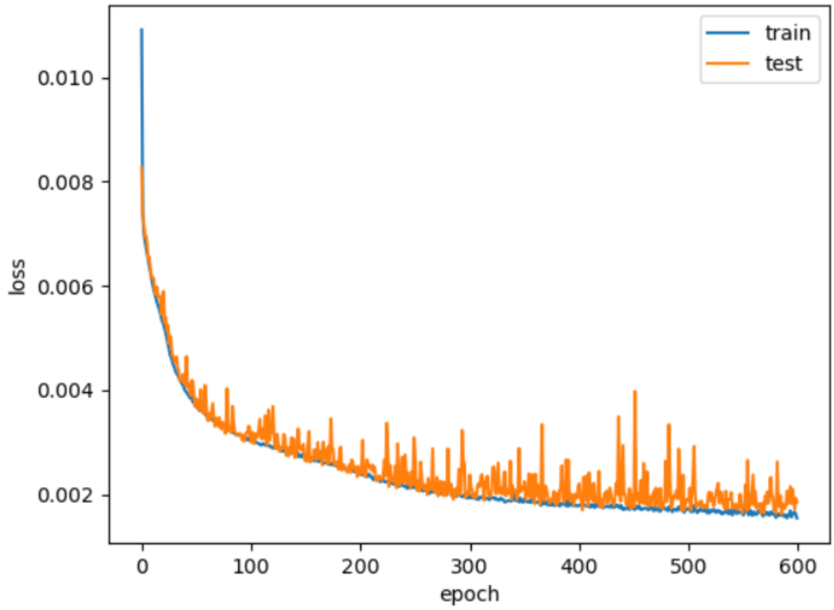

Figure 7.5: Loss as function of the number of epochs for the training and testing process

7.2.2 Application of the feedback control to perturbed cases

In this section, uncertainties and perturbations are considered to evaluate the effectiveness of the proposed DNNs-based closed-loop control system. Two case studies are examined considering the initial conditions summarized in Table 7.2 and perturbing the aerodynamic coefficients to affect the trajectory. In one case, only a random noise is added to both coefficients, while in the other case also the drag coefficient equation has been varied to represent a more prohibitive condition. Two conclusive Monte Carlo analyses demonstrated the algorithm's effectiveness in the perturbed cases for different initial conditions.

Case studies with perturbations

This subsection discusses the feedback control algorithm application to two perturbed cases. In the first case (defined as DNNs-1 in Figure 7.8), the drag coefficient trend has been varied considering the following parameters: $C_{d_0} = 0.6$, $C_{d_1} = 0$, and $C_{d_2} = -0.2$, in addition to the inclusion of a random disturbance to both aerodynamic coefficients. The second case (defined as DNNs-2 in Figure 7.8) involves a random bias without affecting the trend of the coefficients. The random noise has been modeled with a normal distribution of random numbers ranging between -0.2 to 0.2. Figure 7.8 shows the states and control variables in the nominal and controlled cases.

The latitude and longitude profile in Figure 7.8b shows a good degree of overlap between the three scenarios, with final errors lower than 1 km for all the cases. It underlines the ability of the controller to properly update the control variables, facing the perturbations and ensuring limited targeting errors. Figure 7.8a shows the altitude profiles, initially coinciding before gradually diverging and then converging to the desired final value of 10 km in all the cases. The three profiles reach the desired final altitude at different final times with respect to the nominal unperturbed

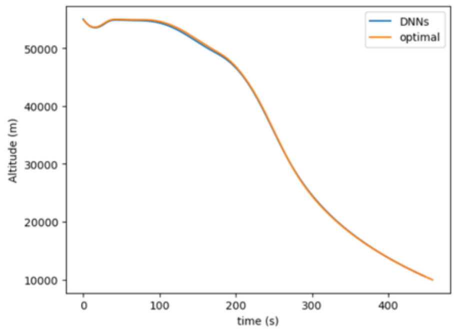

(a) Altitude

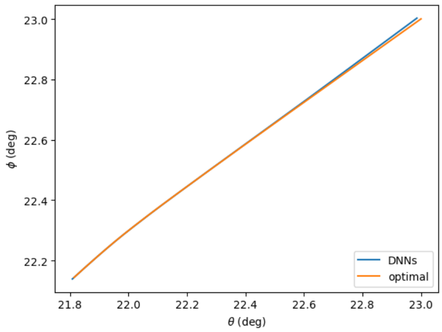

(b) Longitude - Latitude

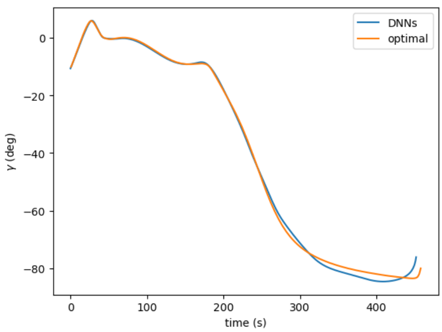

(c) Flight path angle

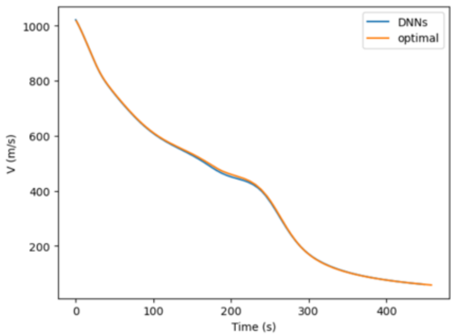

(d) Velocity

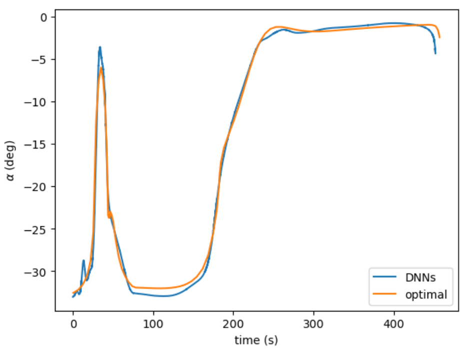

(e) Angle of attack

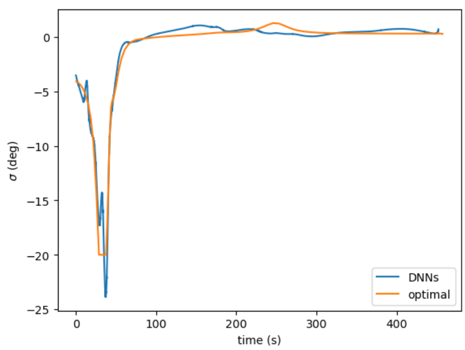

(f) Bank angle

Figure 7.6: Validation of the controller applied to an unperturbed case

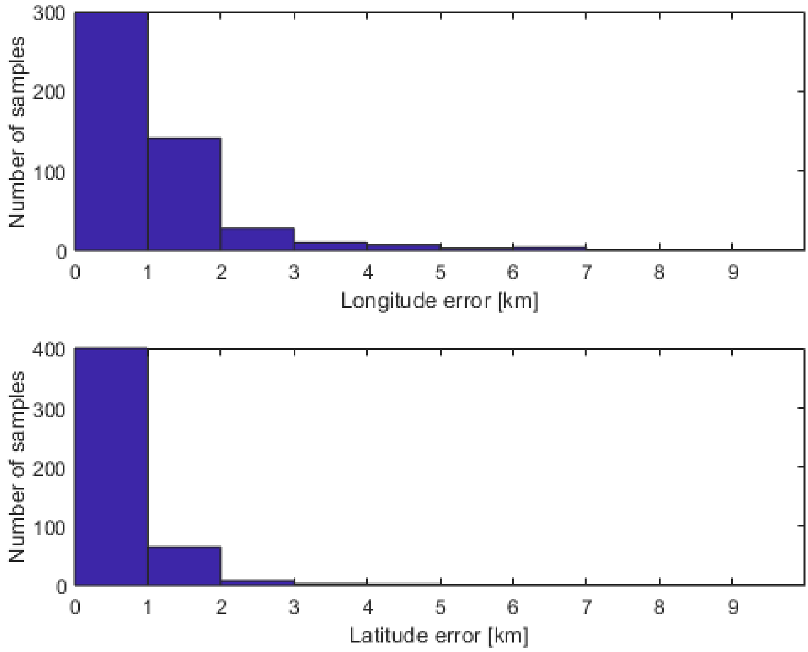

Figure 7.7: Cumulative frequency plot: Monte Carlo analysis for validation

solution. In particular, the first case experiences a difference of time of about 150 s, while the second case just few seconds with respect to the optimal time. As a result, a reduction in targeting error is ensured in greater time compared to the correspondent unperturbed optimal control solution. This difference is more pronounced in cases where the perturbations are more intense, such as in the first case study, characterized by random noise and a different trend for the drag, compared to the second case, only characterized by the addition of a random noise. This outcome is expected since the perturbed problems differ from the original optimal one, and updating the control variables in response to the perturbed state of the satellite may result in a different final time. Figures 7.8d and 7.8c show the velocity and flight path angle profiles. A similar situation occurs, with an initial overlap of the trends, then diverging to finally converge to comparable values at different instant of times. Figures 7.8e and 7.8f show the optimal control variable profiles. They deviate from the nominal profile with the presence also of an oscillatory component. As expected, the deviation entity is greater for the first case, characterized by a greater intensity of perturbations, to ensure the reaching of a desired re-entry point.

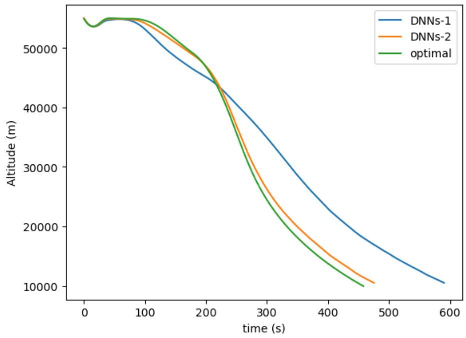

(a) Altitude

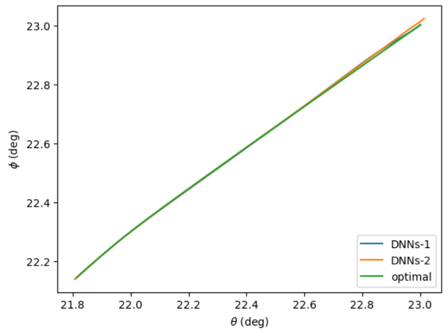

(b) Longitude - Latitude

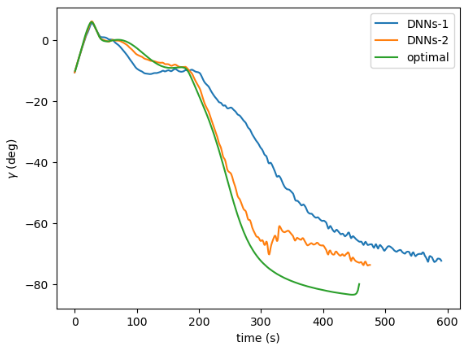

(c) Flight path angle

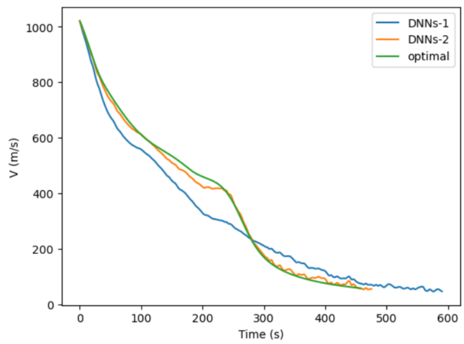

(d) Velocity

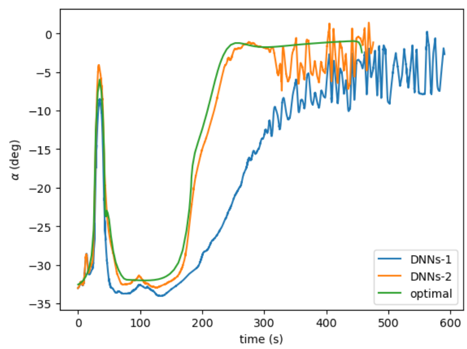

(e) Angle of attack

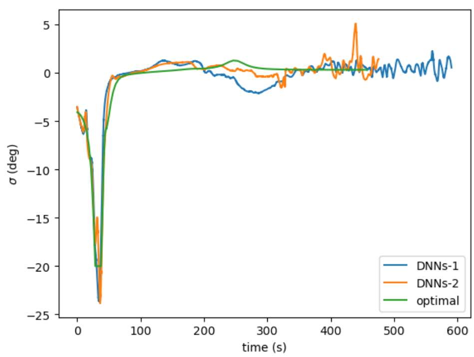

(f) Bank angle

Figure 7.8: State and control variables time history after applying the feedback control

Monte Carlo analysis

The effectiveness of the controller in the perturbed cases has been proven by two Monte Carlo analyses among 500 samples each, considering the same distribution of initial conditions summarized in Table 7.4 and the two kind of perturbations analyzed in the previous subsection. As stated before, the final error on altitude is 0 km because the propagator is set to stop when it reaches the desired final target. In relation to latitude and longitude, Figures 7.9 and 7.10 show the results in terms of latitude and longitude errors in km.

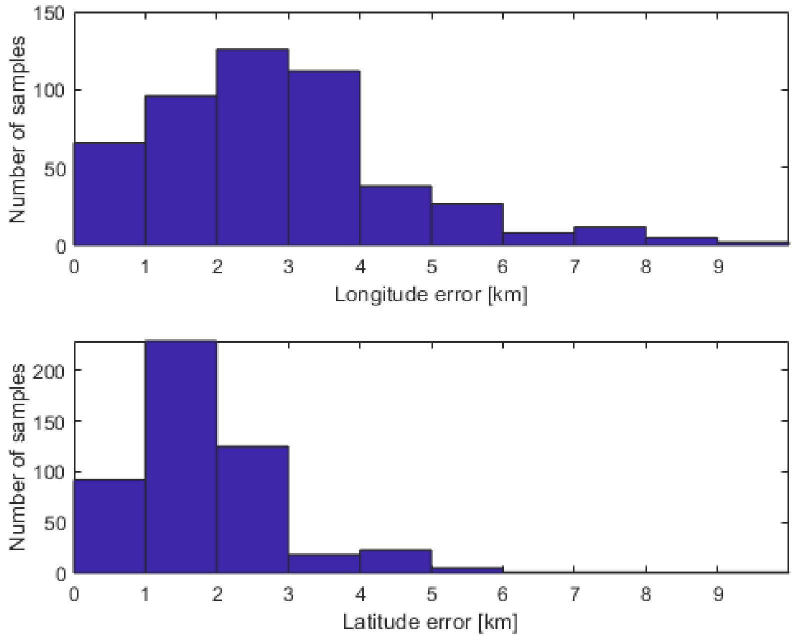

Figure 7.9: Cumulative frequency plot: first Monte Carlo analysis in presence of perturbations

In the first case, Figure 7.9, most samples are characterized by a targeting error lower than 4 km on longitude and 3 km on latitude. The second case, Figure 7.10, is characterized by a targeting error lower than 3 km for both latitude and longitude for most samples. In both cases, characterized by different perturbation levels, the algorithm is able to ensure the reaching of the target point within a limited error. The analyses performed also demonstrate its robustness for different initial conditions. It can be considered a noteworthy solution onboard of satellites as a feedback controller for propellantless devices re-entering on Earth.

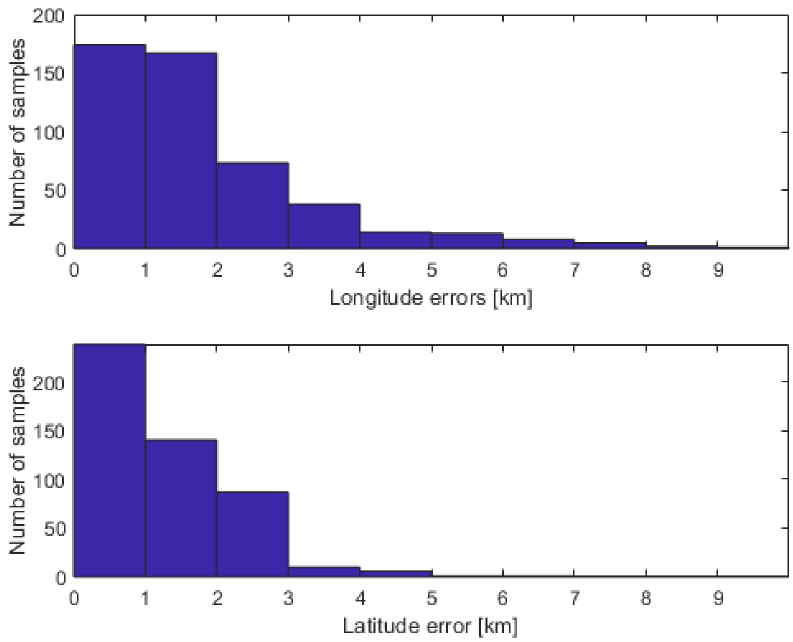

Figure 7.10: Cumulative frequency plot: second Monte Carlo analysis in presence of perturbations

8 Collision Avoidance

This chapter addresses the assessment of a G&C algorithm for aerodynamic-based optimal collision avoidance. This part was carried out in collaboration with the research group led by Prof. Stefanos Fasoulas, who provided the SOURCE satellite data, performed the aerodynamic characterization through ADBSat and supported the formulation of the optimal control problem. Following a similar approach to the previous applications, the proposed methodology integrates optimal control theory with AI techniques. First, an optimal control algorithm is introduced, characterized by a composed cost function that minimizes orbital decay while maximizing the miss distance between two satellites. Subsequently, an AI-based approach is presented, enabling the prediction of the key parameters of the optimal control profile in real time. Finally, an additional analytical procedure is outlined to adapt the optimal control law in response to perturbations, thereby preserving the optimality of the solutions and maintaining the effectiveness of the cost function [72–75].

8.1 Optimal control problem

8.1.1 Satellite aerodynamics

The specific aerodynamic drag force f_D acting on a spacecraft, resulting from its interaction with the residual atmospheric particles, acts anti-parallel to the relative velocity vector v_{rel} and is defined as:

$$f_D = -12\rho \frac{C_D A_{Ref}}{m} v_{Rel}^2 \frac{v_{Rel}}{v_{Rel}} \tag{8.1}$$

where C_D is the drag coefficient of the satellite, A_{ref} the reference area, m the satellite mass, ρ the atmospheric density and v_{rel} the satellite's velocity relative to the local atmosphere. The latter is defined as:

$$v_{Rel} = v_{Sat} - v_{Rot} - v_{Wind}, \tag{8.2}$$

where v_{Sat} is the inertial velocity of the satellite, v_{Rot} the co-rotational velocity of the atmosphere with the Earth and v_{Wind} thermospheric winds. Within the optimizer, the co-rotational velocity is calculated via:

$$v_{Rot} = \omega_{Earth} \times r_{Sat}, \tag{8.3}$$

where ω_{Earth} is the angular velocity of the Earth with respect to the Earth Centered inertial (ECI) reference frame. For an adequate modeling of thermospheric winds v_{Wind}, the horizontal wind model (HWM) [124], which uses a set of input parameters similar to the NRLMSISE-00 model

[125] which is used to model the atmospheric conditions, is employed. The sensitivity of a satellite to aerodynamic drag forces is identified by the ballistic coefficient β:

$$\beta = \frac{m}{C_D A_{Ref}}, \tag{8.4}$$

which includes all parameters depending on the spacecraft design. Throughout this study, its inverse, defined as:

$$\beta^* = \frac{C_D A_{Ref}}{m}, \tag{8.5}$$

is considered as it represents a more intuitive interpretation of the dependencies. In the LEO regime the atmosphere can be considered particular in nature with negligible inter-molecular collisions. Under these conditions, the forces acting on a spacecraft are the result of the momentum and energy exchange between the incident gas particles and the satellite surfaces, referred to as gas-surface interaction (GSI). To determine the ballistic coefficient of the satellite, the ADBSat software [126], developed at the University of Manchester, is used within this study. The environmental conditions are calculated via the empirical NRLMSISE-00 model [125].

Collision avoidance via aerodynamic drag

The total specific energy of a satellite in a Keplerian orbit can be defined as:

$$\varepsilon = -\frac{\mu}{2a}, \tag{8.6}$$

where a is the semi-major axis and μ the gravitational parameter of the Earth. By definition, the aerodynamic drag acts anti-parallel to the relative velocity, decelerating the satellite and reducing its orbital energy. Due to the interplay of potential and kinetic energy, a deceleration of a satellite effectively results in its acceleration (referred to as the *satellite drag paradox*): An increase in the aerodynamic drag forces experienced by a satellite results in orbital decay and an increased orbital velocity. As the magnitude of the drag force can be modulated via a variation in the inverse ballistic coefficient β^* of the satellite, this represents an effective means to affect the trajectory of the satellite. The idea behind active satellite collision avoidance maneuvers via aerodynamic drag is consequently to deliberately adjust the profile of the ballistic parameter β^* such that a collision at the expected time of closest approach (TCA) is prevented. For that, the trajectory of the maneuvering satellite is compared to that of a virtual reference satellite which follows its trajectory without any adjustments, consequently resulting in the forecasted conjunction. By increasing the drag experienced by the maneuvering satellite, the increase in orbital velocity leads to the build-up of an in-track separation distance Δx relative to the reference satellite. At TCA, the separation distance Δx_{t_f} represents the (in-track) distance to the predicted point of conjunction, which will be referred to as *miss distance*. Note, that it is used here instead of the actual distance between the two objects for the sake of simplicity. This is graphically visualized in Figure 8.1, where the time between reception of the collision warning and TCA is denoted as conjunction time t_c.

An analytic equation for Δx as a function of time has been derived in [54]:

$$\Delta x = \frac{3\bar{\rho}\mu}{4a}\Delta\beta^* t_m^2, \tag{8.7}$$

where $\bar{\rho}$ is the average atmospheric density encountered during the maneuver, t_m the maneuver time and $\Delta\beta^*$ the variation in β^*:

$$\Delta\beta^* = \beta^*_{Sat} - \beta^*_{Ref}, \tag{8.8}$$

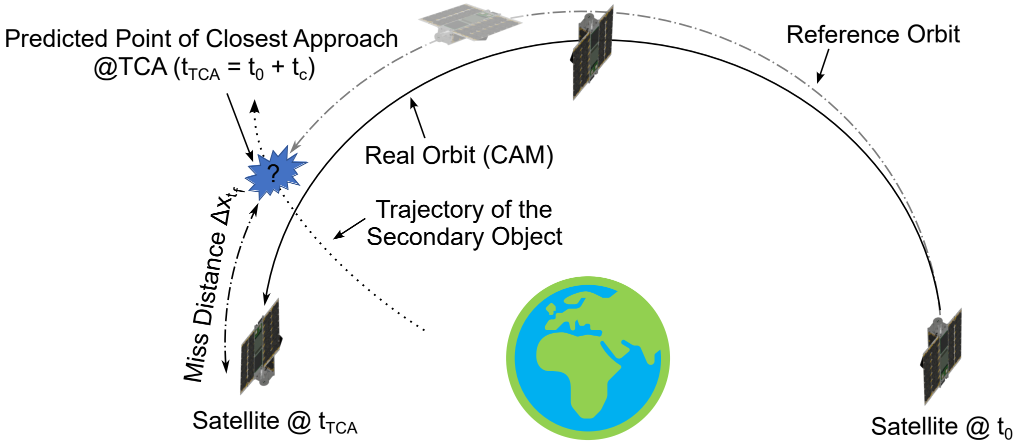

Figure 8.1: Graphical visualization of a collision avoidance maneuver using aerodynamic drag.

where β^*_{Sat} is the commanded value and β^*_{Ref} the reference value. Consequently, via a deliberate variation in the inverse ballistic coefficient β^*_{Sat}, the in-plane separation distance can be actively controlled. The latter represents a means for propellantless orbit control for any asymmetrically shaped satellite and can, e.g. be exploited to exert satellite formation flight and collision avoidance maneuvers [54, 127]. From 8.7, the respective maneuvering time $t_{m,\Delta x}$ required to achieve a desired separation distance Δx can be determined:

$$t_{m,\Delta x} = \sqrt{\frac{4a}{3\bar{\rho}\mu}\frac{\Delta x}{\Delta\beta^*}} \tag{8.9}$$

The time period $t_{m,\Delta x}$ determined via 8.9 can be used as an initial guess for the optimal control problem or to verify the solution in case of a time-optimal maneuver.

Aerodynamic characterization of SOURCE

For the optimal control algorithm assessment, the aerodynamics of the satellite is modeled with ADBSat. It is a software tool for the aerodynamic assessment of satellites developed at the University of Manchester [126, 128]. It employs a panel method with a simple shading algorithm: the analyzed geometry is divided into discrete panels and the interaction of each panel with the incoming flow is assessed individually. The acting forces on the satellite result from the addition of the contributions of all panels and are converted to aerodynamic coefficients.

ADBSat takes several inputs, including the satellite geometry, the epoch, the position along the orbit (specified by latitude, longitude, and altitude), and indices of solar and geomagnetic activity. These indices serve as inputs to the NRLMSISE-00 atmospheric model, which provides estimates of atmospheric density, composition, and temperature. These atmospheric parameters are then used as inputs to the Semi-Empirical Satellite Accommodation Model (SESAM) [129]. Sentman's GSI model assumes diffuse reflection of incident particles with a partial thermal accommodation with the satellite surface. The degree of thermal accommodation is described by the thermal accommodation coefficient $\alpha_T \in [0, 1]$. SESAM enables the determination of α_T based on the number density of atomic oxygen and the temperature of the atmosphere.

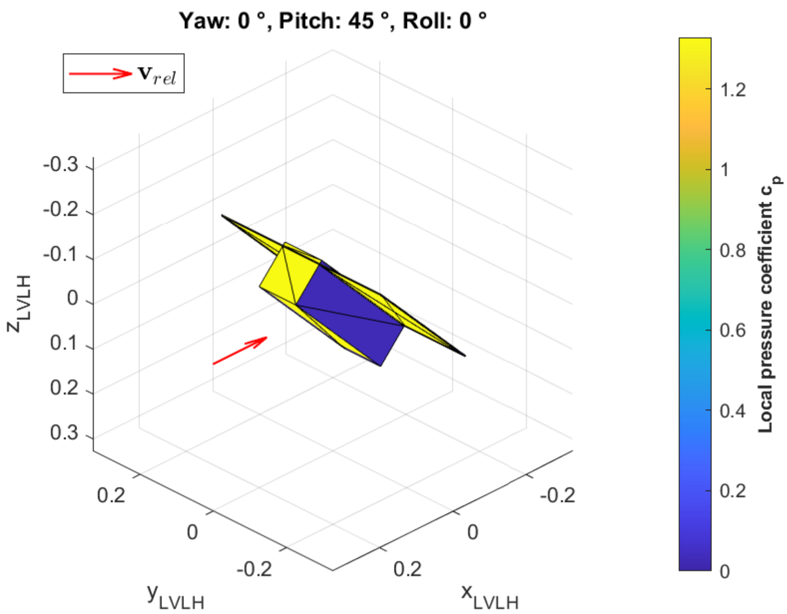

Figure 8.2: Exemplary local pressure coefficient distribution for SOURCE from ADBSat [126, 128].

Parameter	Symbol	Value
Semi-major axis	a	6778.137 km
Eccentricity	e	0.001
Inclination	i	45
RAAN	Ω	0
Argument of perigee	ω	0
True anomaly	θ	0

Table 8.1: Kepler elements of the reference orbit for epoch May 8, 2024, 12:00 UTC.

An output from ADBSat is shown in Figure 8.2. Yellow-shaded panels show an increased local pressure coefficient and thus a contribution to aerodynamic drag as well. The SOURCE satellite is aerodynamically characterized for a reference orbit corresponding to an altitude of 400 km. The initial Keplerian elements at the epoch of interest are listed in 8.1. Solar and geomagnetic activity is set to be of moderate levels (proxy for solar flux and its 81-day average $F_{10.7} = \bar{F}_{10.7} = 140$, geomagnetic activity index $a_p = 15$) [130].

The inverse ballistic coefficient is determined for $n = 100$ evaluation points along one orbital revolution and then averaged. This procedure is repeated for varying angles of attack, the results are presented in Figure 8.3. The inverse ballistic coefficient shows a minimum of $\beta^*_{\text{min}} = 1.2709 \times 10^{-2}$ m^2/kg for an angle of attack of 0. For a flight with maximum drag, the inverse ballistic coefficient yields $\beta^*_{\text{min}} = 8.618 \times 10^{-2}$ m^2/kg for an angle of attack of 90.

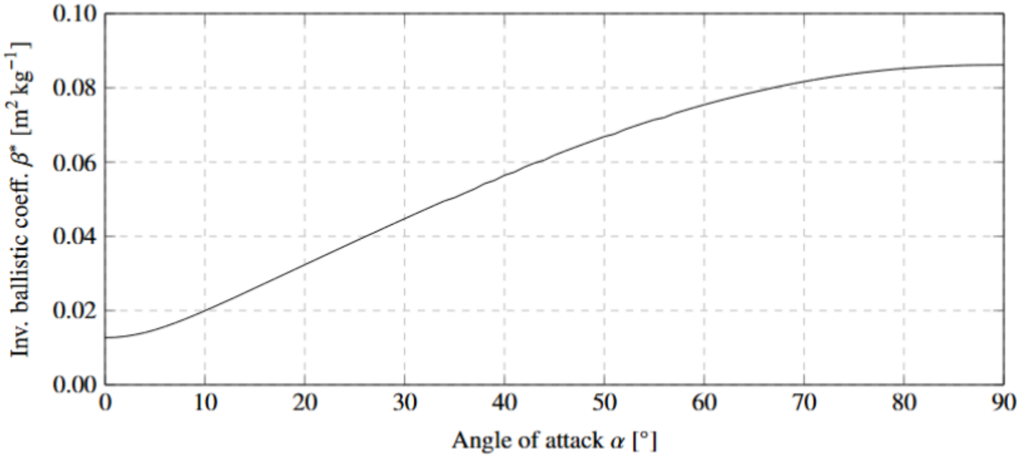

Figure 8.3: Inverse ballistic coefficient over angle of attack for the SOURCE satellite.

8.1.2 Equations of dynamics

The problem is formulated as a single-stage optimization, based on a hp-adaptive Gaussian quadrature orthogonal collocation method and is solved with the GPOPS-II software [115, 116]. The aerodynamic drag is exploited to control the satellite through the ballistic coefficient, which can be adjusted via a respective rotation of the satellite. The formulation of the relative motion between the virtual reference satellite (SOURCE REF) and the actual satellite performing the collision avoidance maneuver (SOURCE CAM) is based on modified relative equinoctial orbital elements $\boldsymbol{\delta\mathcal{E}_{eq}}$ [131]:

$$\boldsymbol{\delta\mathcal{E}_{eq}} = \boldsymbol{\mathcal{E}_{eq,Sat}} - \boldsymbol{\mathcal{E}_{eq,Ref}} \tag{8.10}$$

where the subscript *Sat* referring to the actual satellite and the subscript *Ref* to the virtual reference satellite. Modified equinoctial parameters $\boldsymbol{\mathcal{E}_{eq}}$ are singularity free and formally defined as

$$\begin{aligned}\boldsymbol{\mathcal{E}_{eq}} = \Bigg(a,\ P_1 = e\ \sin(\omega+\Omega),\ P_2 = e\ \cos(\omega+\Omega),\ Q_1 = \tan\left(\frac{i}{2}\right)\ \sin(\Omega),\\ Q_2 = \tan\left(\frac{i}{2}\right)\ \cos(\Omega),\ l = \omega+\Omega+M\Bigg)^T\end{aligned} \tag{8.11}$$

Here, the Keplerian elements $\boldsymbol{\mathcal{E}} = (a, e, i, \Omega, \omega, M)^T$ are the semi-major axis a, the eccentricity e, the inclination i, the right ascension of the ascending node (RAAN) Ω, the argument of perigee ω and the mean anomaly M. Modified equinoctial elements are particularly suitable for trajectory analysis and optimization. Also, they are valid for circular, elliptic, and hyperbolic orbits, exhibiting no singularity for zero eccentricity and orbital inclinations equal to 0 ° and 90 °. The dynamics equations governing the problem are comprised of a set of fourteen equations involving both absolute and relative modified equinoctial orbital elements as well as the rotation of the satellite around the respective axis. This decision to propagate both absolute and relative elements is motivated by the necessity to integrate a high-fidelity density model, such as the NRLMSISE-00 [125], requiring the latitude and longitude evaluation of the satellite at each instant of time. So, the absolute parameters are required for the integration of the problem with high-fidelity density models while the optimal collision avoidance problem is addressed employing the relative formulation.

The relative motion dynamics is modeled using the linearized equations presented by Dell'Elce [131]:

$$\delta\dot{\boldsymbol{\mathcal{E}}}_{eq} = [\boldsymbol{A}(\boldsymbol{\mathcal{E}}_{eq,Ref}, \boldsymbol{f}_{D,Ref})]\delta\boldsymbol{\mathcal{E}}_{eq} + [\boldsymbol{B}(\boldsymbol{\mathcal{E}}_{eq,Ref}, \boldsymbol{f}_{D,Ref})]\Delta\boldsymbol{f}_D \tag{8.12}$$

where $[\boldsymbol{A}(\boldsymbol{\mathcal{E}}_{eq,Ref}, \boldsymbol{f}_{p,Ref})]$ and $[\boldsymbol{B}(\boldsymbol{\mathcal{E}}_{eq,Ref}, \boldsymbol{f}_{D,Ref})]$ are the Jacobian of the Gaussian variation of parameter equations (GVE) with respect to $\boldsymbol{\mathcal{E}}_{eq,Ref}$ and to the perturbing force $\boldsymbol{f}_{D,Ref}$, respectively. $\boldsymbol{\mathcal{E}}_{eq,Ref}$ denotes the modified equinoctial elements of the virtual reference satellite and $\boldsymbol{f}_{D,Ref}$ the specific aerodynamic force acting on it. The respective entries of $[\boldsymbol{A}(\boldsymbol{\mathcal{E}}_{eq,Ref}, \boldsymbol{f}_{D,Ref})]$ and $[\boldsymbol{B}(\boldsymbol{\mathcal{E}}_{eq,Ref}, \boldsymbol{f}_{D,Ref})]$ can be found in Ref. [131]. $\Delta\boldsymbol{f}_D$ is the difference in the specific aerodynamic drag forces between the satellites calculated via

$$\Delta\boldsymbol{f}_D = \boldsymbol{f}_{D,Sat} - \boldsymbol{f}_{D,Ref} \tag{8.13}$$

expressed in the local-vertical/local-horizontal (LVLH) coordinate frame. In contrast to the analytical approach, the density ρ is determined dynamically via the NRLMSISE-00 model [125], representing a more realistic consideration. The inverse ballistic coefficient β^* is determined as a function of the angle of attack α via the fitting of the data from 8.3. For the absolute motion of the virtual reference satellite, Gauss variational equations (GVE) in terms of modified equinoctial elements are employed [132]:

$$\begin{aligned}
\frac{da}{dt} &= \frac{2a^2}{h}\left[(P_2 \sin L - P_1 \cos L)\, f_{p,r} + \frac{p}{r}\, f_{p,t}\right] \\
\frac{dP_1}{dt} &= \frac{r}{h}\left[-\frac{p}{r}\cos L f_{p,r} + \left(P_1 + \left(1 + \frac{p}{r}\right)\sin L\right) f_{p,t} - P_2\left(Q_1 \cos L - Q_2 \sin L\right) f_{p,h}\right] \\
\frac{dP_2}{dt} &= \frac{r}{h}\left[\frac{p}{r}\sin L f_{p,r} + \left(P_2 + \left(1 + \frac{p}{r}\right)\cos L\right) f_{p,t} + P_1\left(Q_1 \cos L - Q_2 \sin L\right) f_{p,h}\right] \\
\frac{dQ_1}{dt} &= \frac{r}{2h}\left(1 + Q_1^2 + Q_2^2\right)\sin L f_{p,h} \\
\frac{dQ_2}{dt} &= \frac{r}{2h}\left(1 + Q_1^2 + Q_2^2\right)\cos L f_{p,h} \\
\frac{dl}{dt} &= n - \frac{r}{h}\left\{\left[\frac{a}{a+b}\left(\frac{p}{r}\right)(P_1 \sin L + P_2 \cos L) + \frac{2b}{a}\right]\ f_{p,r} \ \ldots\right. \\
&\ldots + \frac{a}{a+b}\left(1 + \frac{p}{r}\right)(P_1 \cos L - P_2 \sin L)\ \ f_{p,t} \ \ldots \\
&\left.\ldots + (Q_1 \cos L - Q_2 \sin L)\ \ f_{p,h}\right\}
\end{aligned} \tag{8.14}$$

A simplified rotational dynamics of the spacecraft around its y_{BF} - axis is integrated to obtain a smooth and realistic pitch angle profile $\theta(t)$ which avoids bang-bang type control switches:

$$\ddot{\theta}_{Sat} = I_{Sat,y}^{-1} T_{Sat} \tag{8.15}$$

Here, $I_{Sat,y}$ is the moment of inertia of the satellite around the y_{BF} - axis and $T_{Sat,w}$ is the torque applied to the satellite via its respective attitude control system. The pitch angle is defined with respect to the local-vertical/local-horizontal frame (LVLH). For the sake of simplification, throughout this article the pitch angle θ is used interchangeably with the angle of attack α. In summary, the full state of the control plant is:

$$\begin{bmatrix} \delta\mathcal{E}_{eq} \\ \mathcal{E}_{eq,Sat} \\ \theta_{Sat} \\ \dot{\theta}_{Sat} \end{bmatrix} \tag{8.16}$$

The aerodynamic drag is modulated through a variation of the ballistic coefficient by means of a pitch rotation to satisfy the cost function and the constraints of the problem.

8.1.3 Constraints and cost function

The initial modified equinoctial orbital parameters, as defined in the absolute formulation, represent the initial position of the satellite. Conversely, in the context of the relative formulation, all initial variable values are set to zero, reflecting the initial alignment of the real and virtual satellites. The problem is characterized by the dual objective of minimizing the orbital decay while maximizing the miss distance. It is based on a composed cost function, defined as:

$$J = -\Delta a_{t_f} - W_{\Delta x_{t_f}} \Delta x_{t_f} \tag{8.17}$$

Here, Δa and Δx_{t_f} denote the absolute orbital decay and miss distance, respectively. The absolute orbital decay Δa is defined as the difference between the initial a_{t_0} and the final a_{t_f} semi-major axis:

$$\Delta a_{t_f} = a_{t_f} - a_{t_0}, \tag{8.18}$$

and not to be confused with the (relative) decay δa given in the state vector. The miss distance Δx_{t_f} is approximated via

$$\Delta x_{t_f} = \delta l_{t_f}\, a_{t_0}, \tag{8.19}$$

representing a mean along-track distance between the predicted point of collision and the satellite at TCA. The maneuver time. i.e. the conjunction time t_c , is defined as the time difference between the reception of the collision warning t_0 and the predicted time of closest approach $t_f = t_{TCA}$ and therefore fixed. Throughout the rest of the article, a fixed conjunction time of $t_c = 24\,\mathrm{h}$ is assumed. The weight $W_{\Delta x_{t_f}}$ serves as an adjustable factor, allowing the modulation of the emphasis placed on the respective component of the cost function (the weighting of the additional decay δa is constantly equal to unity). Notably, the orbital decay Δa is per definition (see Equation 8.18) negative, which is why it needs to be considered negative in the cost function (Equation 8.17) in order for its magnitude to be minimized whereas the miss distance Δx_{t_f} is positive for the problem under investigation and consequently needs to be considered positive in the cost function in order to be maximized.

The tunable nature of $W_{\Delta x_{t_f}}$ enables the users to tailor the importance attributed to each aspect of the cost function. For instance, elevated $W_{\Delta x_{t_f}}$ values prioritize the maximization of the miss distance. Thus, through careful adjustment of this weight, the trade-offs involved in the optimization process can effectively be balanced. A proper tuning of the value can be assessed depending on the specific mission scenario and, in particular, the conjunction notice. In the event of an unexpected encounter with an uncooperative and previously unknown spacecraft, the optimal strategy typically involves achieving a desired miss distance in the shortest possible time or maximizing it while fixing the final time as the conjunction time. In such scenarios, a greater emphasis is placed on $W_{\Delta x_{t_f}}$.

$t_{min,analy.}$ (h)	$t_{min,opt.}$ (h)	Δt (h)
7.27	7.37	0.1

Table 8.2: Comparison between the analytically determined maneuver time and the results of the optimal control setup.

$t_{min,opt.}$ (h)	Δx_{t_f} (m)	$\Delta a_{t_f,CAM}$ (m)	$\Delta a_{t_f,REF}$ (m)	δa_{t_f} (m)
7.3747	10000	-78.80	-522.74	-443.94

Table 8.3: Main figures of merit of the verification case.

8.1.4 Validation

In order to validate the optimal control set-up, a test case is run in which a time-optimal solution is determined and compared to the analytical solution presented by Omar and Bevilacqua [54] (see Equation 8.9). This approach ensures, on the one hand, that the simulation infrastructure works adequately and, on the other hand, makes it clear that the starting point of this study is the current state of research. The test is defined such that the optimal control aims to find the optimal maneuver to accomplish a miss distance $\Delta x_{t_f} = 10000$ m in a minimum amount of time $t_{min,opt.}$. In order to make the two test cases comparable, a constant density value of $\bar{\rho} = 4.5 \times 10^{-12}\,\mathrm{kg\,m^{-3}}$ is used for the verification case (in contrast to the dynamically varying density used later on) and the co-rotation of the atmosphere as well as thermospheric winds are neglected. The resulting maneuver times are listed in Table 8.2, the main figures of merit for the maneuver listed in Table 8.2 and the results plotted in Figure 8.4. Here, it can be seen that the resulting angle of attack α profile resembles the well-known bang-bang solution for a time-optimal case. The deviations in the determined maneuver times of 0.1 h can be led back to the fact that for the optimal-solution, the maximum rotational velocity is restricted to $\dot{\theta}_{Sat} = 0.1\,^{\circ}\,\mathrm{s^{-1}}$ to bypass the unrealistic assumption of an instantaneous rotation. Consequently, the resulting time for the optimal maneuver is slightly longer than for the analytical test case.

8.1.5 Results

This section discusses the main results of the optimal control algorithm for collision avoidance. Firstly, it is applied to a reference scenario, which is discussed in detail. Subsequently, a parametric analysis has been performed to investigate the influence of a variation in the weighting factor $W_{\Delta x}$ on the solution.

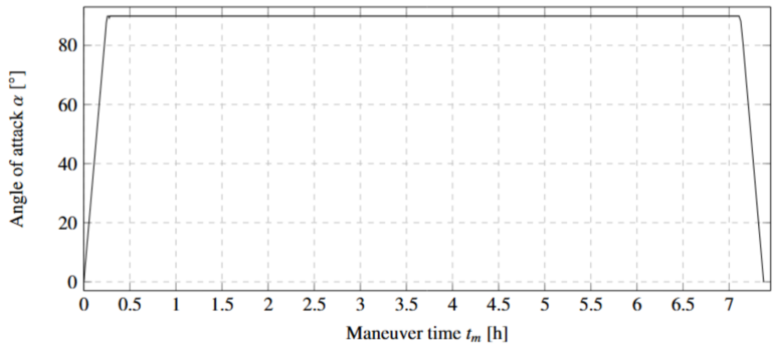

(a)

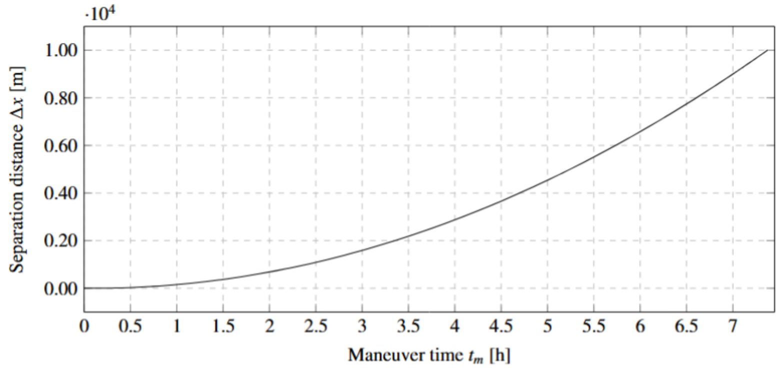

(b)

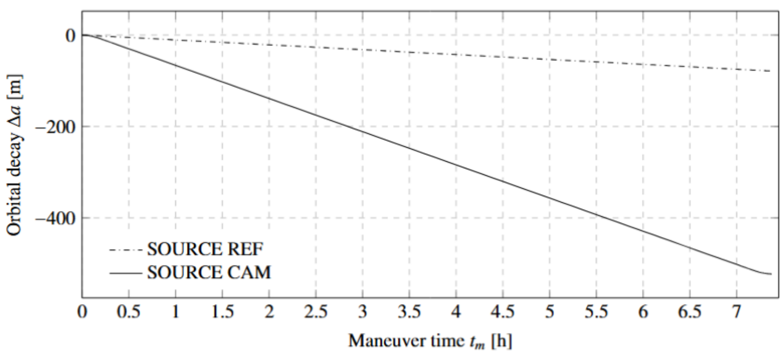

(c)

Figure 8.4: Results of the verification case: time-optimal establishment of a miss distance of $\Delta x_{t_f} = 10000$ m

$W_{\Delta x_{t_f}}$ (−)	Δx_{t_f} (m)	$\Delta a_{t_f,CAM}$ (m)	$\Delta a_{t_f,REF}$ (m)	δa_{t_f} (m)
0.008	22300.6	-354.8	-189.9	-164.9

Table 8.4: Main results of the reference scenario.

Reference scenario

This subsection describes the optimal collision avoidance algorithm application to the SOURCE satellite previously described and considering the initial conditions in Table 8.1. A situation with a conjunction time of $t_c = 24\,\mathrm{h}$ is analyzed considering the following weight of the cost function: $W_{\Delta x_{t_f}} = 0.008$. Figure 8.5 shows the main results, in terms of angle of attack α profile, the separation distance Δx, and the orbital decay Δa whereas Table 8.4 lists the main figures of merit.

Due to the different boundary conditions (fixed time) as well as cost function, the angle of attack profile completely differs from the result of the validation case. While it still exhibits a bang-bang profile, the maximum value is commanded only for the first hours of the maneuver. Then, it is switched back to the nominal configuration which is held constant. The reason for this profile becomes obvious when comparing the profile of the separation distance and the orbital decay with their respective counterparts of the validation case. During the first two hours, additional decay is required in order to establish a secular in-plane drift. Accumulated over time, this drift results in the miss distance at TCA. However, with the mixed cost function from Equation 8.17, not a maximum miss distance is sought but a well balanced mix between the additional decay and the final miss distance. Consequently, the SOURCE satellite rotates back into its minimal drag configuration to passively drift for the rest of the maneuver time. As a consequence of this, the separation distance is characterized by an initial parabolic trend covering the maximum angle of attack time frame, evolving then to a linearly increasing trend with a final value of around 22300.6 m. The orbital decay is characterized by a natural decreasing trend due to the drag (the curve SOURCE REF in Figure 8.5). The execution of the maneuver results in an additional contribution to the orbital decay, affecting the overall time profile (the curve SOURCE CAM in Figure 8.5). The part of the maneuver correspondent to the maximum ballistic coefficient is characterized by a decreasing linear trend of orbital decay, followed by a linear profile practically parallel to the one characterizing the natural orbital decay. In the second phase of the maneuver, characterized by a minimum surface area, the orbital decay consists of the natural decay in the reference configuration plus a constant contribution due to the maneuver. As a result of the well-balanced cost function, the amount of the additional orbital decay is limited to 165 m which is significantly lower than the resulting decay of the verification case 443.94 m even though the maneuver duration is longer ($t_{man.} = 24$ hour vs. 7.37 hour) and the resulting miss distance larger ($\Delta x_{t_f} = 22\,300.6\,\mathrm{m}$ vs. $10\,000\,\mathrm{m}$).

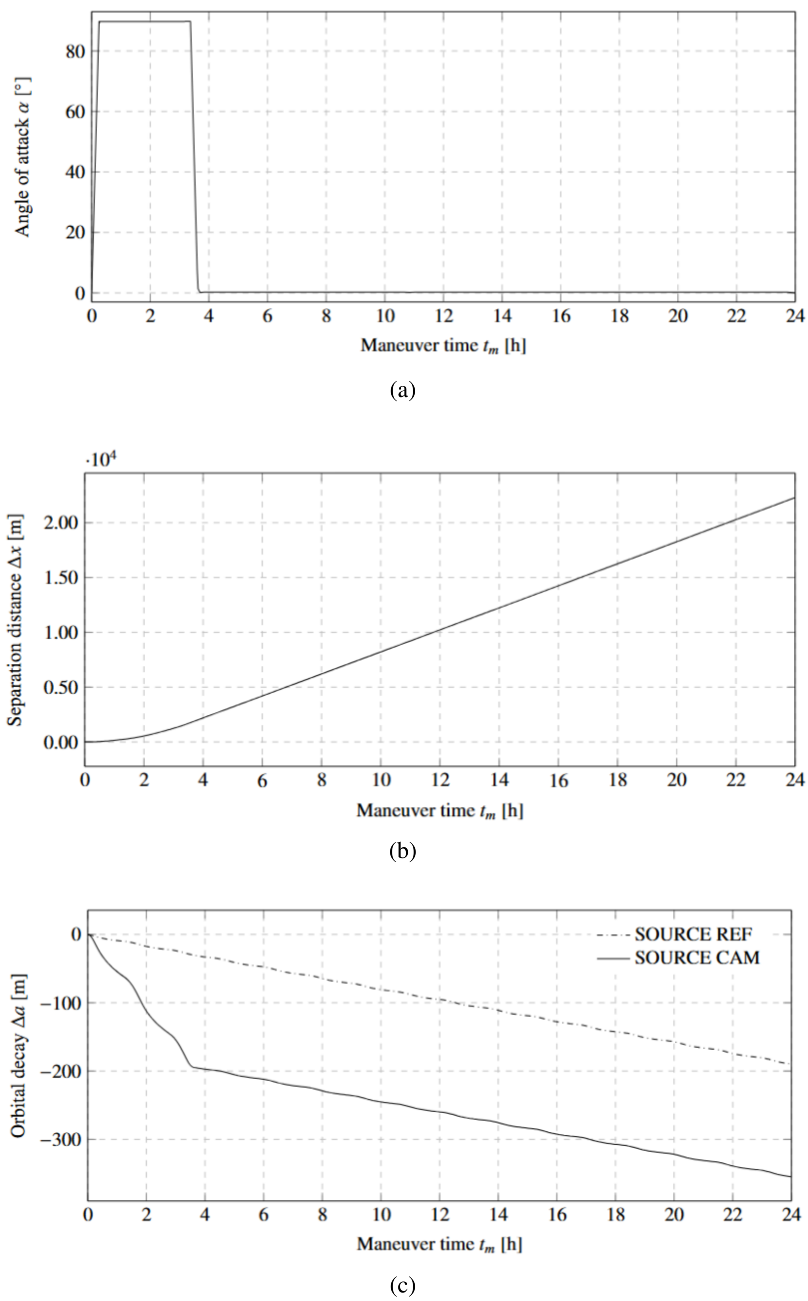

Figure 8.5: Results of the reference case ($W_{\Delta x_{t_f}} = 0.008$).

Parameter study

In order to analyze the sensitivity of the optimal control solution to the respective cost function, a parametric investigation in which $W_{\Delta x_{t_f}}$ was varied within the range of 0.007375 to 0.008500 was conducted. The main figures of merit for this study are summarized in Table 8.5. The evaluation of the additional contribution of orbital decay and miss distance in the different cases resulted in the trends depicted in Figure 8.6. Increasing values of $W_{\Delta x_{t_f}}$ reflect in increasing values of miss distance and, subsequently, orbital decay as the two elements are correlated. For the selected weighting parameter variation range of $W_{\Delta x_{t_f}} \in (0.007375; 0.008500)$, a variation in the resulting in-track separation distance Δx_{t_f} from 11 341.8 m to 28 137.1 m resulted. This represents an increase by almost a factor of three. At the same time, the amount of the additional decay δa_{t_f} increased from 80.7 m to 213.0 m. These results underlines the importance of a proper assessment of the weighting factor to the specific problem at handy to ensure a balance between orbital decay and miss distance given the high sensitivity of the solution on even small variations of $W_{\Delta x_{t_f}}$. For cases characterized by low conjunction notice, the priority is the maximization of the miss distance so greater values of $W_{\Delta x_{t_f}}$ will be considered. In these cases, the optimal control will be characterized by maximum angle of attack for a greater amount of time. This will result in a more important entity of additional decay, which has to be accepted given the limited timescale of the problem. Due to the simple linear relationship between the additional decay and the miss distance (see Figure 8.6), these results can and should also serve the entire community as a reference for future maneuver designs.

No.	$W_{\Delta x_{t_f}}$ $(-)$	Δx_{t_f} (m)	$\Delta a_{t_f,CAM}$ (m)	$\Delta a_{t_f,REF}$ (m)	δa_{t_f} (m)	$\Delta\delta a_{t_f}$ (%) w.r.t. 6)
1.)	0.007375	11341.8	-270.6	-189.9	-80.7	-51.1
2.)	0.007500	14256.5	-292.1	-189.9	-102.2	-38.0
3.)	0.007625	15994.7	-305.4	-189.9	-115.5	-30.0
4.)	0.007750	17294.2	-315.3	-189.9	-125.4	-24.0
5.)	0.007875	19480.8	-332.5	-189.9	-142.6	-13.5
6.)	0.008000	22300.6	-354.8	-189.9	-164.9	0
7.)	0.008125	24076.3	-369.1	-189.9	-179.2	8.7
8.)	0.008250	25319.7	-379.3	-189.9	-189.4	14.9
9.)	0.008375	26334.6	-387.7	-189.9	-197.8	20.0
10.)	0.008500	28137.1	-402.9	-189.9	-213.0	29.2

Table 8.5: Main results of merit of the parameter study.

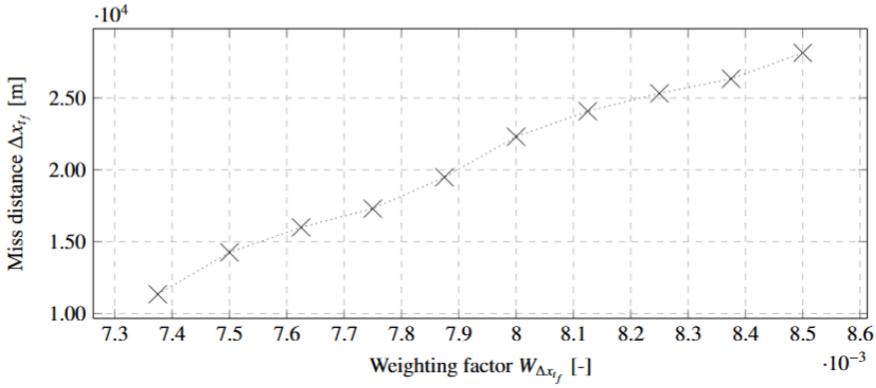

(a)

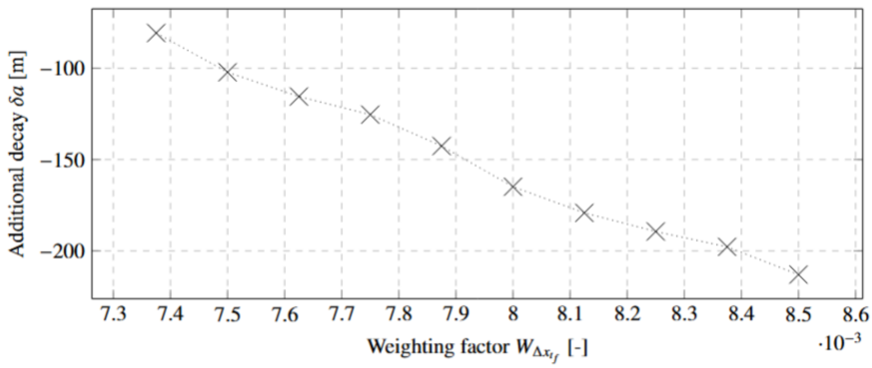

(b)

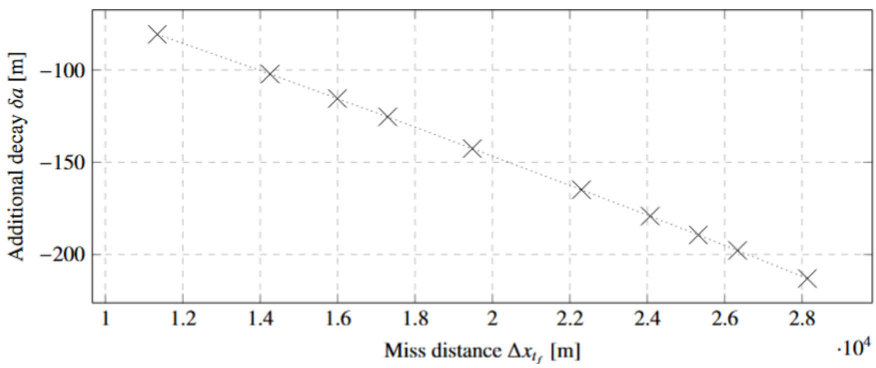

(c)

Figure 8.6: Main variables profiles as function of $W_{\Delta x_{t_f}}$ in the parametric analysis.

8.2 Approach based on Deep Neural Networks

While the optimal control methodology generated very promising results, the maneuver optimization requires a high computational effort and is therefore not suitable for real-time decisions onboard satellites. These reasons motivated the investigation of an alternative approach to enhance the algorithm from [73], making it more suitable for realistic applications by reducing the computational cost while maintaining a good level of accuracy. The proposed solution leverages DNNs to predict the optimal control profile based on initial conditions, a methodology which has been successfully applied for de-orbiting [68, 69].

8.2.1 General structure of the control profile

The angle of attack profile for optimal collision avoidance via aerodynamic drag is characterized by its bang-bang nature (see Figure 8.7a), with the key points identified as t_0 - t_4. The resulting profile can be separated in the following five segments:

- At t_0, the angle of attack is zero ($\alpha_{t_0} = 0°$).
- The angle of attack increases sharply in the time interval between t_0 and t_1. Unlike the vertical line characteristic of a typical bang-bang profile, the slight inclination is a result of the optimizer constraining the rotational velocity of the spacecraft to adhere to its realistic limits.
- Between t_1 and t_2, the angle of attack profile is characterized by a constant maximum value depending on the specific problem.
- At t_2, the angle of attack begins to decrease rapidly until t_3.
- From t_3 to t_4, the angle of attack remains constant at $\alpha = 0°$.

For the present prediction through DNNs, the following simplified hypotheses will be considered:

- Infinite rotation rate: It will be assumed that t_1 coincides with t_0 and t_3 coincides with t_2. These times will be respectively defined as t_0 (corresponding to $t_0 = 0$ s) and t_{switch}. Thus, the slightly inclined lines are treated as perfectly vertical, which corresponds to the assumption that the spacecraft can rotate instantaneously. The latter is schematically displayed in Figure 8.7b.
- Exponential density profile: Although the optimal control algorithm is valid for the high fidelity NRLMSISE-00, the optimal control solutions are generated using an exponential model to estimate the density value, which is then held constant throughout the maneuver. This choice was made due to the significantly higher computational cost associated with generating solutions using the NRLMSISE-00 model, which is impractical for creating a sufficiently large training set.
- Limited element variation: The initial altitude is the only equinoctial element varied in the initial conditions for the training set generation. This approach is motivated by the fact that 1) the density model used is not position-dependent, such as NRLMSISE-00 model and 2) in the case of aerodynamic drag control, the altitude is the dominant factor of influence.

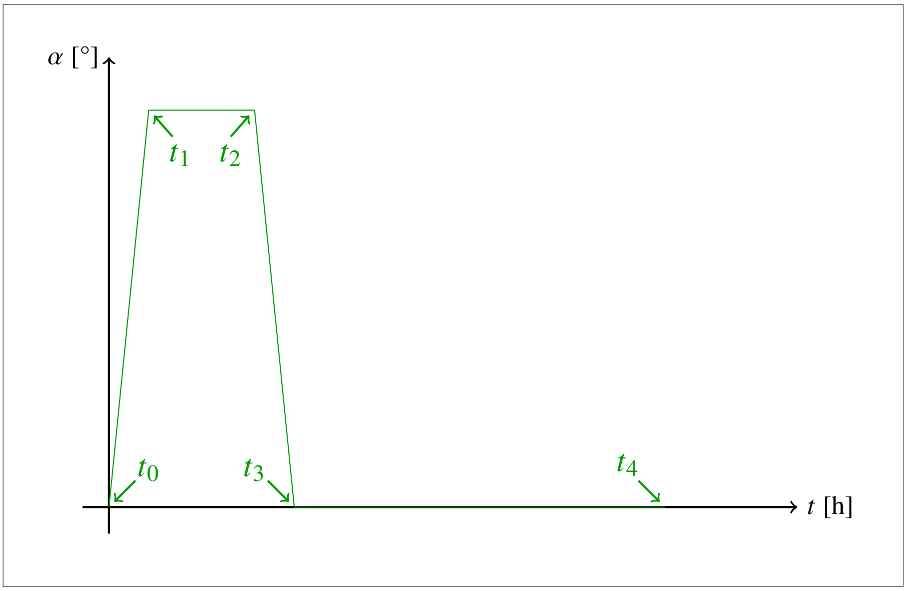

(a)

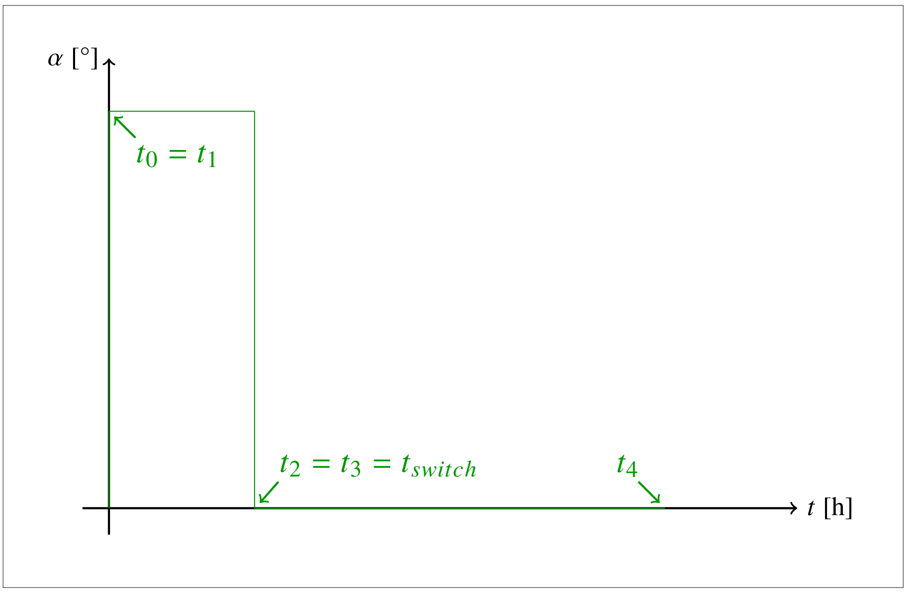

(b)

Figure 8.7: Schematics of a real (a) and a simplified (b) optimal angle of attack profile.

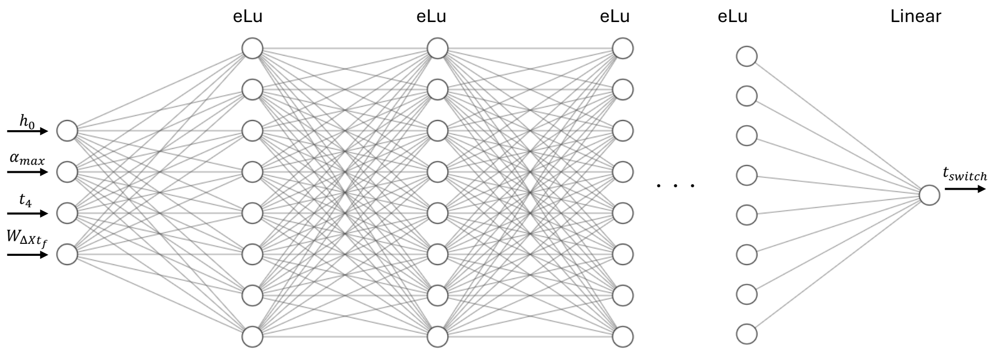

Figure 8.8: Graphical visualization of the DNN design.

The final problem involves the prediction of t_{switch}, given that t_0 is considered 0 s in any case and that the final time t_4 is a known parameter. To achieve this, a DNN with the following four inputs is employed:

1. Initial altitude h_{t_0}
2. Maximum value of the control variable (i.e. maximum angle of attack α_{max})
3. Final time t_f (i.e. the conjunction notice)
4. Weighting factor $W_{\Delta x_{t_f}}$ (Equation 8.17).

After predicting the t_{switch}, the final control law is refined to better reflect the realistic constraints by incorporating a finite rotation rate $|\dot{\alpha}_{max}|$. The respective value can be defined to the problem under investigation by the user. This adjustment brings the theoretical control law closer to a feasible realistic solution, making it more consistent with the practical rotational capabilities of the satellite and closer to an ideal control profile.

8.2.2 Deep Neural Network design and training set

Deep Neural Network design

The input layer of the DNN consists of four neurons, while the output layer contains a single neuron to predict t_{switch}. The DNN is constituted by five hidden layers with fifteen neurons each (see Figure 8.8). For the input and hidden layers a eLu activation function was chosen, leaving room to a linear activation function for the output layer.

Parameter	Value
Learning rate	0.0001
Number of epochs	1000
Batch size	2
Optimizer	Adam

Table 8.6: Summary of the parameters used for the training process for the optimal collision avoidance.

Training set and process

The training set consists of 350 samples, organized in a table with the first four columns representing the inputs and the fifth column representing the output to be predicted (the switching time). Despite the small dataset, the Neural Networks can learn complex patterns and make accurate and general predictions. The implementation of the architecture and the subsequent training process has been performed in the python programming language with Anaconda Navigator. The loss to minimize is the mean square error between the optimal and the predicted switching time. Adam is employed as optimizer. The training process considered a learning rate of 0.0001, a batch size of two and a total of 1000 epochs. Table 8.6 summarizes the main parameters.

Figure 8.9 illustrates the flowchart for the proposed DNN-based guidance algorithm, emphasizing the different steps involved.

8.2.3 Results

This section provides a comprehensive analysis of the results obtained from the proposed guidance algorithm based on DNNs. Firstly, the guidance algorithm is applied to a case study, where its performance is directly compared with the optimal control solution. Subsequently, a Monte Carlo analysis is performed to assess the robustness of the algorithm across a wide range of conditions.

Case study

This section discusses the application of the DNN-based algorithm to a case study, whose initial conditions are summarized in Table 8.7. In Figure 8.10, the angle of attack profile predicted by the proposed DNN-based guidance algorithm is compared with the optimal control solution [72, 73]. For the given case, the finite rotation rate was set to $|\dot{\alpha}_{max}| = 0.25\,^\circ\,\mathrm{s}^{-1}$, which corresponds to achieving a full rotation from $\alpha_{min} = 0°$ to $\alpha_{max} = 90°$ within 15 minutes. The DNN exhibits a high degree of accuracy and negligible error, closely aligning with the optimal solution, as in Figure 8.10.

The solution predicted with DNNs was subsequently propagated using the same models that generated the training data set to assess the impact of the switching time error on the states of the spacecraft. Figure 8.11 reports the miss distance and orbital decay profiles for both the optimal control case and DNN-based propagated case, with the errors summarized in Table 8.8. The propagation resulted in a final miss distance exhibiting a linear increasing trend, in line with the optimal solution. The slight increase in the final miss distance value (error of 1.11 %) can be attributed to the slight differences in the control profiles between the DNN-based and the optimal solutions. Consequently, this variation leads to a slightly higher relative orbital decay for the

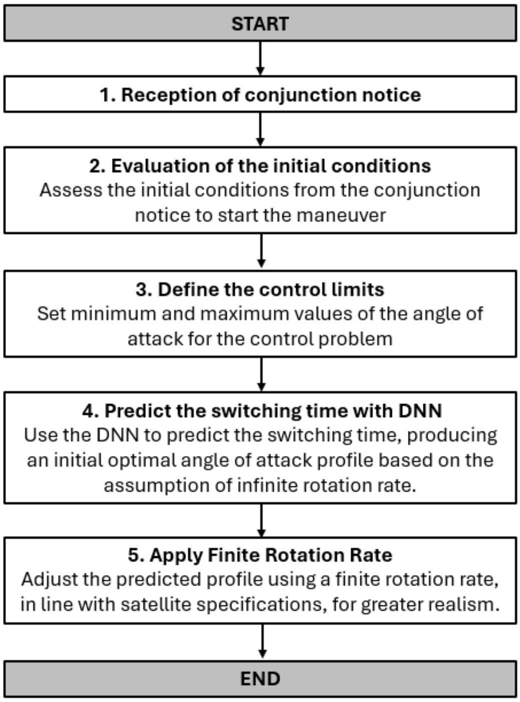

Figure 8.9: Flowchart of the proposed DNN-based guidance algorithm for optimal collision avoidance.

Parameter	Symbol	Value
Semi-major axis	a	6778.137 km
Eccentricity	e	0.001
Inclination	i	45°
RAAN	Ω	0°
Argument of perigee	ω	0°
True anomaly	θ	0°
Maximum angle of attack	α_{max}	90°
Final time	t_f	24 h
Weighting factor	$W_{\Delta x_{t_f}}$	0.007578713

Table 8.7: Initial condition and parameters for the reference case study.

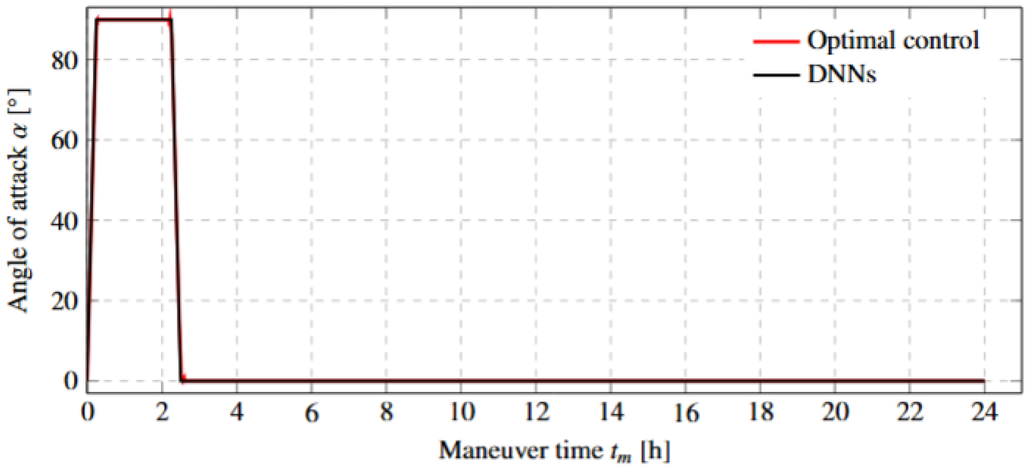

Figure 8.10: Angle of attack α profile over maneuver time t_m predicted by the DNN (black) and the optimal control approach (red).

Case	$\Delta x(t_f)$	Error (%)	$\delta a(t_f)$	Error (%)
Optimal solution	10576	-	-80.9	-
DNN predicted solution	10695	1.12	-81.8	1.11

Table 8.8: Results of the case study.

DNN-based solution (error of 1.12 %). This demonstrates that deviations in the optimal control law prediction do not lead to large errors in the states of the spacecraft, thereby confirming excellent performance and robustness.

Monte Carlo analysis

A conclusive Monte Carlo analysis has been performed to assess the effectiveness and robustness of the proposed DNN-based algorithm in a wide range of conditions. To the aim, a total number of 250 different initial conditions within the ranges specified in Table 8.9 have been considered. In all cases, the switching time has been predicted and compared with the correspondent optimal value.

Figure 8.12 indicates the distribution of the absolute difference between the optimal switching time and the one predicted with the proposed DNN-based algorithm for all 250 samples. It can be

Parameter	Range	Distribution
Altitude	[350 km; 500 km]	Uniform
Weighting factor	[0.007; 0.008]	Uniform
Final time	[16 h; 32 h]	Uniform

Table 8.9: Distribution of initial conditions for the Monte Carlo analysis.

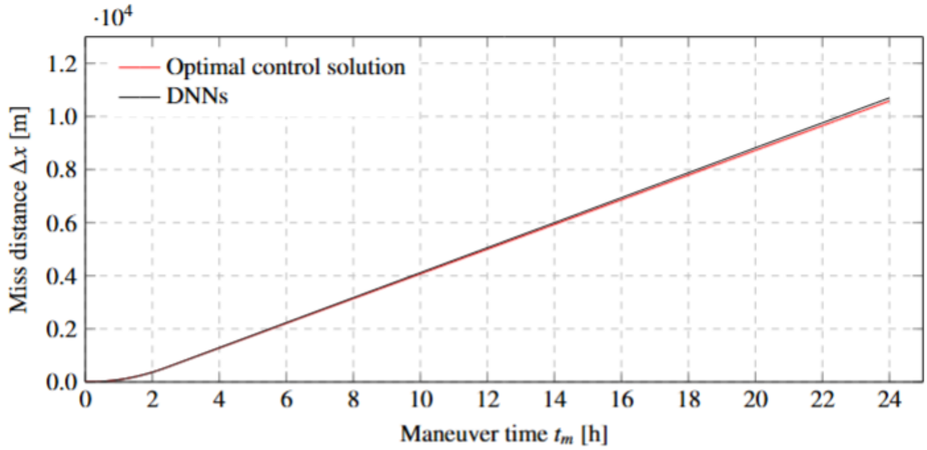

(a)

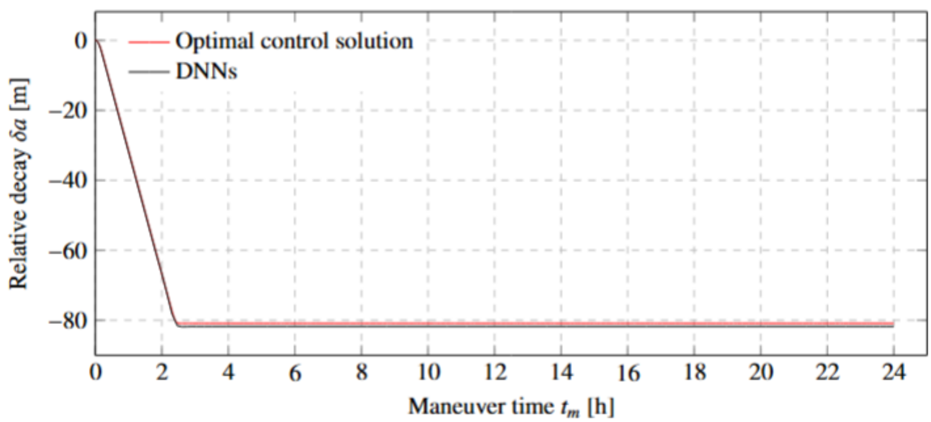

(b)

Figure 8.11: Nominal case results: comparison between optimal control solution (red) and DNN-based solution (black).

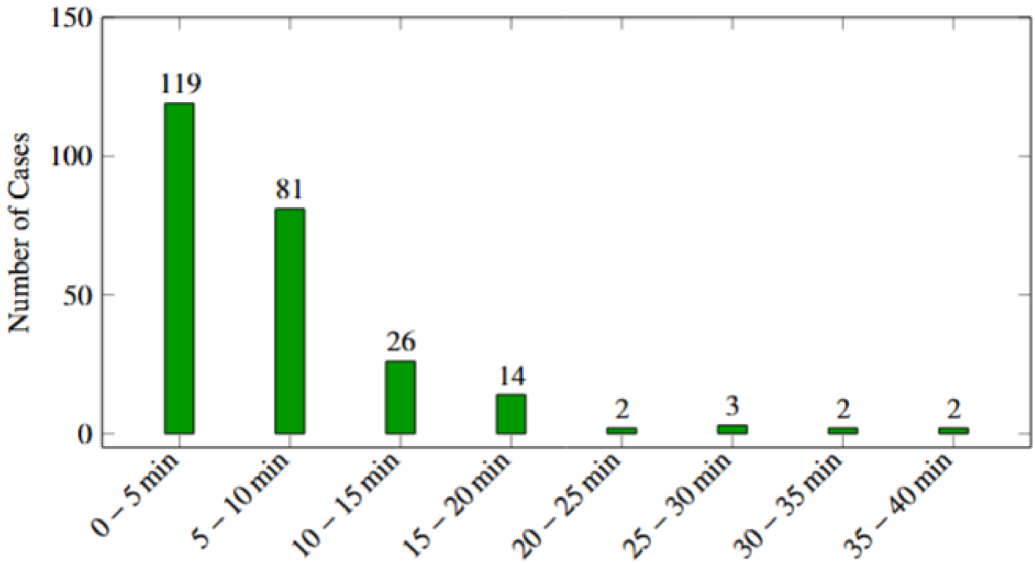

Figure 8.12: Distribution of the absolute error of the predicted switching time.

seen that in 96 % of the cases, the predictions are within an error of less than 20 min with the highest number of cases (80 %) occurring even in the range of below 10 min. These findings substantiate the statement that the case study represents by no means an particularly suitable individual case and that in a large number of cases the results fit even better. Once the DNN is trained, the computational cost to predict a single solution is on the order of a few seconds, in contrast to the minutes required by the optimal control algorithm. This clearly highlights the computational savings provided by the DNN-based approach.

8.2.4 Iterative feedback control algorithm

The proposed AI-based guidance algorithm has been trained and tested using exponential density and a low-fidelity aerodynamic panel method. Consequently, discrepancies and suboptimal performance arise when faced with unpredictable perturbations and high-fidelity models. This section introduces an iterative method to adapt the predicted optimal control laws, enhancing robustness and minimizing performance loss in high-fidelity scenarios.

Parameter	Unit	Value
h	km	300
ρ	$\mathrm{kg\,m^{-3}}$	1.84×10^{-11}
T	K	874.05
P	Pa	7.62×10^{-6}
v	$\mathrm{m\,s^{-1}}$	7730
n_{tot}	-	6.31×10^{14}
O	%	87.3
N_2	%	12.3
O_2	%	0.4

Table 8.10: Atmospheric conditions at 300 km altitude.

Performance of the guidance algorithm in off-nominal conditions

The optimal control profile predicted using an exponential density model was further propagated through a high-fidelity model for both atmospheric density and aerodynamics. This allowed for performance evaluation under off-nominal conditions and assessment of a possible parameter that can be modulated to adapt the profiles accordingly. The high-fidelity density model integrates the horizontal thermospheric wind via the Horizontal Wind Model [124] and a dynamically varying density profile from the NRLMSISE-00 model [125]. To examine the atmospheric interactions with the satellite surface, the DSMC method [133] was employed for a refined aerodynamic assessment. The free-stream conditions were derived from the NRLMSISE-00 model at an altitude of 300 km, assuming a solar flux of $F10.7 = F10.7_{\text{avg}} = 140$ sfu and a geomagnetic index of $Ap = 15$ (Table 8.10).

The flow velocity is given by:

$$v = \sqrt{\frac{\mu}{r}} \tag{8.20}$$

where μ is the gravitational constant of the Earth, and r is the circular orbital radius, defined as the sum of Earth's radius and the orbital altitude.

The satellite surface is assumed to be isothermal at $T_w = 300$ K. The computational domain ($1\ \mathrm{m}^3$) was defined with free-stream conditions from Table 8.10. A multi-level mesh was used, with refinement near the satellite surface. The timestep was set to 8.5×10^{-8} s, ensuring approximately 30 particles per cell for statistical reliability. The final mesh contained 114000 cells and simulated 3×10^6 molecules. The Maxwell Gas-Surface Interaction model was used to evaluate satellite drag and lift, with an accommodation coefficient of $\alpha_{acc} = 1$, indicating fully diffuse particle re-emission. Simulations were conducted for angles of attack in the range [0°, 90°] with 15° increments. Figure 8.13 presents the resulting drag and lift coefficients, using the maximum cross-sectional area at 90° as the reference. As expected, lift is significantly lower than drag and can be considered negligible in this study.

Based on these high-fidelity models, different analyses have been performed with different weighting factors, as illustrated in Figure 8.14.

The propagation within the high-fidelity models introduce significant discrepancies in miss distance (Δx) and relative decay (δa). These deviations emphasize the strong influence of complex

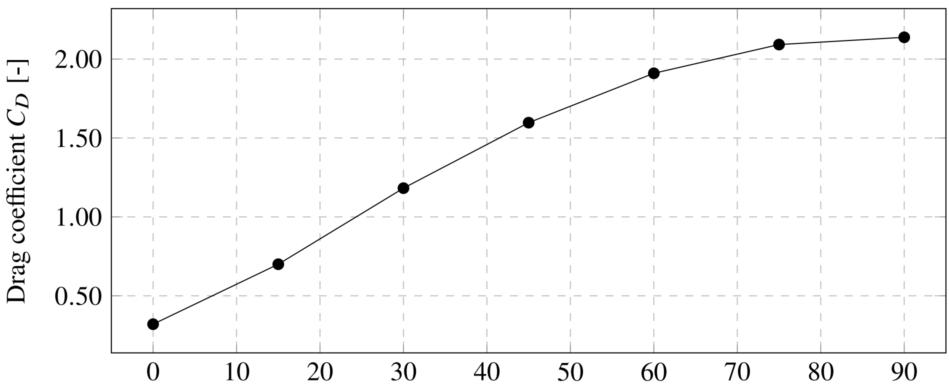

(a)

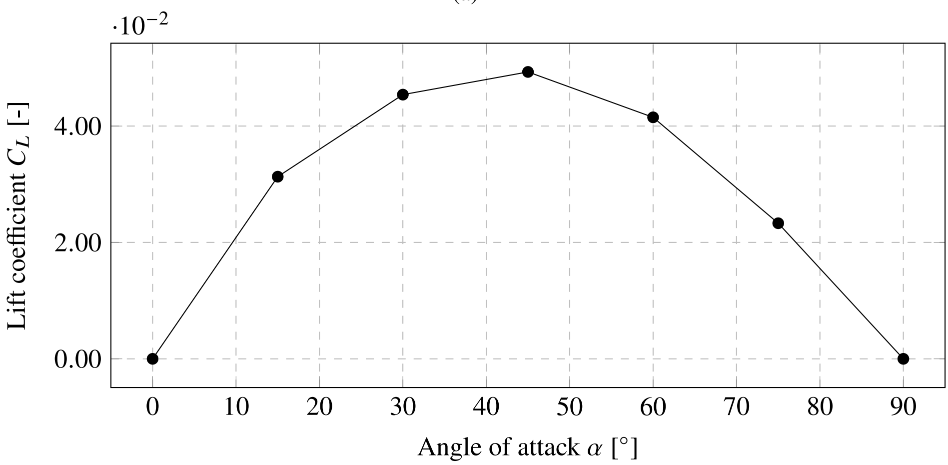

(b)

Figure 8.13: Drag (a) and lift (b) coefficients as functions of angle of attack α for the SOURCE satellite using DSMC.

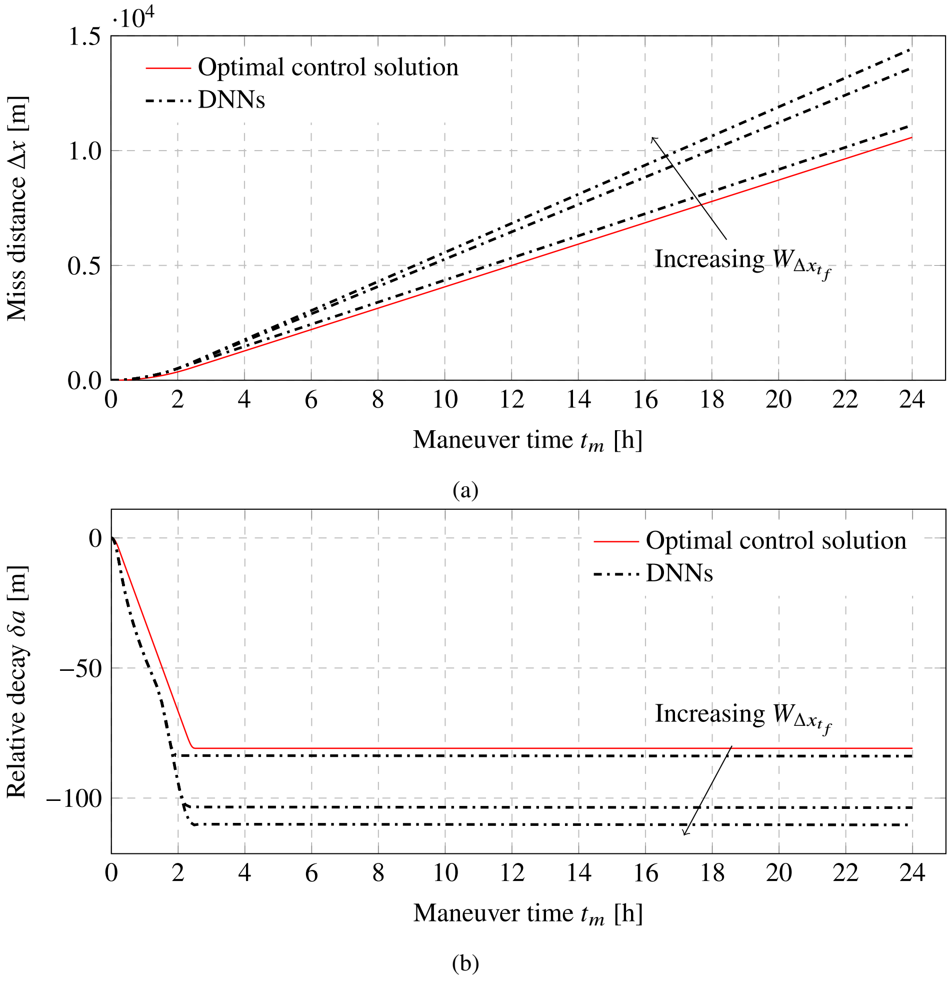

Figure 8.14: High-fidelity model: comparison between optimal control solution (red) and DNN-based solutions for different weighting factors (black).

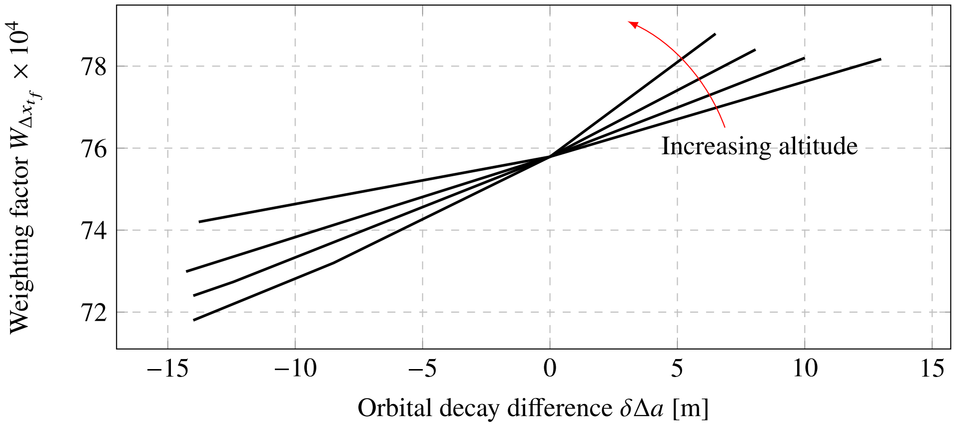

Figure 8.15: Weighting factor as function of the orbital decay difference for t = 1.2 days.

atmospheric phenomena. To mitigate these discrepancies, the weighting factor $W_{\Delta x_{t_f}}$ can be tuned. Proper adjustment enhances the predictive accuracy of the DNN-based solutions, aligning them more closely with the optimal control solution. As shown in Figure 8.14, once refined and propagated through the high-fidelity atmospheric model, the DNN-based solutions exhibit reduced deviations, demonstrating that tuning weighting factors effectively compensates for atmospheric fluctuations and perturbations.

Iterative control method

Based on the results, a method for automating the estimation of the weighting factor is proposed. This method evaluates the difference between the real-time orbital decay and the reference profile $\Delta(\delta a)$. Initially, different cases with varying perturbation levels are considered, leading to different deviations in the orbital decay compared to the nominal profile at the same time instant. The time instant is fixed at $t = 1.2$ days. For each case, the weighting factor used to update the control law is plotted as a function of the orbital decay difference at that specific time (see Figure 8.15). This analysis has been conducted for different initial altitude values to assess their impact, as altitude is the primary factor directly influencing atmospheric density.

The trend follows a parabolic path and rotates counterclockwise as altitude increases, as indicated by the arrow. This pattern allows for a generalized extrapolation of the orbital decay differences across a broad range of altitudes. Once the updated weighting factor is estimated, the trained DNN is employed to predict the corresponding time for updating the control profile. In the present study, this process is applied specifically at $t = 1.2$ days, although it can be utilized at any time instance selected by the user. The iterative procedure for updating the profiles is summarized in the following steps:

1. Define the initial conditions, depending on the real state of the satellite, and predict the control profile using the DNN to obtain the orbital decay profile under nominal conditions.

2. Compare the current satellite state with the nominal state and use the parabolic trends to extrapolate the updated weighting factor based on the difference of the orbital decay and initial altitude.

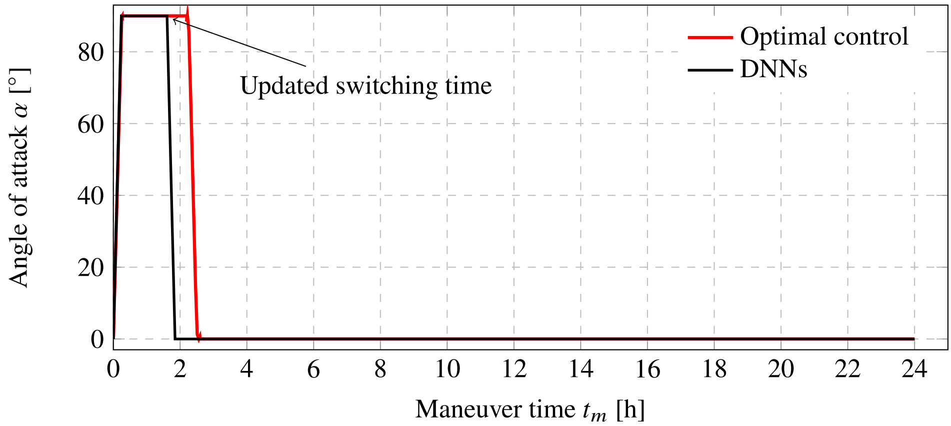

Figure 8.16: Comparison between the nominal optimal control law and the updated one.

3. Use the DNN to predict the new switching time corresponding to the updated weighting factor.

4. Update the control profile based on the prediction of the DNN.

8.2.5 Results

The proposed iterative procedure has been applied to the case in Table 8.7 using a high-fidelity aerodynamic model, implemented via DSMC just described (Figure 8.13), alongside the NRLMSISE-00 density model. A random component was added to the density to account for the unpredictable elements of the system. At this point the control algorithm has been applied to the case study with the following steps:

1. The difference between the ideal and real orbital decay at $t = 1.2$ days is -13.4205 m.

2. Based on the initial altitude and this orbital decay difference, the parabolic trends shown in Figure 8.15 have been employed to extrapolate the updated weighting factor, resulting in a value of 0.00727851.

3. The trained DNN has been used to predict the updated switching time, which is found to be 110.88 minutes.

4. The optimal control law is then updated based on the new switching time.

Figure 8.16 compares the nominal optimal control law with the updated one predicted after applying the control procedure. Additionally, in Figure 8.17 the orbital decay and miss distance are shown. Table 8.11 provides a summary of the main parameters in both the controlled and uncontrolled cases.

The application of this procedure leads to enhanced performance with minimal loss of optimality compared to the uncontrolled case, significantly reducing the final error in both miss distance and orbital decay. Moreover, it ensures only a limited loss of optimality, even in off-nominal and unpredictable scenarios like the one considered here. This analysis also highlighted the impact of a

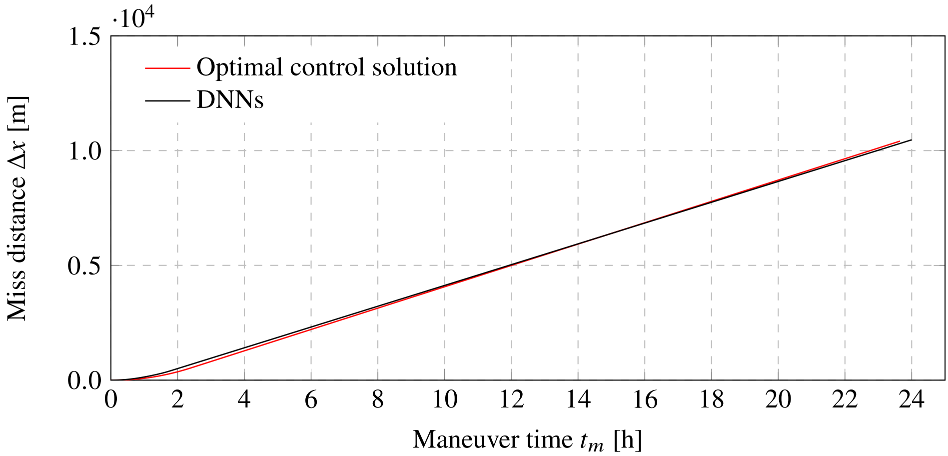

(a)

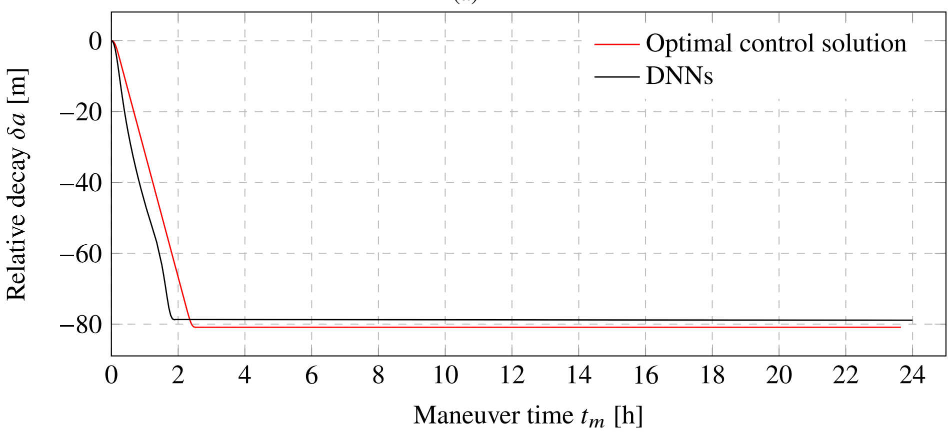

(b)

Figure 8.17: Miss distance and orbital decay profiles for the high-fidelity scenario in the controlled case.

Parameter	Value
Error for orbital decay - uncontrolled	40.5 %
Error for orbital decay - controlled	1.5 %
Error for miss distance - uncontrolled	39.1 %
Error for miss distance - controlled	1 %
Difference of orbital decay at t = 1.2 days	−13.4205 m
Updated switching time - controlled	110.88 min
Updated weighting factor - controlled	0.00727851

Table 8.11: Summary of the parameters for the control process.

high-fidelity aerodynamic model on control system design, emphasizing the strong interconnection between these two aspects when planning a mission in LEO.

Conclusions

This dissertation addressed one of the most pressing challenges in the actual context of space operations in LEO: the development of sustainable, autonomous, and propellantless G&C strategies, particularly tailored for small satellite platforms, such as CubeSats. The main objective was to develop a hybrid framework that combines AI and optimal control theory, using aerodynamic forces in LEO as the primary means for orbital control. This approach aims to reduce reliance on traditional propulsion systems, which are often impractical for small-scale spacecraft due to stringent constraints on mass and volume. The research has been structured around two closely interconnected paths. The first involved the high-fidelity aerodynamic characterization of propellantless control devices for atmospheric re-entry, including both deployable and inflatable solutions. This was achieved through an extensive numerical simulation campaign combining CFD and DSMC techniques, enabling accurate modeling of aerodynamic interactions across all flow regimes encountered in LEO, including the transitional regime. The second component introduced a hybrid G&C architecture that merges optimal control theory with AI methods to enable real-time, autonomous decision-making while preserving performance, control optimality and robustness to perturbations and uncertainties. The proposed G&C framework was validated through three representative mission scenarios. The first focused on a time-optimal drag-based de-orbiting strategy designed to ensure precise targeting at the atmospheric re-entry interface. In this case, a novel pattern of the optimal control solution was identified. Based on this, a dedicated algorithm was implemented and used to generate a dataset of optimal solutions, which was used to train an AI-based model capable of estimating the control parameters in real time. The second scenario investigated a controlled re-entry and landing maneuver in which AI techniques were employed to provide adaptive feedback in response to varying aerodynamic conditions. The results demonstrated strong robustness in ensuring accurate landing even in the presence of atmospheric disturbances. Finally, the framework was applied to a collision avoidance scenario, where aerodynamic surfaces were used to maximize the miss distance while minimizing orbital decay with respect to an incoming debris. After applying the optimal control strategy, the AI module enabled real-time execution of the maneuver while maintaining robustness and near-optimal performance under external perturbations. The analysis also demonstrated the important role of high-fidelity aerodynamic models in control system design, highlighting their strong interconnection when planning LEO missions From a broader perspective, this dissertation demonstrates that aerodynamic forces in LEO can be harnessed as a valuable and controllable means of orbital actuation. The results proved that, when supported by accurate aerodynamic modeling and optimal AI-driven decision-making, these forces can serve as the foundation of propellantless control systems. This changes the way orbital maneuvering is conceived for small satellites, showing that aerodynamic-based control represents a feasible and efficient strategy for future missions. The outcomes of this research also establish a new paradigm for G&C design in small spacecraft. By combining optimal control theory with data-driven approaches, the work bridges the gap between analytical optimal control and real-time implementation, overcoming one of the major limitations of traditional approaches. Looking ahead, the implications of this work are significant for the broader space community. The demonstrated feasibility of propellantless aerodynamic control opens the door to a new generation of small satellites that are lighter, more autonomous, and more sustainable. The methodologies presented here could be extended to multi-satellite coordination, formation flying, and end-of-life disposal strategies, contributing to safer and cleaner orbital operations. Moreover, the integration of AI into aerodynamic control architectures could accelerate the transition toward self-governing spacecraft capable of handling complex mission tasks with minimal ground intervention. In conclusion, this dissertation not only advances the state-of-art in propellantless orbital maneuvering but also proves that the combination of AI, optimal control theory, and high-fidelity aerodynamic modeling can serve as a cornerstone for the next generation of space systems. By demonstrating the practical feasibility of fully propellantless G&C, this work lays the foundation for future autonomous, low-cost, and environmentally responsible missions in an increasingly congested and contested orbital environment.

Bibliography

[1] C. Pardini and L. Anselmo, *Evaluating the impact of space activities in low earth orbit*, Acta Astronautica **184**, 11–22 (2021).

[2] NASA, Leo economy: Frequently asked questions, https://www.nasa.gov/humans-in-space/leo-economy-frequently-asked-questions/ (n.d.), accessed: 2025-07-01.

[3] Dragonfly Aerospace, What are some applications of a leo satellite?, https://dragonflyaerospace.com/what-are-some-applications-of-a-leo-satellite/ (2022), accessed 2025-07-01.

[4] EY, Why it's time for investors to get into low earth orbit satellites, https://www.ey.com/en_us/insights/aerospace-defense/why-its-time-for-investors-to-get-into-low-earth-orbit-satellites (2023), accessed 2025-07-01.

[5] L. Garrett, Nasa calls for continuous american 'heartbeat' in leo, https://www.ascend.events/news/nasa-calls-for-continuous-american-heartbeat-in-leo/ (2025), accessed: 2025-07-01.

[6] S. R. Omar and R. Bevilacqua, *Hardware and gnc solutions for controlled spacecraft re-entry using aerodynamic drag*, Acta Astronautica **159**, 49–64 (2019).

[7] D. Guglielmo, S. R. Omar, R. Bevilacqua, L. Fineberg, J. Treptow, B. Poffenberger, and Y. Johnson, *Drag deorbit device: a new standard reentry actuator for cubesats*, AIAA Journal of Spacecraft and Rockets **56**, 129–145 (2019).

[8] A. Fedele, S. Carannante, M. Grassi, and R. Savino, *Aerodynamic control system for a deployable re-entry capsule*, Acta Astronautica **181**, 707–716 (2021).

[9] W. Okolo, B. Margolis, S. D'Souza, and J. Barton, Pterodactyl: Development and Comparison of Control Architectures for a Mechanically Deployed Entry Vehicle, in *AIAA SciTech 2020 Forum* (2020) p. 2012.

[10] A. Alunni, S. D'Souza, B. Yount, W. Okolo, B. Nikaido, B. Margolis, B. Johnson, K. Hibbard,

J. Barton, G. Lopez, and Z. Hays, Pterodactyl: trade study for an integrated control system design of a mechanically deployed entry vehicle, in *AIAA SciTech 2020 Forum* (2020) p. 1014.

[11] E. Gaglio, R. Guida, A. Cecere, S. Mungiguerra, and R. Savino, Assessment of a deployable aerodynamic control system for microsatellites recovery, in English*Proceedings of the International Astronautical Congress, IAC*, Vol. 2022-September (International Astronautical Federation, IAF, 2022).

[12] KSat e.V., Project source, https://www.ksat-stuttgart.de/en/our (2024), accessed: 2025-07-10.

[13] D. Galla, S. Klinkner, G. H. Herdrich, S. Fasoulas, M. Pfeiffer, P. Nizenkov, A. Pagan, K. Boltenhagen, H. Kuhm, M. Laepple, A. Stier, and R. Schweigert, The Educational Platform SOURCE - A CubeSat Mission on Demise Investigation Using In-situ Heat Flux Measurements, in *70th International Astronautical Congress (IAC)* (Washington D.C., United States, 2019).

[14] D. Galla, S. Klinkner, G. H. Herdrich, C. Kaiser, H. Kuhm, and H. Fischer, The Detailed Design of the SOURCE Satellite for Demise Investigation, in *International Symposium on Space Technology and Science (ISTS)* (Beppu, Japan, 2022).

[15] S. R. Omar and R. Bevilacqua, Spacecraft de-orbit point targeting using aerodynamic drag, in *AIAA SciTech Forum* (American Institute of Aeronautics and Astronautics, 2017).

[16] S. R. Omar, R. Bevilacqua, D. Guglielmo, L. Fineberg, J. Treptow, S. Clark, and Y. Johnson, *Spacecraft deorbit point targeting using aerodynamic drag*, AIAA Journal of Guidance, Control, and Dynamics **40**, 1–7 (2017).

[17] S. R. Omar and R. Bevilacqua, *Guidance, navigation and control solutions for spacecraft re-entry point targeting using aerodynamic drag*, Acta Astronautica **155**, 389–405 (2019).

[18] D. L. Akin, Applications of Ultra-Low Ballistic Coefficient Entry Vehicles to Existing and Future Space Missions, in *AIAA SPACE 2010 Conference & Exposition* (2010).

[19] R. Monti and G. Zuppardi, *Elementi di Aerodinamica Ipersonica*, 2nd ed. (Liguori Editore, 2012).

[20] L. M. et al., IRDT-2R Mission, First Results, in *Thermal Protection Systems and Hot Structures*, Vol. 631 (2006) p. 5.

[21] L. M. et al., Irdt-inflatable re-entry and descent technology automated transfer vehicle reentry flow and explosion assessment view project mars metnet mission view project (2003).

[22] S. J. Hughes, F. M. Cheatwood, R. A. Dillman, H. S. Wright, J. A. del Corso, and A. M. Calomino, Hypersonic Inflatable Aerodynamic Decelerator (HIAD) technology development overview, in *21st AIAA Aerodynamic Decelerator Systems Technology Conference and Seminar* (2011).

[23] D. K. Litton *et al.*, Inflatable Re-Entry Vehicle Experiment (IRVE) - 4 overview, in *21st AIAA Aerodynamic Decelerator Systems Technology Conference and Seminar 2011* (2011).

[24] S. Hughes *et al.*, Inflatable Re-entry Vehicle Experiment (IRVE) Design Overview, in *18th*

AIAA Aerodynamic Decelerator Systems Technology Conference and Seminar (2005).

[25] M. C. Lindell *et al.*, Structural analysis and testing of the Inflatable Re-entry Vehicle Experiment (IRVE), in *Collection of Technical Papers - AIAA/ASME/ASCE/AHS/ASC Structures, Structural Dynamics and Materials Conference 2* (2006) pp. 1303–1321.

[26] J. A. del Corso *et al.*, Advanced high-temperature flexible TPS for inflatable aerodynamic decelerators, in *21st AIAA Aerodynamic Decelerator Systems Technology Conference and Seminar 2011* (2011).

[27] R. A. S. Beck *et al.*, Overview of initial development of flexible ablators for hypersonic inflatable aerodynamic decelerators, in *21st AIAA Aerodynamic Decelerator Systems Technology Conference and Seminar 2011* (2011).

[28] A. M. Cassell *et al.*, Overview of the hypersonic inflatable aerodynamic decelerator large article ground test campaign, in *21st AIAA Aerodynamic Decelerator Systems Technology Conference and Seminar 2011* (2011).

[29] A. M. Cassell *et al.*, Design and execution of the hypersonic inflatable aerodynamic decelerator large-article wind tunnel experiment, in *AIAA Aerodynamic Decelerator Systems (ADS) Conference 2013* (2013).

[30] C. D. Kazemba *et al.*, Determination of the deformed structural shape of HIADs from photogrammetric wind tunnel data, in *AIAA Aerodynamic Decelerator Systems (ADS) Conference 2013* (2013).

[31] J. S. Green, R. E. Lindberg, and B. J. Dunn, Morphing hypersonic inflatable aerodynamic decelerator, in *AIAA Aerodynamic Decelerator Systems (ADS) Conference 2013* (2013).

[32] E. V. et al., Adaptive deployable entry and placement technology (ADEPT): A feasibility study for human missions to Mars, in *21st AIAA Aerodynamic Decelerator Systems Technology Conference and Seminar* (2011).

[33] J. O. Arnold, Y.-K. Chen, D. K. Prabhu, M. E. Bittner, E. Venkatapathy, *et al.*, Arcjet testing of woven carbon cloth for use on adaptive deployable entry placement technology, in *2013 IEEE Aerospace Conference* (2013) aRC-EDAA-TN6341.

[34] A. C. et al., System level aerothermal testing for the Adaptive Deployable Entry and Placement Technology (ADEPT), in *International Planetary Probe Workshop (IPPW-13)* (2016) aRC-E-DAA-TN32668.

[35] E. B. et al., IRENE: Italian re-entry Nacelle for microgravity experiments (2011).

[36] B. J. Reddish *et al.*, *Pterodactyl: Aerodynamic and Aerothermal Modeling for a Symmetric Deployable Earth Entry Vehicle with Flaps*, Technical Report (NASA, 2020).

[37] A. I. Alunni *et al.*, *Pterodactyl: Trade Study for an Integrated Control System Design of a Mechanically Deployable Entry Vehicle*, Technical Report (NASA, 2020).

[38] S. N. D'Souza and N. Sarigul-Klijn, *Survey of planetary entry guidance algorithms*, Progress in Aerospace Sciences **68**, 64–74 (2014).

[39] R. P. Patera and W. H. Ailor, *The realities of reentry disposal*, Advances in the Astronautical Sciences **99**, 1059–1071 (1998).

[40] R. P. Patera and W. H. Ailor, *Spacecraft reentry strategies: meeting debris mitigation and ground safety requirements*, Proceedings of the Institution of Mechanical Engineers, Part G: Journal of Aerospace Engineering **221**, 947–953 (2007).

[41] J. Virgili, P. C. E. Roberts, and N. C. Hara, *Atmospheric interface reentry point targeting using aerodynamic drag control*, AIAA Journal of Guidance, Control, and Dynamics **38**, 403–413 (2015).

[42] S. Dutta, A. Bowes, A. M. D. Cianciolo, C. Glass, and R. W. Powell, Guidance scheme for modulation of drag devices to enable return from Low Earth orbit, in *AIAA Atmospheric Flight Mechanics Conference* (2017) paper 0467, January.

[43] J. Virgili and P. C. E. Roberts, *deltadsat: a qb50 cubesat mission to study rarefied-gas drag modelling*, Acta Astronautica **89**, 130–138 (2013).

[44] A. Fedele, S. Omar, S. Cantoni, R. Savino, and R. Bevilacqua, *Precise re-entry and landing of propellantless spacecraft*, Advances in Space Research **68**, 4336–4358 (2021).

[45] A. Rossi and G. Valsecchi, *Collision risk against space debris in earth orbits*, Celest. Mech. Dyn. Astron. **95**, 345–356 (2006).

[46] D. J. Kessler and B. G. Cour-Palais, *Collision frequency of artificial satellites: The creation of a debris belt*, J. Geophys. Res. Space Phys. **83**, 2637–2646 (1978).

[47] A. Sandberg and T. Sands, *Autonomous trajectory generation algorithms for spacecraft slew maneuvers*, Aerospace **9** (2022).

[48] K. Raigoza and T. Sands, *Autonomous trajectory generation comparison for de-orbiting with multiple collision avoidance*, Sensors **22** (2022).

[49] E. Wilt and T. Sands, *Microsatellite uncertainty control using deterministic artificial intelligence*, Sensors **22** (2022).

[50] B.-R. Huang and T. Sands, *Novel learning for control of nonlinear spacecraft dynamics*, J. Appl. Math **1** (2021).

[51] P. Yao and T. Sands, *Micro satellite orbital boost by electrodynamic tethers*, Micromachines **12** (2021).

[52] T. Williams and Z.-S. Wang, *Uses of solar radiation pressure for satellite formation flight*, Internat. J. Robust Nonlinear Control **12**, 163–183 (2002).

[53] S. Tsujii, M. Bando, and H. Yamakawa, *Spacecraft formation flying dynamics and control using the geomagnetic lorentz force*, J. Guid. Control Dyn. **36**, 136–148 (2013).

[54] S. R. Omar and R. Bevilacqua, *Spacecraft collision avoidance using aerodynamic drag*, J. Guid. Control Dyn. **43**, 567–573 (2020).

[55] A. W. Koenig and S. D'Amico, *Robust and safe n-spacecraft swarming in perturbed near-circular orbits*, J. Guid. Control Dyn. **41**, 1643–1662 (2018).

[56] D. Mishne and E. Edlerman, *Collision-avoidance maneuver of satellites using drag and solar radiation pressure*, J. Guid. Control Dyn. **40**, 1191–1205 (2017).

[57] F. Turco, C. Traub, S. Gaißer, J. Burgdorf, S. Klinkner, and S. Fasoulas, *An analysis tool*

for collision avoidance manoeuvres using aerodynamic drag, Acta Astronaut. **211**, 116–129 (2023).

[58] F. Turco, C. Traub, S. Gaißer, J. Burgdorf, S. Klinkner, and S. Fasoulas, *Analysis of collision avoidance manoeuvres using aerodynamic drag for the flying laptop satellite*, Aerotecnica Missili Spazio **103**, 61–71 (2024).

[59] D. R. Olave, N. C. Jara, R. C. Palharini, R. S. A. Palharini, E. Gaglio, and R. Savino, *Inflatable aerodynamic decelerator for cubesat reentry and recovery: Altitude effects on the flowfield structure*, Aerospace Science and Technology **138**, 108358 (2023).

[60] N. Caqueo, R. C. Palharini, R. S. A. Palharini, E. Gaglio, and R. Savino, *Inflatable aerodynamic decelerators for cubesat reentry and recovery: Surface properties*, Aerospace Science and Technology **149**, 109151 (2024).

[61] N. C. Jara, D. R. Olave, R. C. Palharini, E. Gaglio, R. S. A. Palharini, and R. Savino, *Inflatable aerodynamic decelerator for cubesat reentry and recovery: Iad geometrical effects on the flowfield structure*, Aerospace Science and Technology **141**, 108571 (2023).

[62] E. Gaglio, A. Cecere, R. Guida, S. Mungiguerra, R. Savino, N. Caqueo Jara, and R. Cassineli Palharini, Aerodynamic analysis of a flap-based deployable re-entry system in different flight conditions, in *25th AIAA International Space Planes and Hypersonic Systems and Technologies Conference* (2023) p. 3000.

[63] D. V. Sepulveda, R. C. Palharini, E. Gaglio, and R. Savino, *Aerodynamic analysis of a flap-based deployable re-entry system under rarefied conditions*, *34th ICAS Congress* (2024).

[64] E. Gaglio, M. Visone, M. Lanzetta, S. Mungiguerra, A. Cecere, and R. Savino, *Mixed-compression supersonic intake and engine–airframe integration*, Journal of Spacecraft and Rockets **60**, 1100–1111 (2023).

[65] E. Gaglio, A. Cecere, S. Mungiguerra, R. Savino, M. Visone, and M. Lanzetta, in *ASCEND 2021* (2021) p. 4200.

[66] A. Sannino, E. Gaglio, S. Mungiguerra, A. Cecere, and R. Savino, *Aerodynamic study of a 3u cubesat for drag-based in-plane orbital maneuvers in very low earth orbit*, Acta Astronautica (2025).

[67] E. Gaglio and R. Bevilacqua, *Time optimal drag-based targeted de-orbiting for low earth orbit*, Acta Astronautica **207**, 316–330 (2023).

[68] E. Gaglio and R. Bevilacqua, Machine Learning Based Guidance for Optimal Spacecraft De-Orbiting, in *Proceedings of the 74th International Astronautical Congress (IAC)* (Baku, Azerbaijan, 2023) 2–6 October 2023.

[69] E. Gaglio and R. Bevilacqua, *Drag-based analytical optimal de-orbiting guidance from low earth orbit via deep neural networks*, Acta Astronaut. **218**, 383–397 (2024).

[70] E. Gaglio and R. Bevilacqua, A Novel Time-Optimal Algorithm for an Aerodynamic-Based Targeted Re-Entry, in *Proceedings of the 4th IAA Conference on Space Situational Awareness* (International Academy of Astronautics (IAA), Daytona Beach, FL, USA, 2024).

[71] E. Gaglio and R. Bevilacqua, *Machine learning-based quasi-optimal feedback control for a*

propellantless re-entry, Acta Astronautica **228**, 274–284 (2025).

[72] E. Gaglio, C. Traub, F. Turco, J. O. Murcia-Piñeros, R. Bevilacqua, and S. Fasoulas, Optimal Spacecraft Collision Avoidance Using Aerodynamic Drag, in *Proceedings of the 4th IAA Conference on Space Situational Awareness* (International Academy of Astronautics (IAA), Daytona Beach, FL, USA, 2024).

[73] E. Gaglio, C. Traub, F. Turco, J. O. M. Pineros, R. Bevilacqua, and S. Fasoulas, *Optimal drag-based collision avoidance: Balancing miss distance and orbital decay*, Acta Astronautica **228**, 295–305 (2025).

[74] E. Gaglio, C. Traub, A. Sannino, S. Mungiguerra, F. Turco, S. Fasoulas, R. Savino, and R. Bevilacqua, Machine Learning-Based Quasi-Optimal Feedback Control for a Propellant-less Collision Avoidance in Very Low Earth Orbit, in *Proceedings of the 2nd International Symposium on Very Low Earth Orbit Missions and Technologies*, VLEO2025-9-03 (2025).

[75] E. Gaglio, C. Traub, A. Sannino, S. Mungiguerra, F. Turco, S. Fasoulas, R. Savino, and R. Bevilacqua, *Quasi-optimal guidance and control in very low earth orbit via deep learning for drag-based collision avoidance*, Acta Astronautica **235**, 362–374 (2025).

[76] E. Gaglio and R. Bevilacqua, *Cislunar satellite motion prediction via hybrid parametric and deep learning models*, Acta Astronautica **237**, 381–394 (2025).

[77] E. Gaglio and R. Bevilacqua, Hybrid Strategies for Cislunar Stability and Motion, in *Proceedings of the 35th AAS/AIAA Space Flight Mechanics Meeting*, AAS 25-401 (2025).

[78] J. Murcia-Piñeros, R. Bevilacqua, E. Gaglio, A. B. Prado, and R. V. De Moraes, Optimization of Aero-gravity assisted maneuvers for spaceplanes at high atmospheric flight on Earth, in *AIAA SCITECH 2024 Forum* (2024) p. 1459.

[79] J. O. Murcia-Piñeros, R. Bevilacqua, E. Gaglio, A. F. Prado, and R. V. Moraes, *Spaceplane model predictive control and guidance for aerogravity assisted maneuvers above earth*, Acta Astronautica **238**, 1266–1279 (2026).

[80] S. R. Carná and R. Bevilacqua, *High fidelity model for the atmospheric re-entry of cubesats equipped with the drag de-orbit device*, Acta Astronautica **156**, 134–156 (2019).

[81] J. J. Bertin and R. M. Cummings, *Critical hypersonic aerothermodynamic phenomena*, Annu. Rev. Fluid Mech. **38**, 129–157 (2006).

[82] F. R. Menter, M. Kuntz, and R. Langtry, *Ten Years of Industrial Experience with the SST Turbulence Model*.

[83] S. Saha and D. Chakraborty, *Hypersonic intake starting characteristics–a cfd validation study*, Defence Science Journal **62**, 147–152 (2012).

[84] S. Emami, C. A. Trexler, A. H. Auslender, and J. P. Weidner, *Experimental Investigation of Inlet-Combustor Isolators for a Dual-Mode Scramjet at a Mach Number of 4*, NASA Technical Report NASA-TM-106566 (NASA, 1995) accessed on 2025-10-06.

[85] E. Josyula and J. Burt, *Review of Rarefied Gas Effects in Hypersonic Applications*, Tech. Rep. (Air Force Research Lab Wright-Patterson AFB OH, 2011).

[86] T. E. Schwartzentruber, M. S. Grover, and P. Valentini, *Direct molecular simulation of*

nonequilibrium dilute gases, J. Thermophys. Heat Transf. **32**, 892–903 (2018).

[87] T. E. Schwartzentruber and I. D. Boyd, Progress and future prospects for particle-based simulation of hypersonic flow, in *43rd Fluid Dynamics Conference* (2013) pp. 1–19.

[88] G. A. Bird, *Molecular Gas Dynamics and the Direct Simulation of Gas Flows*, 1st ed. (Oxford Science Publications, 1994).

[89] I. D. Boyd and T. E. Schwartzentruber, *Nonequilibrium Gas Dynamics and Molecular Simulation* (Cambridge University Press, 2017).

[90] F. J. Alexander and A. L. Garcia, *The direct simulation monte carlo method*, Comput. Phys. **11**, 588 (1997).

[91] A. L. Garcia, Direct simulation Monte Carlo: theory, methods, and open challenges, in *Proceedings of the Models and Computational Methods for Rarefied Flows, NATO Conf. Proc. RTO-EN-AVT-194* (2011) pp. 1–12.

[92] G. A. Bird, *Recent advances and current challenges for dsmc*, Comput. Math. Appl. **35**, 1–14 (1998).

[93] G. A. Bird, *Forty years of dsmc, and now?*, AIP Conference Proceedings **585**, 372–380 (2001).

[94] T. J. Scanlon, E. Roohi, C. White, M. Darbandi, and J. M. Reese, *An open source, parallel dsmc code for rarefied gas flows in arbitrary geometries*, Comput. Fluids **39**, 2078–2089 (2010).

[95] C. White, M. Borg, T. Scanlon, S. Longshaw, B. John, D. Emerson, and J. Reese, *dsmcfoam+: an openfoam based direct simulation monte carlo solver*, Comput. Phys. Commun. **224**, 22–43 (2018).

[96] C. Borgnakke and P. S. Larsen, *Statistical collision model for monte carlo simulation of polyatomic gas mixture*, J. Comput. Phys. **18**, 405–420 (1975).

[97] G. Bird, in *Progress in Astronautics and Aeronautics*, Vol. 118 (1989) p. 211.

[98] J. Allègre, D. Bisch, and J. Lengrand, *Experimental rarefied density flowfield at hypersonic conditions over 70–degree blunted cone*, Journal of Spacecraft and Rockets **34**, 714–718 (1997).

[99] J. Allègre, D. Bisch, and J. Lengrand, *Experimental rarefied aerodynamic forces at hypersonic conditions over 70–degree blunted cone*, Journal of Spacecraft and Rockets **34**, 719–723 (1997).

[100] J. Allègre, D. Bisch, and J. Lengrand, *Experimental rarefied heat transfer at hypersonic conditions over 70–degree blunted cone*, Journal of Spacecraft and Rockets **34**, 724–728 (1997).

[101] W. Saric, J. Muylaert, and C. Dujarric, *Hypersonic experimental and computational capability, improvement and validation, vol. 1*, Tech. Rep. (Advisory Group for Aerospace Research and Development, Neuilly-sur-Seine, 1996).

[102] J. Muylaert, A. Kumar, and C. Dujarric, *Hypersonic Experimental and Computational Capa-*

bility, Improvement and Validation, Tech. Rep. (North Atlantic Treaty Organization, Advisory Group for Aerospace Research & Development, 1998).

[103] J. Moss, V. Dogra, and R. Wilmoth, *DSMC simulations of Mach 20 nitrogen about 70-degree blunted cone and its wake*, Tech. Rep. NASA TM-107762 (NASA, 1993).

[104] C. L. Darby, W. W. Hager, and A. V. Rao, *An hp-adaptive pseudospectral method for solving optimal control problems*, Optimal Control Applications and Methods **32**, 476–502 (2011).

[105] tf.keras.activations — tensorflow api documentation, `https://www.tensorflow.org/api_docs/python/tf/keras/activations`, accessed: 2025-08-18.

[106] A. L. Maas, A. Y. Hannun, A. Y. Ng, *et al.*, Rectifier nonlinearities improve neural network acoustic models, in *Proc. icml*, Vol. 30 (Atlanta, GA, 2013) p. 3.

[107] K. He, X. Zhang, S. Ren, and J. Sun, Delving deep into rectifiers: Surpassing human-level performance on imagenet classification, in *Proceedings of the IEEE international conference on computer vision* (2015) pp. 1026–1034.

[108] D.-A. Clevert, T. Unterthiner, and S. Hochreiter, *Fast and accurate deep network learning by exponential linear units (elus)*, arXiv preprint arXiv:1511.07289 **4**, 11 (2015).

[109] A. Zaras, N. Passalis, and A. Tefas, in *Deep learning for robot perception and cognition* (Elsevier, 2022) pp. 17–34.

[110] V. Carandente, G. Zuppardi, and R. Savino, *Aerothermodynamic and stability analyses of a deployable re-entry capsule*, Acta Astronautica **93**, 291–303 (2014).

[111] NOAA/NASA/USAF, *U.S. Standard Atmosphere* (U.S. Government Printing Office, 1976).

[112] E. Gaglio, R. Guida, A. Cecere, S. Mungiguerra, R. Savino, *et al.*, Assessment of a deployable aerodynamic control system for microsatellites recovery, in *Proceedings of IAC 2022* (2022).

[113] A. Fedele, S. Omar, S. Cantoni, R. Savino, and R. Bevilacqua, Precise Re-Entry and Landing of Propellantless Low Earth Orbit Spacecraft, in *2nd IAA Conference on Space Situational Awareness (ICSSA)* (Arlington, VA, USA, 2020).

[114] B. J. Reddish, B. E. Nikaido, S. N. D'Souza, V. M. Hawke, Z. B. Hays, and H. S. Kang, Pterodactyl: Aerodynamic and Aerothermal Modeling for a Symmetric Deployable Earth Entry Vehicle with Flaps, in *AIAA SciTech Forum* (2021).

[115] M. A. Patterson and A. V. Rao, *GPOPS-II: a matlab software for solving multiple-phase optimal control problems using hp-adaptive gaussian quadrature collocation methods and sparse nonlinear programming*, ACM Transactions on Mathematical Software **41**, 1:1–1:37 (2014).

[116] A. V. Rao, D. A. Benson, C. L. Darby, C. Francolin, M. A. Patterson, I. Sanders, and G. T. Huntington, *Algorithm 902: GPOPS, a matlab software for solving multiple-phase optimal control problems using the gauss pseudospectral method*, ACM Transactions on Mathematical Software **37**, Article 22 (2010).

[117] D. A. Benson, G. T. Huntington, T. P. Thorvaldsen, and A. V. Rao, *Direct trajectory optimization and costate estimation via an orthogonal collocation method*, AIAA Journal of Guidance, Control, and Dynamics **29**, 1435–1440 (2006).

[118] G. T. Huntington and A. V. Rao, *Optimal reconfiguration of tetrahedral spacecraft formations using the gauss pseudospectral method*, AIAA Journal of Guidance, Control, and Dynamics **31**, 689–698 (2008).

[119] G. Baù, J. Hernando-Ayuso, and C. Bombardelli, *A generalization of the equinoctial orbital elements*, Celestial Mechanics and Dynamical Astronomy **133**, 1–29 (2021).

[120] M. Walker, B. Ireland, and J. Owens, *A set of modified equinoctial orbital elements*, Celestial Mechanics **36**, 409–419 (1985).

[121] R. Brouke and P. Cefola, *On the equinoctial orbital elements*, Celestial Mechanics **5**, 303–310 (1972).

[122] C. Sánchez-Sánchez and D. Izzo, *Real-time optimal control via deep neural networks: study on landing problems*, Journal of Guidance, Control, and Dynamics **41**, 1122–1135 (2018).

[123] N. X. Vinh, A. Busemann, and R. D. Culp, *Hypersonic and planetary entry flight mechanics*, NASA Sti/Recon Technical Report A **81**, 16245 (1980).

[124] D. P. Drob, J. T. Emmert, J. W. Meriwether, J. J. Makela, E. Doornbos, M. Conde, G. Hernandez, J. Noto, K. A. Zawdie, S. E. McDonald, J. D. Huba, and J. H. Klenzing, *An update to the horizontal wind model (hwm)* (2015).

[125] J. M. Picone, A. E. Hedin, D. P. Drob, and A. C. Aikin, *NRLMSISE-00 empirical model of the atmosphere: Statistical comparisons and scientific issues*, Journal of Geophysical Research: Space Physics **107**, SIA 15–1–SIA 15–16 (2002).

[126] L. A. Sinpetru, N. H. Crisp, D. Mostaza-Prieto, S. Livadiotti, and P. C. E. Roberts, *ADBSat: Methodology of a novel panel method tool for aerodynamic analysis of satellites*, Computer Physics Communications **275**, 108326 (2022).

[127] F. Turco, C. Traub, S. Gaißer, J. Burgdorf, S. Klinkner, and S. Fasoulas, *An analysis tool for collision avoidance manoeuvres using aerodynamic drag*, Acta Astronautica **211**, 116–129 (2023).

[128] L. Sinpetru, N. H. Crisp, P. C. E. Roberts, V. Sulliotti-Linner, V. Hanessian, G. H. Herdrich, F. Romano, D. Garcia-Alminana, S. Rodriguez-Donaire, and S. Seminari, *ADBSat: Verification and validation of a novel panel method for quick aerodynamic analysis of satellites*, Computer Physics Communications **275**, 108327 (2022).

[129] B. M. Pilinski, M. D.; Argrow and S. E. Palo, *Semiempirical model for satellite energy-accommodation coefficients*, Journal of Spacecraft and Rockets **47**, 951–956 (2010).

[130] International Organization for Standardization, Space environment (natural and artificial) - Earth's atmosphere from ground level upward: ISO 14222:2022(E) (2022-03).

[131] L. Dell'Elce, *Satellite orbits in the atmosphere*, Ph.D. thesis, Université de Liège (2015).

[132] R. H. Battin, *Introduction to the mathematics and methods of astrodynamics* (American Institute of Aeronautics and Astronautics, 2000).

[133] G. A. Bird, *Molecular Gas Dynamics and the Direct Simulation of Gas Flows* (Clarendon, Oxford, 1994)